Durham E-Theses

Crustal structure of the Baltic shield beneath the Sea of Bothnia; BABEL line 6

Matthews, P.A.

How to cite:

Matthews, P.A. (1993) *Crustal structure of the Baltic shield beneath the Sea of Bothnia; BABEL line 6*, Durham theses, Durham University. Available at Durham E-Theses Online: http://etheses.dur.ac.uk/5720/

Use policy

The full-text may be used and/or reproduced, and given to third parties in any format or medium, without prior permission or charge, for personal research or study, educational, or not-for-profit purposes provided that:

- a full bibliographic reference is made to the original source
- a link is made to the metadata record in Durham E-Theses
- the full-text is not changed in any way

The full-text must not be sold in any format or medium without the formal permission of the copyright holders.

Please consult the full Durham E-Theses policy for further details.

Academic Support Office, Durham University, University Office, Old Elvet, Durham DH1 3HP
e-mail: e-theses.admin@dur.ac.uk Tel: +44 0191 334 6107
http://etheses.dur.ac.uk

Crustal Structure of the Baltic Shield beneath the Sea of Bothnia: BABEL line 6

by

P. A. Matthews

The copyright of this thesis rests with the author.
No quotation from it should be published without
his prior written consent and information derived
from it should be acknowledged.

A thesis submitted for the degree of Doctor of Philosophy
at the University of Durham

Department of Geological Sciences
University of Durham
1993

- 2 JUL 1993

Where were you when I laid the earth's foundations ?

Tell me, since you are so well informed !

Who decided the dimensions of it, do you know ?

Or who stretched the measuring line across it ?

What supports its pillars at their bases ?

Who laid its corner stone

When all the stars of morning were singing for joy,

and the Sons of God in chorus were chanting praise ?

Job 38:4-7

ABSTRACT

As part of the 1989 BABEL project, Durham University recorded large quantities of high resolution wide-angle data from six deep seismic lines shot in the Gulf of Bothnia. Fifteen analogue and three digital seismic recording stations were used, located in Sweden around the Sea of Bothnia. The wide-angle data is of very high quality due to the low noise and good transmission of seismic energy through the cratonic crust of the Baltic Shield.

BABEL line 6 is a 240 km long, north-south profile in the western half of the Sea of Bothnia that runs almost parallel to several deep seismic refraction profiles previously acquired in Sweden and Finland. A crustal model has been developed for this line from P- and S-wave wide-angle data recorded at five of the online recording stations and from the normal-incidence data.

This model has been generated by raytracing methods using a modified version of the BEAM87 gaussian beam package. Wide-angle arrivals are interpreted as diving rays and wide-angle reflections and as 'diffraction-type' arrivals from offsets on reflecting boundaries. The wide-angle reflections appear to correspond to the boundaries between high and low reflectivity zones in the normal-incidence data. The 'diffraction-type' arrivals appear to be related to surface features such as the Ljusnan tectonic zone and the Aranda rift. There is no evidence for a Moho trench similar to those seen on neighbouring profiles. Several high velocity layers are required in the model. These may be the related to the numerous post-orogenic intrusions that have occurred in the Svecofennian region of the Baltic Shield.

Traditional approaches to modelling wide-angle data assume that the crust consists of a series of extensive, quasi-horizontal, layers. There are several problems with this approach. In particular it does not explain the patchy reflectivity seen in the normal-incidence data or the rapid variation in amplitude seen along wide-angle arrivals in high resolution data sets. Apparently continuous wide-angle arrivals may be generated from a series of short length reflectors. These show an amplitude variation similar to that seen in the experimental data. This suggests that wide-angle arrivals may arise from the assemblages of reflectors that are often imaged on normal-incidence data.

ACKNOWLEDGEMENTS

BABEL was an international collaboration between people from many different institutions and from various countries. I am grateful to all those who have been part of the BABEL project; to the members of the BABEL working group, to Hans Palm of Uppsala university for surveying the recording sites prior to the project and to everyone else who was involved in the fieldwork. In particular, I am grateful to Erich Lippmann for organising the logistics of the Durham side of the experiment and for all his hard work during the project.

I would like to thank my supervisor, Dr Roger Long, for his advice, discussions, programs and several interesting and scenic conferences! I would also like to thank Lesley McEleavey for her work in playing out various Geostore records, Dave Stevenson for his programs and endless help with temperamental computer systems, Cliff Prescott and Chris Peirce for 'Razzle-Dazzle', Danny Graham for his work on BABEL line 1 and British Petroleum for funding this studentship.

I am also grateful to the many people who have helped keep me going through this project, especially to my parents for their long and sympathetic phone calls and, of course, to the geophysics rabble: Chris, Dave, Danny, Ed, Miles, Neville, Peter, and Richard, for software, sympathy, proof-reading and beer. May the SUNs never go down on them!

CONTENTS

Abstract i
Acknowledgements ii
Contents iii
List of Figures vii
List of Tables x

I - INTRODUCTION 1

II - GEOLOGICAL EVOLUTION OF THE BALTIC SHIELD 6
2.1 The Baltic Shield 6
2.2 The Archaean dmain 10
2.3 The Svecokarelian dmain 10
2.3.1 The Karelides 12
2.3.2 The Svecofennides 12
2.3.3 Late Svecofennian mgashears 15
2.4 The Southwest Scandinavian dmain 16
2.5 Palaeomagnetic results 17
2.6 Geology of the Bothnian Sea 17
2.7 Water depth and near-surface geology beneath line 6 22

III - GEOPHYSICAL STUDIES OF THE BALTIC SHIELD 24
3.1 Deep seismic wide-angle reflection profiles24 .....
3.1.1 Sylen-Porvoo 25
3.1.2 Blue Road 27
3.1.3 FENNOLORA 29
3.1.4 SVEKA 31
3.1.5 BALTIC 34
3.2 Other crustal studies 35
3.2.1 Permanent seismic stations 35
3.2.2 Aeromagnetic and gravity surveys 36
3.2.3 Geoelectric studies 40

3.2.4 Heat flow 40
3.3 Generalised structure of the Baltic Shield 42

IV - BABEL 1989: DATA ACQUISITION 44
4.1 The BABEL profiles 44
4.2 Marine shots 46
4.3 Seismic recording stations 49
4.4 Equipment 52
4.4.1 Analogue Geostore array 52
4.4.2 Digital PDAS recorders 54
4.4.3 Frequency response 56

V - DATA CONVERSION 58
5.1 Conversion to SEGY-WAR 58
5.1.1 Conversion from PDAS format to SEGYi format 60
5.1.2 Conversion from Geostore format to SEGYi format 63
5.2 Internal clock drift 65

VI - THE BABEL DATA SECTIONS 68
6.1 Wide-angle data 68
6.1.1 Frequency analysis 68
6.1.2 Filtering 73
6.1.3 Other wide-angle data processing 75
6.1.4 Plotting 76
6.1.5 Wide-angle data sections 77
6.1.6 Selection of arrivals 90
6.1.7 Errors 91
6.2 Normal-incidence data 92
6.2.1 Frequency spectra 92
6.2.2 Crustal reflectivity patterns 92
6.2.3 BABEL line 6 normal-incidence data 95

VII - BEAM87 - GAUSSIAN BEAM RAY-TRACING 98
7.1 Modelling wide-angle data 98
7.2 Amplitude calculations along raypaths 100
7.2.1 Simple case: a sloping fluid/solid boundary 101
7.2.2 Laterally varying fluid 104
7.2.3 More complex cases 105

7.3 Problems with generalised ray theory 110
7.4 The Gaussian beam method 110
7.4.1 B87_RTNI (raytracing) 111
7.4.2 B87_RPNI (Plotting of rays, travel-times and amplitudes) 113
7.4.3 B87_GBNI (Gaussian beam method) 114
7.4.4 B87_SYNTNI (Synthetic seismogram generation) 117
7.4.5 Synthetic seismogram plotting 118

VIII - RESULTS FROM RAYTRACING 119
8.1 Introduction 119
8.2 Diffraction-type arrivals 120
8.3 Modelling BABEL line 6 123
8.4 Travel time modelling 124
8.4.1 Reversed model: P-wave data from, BS5P and Z2A 125
8.4.2 S-wave modelling 127
8.4.3 Normal-incidence data 127
8.5 The line 6 model 137
8.5.1 Upper crust (layers 1, 2, 3 and 4) 137
8.5.2 Mid crust (layers 5, 6 and 7) 138
8.5.3 Lower crust (layers 8 and 9 140
8.5.4 The Moho (base of layer 10) 141
8.5.5 The Moho trench model 141
8.5.6 Mantle reflectors 147
8.5.7 P- and S-wave velocities 147
8.6 Synthetic seismogram modelling 151
8.6.1 BS5P 151
8.6.2 Z2A 154
8.6.3 Normal-incidence synthetic section 156
8.7 Comparison of the results from the line 6 model with the experimental data from BS5, Z5A and Z1A 158
8.7.1 BS5 158
8.7.2 Z5A 161
8.7.3 Z1A 161
8.8 Summary 165

IX - INTERPRETATION OF THE LINE 6 MODEL 166
9.1 Comparison to previous Deep Seismic refraction profiles 166
9.2 Geophysical interpretation: gravity and magnetics 172

9.3 Comparison to other BABEL profiles 175
9.4 Tectonic interpretation 178
9.4.1 Jotnian dolerite sills 178
9.4.2 Southern and central Svecofennian provinces 182
9.4.3 Reflectivity patterns 182
9.4.4 High velocity layers and intrusions 183
9.4.5 Archaean basement and mantle reflectors 184
9.4.6 Baltic-Bothnian shear zone 186
9.4.7 Relation of surface faults to crustal structure 186
9.4.8 Evolutionary models 189

X - IS TRADITIONAL RAYTRACING ADEQUATE ? 191
10.1 Problems with the traditional raytracing approach 192
10.1.1 General problems 192
10.1.2 Problems with the line 6 model 193
10.2 Alternative crustal models 194
10.2.1 A simple sinusoidal reflector 196
10.2.2 Lower crustal lenses 196
10.2.3 Short length reflectors in the lower crust 200
10.2.4 The WART 204
10.3 The nature of the lower crust and the seismic Moho 209

XI - SUMMARY AND FUTURE WORK 211
11.1 Summary 211
11.1.1 The BABEL data 211
11.1.2 Geological and tectonic results 212
11.1.3 Wide-angle data and crustal structure 213
11.2 Future work 214
11.2.1 Further work on the BABEL data 214
11.2.2 Future geophysical surveys in the Gulf of Bothnia 215
11.2.3 Development of wide-angle techniques 216

References 218
Appendix A 225
Appendix B 227

LIST OF FIGURES

CHAPTER I

Figure 1.1. Location of the 1989 BABEL profiles 2
Figure 1.2. Traditional wide-angle arrivals 4

CHAPTER II

Figure 2.1. Outline of the geology of the Baltic Shield 7
Figure 2.2. Precambrian geology of the Baltic shield 9
Figure 2.3. Cartoons of the growth of the Baltic Shield 11
Figure 2.4.. Palaeoenvironments of the Svecofennides 13
Figure 2.5. Strike-slip megashears in the Baltic Shield 15
Figure 2.6 Palaeomagnetic history of Fennoscandia 18
Figure 2.7. Bathymetry map of the Sea of Bothnia 19
Figure 2.8 Locations of major faults within the Sea of Bothnia 20
Figure 2.9. Lithology map of the Sea of Bothnia. 21
Figure 2.10.. Water depth and related surface geology along BABEL line 6 23

CHAPTER III

Figure 3.1. Deep seismic refraction profiles in the Svecofennides 25
Figure 3.2. Sylen-Porvoo profile 26
Figure 3.3. Blue Road profile 28
Figure 3.4. FENNOLORA profile 30
Figure 3.5. Location of the BALTIC and SVEKA profiles 32
Figure 3.6. Crustal models for the SVEKA and BALTIC profiles 33
Figure 3.7. Earthquake epicentres in Fennoscandia from 1375 to 1989 36
Figure 3.8 **a)** Postglacial uplift in Fennoscandia
b) Bouger anomalies in the Sea of Bothnia 37
Figure 3.9 **a)** Magnetic anomaly map of the Sea of Bothnia
b) Sketch map of aeromagnetic anomalies 39
Figure 3.10. **a)** Crustal conductivity anomalies
b) Regional heat-flow density 41
Figure 3.11. Moho depth isolines compiled prior to BABEL 43

CHAPTER IV

Figure 4.1. Location map of the BABEL profiles 45
Figure 4.2. Configuration of the S/V MINTROP airgun array 47
Figure 4.3. Farfield source signature and frequency spectrum 47
Figure 4.4. Locations of recording stations operated by Durham 50
Figure 4.5. Diagrams of the Geostore and PDAS recorders 53
Figure 4.6. **a)** Normalised seismometer response curves
b) PDAS anti-aliasing filter
c) Store-14 (Geostore playback) filter 57

CHAPTER V

Figure 5.1. Flow chart of conversion to SEGYi format 59
Figure 5.2. Playback system for the field data 60
Figure 5.3. MSF radio time signal from Rugby, England 62
Figure 5.4. PDAS files as a continuous stream of data 63
Figure 5.5. Clock drifts for the Geostore and PDAS recorders 66

CHAPTER VI

Figure 6.1. Unfiltered frequency spectra for BS5P and Z2A 69
Figure 6.2. Variation of frequency content with distance for BS5P 71
(**Overlay** Variation in resonant frequency of the water column)

Figure 6.3. Variation of frequency content with distance for Z2A 72
Figure 6.4 The Hanning window filter. 73
Figure 6.5. Filtered frequency spectra for BS5P and Z2A 74
Figure 6.6. Parameters used to define seismic wiggle traces 76
Figure 6.7. Comparison between the BABEL line 6 and FENNOLORA data 78
Figure 6.8. BABEL common station sections used in modelling line 6 80
a) Station BS5P. Vertical component PDAS data 81
b) Station BS5P. Vertical component P-wave data 82
c) Station BS5P. Transverse component PDAS data 83
d) Station BS5P. Transverse component S-wave data 84
e) Station BS5. Vertical component Geostore data. 85
f) Station Z5A. Vertical component Geostore data 86
g) Station Z2A. Vertical component Geostore data 87
h) Station Z1A . Vertical component Geostore data 88
Figure 6.9. Frequency spectra of the line 6 normal-incidence data 93
Figure 6.10. Line 6 normal-incidence data 96

CHAPTER VII

Figure 7.1. Flow chart of the BEAM87 raytracing package 99
Figure 7.2, Simple two layer fluid/solid model 100
Figure 7.3. Variation of the ratio T^F:T^R for a simple fluid/solid model. 103
Figure 7.4. Two layer fluid/solid model with laterally varying upper medium. 104
Figure 7.5. Amplitudes calculations along raypaths 106
Figure 7.6. Amplitude calculations for a water layer overlying gradational crust 107
Figure 7.7. Variation of T^F:T^R with incident angle for model in Figure 7.6 108
Figure 7.8. Effect of applying the coefficients of conversion 109
Figure 7.9. Amplitude profile of a Gaussian beam 115

CHAPTER VIII

Figure 8.1. Travel-time curves for a reflection and for a diffraction 120
Figure 8.2. Unreduced travel-time curves for the digitised arrivals from station BS5P 121
Figure 8.3. An example of a raytraced divergent reflection 122
Figure 8.4. BABEL line 6 final model 126
Figure 8.5. Results of raytracing for BS5P and Z2A 128
a) layers 1, 2, 3 and 4 129
b) layers 5, 6 and 7 130
c) layer 8 131
d) layer 9 132
e) layer 10 ('Moho') 133
f) layers 11 and 12. 134
Figure 8.6. S-wave arrivals calculated from the line 6 model 135
Figure 8.7. Arrivals calculated from the line 6 model overlaid on the NI data 136
Figure 8.8. Modelled arrivals from the Moho trench for Z2A 143
Figure 8.9. Modelled arrivals from the Moho trench for BS5P 144
Figure 8.10. S-wave reflections from the horizontal Moho and from the Moho trench 145
Figure 8.11. Arrivals from the Moho trench model overlaid on the NI data 146
Figure 8.12. 3D representation of the P- and S-wave velocities in the line 6 model 148
Figure 8.13. 1D velocity profiles through the line 6 model 150
Figure 8.14. Synthetic seismograms for station BS5P for
a) all elementary waves
b) elementary waves plus their first peg-leg water multiple 152
Figure 8.15. Experimental data and BEAM87 synthetic section for BS5P 153
Figure 8.16. Experimental data and BEAM87 synthetic section for Z2A 155
Figure 8.17. Normal-incidence data and the synthetic normal-incidence section 157
Figure 8.18. Ray diagram and travel-times for station BS5 159
Figure 8.19. The horizontal and trench models compared to the data from BS5. 160
Figure 8.20. Ray diagram and travel-times for station Z5A 162
Figure 8.21. The horizontal and trench models compared to the data from Z5A 163
Figure 8.22. Ray diagram and travel-times for station Z1A 164

CHAPTER IX
Figure 9.1. Velocity profiles for Blue Road, Sylen-Porvoo, BABEL line 7 and BABEL line 6 167
Figure 9.2. Comparison of the BABEL line 6 model to FENNOLORA 168
Figure 9.3. FENNOLORA model (Guggisberg *et al.*, 1991) 169
Figure 9.4. Velocities for BABEL line 6, SVEKA and BALTIC profile 171
Figure 9.5. **a)** Normal-incidence data for northern half of BABEL line 1
b) Normal-incidence data for BABEL line 6
c) Normal-incidence data for BABEL line 7 ..... .173
Figure 9.6. **a)** Crustal structure along line 1 according to Graham (1993);
b) Crustal structure along line 7 according to Bruguier (1992) 176
Figure 9.7. Models for BABEL line 7 and 1 (Heikkinen and Luosto, 1992) 177
Figure 9.8. Cartoon of the structure of the crust along BABEL line 6 179
Figure 9.9. **a)** Variation in water depth and surface geology along line 6.
b) Raytraced model for line 6.
c) Normal-incidence data for line 6 180
Figure 9.10. Possible dolerite sills on BABEL line 6 and 1 181
Figure 9.11. NI data with the parts of the boundaries defined by the wide-angle arrivals 185
Figure 9.12. Location of features on BABEL lines 6, 1 and 7 and FENNOLORA. 187
Figure 9.13. Tectonic interpretation of FENNOLORA (Guggisberg *et al.*, 1991). 188
CHAPTER X
Figure 10.1. Normalised wide-angle data for line 6, BS5P 195
Figure 10.2. Ray diagram and synthetic section for a simple sinusoidal boundary 197
Figure 10.3. Normal-incidence arrivals from the sinusoidal boundary 198
Figure 10.4. Ray diagram and synthetic section for crustal lenses 199
Figure 10.5. Normal-incidence arrivals from crustal lenses 201
Figure 10.6. Lower crust consisting of short length reflectors 202
Figure 10.7. Effect of variable angle and length of reflectors in the lower crust 203
Figure 10.8. Decay of a crustal step (Kusznir and Matthews, 1988) 205
Figure 10.9. Arrivals for the decay structure in Figure 10.8 206
Figure 10.10. Cartoon of a WART (wide-angle reflection type) 207
Figure 10.11. Normal-incidence arrivals from a WART 208
APPENDIX B
Figure Bi. Flow chart for CONVERT.C 228-229
Figure Bii. PDAS files as a stream of data and blank data gaps 232

LIST OF TABLES

CHAPTER II

Table 2.1. Summary of the geological evolution of the Baltic Shield 8

CHAPTER IV

Table 4.1. Coordinates of BABEL lines 6, 6a and 6b 48

Table 4.2. Locations of the recording stations run by Durham University 52

CHAPTER V

Table 5.1. Example of a PDAS file header 61

APPENDIX B

Table Bi. Example options file for CONVERT.C 230

Table Bii. Example of a ASCII header for a gainranged PDAS file 230

Table Biii. Format of the station file for CONVERT.C 231

Table Biv. Format of the event file for CONVERT.C 232

CHAPTER I
INTRODUCTION

In 1989 a major deep seismic survey was shot in the Fennoscanadian Baltic Shield. Project BABEL (Baltic And Bothnian Exploration of the Lithosphere) consisted of nine profiles that extended over 1000 km from the edge of the Archaean craton into Phanerozoic Europe and crossed crust that varies from 55 to 35 km in thickness and from 2.5 to 1.0 Ga in age (BABEL working group, 1993a, BABEL working group, 1993b).

The experiment had two main aims: to compare the seismic signature of the early Proterozoic crust of the Baltic Shield with the Phanerozoic crust around the UK and to investigate the transition into Phanerozoic Europe across the Tornquist zone. BABEL also aimed to answer some geological questions about the Baltic Shield. For example, from what time onwards it is appropriate to apply plate tectonic theories to explain the growth of the Shield? How far south does the Archaean basement extend? What is the cause of the large variation in Moho depth seen on previous deep seismic refraction profiles? Are there deep seated megashears controlling surface faults? How are the different geological regions in Sweden and Finland connected across the Gulf?

The geological evolution of the Baltic Shield is poorly understood. It is believed to have evolved from an Archaean nucleus in the northern part of the present Baltic Shield and then to have grown to the South in a series of orogenic events (Berthelsen and Marker, 1986, Gaál and Gorbatschev, 1987). This growth is usually described in terms of plate tectonics although this is disputed by some authors. A description of the geological evolution of the region is given in chapter II.

The BABEL profiles consisted of nine seismic lines that lay mainly in the Svecofennides of the Baltic Shield. Shots were fired in the Gulf of Bothnia and in the Baltic Sea and were recorded both at normal-incidence and at wide-angle. Durham University recorded wide-angle data from the northern BABEL lines (line 1 -7, Figure 1.1) using 15 analogue stations located in Sweden around the Sea of Bothnia[1]. These

1 The Gulf of Bothnia is divided into two sections: the northerly Bay of Bothnia and the larger southern Sea of Bothnia.

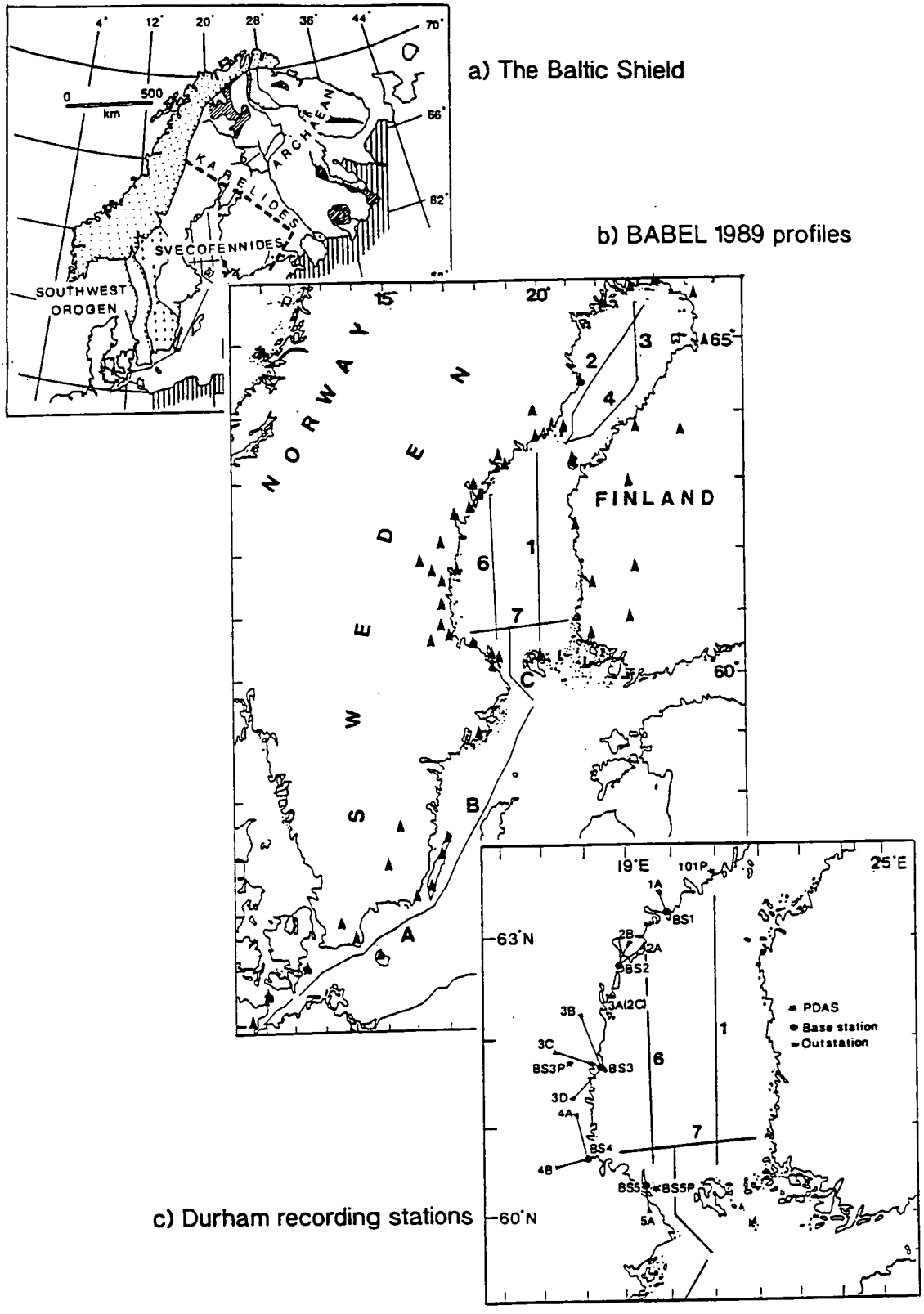

Figure 1.1. Location map of the 1989 BABEL profiles. **a)** The main geological regions of the Baltic Shield, **b)** The BABEL profiles, **c)** BABEL line 6 and the Durham recording stations.

analogue stations were supplemented by two digital recorders (the field work for the BABEL project is described in chapter IV).

This thesis is concerned with the results from BABEL line 6; an approximately 240 km north-south profile in thewestern half of the Sea of Bothnia (Figure 1.1). This profile lies entirely within the Proterozoic Svecofennian domain of the Baltic Shield which consists of metavolcanic, metasediments and numerous granitoid intrusions and runs parallel to BABEL line 1 and to several of the previous deep seismic profiles in Fennoscandia.

Most of the previous wide-angle/refraction surveys across the Baltic shield have been shot on land. The BALTIC and SVEKA profiles in Finland lay about 150 km to the east of the Gulf of Bothnia. The FENNOLORA profile ran immediately to the west of the Gulf and is the closest of the previous profiles to line 6. The results from these profiles, and from others that lie partially in the Svecofennides, are described in chapter III, along with the results from other geophysical explorations of the Baltic Shield. Moho depth maps generated from these results suggested that the deep Moho seen on the BALTIC and SVEKA profiles could be connected to the deep crust on the FENNOLORA profile across the Sea of Bothnia, rather than with the more northerly Ladoga-Bothnian Bay tectonic zone. Few studies have been made within the Gulf of Bothnia and the BABEL project was designed to fill the gap in the deep seismic coverage of the Shield.

Long offset profiles (such as those recorded for BABEL by Durham) are often referred to as wide-angle reflection profiles rather than refraction profiles. Refracted headwaves along interfaces are not usually seen in long offset data, as these have a much lower amplitude than the diving rays from the media underlying the interface (Červený, 1966). In wide-angle reflection surveys, a particular set of arrivals has traditionally been identified (Figure 1.2a): Pg (diving ray into the crystalline basement which forms the first arrival on the data sections), PmP (reflection from the seismic Moho) and Pn (diving ray beneath the Moho into the mantle). Between Pg and PmP, other wide-angle arrivals are seen from intra-crustal discontinuities. Similar arrivals have been identified for S-wave data. These arrivals have been interpreted using computer software packages to give a model of the crust which consists of a series of roughly horizontal layers separated by reflecting boundaries with sharp velocity discontinuities (Figure 1.2b).

In recent years good quality coincident wide-angle and normal-incidence data have been recorded using large airgun arrays and land recording stations, for example in the 1987 BIRPS/MOBIL project (Matthews, 1989, West, 1990, Blundell *et al.*, 1991), as part of the GLIMPCE project (GLIMPCE seismic refraction working group, 1989) and as part of the EUGENO-S profile (Lund *et al.*, 1987). The use of airgun

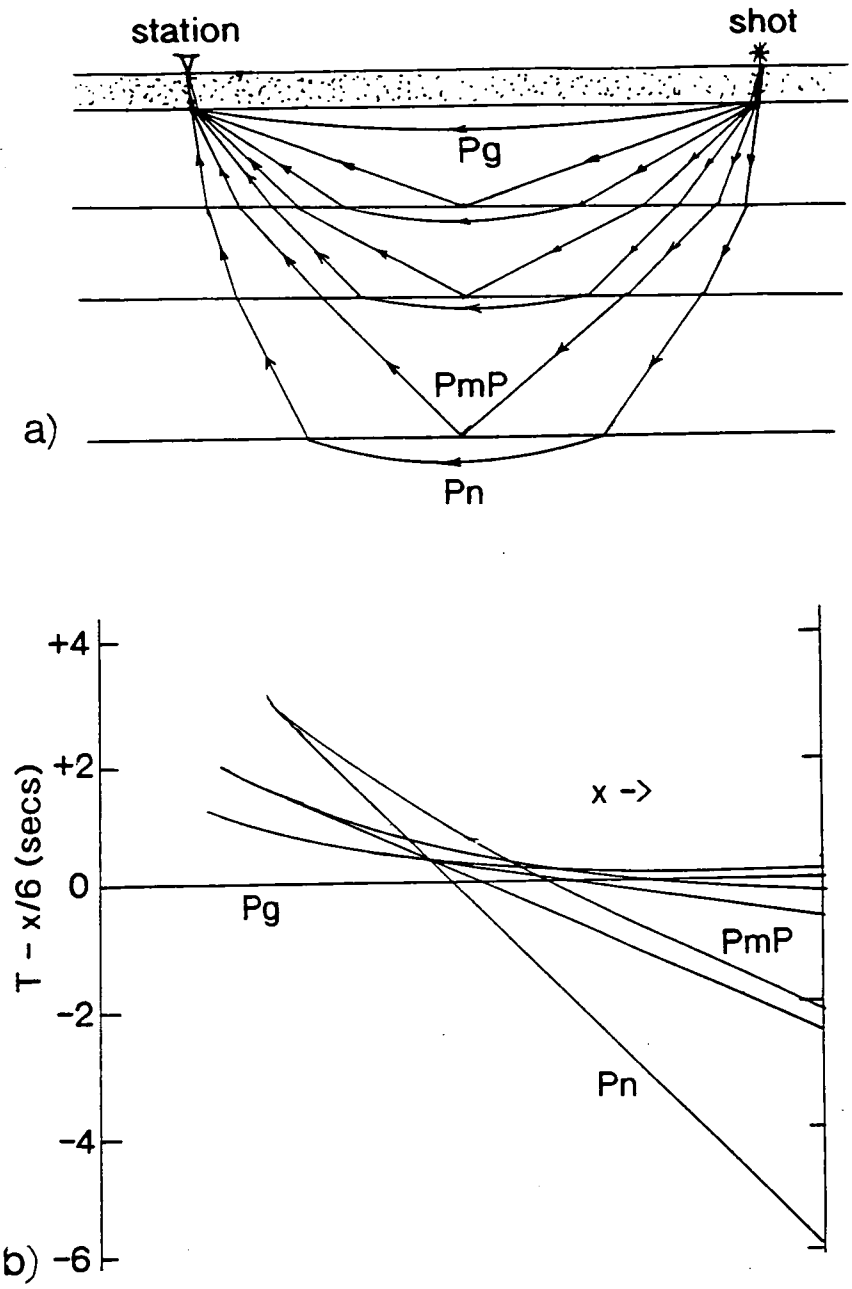

Figure 1.2 a) Cartoon of arrivals traditionally identified from wide-angle data. **b)** Location of these arrivals on a typical wide-angle data section (offsets at which particular arrivals are seen depends on the thickness of the crust).

sources permits a much closer shot spacing than is usually possible in land wide-angle surveys where shotpoints are widely spaced due to the cost and destructive nature of the explosive sources.

The increased resolution of these more recent surveys has revealed a much more complex series of arrivals than was previously recognised. What were originally identified as single wide-angle reflections or diving rays often appear to consist of a

series of overlapping and interfering arrivals in the higher resolution data. Rapid changes in amplitude and phase are seen along apparently continuous arrivals and arrivals with high apparent velocity have been identified which do not appear to be typical wide-angle reflections or diving rays. As a result of this increased complexity, the concept of wide-angle arrivals sampling the gross structure of a horizontally layered crust has been called into question.

The BABEL project provided a large quantity of good quality, high resolution wide-angle data due to the quiet recording sites. This provided an opportunity to investigate the causes of the complex features seen in the wide-angle data and to relate them to the features seen in the coincident normal-incidence data.

CHAPTER II

GEOLOGICAL EVOLUTION OF THE BALTIC SHIELD

2.1. The Baltic Shield

Figure 2.1 shows the position of the BABEL profiles in relation to the main geological regions of the Precambrian Baltic Shield. In general, the Shield youngs from northeast to southwest, with crustal ages ranging from 3.1 Ga in Northern Finland to 0.9 Ga in Southern Sweden. Several mechanisms have been suggested to explain the evolution of the Baltic Shield: by ensialic tectonic evolution; as the result of basement reactivation (Witschard, 1984), by block tectonics and intrusion without the need for large scale horizontal movement (Welin, 1987) or by plate tectonic processes operating on a Precambrian time scale (Berthelsen and Marker, 1986, Gaál and Gorbatschev, 1987). The latter of these mechanisms is now becoming the most prevalent explanation. There follows a short description of the geological history of the Baltic Shield in terms of plate-tectonics (a more detailed description of the different geological regions is given later in this chapter).

The Baltic Shield developed from an Archaean nucleus in a series of belts formed during 3 major orogenic cycles: the Archaean, the Svecokarelian and the Southwest Scandinavian (Gothian). Large scale accretion of the Shield began around 3.5-3.1 Ga with the formation of the Archaean nucleus (the northeast half of the present Archaean craton). About 2.9 Ga, a geosyncline formed to the east of this nucleus, followed by the development of a subduction zone. The Archaean craton consolidated as a result of this subduction at about 2.5 Ga.

During the early Proterozoic the craton was rifted and intruded by numerous dyke swarms and a spreading ocean developed. This closed around 1.9 Ga during the Svecokarelian Orogeny, forming a Proterozoic collision suture within the Archaean craton. At the beginning of the Svecokarelian Orogeny (c. 2.25 Ga) a passive continental margin developed at the southern edge of the craton. The Karelides formed in a geosyncline above this passive margin and are underlain by Archaean crust. This passive margin then evolved into an active margin, with north-eastwards subduction beneath the craton which resulted in the widespread intrusion of Svecofennian granitoids into the Archaean crust and the overlying Karelides. This period of

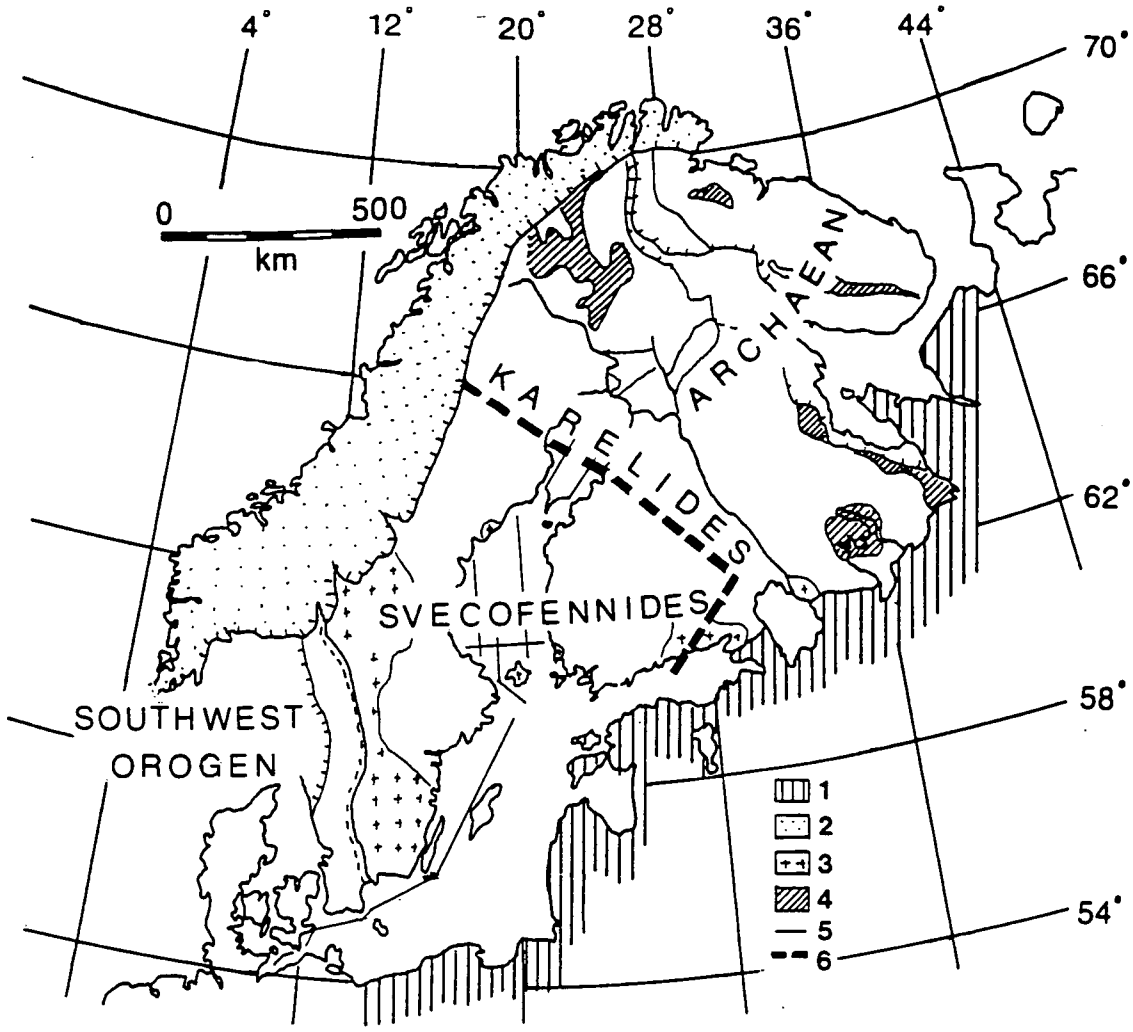

Figure 2.1. Outline of the geology of the Baltic Shield (after Gaál, 1986). Legend: 1. Phanerozoic platform cover, 2. Caledonides, 3. Rapakivi granites and porphyry belt, 4. Early Proterozoic greenstone belts, 5. BABEL profiles, 6. Ladoga-Bothnian Bay zone.

subduction ended around 1.9-1.8 Ga when the site of subduction is believed to have moved to an intra-ocean location to the south. The Svecofennian crust was accreted within an ocean basin between this new region of subduction and the Archaean craton.

The bulk of the rest of the Baltic Shield was formed in the Southwest Scandinavian (Gothian) Orogeny during which the Rapakivi granites were emplaced into the Svecofennian crust. Most of Southwest Scandinavian (Gothian) crust was reworked during the Sveconorwegian-Grenvillian Orogeny. This was the last major period of orogenic growth of the Shield. The western margin of the Shield was formed during the Caledonian Orogeny. The growth of the Baltic Shield is summarised in Table 2.1. The formation of the Baltic Shield ended about 1.0 Ga after 4 main periods of crustal growth: two in the Archaean and two in the Proterozoic.

A R C H A E A N	3.5 - 3.2 Formation of Baltic Shield begins. 2.9 Proto-continent exists with geosyncline to the East.	Early Archaean (Saamian) > 2.9 Ga
	2.8 Development of subduction zone to the east of proto-continent and start of the collisional stage. Western-most Greenstone belts generated in back-arc rift system.	Late Archaean (Lopian) 2.9 -2.5 Ga
P R O T E R O Z O I C	2.5 Archaean crust consolidated. 2.25 - 2.0 Rifting and development of spreading ocean in craton. Intrusion of dykes. Resealed along Kola suture zone by onset of Svecokarelian orogeny. 2.1 Passive continental margin develops along southern edge of Archaean craton. 2.08 Jautlian platform carbonates deposited. 2.05 Karelian greywackes and turbidites deposited on passive margin. 2.0 NE dipping subduction zone formed at passive margin. 1.9 Rifted Archaean craton sealed by collision, preceded by subduction and formation of Kola suture.	Svecokarelian 1.9 - 1.7 Ga (Karelian 2.1-2.0 Ga)
	1.88 - 186 Peak of intrusive activity. 1.8 Primitive Svecofennian crust formed.	(Svecofennian 1.93-1.87 Ga)
	1.67 - 1.59 Intrusion of Åland Archipelago.	Southwest Scandinavian (Gothian) 1.78 -1.55 Ga
	Period of relative quiet with intermittent mafic intrusions. 1.4 - 1.3 Sub-Jotnian magmatism. 1.3 - 1.2 Jotnian sandstone deposited in eroded Svecokarelides.	Hallandian 1.5 -1.4
	Reworking of the Gothian Orogen in the S-W of the Shield.	Sveconorwegian-Grenvillian 1.2 -1.0 Ga
	Formation of western margin of Baltic Shield.	Caledonian 0.6 -0.4 Ga

Table 2.1. Summary of the geological evolution of the Baltic Shield in the Precambrian.

BABEL line 6, in the Bothnian Sea, lies in the Svecofennian domain of the Baltic Shield. The basement, if any, of the Svecofennian supracrustal rocks is unknown, although it has been suggested that the northern volcanic belt of the Svecofennian domain may be underlain by Archaean crust (Lundström, 1987). Others suggest that the Ladoga-Bothnian Bay suture zone (Figure 2.1) marks the southern edge of the Archaean craton and only the Karelides are underlain by Archaean basement (Gaál, 1986, BABEL working group, 1990). Lundqvist (1987) argues that all of the Svecofennides may be underlain by Archaean granitoid rocks that were uplifted and eroded during the early parts of the Svecofennian Orogeny (1.90-1.85 Ga).

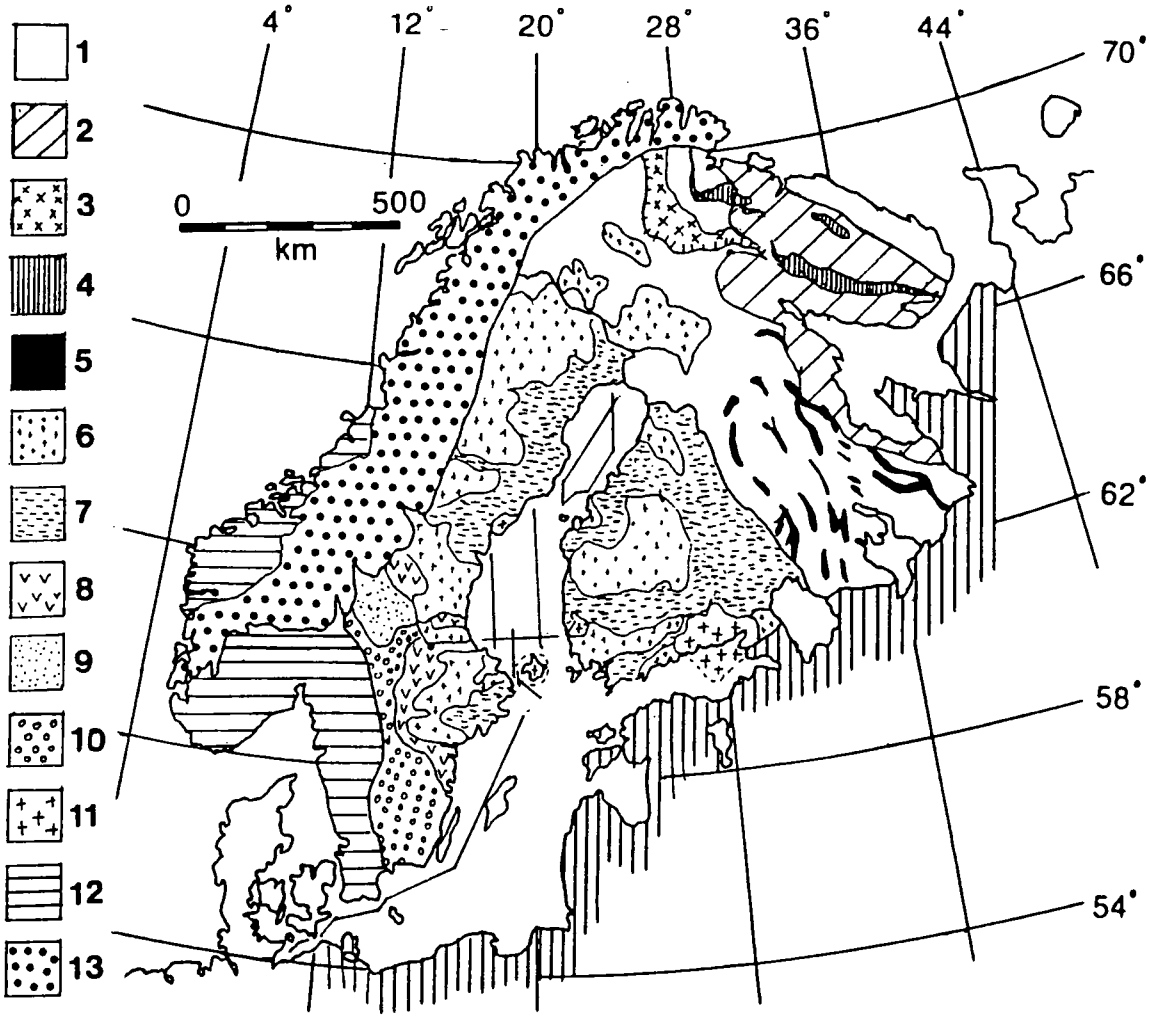

Figure 2.2. Precambrian geology of the Baltic shield (after Gaál, 1986). Legend: 1. Archaean granitoids, migmatites and grey gneisses, 2. Belomorian and Kolan gneisses, 3. Lapland granulite belt, 4. Kola suture zone, 5. Late Archaean greenstone belts, 6. Synorogenic to postorogenic Svecokarelian granitoids, 7. Metagreywackes and metapelites, 8. Island arc volcanics and related sediments, 9. Jotnian and sub-Jotnian rocks, 10. Trans-Scandinavian granite-porphyry belt, 11. Rapakivi granites, 12. Granite and gneisses of the Southwestern Scandinavian domain, 13. Caledonides.

Welin (1987) proposes a similar evolution, as the result of the subsidence of a block of Archaean crust to the west of the Ladoga-Bothnian Bay zone, and adds that the lack of ophiolites and the limited quantity of basic and ultrabasic rocks within the Svecofennides indicates that the basement was continental rather than oceanic. Both Lundqvist and Welin explain the evolution of this region by block-tectonics rather than by plate-tectonic processes. Gaál and Gorbatschev (1987) have also suggested that the basement to the Svecofennides may be older than the overlying rocks but that it is still of Proterozoic rather than Archaean age. Figure 2.2 shows the geology of the Precambrian shield in more detail.

2.2 The Archaean domain

The Archaean domain contains rocks from both the Saamian and Loppian Orogenies and most of the crust was formed in the late Archaean (Table 2.1). Gorbonov *et al.* (1985) propose that the Archaean nucleus formed under conditions that existed only in the early stages of the formation of primordial crust by differentiation of the mantle. At about 2.9 Ga, a geosyncline evolved to the east of the Archaean nucleus of pre-2.9 Ga ensialic crust (Gaál, 1986). This developed into a west or south-westwards dipping subduction zone (or possibly a series of sub-parallel subduction zones) at around 2.8 Ga (Figure 2.3a). A north-northwest trending island arc belt was formed, with a geosyncline to the east and with greenstone belts being deposited in a back-arc rift system. These form the westernmost greenstone belts of Finland and Norway (Figure 2.2). This juxtaposition of greenstone and gneiss belts suggests such a subduction environment (Gaál and Gorbatschev, 1987). Further to the west, platform sediments were deposited on the Archaean nucleus. The craton consolidated at about 2.5 Ga.

In the early Proterozoic (2.25 - 2.0 Ga) the Archaean craton was subjected to a period of rifting and a spreading ocean opened, running NW-SE. At the onset of the Svecokarelian Orogeny, a SW dipping subduction zone developed within this ocean and an island arc system was formed (Figure 2.3b). The ocean was closed at about 1.9 Ga creating the Kola suture zone (Figure 2.2) in the north of the Baltic Shield (Berthelsen and Marker, 1986, Gaál *et al.*, 1989). This suture zone forms a band of Proterozoic rocks that separates the northern and southern Archaean rocks and is the northern boundary of Svecokarelian deformation; structures to the north of this are late Archaean. During the Svecokarelian cycle, the southern craton was intruded by numerous granitic diapirs due to the subduction of the younger crust beneath the Archaean (Gaál, 1986).

2.3 The Svecokarelian domain

The Svecokarelian domain consists of two Proterozoic regions: the northern Karelides and the southern Svecofennides. Originally these two regions were thought to have different ages and origins and to have evolved in two separate orogenies, the Karelian (2.1-2.0 Ga) and the Svecofennian (1.93-1.87 Ga). More recently it has become common to talk of a single event, the Svecokarelian Orogeny (1.9-1.7 Ga), retaining the terms 'Svecofennides' and 'Karelides' to refer to regions that are different but which are coeval. Gaál and Gorbatschev (1987) argue that this more recent terminology may not be correct, as further geological work has indicated that the

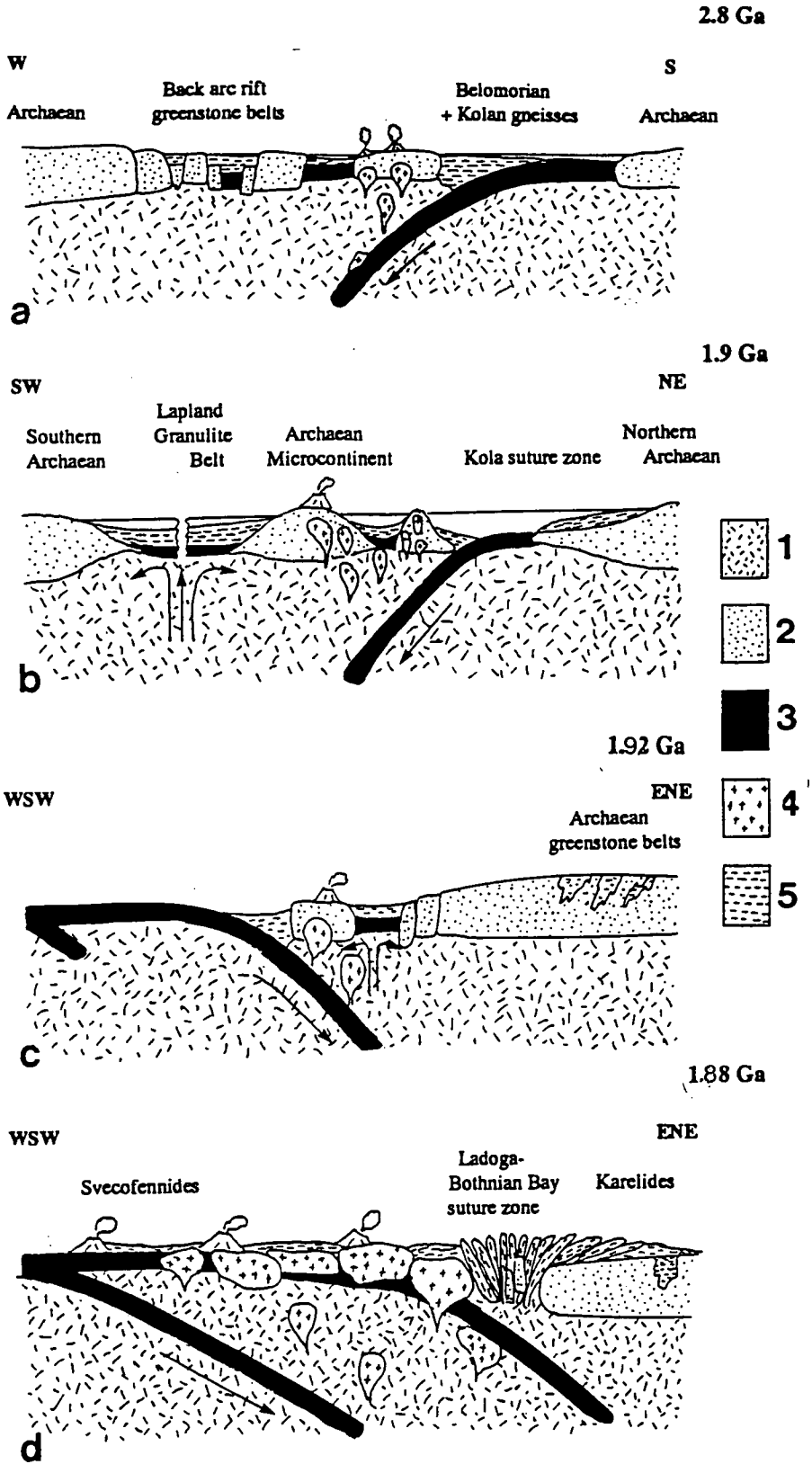

Figure 2.3 a) Late Archaean cycle of the Baltic Shield (after Gaál, 1986). b) Development of the Kola suture zone (after Berthelsen and Marker, 1986). c) Evolution of the Karelides (after Gaál, 1986). d) Evolution of the Svecofennides (after Gaál, 1986). Legend: 1. Mantle, 2. Continental crust, 3. Oceanic crust, 4. Igneous rocks, 5. Sedimentary and volcano-sedimentary rocks.

Karelian and Svecofennian rocks may differ in age, and they suggest that the idea of a single 'Svecokarelian Orogeny' is misleading. In this section the concept of a single Svecokarelian unit will be retained but subdivided by age into two regions, Karelides (pre 2.0 Ga) and Svecofennides (post 2.0 Ga).

2.3.1 The Karelides

Karelides are generally considered to be the part of the Svecokarelides that are underlain by Archaean crust (Table 2.1). The geosyncline in which the Karelides were deposited, developed at about 2.1 Ga at a passive continental margin to the south of the Archaean craton. The Karelides are underlain by the Jautlian group, the lower sections of which belong to the basement rocks and the upper group (c. 2.08 Ga) of carbonates, metapelites, etc., to a shelf environment. The Kalevian group of metaturbidites form the main sediments of the Karelides and were deposited in a shelf to near-shelf environment. It has been suggested that they may have been deposited in a marginal basin that evolved as the result of the transition from a passive margin to an active one (Gaál, 1986). Welin (1987) proposes a non-plate tectonic explanation for the evolution of the Karelides by the subsidence of a western continental block that resulted in the abrupt interruption of deposition and a facies change due to marine transgression. The 'Karelian' granites, which have led to confusion between Svecokarelian and Karelian/Svecofennian Orogenies, are the result of Svecofennian plutonism due to subduction of Svecofennian crust beneath the Archaean craton (Gaál and Gorbatschev, 1987).

Around 2.0 Ga the passive margin evolved into a north-eastwards dipping subduction zone (Figure 2.3c) which persisted until about 1.9 Ga when the site of subduction is believed to have moved southwards to an intra-oceanic position. Berthelsen and Marker (1986) suggest that the deposition of Svecofennian crust did not occur until the site of subduction shifted to beyond the present borders of the Svecofennian province.

2.3.2 The Svecofennides

The Ladoga-Bothnian Bay zone marks the boundary between the Karelides and the Svecofennides and is the most important metal producing region within the Baltic Shield. The zone is thought to be the faulted remains of an island arc system generated during the c. 2.0 Ga subduction beneath the Archaean craton (Gaál, 1986). Apart from the island arc system, this subduction contributed little to the formation of new continental crust.

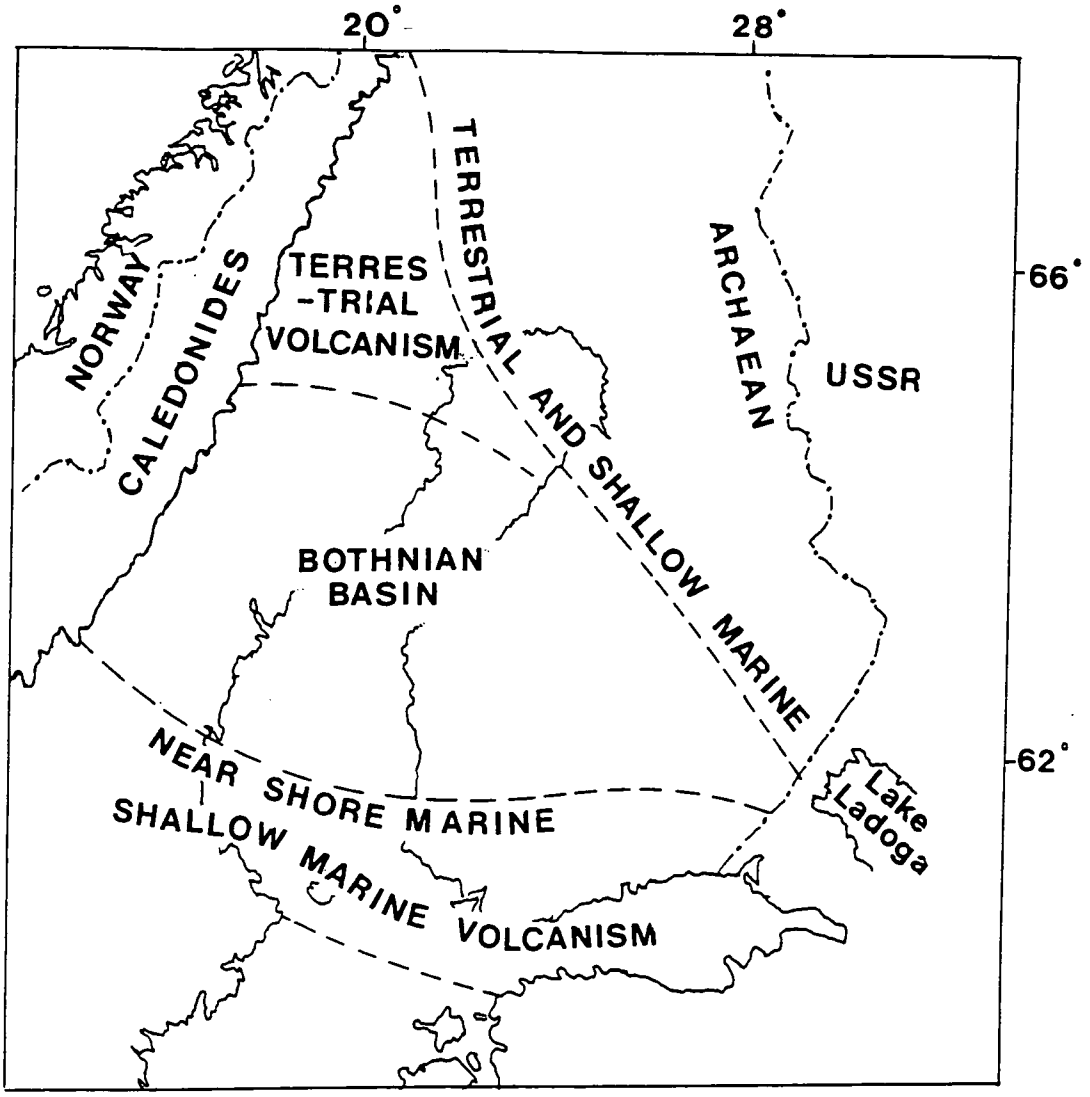

Figure 2.4.. Palaeoenvironments of the Svecofennides (after Welin, 1987 and Gaál and Gorbatschev, 1987).

The Svecofennides are the result of the main period of crustal accretion of the Baltic Shield. The primitive Svecofennian crust was formed by magmatic and sedimentary accretion and is widely accepted to be the remains of an island arc environment within a marginal basin (Figure 2.3d). The Svecofennides can be divided into three different palaeoenvironments; northern and southern volcanic provinces separated by a central province of metaturbidites and metagreywackes with subordinate volcanics that were deposited in the Bothnian basin (Figure 2.4). The boundaries between these regions have been obscured by numerous granitoid intrusions. BABEL line 6 runs northwards from the Southern volcanic belt into the Bothnian basin. According to Lundström (1987), the transition from the northern to the central Svecofennian province marks the southern boundary of underlying Archaean crust. The volcanic belts surround the central basin, forming a U-shape,

opening to the west. Both volcanic belts appear to have originated in a continental margin environment. The northern belt shows a transition north-eastwards from marine to continental vulcanism and the southern shows shallow marine vulcanism. The Svecofennian metasediments may have formed partly from the erosion of Archaean and Jautlian bed-rock to the north and east of the Bothnian basin (Lundström, 1987) and partly by the erosion of rapidly uplifted Svecofennian plutonic rocks. The Archaean contribution to the sediments is greatest in east Finland close to the Archaean basement and in west-central Sweden which may indicate that the whole Svecofennian domain is underlain by Archaean crust (Welin, 1987).

The Svecofennian domain contains extensive granitoid rocks that can be divided into early-, late- and post-orogenic groups*. The early-orogenic group (1.9-1.87 Ga) make up the bulk of the Svecofennides. Isotopic and geochemical evidence suggests that they formed from newly separated mantle material. Declining activity seems to have persisted till 1.85 Ga. Between 1.87 and 1.83 Ga the Svecofennian crust had consolidated sufficiently for the intrusion of large dolerite dyke swarms and for rifting to occur (Lundström, 1987). Late-orogenic Svecofennian plutonism began about 1.83 Ga and continued until 1.77 Ga. The late- and post-orogenic rocks are crustal in origin and in the two volcanic belts they form numerous dyke networks and minor plutons, while in the basin they occur as large masses. The ages of the early and late groups of granitoids correspond roughly to the two main periods of deformation in the Svecofennian. Early folds have varying orientation depending on their geographic location while late folds are more uniform.

Post-orogenic granitoids occur as minor isolated intrusions. Many of them occur in the Archaean domain in NE-SW trending fault zones. Their ages are similar to those of the Trans-Scandinavian granite-porphyry belt and both may have occurred as the result of intensified subduction to the west (Gaál and Gorbatschev, 1987). During the Southwest Scandinavian (Gothian) Orogeny, Jotnian sandstones were deposited in the deeply eroded Svecokarelides and the Rapakivi granites of the Åland Archipelago were emplaced as part of a broad belt extending from northern Sweden to southern Finland. The reworking of the Svecofennian crust in subsequent orogenies has been moderate compared to that of the Archaean and Southwest Scandinavian crust.

* Recent work suggests that the division of granitoid rocks may be more complex than this (Andersson, 1991) but this terminology will be retained in this discussion for simplicity.

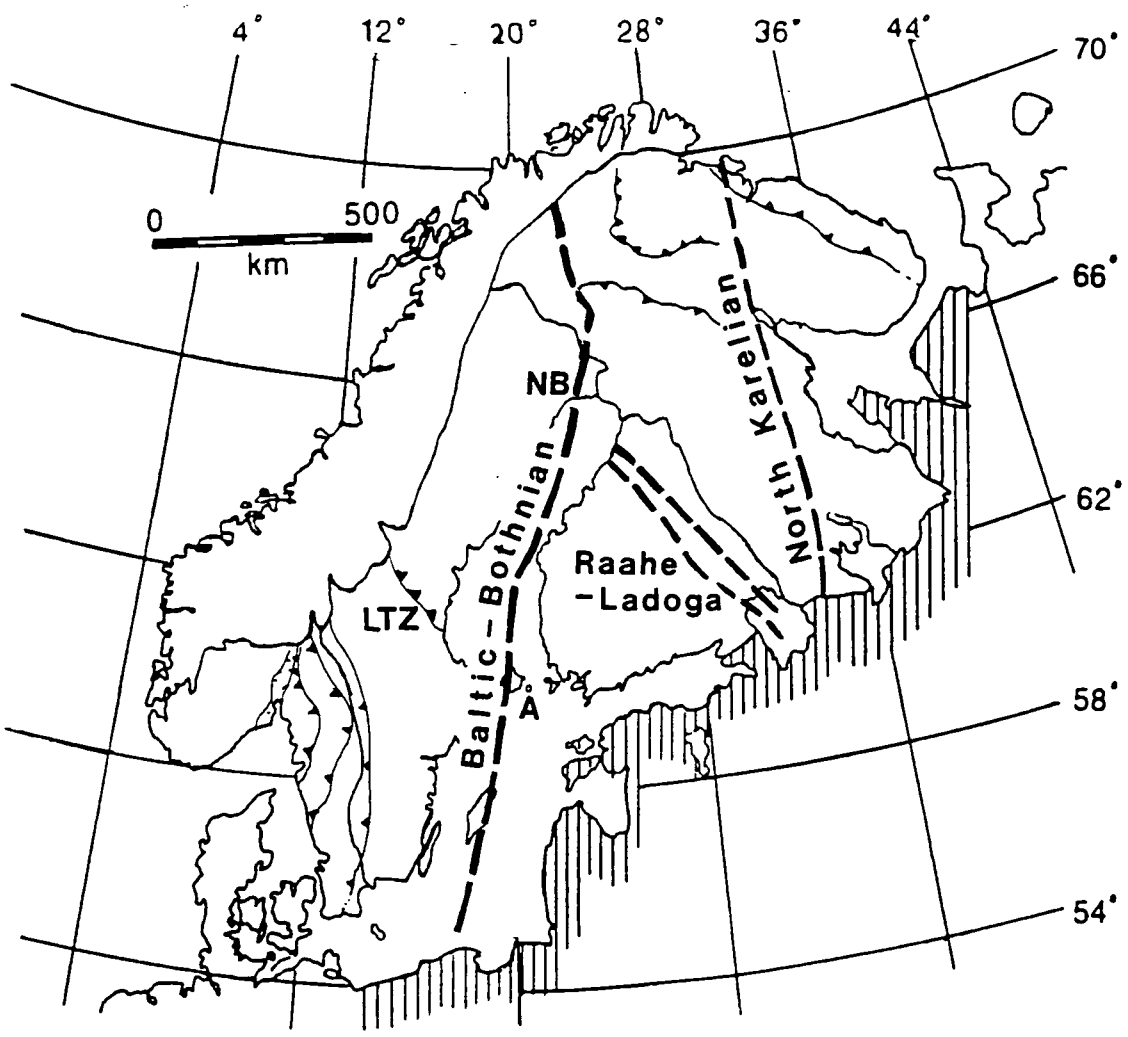

Figure 2.5. Strike-slip megashears in the Baltic Shield (after Berthelsen and Marker, 1986). NB - Norrbotten, Å - Åland Archipelago. LTZ - Ljusnan thrust zone.

2.3.3 Late Svecokarelian megashears

Berthelsen and Marker (1986) suggest that, when the Svecokarelian crust consolidated and began to react as a rigid unit at about 1.8 Ga, a series of large strike-slip faults or megashears evolved: the Raahe-Ladoga, the North Karelian and the Baltic-Bothnian shear zones (Figure 2.5). All the zones are characterised by ductile deformation. The proposed Baltic-Bothnian shear zone runs from the Caledonides in the north, through Norra Norrbotten in Sweden, along the length of the Gulf of Bothnia and through the Åland Archipelago into the Baltic Sea. Onshore the shear-zone is 50-100 km wide and in the Gulf of Bothnia and in the Baltic Sea the fault is hidden by Jotnian (1.4-1.2 Ga) and younger sediments. The Åland Archipelago (1.67-1.59 Ga) is not visibly affected by the megashear and therefore probably post-dates it. Within the Gulf of Bothnia, displacements along the shear zone can be estimated by comparing the geology in Sweden and Finland. Berthelsen and Marker (1986) propose two episodes of activity; a dextral displacement of >100 km between 1.9 and 1.85 Ga

and a later sinistral movement of at least 225 km between 1.84 and 1.80 Ga. In previous wide-angle and normal-incidence seismic reflection studies, shear zones have been shown to produce Moho offsets and diffractions (Matthews, 1989, West, 1990) and the Baltic-Bothnian shear zone may be expected to give rise to similar features in the BABEL data.

2.4 The Southwest Scandinavian domain

The Southwest Scandinavian domain forms the westernmost part of the Baltic Shield and consists mainly of rocks of the Southwest Scandinavian (Gothian) Orogeny (1.78-1.55 Ga). At the same time as these rocks formed, large quantities of acidic magmas were emplaced into the Svecofennides. The Southwest Scandinavian domain is separated from the rest of the Baltic Shield by the Trans-Scandinavian granite-porphyry belt (Figure 2.2) and a neighbouring belt of faulting and shearing known as the Protogine zone. Gaál and Gorbatschev (1987) suggest that these two zones have Svecofennian crustal ages but were subsequently re-metamorphosed and intruded by Gothian crustal rocks. The crustal provinces added to the western margin of the Shield were probably accreted as the result of subduction and the episodic nature of the accretion may be due to step-wise shifts of the subduction zone away from the Shield nucleus. Subduction sutures have been more or less erased by magmatic intrusions and there is no geological evidence that early to mid-Palaeozoic accretion was accompanied by large scale continent-continent collision, although the southern Shield has been strongly re-worked by the Sveconorwegian-Grenvillian Orogeny and this may have obscured any such suture.

Post-Gothian additions to the crust are relatively minor. The Hallandian Orogeny (1.5-1.4 Ga) was a period of relative quiet in the Baltic Shield apart from intermittent mafic intrusions and sporadic granitic magmatism. Most of the Southwest Scandinavian (Gothian) rocks were reworked by the Sveconorwegian Orogeny (1.25-0.9 Ga) but little new crust was accreted. This orogeny is thought to be coeval with the Grenvillian Orogeny of the Canadian Shield (Gaál, 1986) and is considered to have been accompanied by continent-continent collision. If so, then the collision suture lies beneath the shelf off southern Norway and has been overprinted by Caledonian deformation. The Caledonides form the western boundary of the shield and contain rocks from all the previously mentioned groups, suggesting that the shield extended to the west before the beginning of the Caledonian Orogeny.

2.5 Palaeomagnetic results

Pesonen *et al.* (1989) have studied the apparent polar wander path for Fennoscandia (Figure 2.6a) and suggest that the anorogenic rifting and magmatism between about 1.45 and 1.25 Ga may have resulted from the passage of the Fennoscandian plate over a thermal upwelling or hotspot. They were unable to construct polar wander paths for separate blocks of Fennoscanadian crust due to a lack of data, so the area is treated as a single plate. Their results show that Fennoscandia has undergone major latitudinal shifts and considerable rotation during its geological history although it has been mainly confined to within 30° of the equator.

During the Svecofennian (Svecokarelian) Orogeny, Fennoscandia underwent a large anticlockwise rotation with a slow rate of drift while in the Sveconorwegian-Grenvillian Orogeny the latitudinal drift was more rapid and the direction of rotation was first clockwise and then anticlockwise (Figure 2.6b and 2.6c). The most pronounced peak in both the drift and rotational velocities occurred during the anorogenic magmatism and rifting of the sub-Jotnian interval (Table 2.1). One explanation of this is that a small plate bearing Fennoscandia drifted across a hot spot. Both the small size of the plate and the thermal upwelling may increase the drift velocity. This explanation is also supported by the numerous intrusions associated with this interval that decrease in age from east to west, consistent with the transition of the plate across a hotspot. The sub-Jotnian magmatism ceased at about 1.3 Ga when Jotnian rifting commenced.

2.6 Geology of the Bothnian Sea

BABEL lines 6, 7 and 1 lie in the Bothnian Sea which is a shallow depression within the Svecofennian Domain. Lines 6 and 1 cross from the central Svecofennian province of metaturbidites and metagreywackes into the southern volcanic province and line 7 lies entirely in the southern volcanic province. The geology of the Bothnian Sea is important in relating the geology of Sweden to that of Finland and particularly in tracing features which may have been displaced by the Baltic-Bothnia megashear. The following account is based on Winterhalter (1972) who combined echo-sounding, seismic reflection profiling and sea floor sampling, over the period 1962 to 1972, to give information on the bathymetry, morphology and geology of the Bothnian Sea.

The Bothnian Sea is a shallow epeiric sea which has undergone continental glaciation. The present depression probably dates from the late Tertiary. Post-glacial uplift in central Fennoscandia has controlled the recent evolution of the Sea and it is

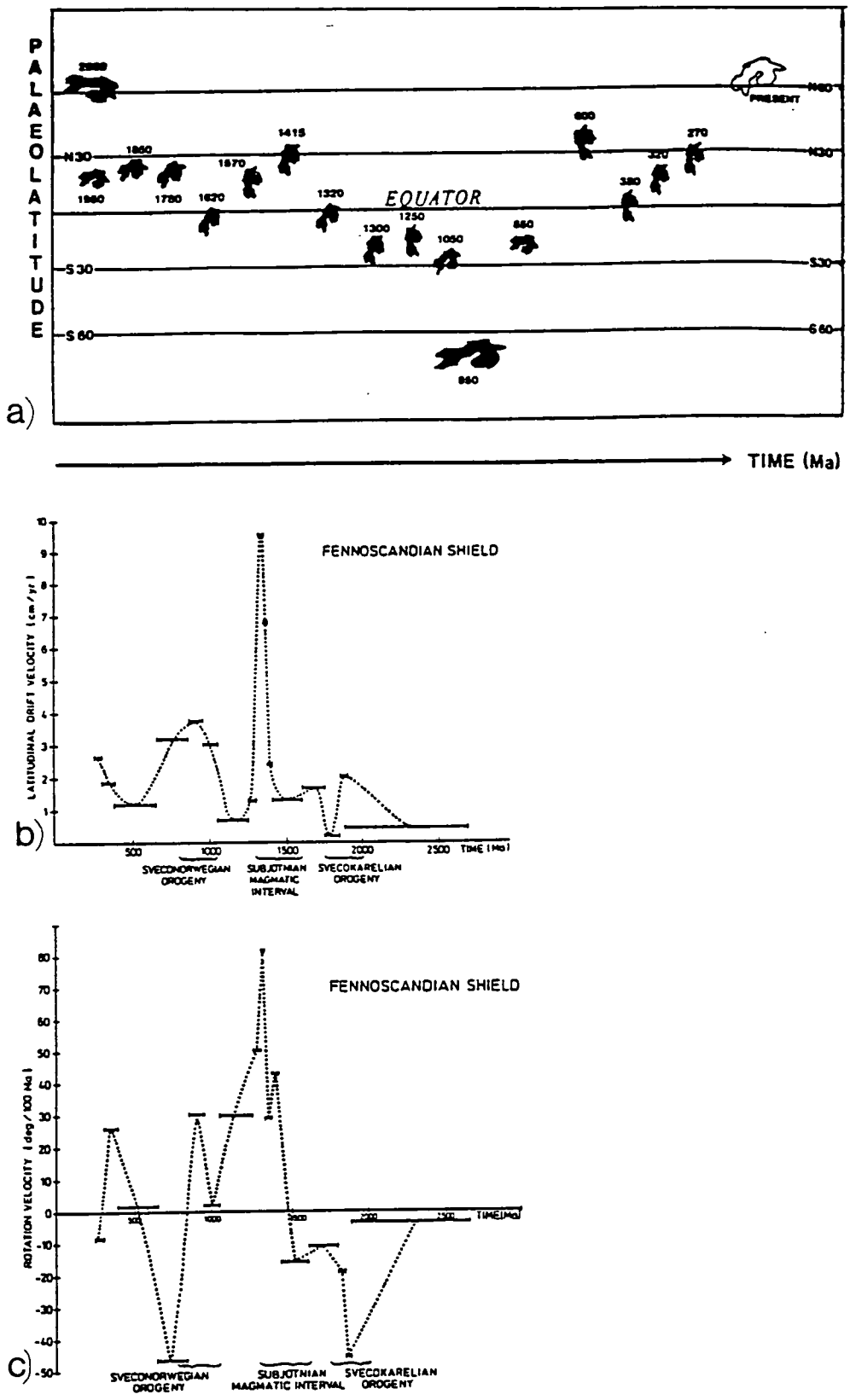

Figure 2.6 a) Palaeolatitude drift history of Fennoscandia from the Archaean to the Permian. The variation in size of Fennoscandia is due to the projection; lateral growth during orogenies is not shown. **b)** Latitudinal drift velocity of Fennoscandia (cm/yr). **c)** Rotational velocity of Fennoscandia (°/100 Ma) (Pesonen et al., 1989).

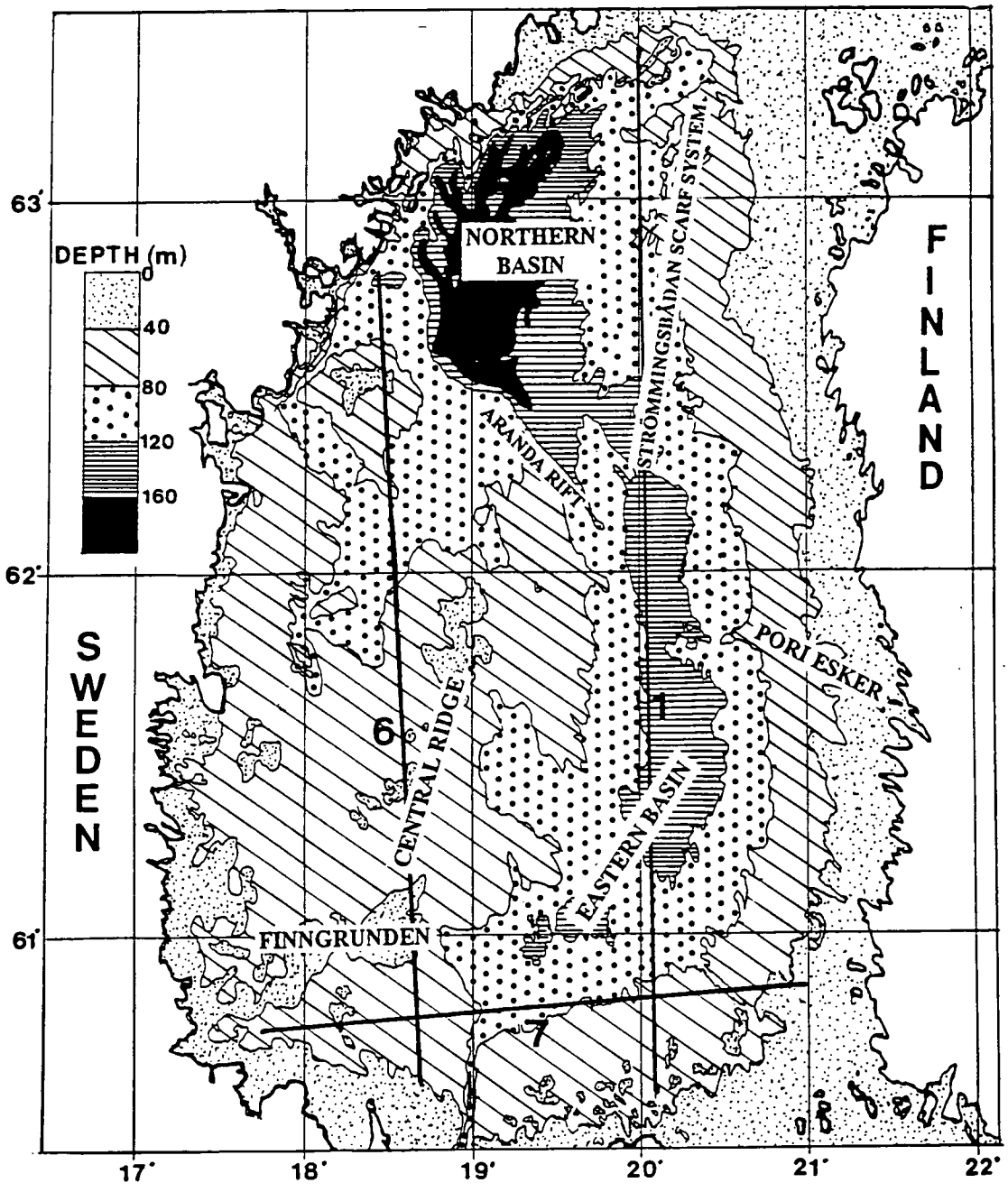

Figure 2.7. Bathymetry map of the Bothnian Sea (after Winterhalter, 1972).

likely that it has never been shallower than at present. The average depth of the sea is about 68 m (Figure 2.7) but is very variable along the length of the BABEL profiles. In general, the Bothnian Sea deepens to the east and north. The water depth along the BABEL lines is highly variable, ranging from over 150 m in the middle of line 1 to less than 20 m at the southern end of line 6 (the shooting of line 6 was curtailed due to the shallow water depth). The effect of this variation in water depth on wide-angle and normal-incidence seismic data will be considered further in chapter VI.

The eastern and western coastlines of the Bothnian Sea are quite different. The western (Swedish) side is rugged and strong faulting has probably occurred, while the

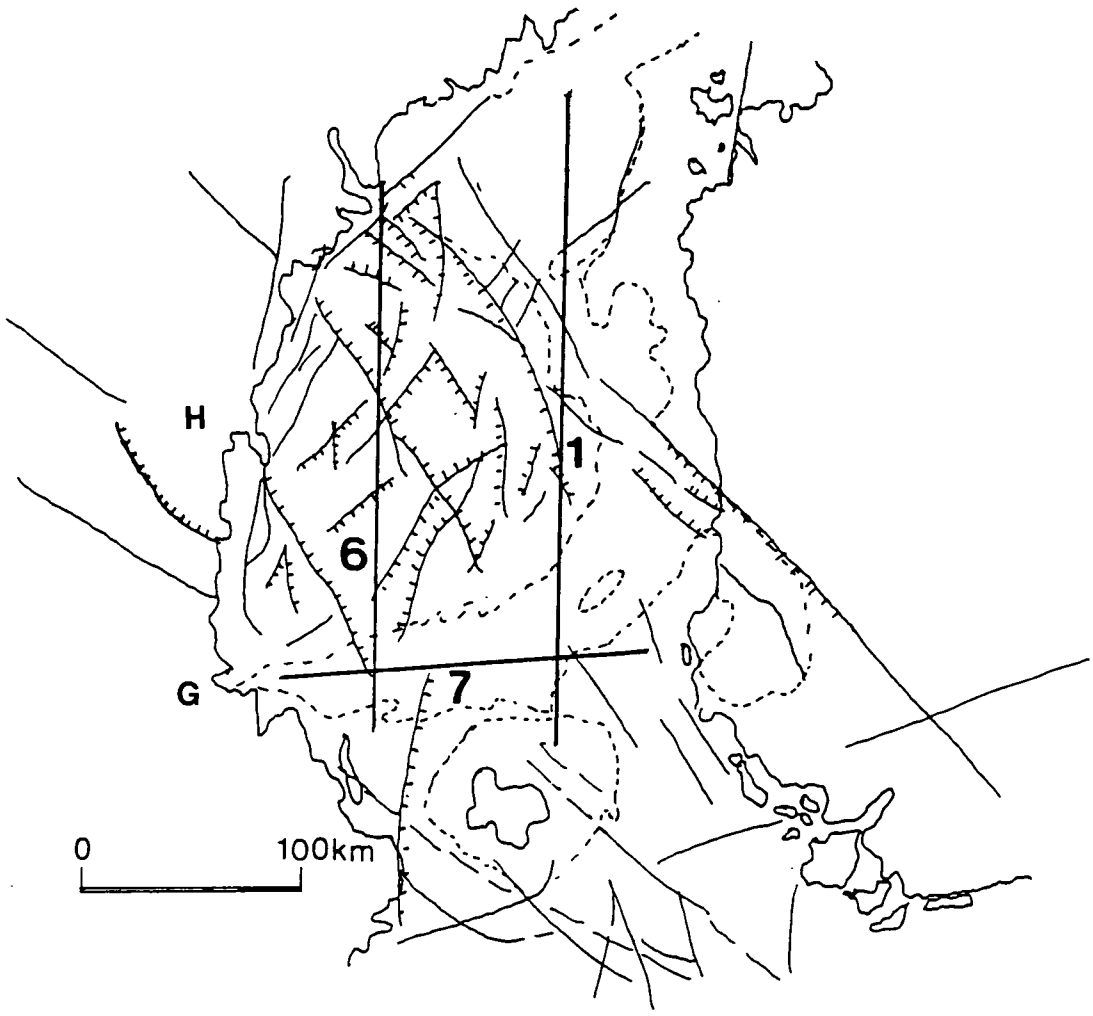

Figure 2.8. Locations of major faults within the Bothnian Sea (after Berthelsen and Marker, 1986). Thick solid lines indicate the BABEL profiles 6, 1 and 7. H=Härnösand, G=Gävle.

eastern (Finnish) side shows low, gently slopping, coastal plains due to simple downwarping. Figure 2.8 shows the patterns of major surface faults in the Bothnian Sea and on the neighbouring coasts (after Berthelsen and Marker, 1986). The complexity of the faulting decreases from west to east across the Sea.

The coastal rocks around the Bothnian Sea are predominantly igneous and metamorphic rocks of Precambrian age, although Palaeozoic sedimentary rocks may be found as fissure fillings in southwestern Finland and on the Åland Archipelago. Numerous boulders of Cambrian and Ordovician age can be found between Härnösand and Gävle which has led to suggestions that much of the sea floor is covered by Proterozoic Jotnian sandstone and Cambrian and Ordovician sandstones, limestones and shales. The main features within the Sea are pre-glacial although small scale structures are glacial and post-glacial.

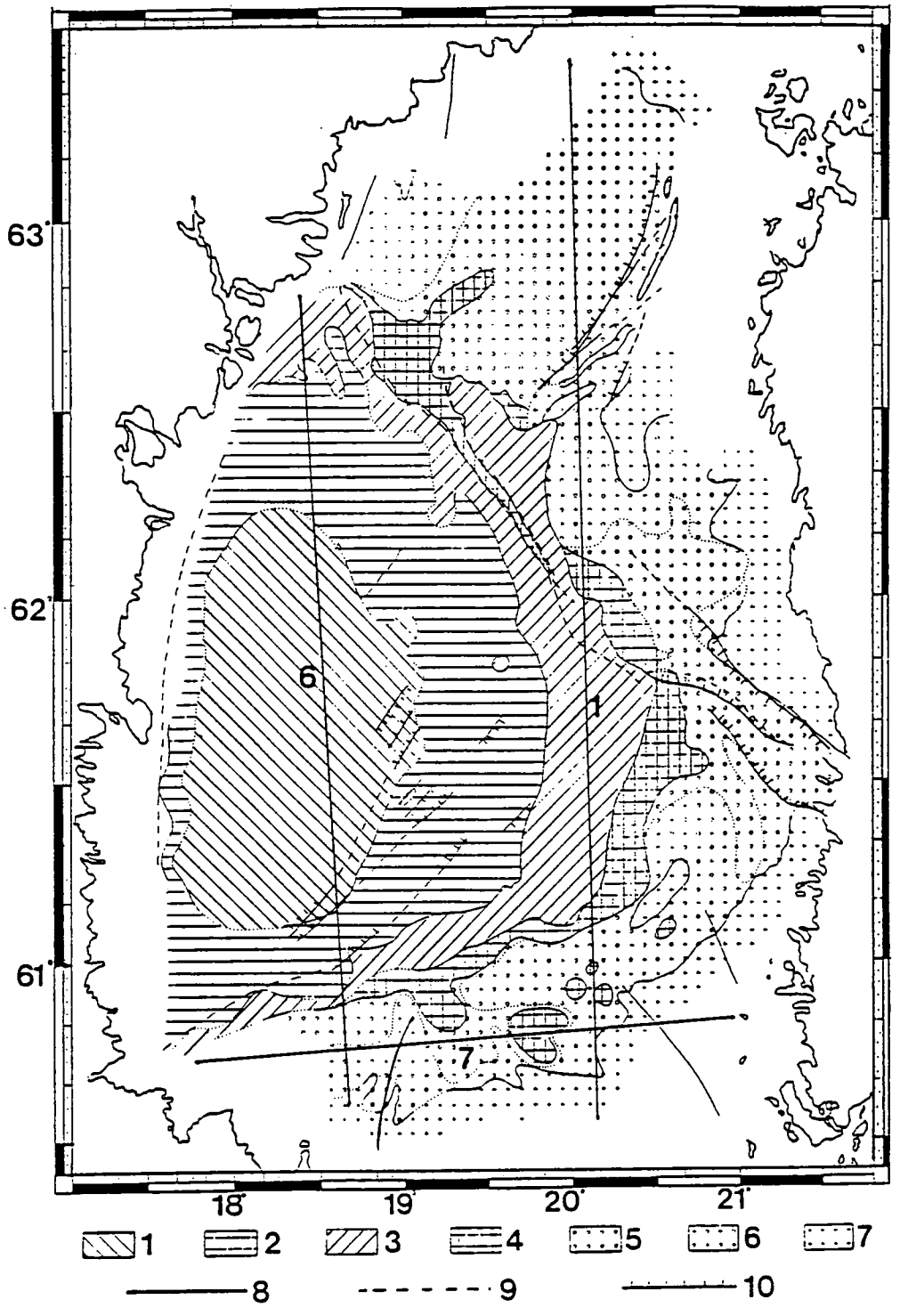

Figure 2.9. Lithology map of the Sea of Bothnia. Legend: 1. Upper part of Middle Ordovician limestone sequence exhibiting poor acoustic penetration, 2. Middle Ordovician Orthoceras-limestone sequence, 3. Cambrian and Lower Ordovician shales, slitstones and sandstones, 4. Outliers of Lower Palaeozoic strata, 5. Sandstone (probably Jotnian) 6. Alternating occurrences of sandstones and crystalline bed-rock, 7. Igneous and metamorphic rocks, 8. BABEL profiles, 9. Assumed fault lines, 10. Fault lines from bathymetric and reflection data, (Winterhalter, 1972).

2.7 Water depth and near-surface geology beneath line 6

Figure 2.9 shows a lithological map of the Bothnian Sea according to Winterhalter (1972) and the BABEL profiles in that region. Line 6 crosses a region of Middle Ordovician limestone. Winterhalter (1972) found that there was poor acoustic penetration through this limestone and the effects of this are seen in the normal-incidence data for this line (chapter VI). Figure 2.10 shows the water depth profile for BABEL line 6 measured during the BABEL project, and interpreted according to the lithology map (Figure 2.9) and bathymetry map (Figure 2.7). Line 6 runs from the southern end of the Bothnian Sea across the Fingrunden high, the Central ridge and Vänta Litets Grund to the southern edge of the Northern basin. The Aranda rift is seen as a sharp change in water depth to the north of the line. Apart from this, the major changes in water depth occur where the lithology changes. The small region of Jotnian sandstone is characterised by relatively flat topography. Winterhalter (1972) also noted a correlation between flatness of topography and sedimentary rocks.

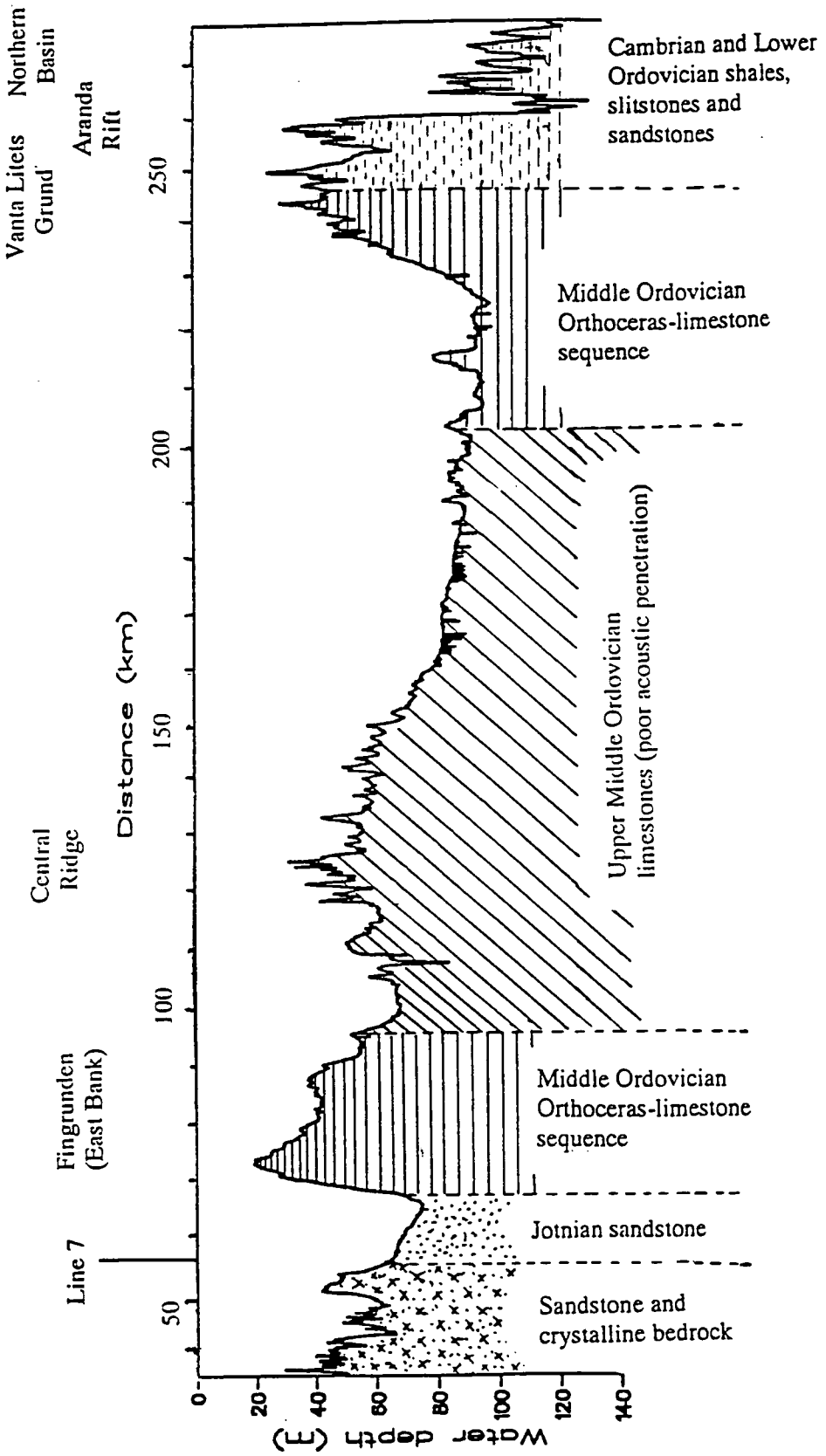

Figure 2.10. Water depth and related surface geology along BABEL line 6. Dotted lines indicate changes in surface geology, not dip of beds.

CHAPTER III

GEOPHYSICAL STUDIES OF THE BALTIC SHIELD

Many investigations of the Baltic Shield have been undertaken using seismic and other geophysical methods in an attempt to solve some of the questions raised by geological studies of the area. BABEL is the most recent and highest resolution deep seismic project to have been shot in Fennoscandia and fills an important gap in the previous seismic coverage. Lines 6 and 1 run almost parallel to several of the previous deep seismic refraction profiles shot on land in Finland and Sweden. Line 7 lies approximately along the line of an older unreversed deep seismic profile; the Sylen-Porvoo line (these two are the only east-west lines within the Sea of Bothnia). The results from deep seismic profiles prior to BABEL and from other geophysical studies of the Baltic Shield are summarised in this chapter and will be compared to the raytraced model for BABEL line 6 in chapter IX.

3.1 Deep seismic wide-angle reflection profiles

There have been several deep seismic crustal studies of the Baltic Shield in Fennoscandia since the first seismic refraction profile in Finland in 1958. The resolution of these has improved over time with the use of temporary recording stations, closer shot spacing and improved modelling processes. Some of the earliest profiles have been reinterpreted using modern techniques. Only profiles that were shot, or have been reinterpreted, since 1970 will be considered in this section. Five of these seismic profiles lie within, or cross, the Svecofennian domain of the Baltic Shield near to the Gulf of Bothnia. These are listed below in chronological order and their locations are shown in Figure 3.1.

SYLEN-PORVOO	1965
BLUE ROAD	1972
FENNOLORA	1979
SVEKA	1981
BALTIC	1982
BABEL	1989

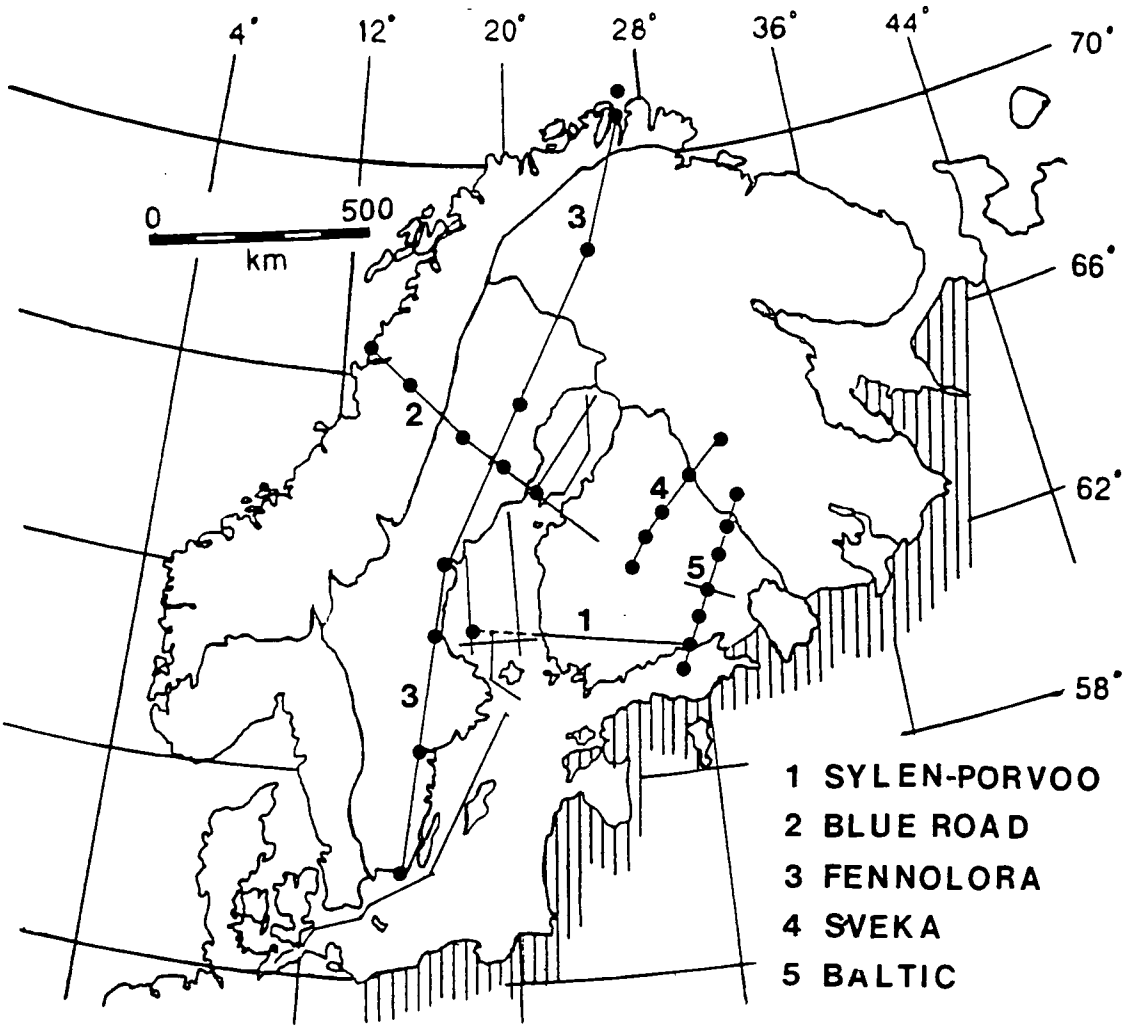

Figure 3.1. Deep seismic refraction profiles in the Svecofennian region of the Baltic Shield. Unnumbered profiles are from the 1989 BABEL project.

3.1.1 Sylen-Porvoo

The Sylen-Porvoo profile was shot in 1965 at the southern end of the Sea of Bothnia. It consisted of a series of sea-based explosive shots fired along the Pyhäanta-Sylen sea line that were recorded at seven permanent land stations in Finland between Pyhäanta and Porvoo (Figure 3.2a). The profile runs close to BABEL line 7 and crosses line 1 but does not extend as far west as line 6 (Figure 3.1). All but two of the recording stations were sited within the Svecofennides; the remaining two (PYH and LAI in Figure 3.2a) were sited on a large Rapakivi granite intrusion. In total 150 underwater shots were fired, with station-shot offsets ranging from 17 to 411 km.

The data from 49 of the largest shots have been reinterpreted by Luosto (1986), despite the fact that the profile was unreversed and the original recordings

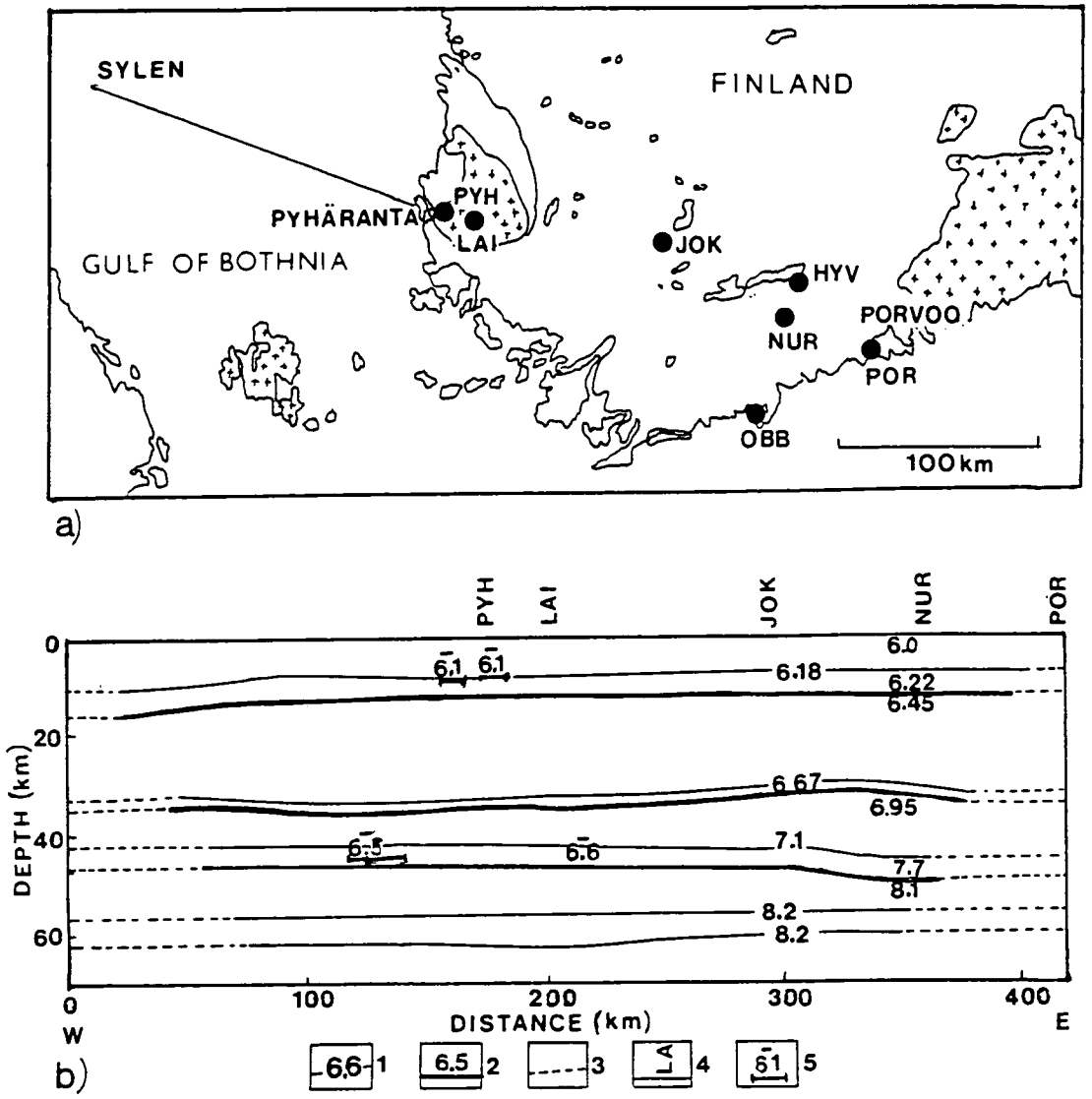

Figure 3.2 a) Location of the Sylen-Pyhäanta sea line and the land-based recording stations of the Sylen-Porvoo project. **b)** 2D model of the crustal structure along the Sylen-Porvoo profile. Legend: 1. velocity isoline, 2. seismic discontinuity with P-wave velocity above it, 3. continuation of isoline or boundary, 4. seismic recording station, 5. reflection element with the average velocity of the upper media, (after Luosto, 1986).

exist only as paper copies (in many cases recorded with slow paper speeds). The data was modelled using the seismic raytracing program SEIS83 (a forerunner of the BEAM87 program used to model the BABEL line 6 data) and a starting model based on 1D velocity gradients calculated at individual stations. The resulting 2D model is shown in Figure 3.2b.

Boundaries in the model are generally horizontal and there are no major changes in depth. The average P-wave crustal velocity* is 6.6 km/s. Crustal thickness increases towards the east from 46 to 49 km, with an upper mantle velocity of 8.1 km/s. The reflecting boundary at a depth of 32 km is overlain by a 1 km thick layer in which the velocity increases sharply from 6.67 to 6.9 km/s. Luosto (1986) suggests that this may form a mid-crustal transition zone. The Moho boundary is overlain by a similar zone, approximately 4 km thick, in which velocities increase from 7.1 to 7.7 km/s.

In the mantle, a low velocity zone is seen at depths of 60-63 km and there may be a second zone at around 80 km depth. A reflecting boundary with a velocity step of at least 0.2 km/s was modelled at a depth of 90 km beneath the stations labelled NUR and POR (Figure 3.2a). This is not shown in the Sylen-Porvoo model in Figure 3.2b.

3.1.2 Blue road

The Blue Road profile was shot in 1972 and runs roughly NW-SE to the north of the Sea of Bothnia but still mainly within the Svecofennian domain. The profile extends 600 km from the Norwegian coast, through Sweden and the neck of the Bay of Bothnia and 100 km into southern Finland (Figure 3.3a). Shots were fired at five shot points, roughly 100 km apart, in the Bay and in small lakes. Several reversed data sections were recorded with an average station spacing of 4 km (Hirschleber *et al.*, 1975). The data have been interpreted to give models of the crust and lower lithosphere using several different methods.

The first arrivals for the different shot points where interpreted by raytracing to give a set of 1D crustal velocity profiles (Hirschleber *et al.*, 1975). The velocity profiles showed a simple crust with a near-surface P-wave velocity of 5.7 to 6.2 km/s. Between 15 and 20 km depth the velocities were between 6.0 and 6.2 km/s and in the lower crust the velocity increased from 6.5 to 6.8 km/s. The mantle velocity was a constant 8.0 km/s for all of the shot points. The ray equations for constant velocity media (and for a continuous series of constant velocity layers) and the 1D velocity profiles were used to calculate wavefronts and depths, giving the 2D structure of the Moho. The resulting boundary had a very small reflection coefficient and gently undulated between depths of 37 and 40 km. No thickening of the crust was found beneath the Caledonian mountains.

Lund (1979) developed a more complex model for the lower lithosphere from P-wave and S-wave data. This model, derived using the reflectivity method (Fuchs and

* Unless otherwise stated, the term 'velocity' refers to the P-wave velocity.

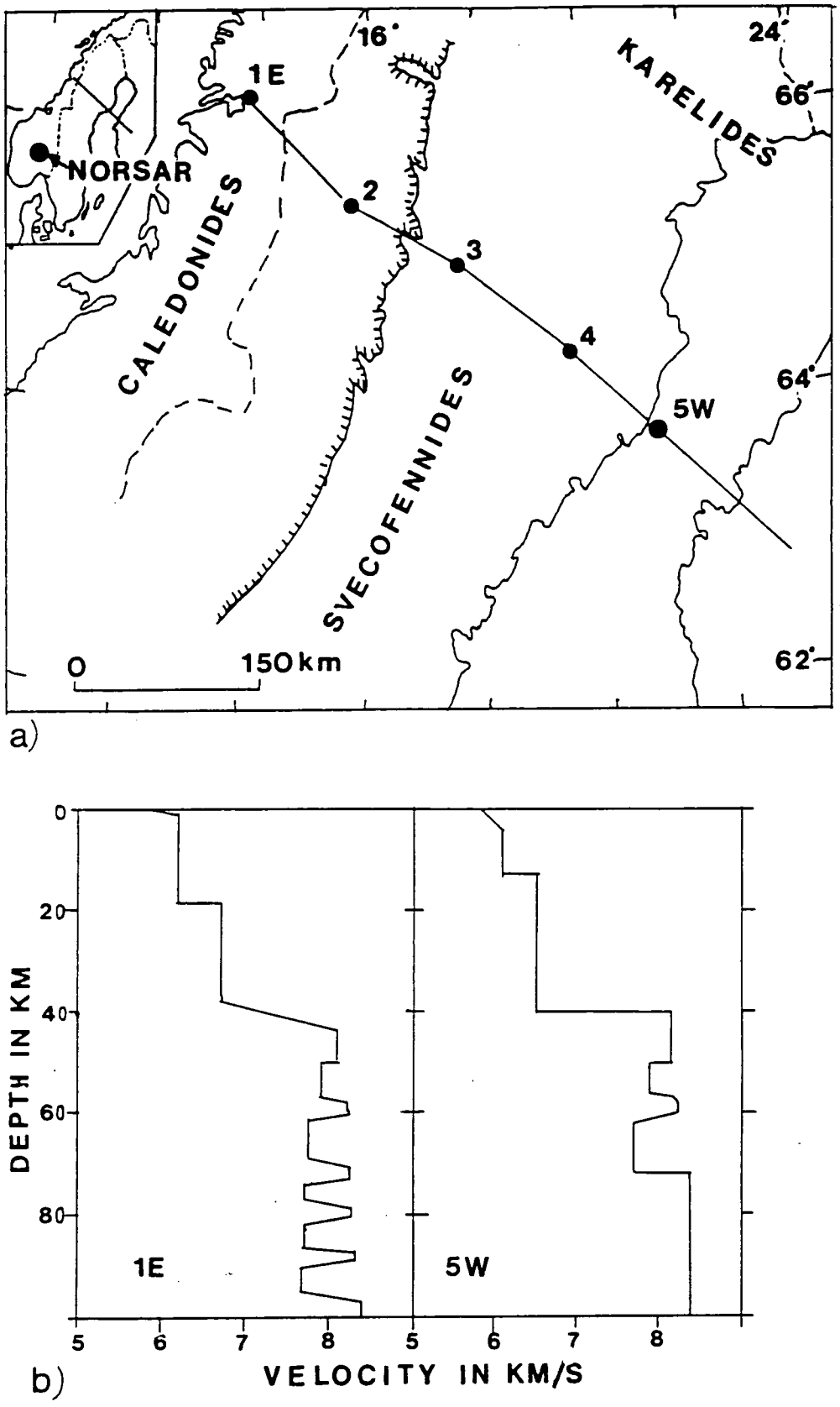

Figure 3.3. **a)** Location of the Blue Road profile and shot points (dots) and of the NORSAR permanent seismic array (after Lund, 1979, Cassell and Fuchs, 1979). **b)** Proposed velocity-depth models for shotpoint 1E in the Caledonides and 5W in the Gulf of Bothnia (Cassell and Fuchs, 1979).

Müller, 1971) , shows a lower lithosphere consisting of a series of alternating high and low velocity channels with no first order discontinuities between them. The SmS reflection was very strong, suggesting a sharp crust-mantle transition. Directly beneath the Moho there is a 4 km thick high velocity layer (8.3 km/s) which curtails the Pn arrival. Beneath this layer the mantle velocity increases to 8.47 km/s at 78 km and to 8.50 km/s at 95 km with velocities of around 8.0 km/s in between.

Cassell and Fuchs (1979) combined the results of the two previous interpretations to derive a detailed velocity model of the subcrustal lithosphere using a modified form of SEIS83. Velocity profiles from a shotpoint to the west of the line (in the Caledonides) and to the east of the line (in the Bay of Bothnia) are shown in Figure 3.3b. The crust is modelled as two homogeneous layers and the Moho is modelled as a first order discontinuity beneath the Svecofennides and as a 6 km thick transition zone beneath the Caledonides. The lower lithosphere consists of several high velocity layers embedded in material of a normal to low seismic velocity (these alternating layers of high and normal velocity were required to model subcrustal arrivals with different travel-times but with similar velocities). The high velocity layers were found to have an average thickness of 1.8 km and were of limited length, possibly no more than 100-160 km. Fewer layers were seen beneath the Svecofennides than beneath the Caledonides.

The crustal models from the Blue road profile were used to partially reinterpret the NORSAR data (Cassell and Fuchs, 1979). This data set consisted of fourteen nuclear explosions in Russia recorded between 1971 and 1976 at the permanent NORSAR seismic array in Norway (Figure 3.3a) and had previously been interpreted to give a model of the upper mantle structure beneath Fennoscandia with monotonously increasing velocities (King and Calcagnile, 1976). The insertion of the low velocity zones found from the Blue Road data into the NORSAR model resolved the discrepancies seen between observed and theoretical amplitudes.

3.1.3 FENNOLORA

The FENNOLORA profile was shot in 1979 as part of the European Geotraverse (EGT) project. The profile runs 1800 km along the Scandinavian Peninsula and the western coast of the Sea of Bothnia and is the closest profile to BABEL line 6. Shots were fired at seven shot points (B to H, Figure 3.4a) with about 250 km between shot points and an average recording site spacing of 3.5 km (the segment of FENNOLORA between shot points D and E is roughly parallel to Line 6). Initial models of the FENNOLORA data showed a 2 layer crust separated by a pronounced mid-crustal boundary at a depth of about 20 km which deepened to the north (Lund, 1990). Low velocity zones were found in the upper crust and have also

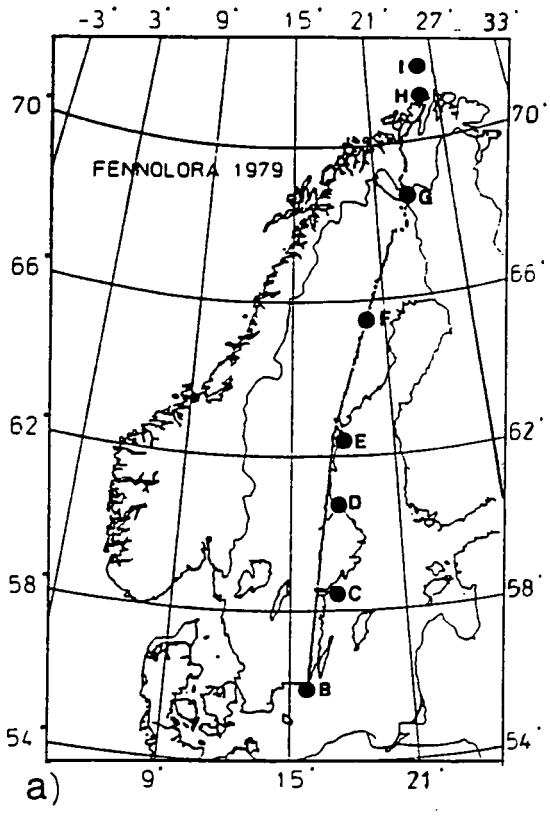

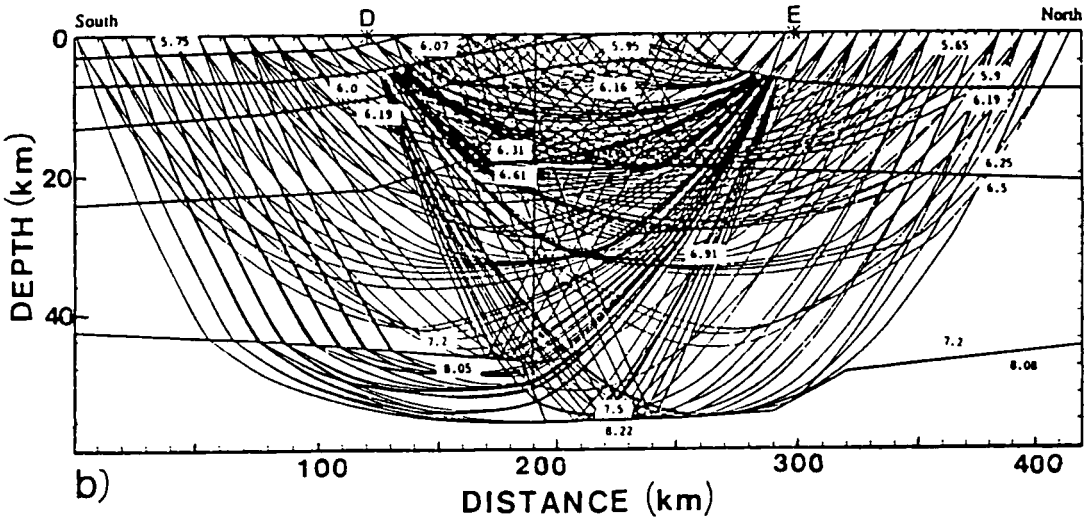

Figure 3.4 **a)** Location of the FENNOLORA profile showing the positions of shot points (large dots) and the individual recording stations (small dots). **b)** 2D crustal velocity-depth structure beneath shot points D and E. Values shown are P-wave velocities in km/s (Guggisberg *et al.*, 1991).

been observed in travel-time interpretations of the FENNOLORA S-wave data (Kullinger and Lund, 1986). Hauser and Stangl (1990) modelled both P-wave and S-wave data and found several differences between the P- and S-wave models. In both models there was a sharp first order crust/mantle boundary overlaying a layered mantle but the S-wave model contained a thin transition zone above the Moho. The ratio of P-wave to S-wave velocity differed in the upper and lower crust. In the upper crust $v_p/v_s < \sqrt{3}$ while $v_p/v_s > \sqrt{3}$ in the lower crust.

The detailed results from the FENNOLORA line are summarised by Guggisberg *et al.* (1991). Negative reduced travel-times were found for the Pg arrival

out to 50 km offset, indicating the absence of sediments along the line. The Pn arrival was first seen at offsets of about 200 km. 1D velocity profiles were constructed and used as the basis for 2D raytracing with SEIS83. Due to the shotpoint separation of 250 km, information on the crust could only be found from neighbouring shot points; arrivals from more distant shot points travelled through the mantle rather than the crust.

The 2D raytraced model for the section of the FENNOLORA profile neighbouring BABEL line 6 is shown in Figure 3.4b. The crust is divided into distinct upper and lower layers. The upper crust has an average thickness of 20 km and the velocity increases from 6.0 to 6.4 km/s. To the south of shotpoint D, a basin-like region is seen in the first 5-10 km depth with a velocity of 5.75 km/s. Between C and D there are a series of alternating high and low velocity layers in the upper crust. These low velocity zones are of limited lateral extent. The zones of reduced velocity in the upper crust are explained by Guggisberg *et al.* (1991) as batholiths and the thinner low velocity zones are explained as granites and granitoids. No major velocity inversions (>0.1 km/s change in velocity) are seen. At the boundary between upper and lower crust the velocity step is small (about 0.3 km/s). The lower crust is quite uniform with a gradual velocity increase from 6.5-6.6 km/s beneath the mid crustal boundary to about 7.2 km/s at the base of the crust. In some regions along the profile (such as between D and E) the crust/mantle boundary deepens considerably and velocities increase to 7.4-7.5 km/s at the base of the crust. The velocity step across the Moho is large along the entire length of the FENNOLORA profile, of the order of 1.3 km/s except beneath the thickened zones where the step is only 0.7 km/s. The deep Moho between D and E coincides with a surface thrust zone (Figure 2.10, Berthelsen and Marker, 1986, Guggisberg *et al.*, 1991).

3.1.4 SVEKA

The SVEKA profile runs 320 km NE-SW from Jyvãskylã to Kajaani in Finland (Figure 3.5). It was shot in 1981 using explosive sources roughly 80 km apart in 5 small lakes. These shots were recorded at 2 km intervals (Luosto *et al.*, 1984). The profile is parallel to the northernmost BABEL lines in the Bay of Bothnia (lines 2, and 4) and is the nearest deep seismic profile in Finland to line 6.

Although the SVEKA profile is more northerly than line 6, it lies partially within the same geological domain. The profile crosses from the Svecofennides/ Svecokarelides in the south-west to the Archaean domain in the north-east across the Ladoga-Bothnian Bay zone (Figure 2.1). Magnetotelluric and gravity measurements were also made near to the profile and showed lateral electrical heterogenities and a

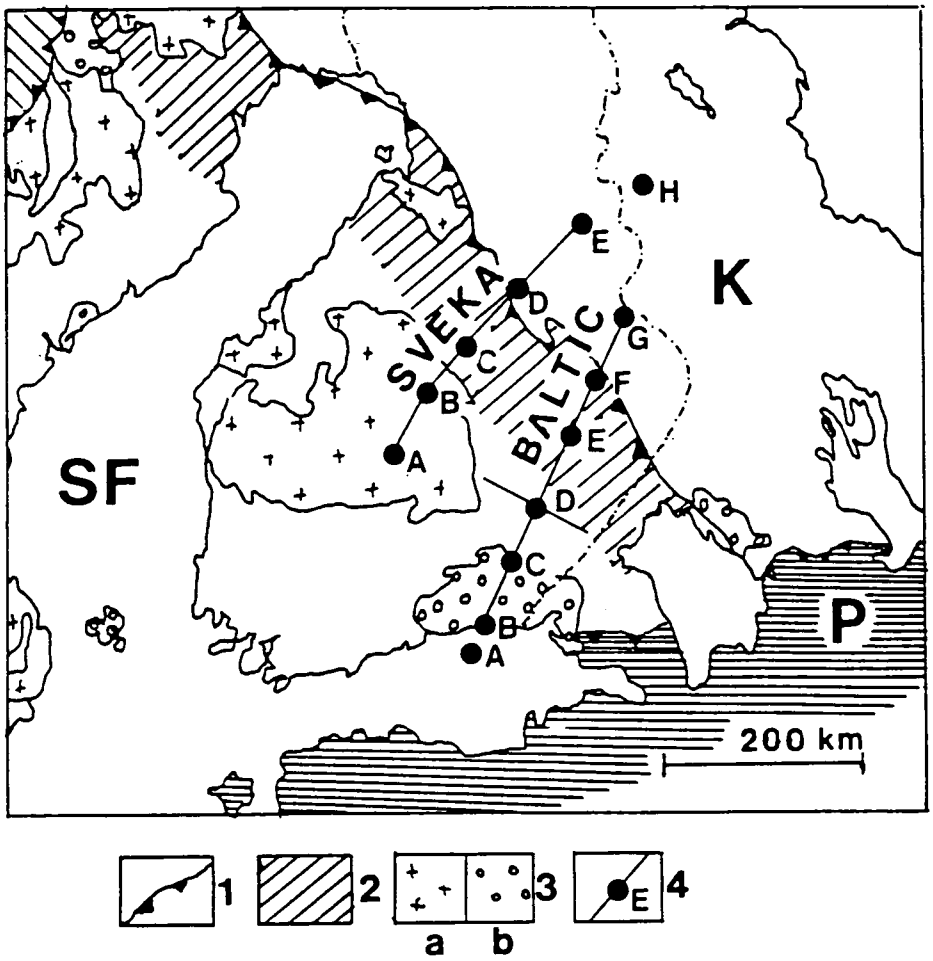

Figure 3.5 Location of the BALTIC and SVEKA DSS profiles in relation to the major geological features of the region (after Luosto *et al.*, 1990). Legend: 1. Borders of the main tectonic zones, 2. Ladoga-Bothnian Bay zone, 3. Proterozoic granites (a) 1.9-1.8 Ga, (b) 1.7-1.5 Ga, 4. profiles and shot points.

regional increase in gravity towards the north-eastern end of the profile. As well as crustal arrivals, fragmentary P-wave reflections from a discontinuity beneath the Moho were identified and changes in phase and amplitude with offset were seen. Luosto *et al.* (1984) suggested that these changes might indicate the presence of crustal blocks separated by deep fractures. Grad and Luosto (1987) used 2D ray tracing with SEIS83 to model P-wave and S-wave data from SVEKA, giving the model shown in Figure 3.6a (the S-wave data was modelled using the boundaries of the initial P-wave model).

The model shows a distinct division into upper and lower crust with v_p/v_s ratios less than $\sqrt{3}$ in the upper crust and greater than $\sqrt{3}$ in the lower crust, as for the FENNOLORA. Below the Moho the ratio of P-wave to S-wave velocity is $\sqrt{3}$. In the upper crust there is a 3-7 km thick low-velocity zone (shown hatched in Figure 3.6a) which may be interrupted by thin high-velocity slabs (Luosto and Korhonen, 1986). At roughly 20 km depth there is a velocity step from 6.35 to 6.6 km/s across the boundary between upper and lower crust. This gives rise to strong refracted and

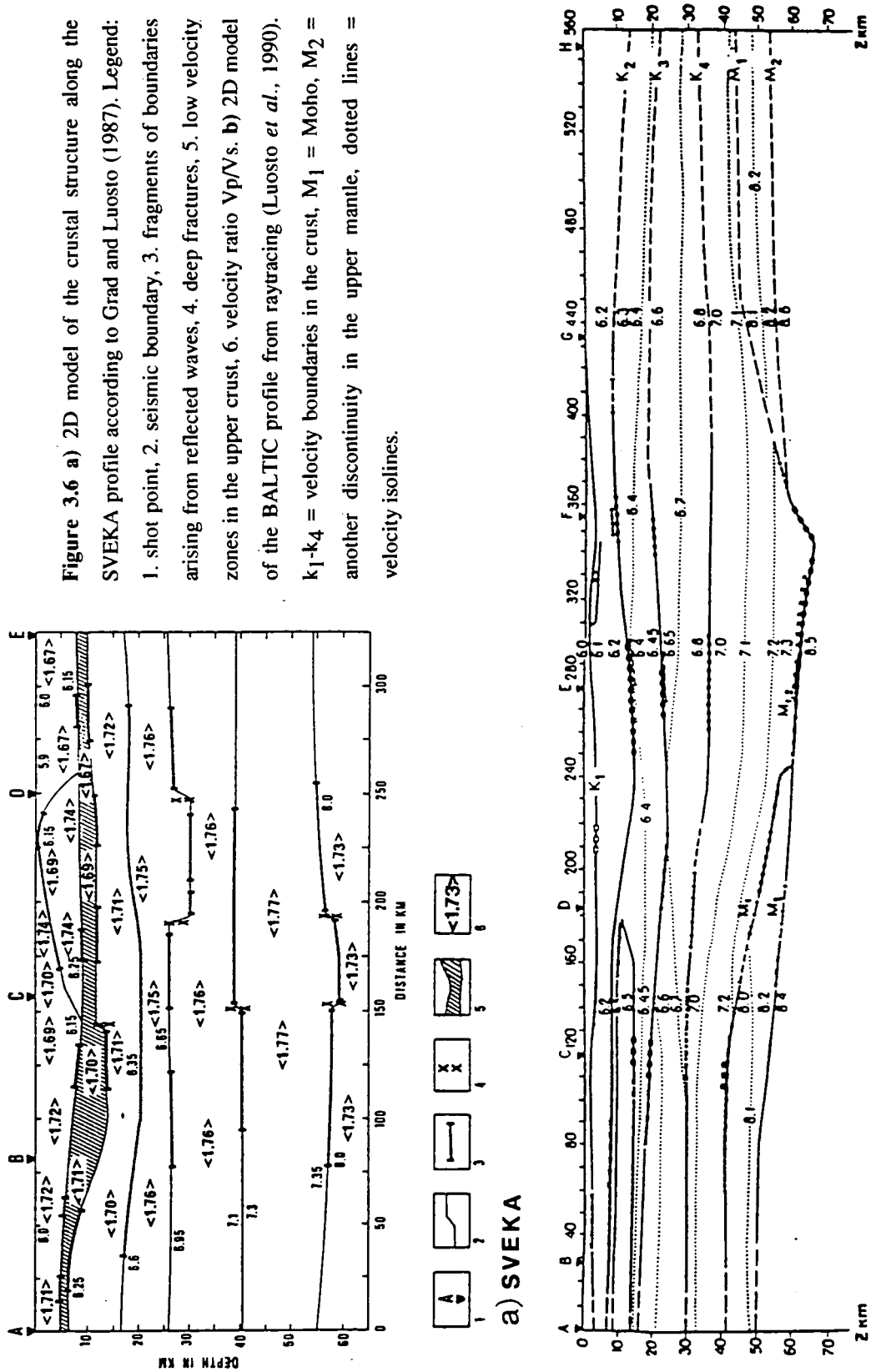

Figure 3.6 a) 2D model of the crustal structure along the SVEKA profile according to Grad and Luosto (1987). Legend: 1. shot point, 2. seismic boundary, 3. fragments of boundaries arising from reflected waves, 4. deep fractures, 5. low velocity zones in the upper crust, 6. velocity ratio Vp/Vs. **b)** 2D model of the BALTIC profile from raytracing (Luosto *et al.*, 1990). k_1-k_4 = velocity boundaries in the crust, M_1 = Moho, M_2 = another discontinuity in the upper mantle, dotted lines = velocity isolines.

reflected phases. The lower crust is divided into three layers: the uppermost with a velocity of about 6.6 km/s, the second with a velocity of 7.0 km/s and the lowest with a velocity of 7.3 km/s. The mantle velocity is 8.0 km/s and crustal thickness in the model varies from 55 to 59 km. The SmS arrival is much stronger than the PmP, suggesting that there is a greater S-wave than P-wave velocity contrast across the Moho.

Deep fractures extend almost through the crust, separating it into different blocks. These fractures are seen as steps on the boundaries of the 2D model. The block beneath the Ladoga-Bothnian Bay zone has a thicker crust than the other blocks and coincides with a negative gravity anomaly.

3.1.5 BALTIC

The BALTIC profile was recorded in 1982 in Finland to the east of, and almost parallel to, the SVEKA line (Figure 3.5). The southern end of the profile lies at roughly the same latitude as the southern end of line 6 but, as a result of the NW-SE trend of the geological domains of the Baltic Shield, only the southern part of the line lies in the Svecofennides. The main profile extended 450 km from the Rapakivi massif in the south, across the Ladoga-Bothnian Bay zone and into the Archaean domain. A 130 km transverse profile was shot near to the middle of the main profile (close to shotpoint D). Shots were fired at seven shot points; two in the Gulf of Finland and 5 in small lakes in Finland. Large explosions from a quarry just inside Russia were also recorded (shotpoint H). The shotpoint spacing varied from 30 to 100 km. Shots were recorded by 48 stations with an average spacing of 2 km (Luosto *et al.*, 1985).

Luosto *et al.* (1990) modelled both the S-wave and P-wave data along the BALTIC profile. Initial models were generated by calculating travel-times of refracted waves with different reduction velocities and comparing them to the observed data and by using a generalised inversion method (Buyanov, 1986). These models were used as a starting point for raytracing with SEIS83. The final 2D model for the BALTIC profile is shown in Figure 3.6b. The crust is separated into five layers with the near-surface P-wave velocities varying from 5.8 to 6.1 km/s. To the southern end of the profile there is a high velocity wedge in the third layer with a velocity of 6.5 km/s. This lies directly beneath the Rapakivi massif. Between shotpoints E and F an anomalous high velocity body (V_P = 6.4 km/s) is seen in the upper crust which is associated with the Outokumpu ore formation (Luosto and Korhonen, 1986).

Laterally, the crust is divided into three distinct blocks. In the southern and northern blocks the crust is 40-50 km thick and the Moho is marked by two boundaries: M_1 and M_2. The velocity beneath the upper boundary (M_1) is 8.0 km/s

and the velocity beneath the lower (M_2) is 8.4-8.5 km/s. In the central block, between shot points E and F, these two boundaries are coincident and the crustal thickness is 60 -65 km. In all three blocks the crust/mantle boundary is sharp; in the central section the velocity step is 1.2 km/s. Luosto *et al.* (1990) also suggest that there may be a series of thin high and low velocity layers beneath the Moho. As on the SVEKA profile, the Ladoga-Bothnian Bay zone is seen as a region of anomalously thick crust.

The v_p/v_s ratio differs between the blocks. In the southern block the values are higher than average, in the central block the ratios are roughly $\sqrt{3}$ and in the northern block they are lower than average. The high values to the south may be due to the Rapakivi body which may have retained a higher plasticity since its intrusion into the Svecofennian crust (Luosto and Korhonen, 1986). This may also explain the discrepancies between the southern part of the BALTIC model and the model for the neighbouring SVEKA profile; the BALTIC model shows a thinner crust, lower S-wave velocities, a crust/mantle transition zone and a high velocity layer in the upper crust. The three blocks correspond to the three different geological regions crossed by the profile: the Svecofennian, the Ladoga-Bothnian Bay zone and the Archaean. The crust beneath BABEL line 6 should be similar to the southernmost of the three blocks.

3.2 Other crustal studies

3.2.1 Permanent seismic stations

Fennoscandia has a good network of permanent seismographic stations including the wide aperture NORSAR array mentioned previously (section 3.1.2). Bungum *et al.* (1980) used data from eleven of these permanent stations and the results from the NORSAR array to estimate the crustal thickness of the Baltic Shield. Their results agree well with those of the deep seismic profiles and show thin crust (28-33 km) in southern Fennoscandia bordering to Kattegat, Skagerrak and the North Sea and thicker crust of about 45 km beneath the Sea of Bothnia.

Figure 3.7 shows the epicentres of earthquakes recorded in Fennoscandia between 1375 and 1989. The total number of events exceeds 5700 and 46% of these have been reported since 1980 (Ahjos, 1990). The majority of epicentres around the coast of the Gulf of Bothnia are on the Swedish side. This agrees with geological results which have shown this coastline to be highly faulted while the Finnish side has a more gentle topography.

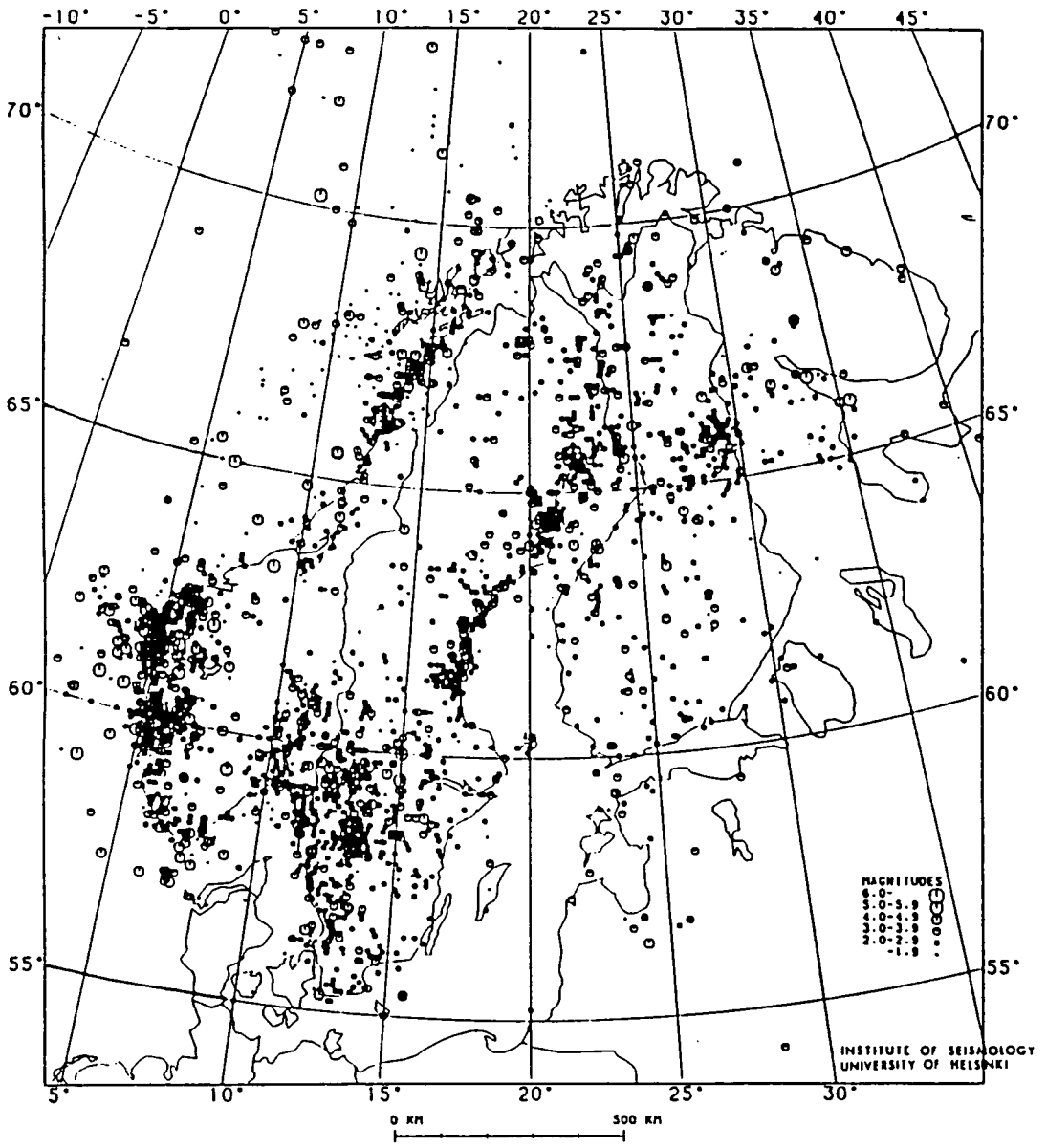

Figure 3.7. Earthquake epicentres in Fennoscandia from 1375 to 1989 (Ahjos, 1990).

Fennoscandia is undergoing post-glacial rebound at present with a maximum rate of 1 cm yr^{-1} in the Bay of Bothnia (Figure 3.8a, Bungum *et al.*, 1980). This post-glacial uplift does not appear to correlate with the variation in crustal thickness. This is understandable if the rebound is not a crustal effect but that it is due to flow in the lower lithosphere or asthenosphere.

3.2.2 Aeromagnetic and gravity surveys

Long-wavelength free-air gravity anomalies from satellite observations show Fennoscandia as a negative anomaly within a geodetic high plateau (Bungum et al., 1980). Figure 3.8b shows the Bouger anomaly map of the Gulf of Bothnia based on

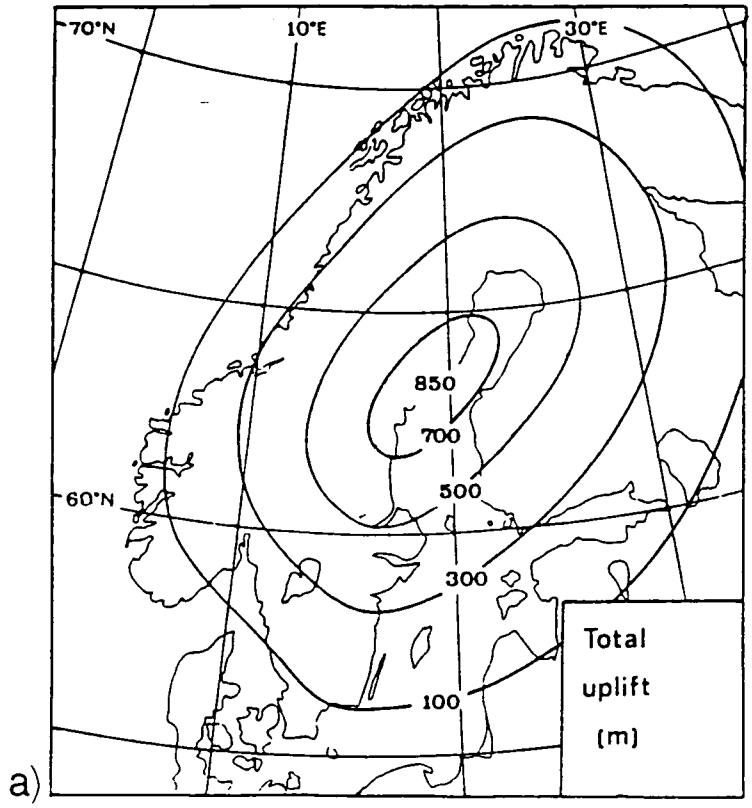

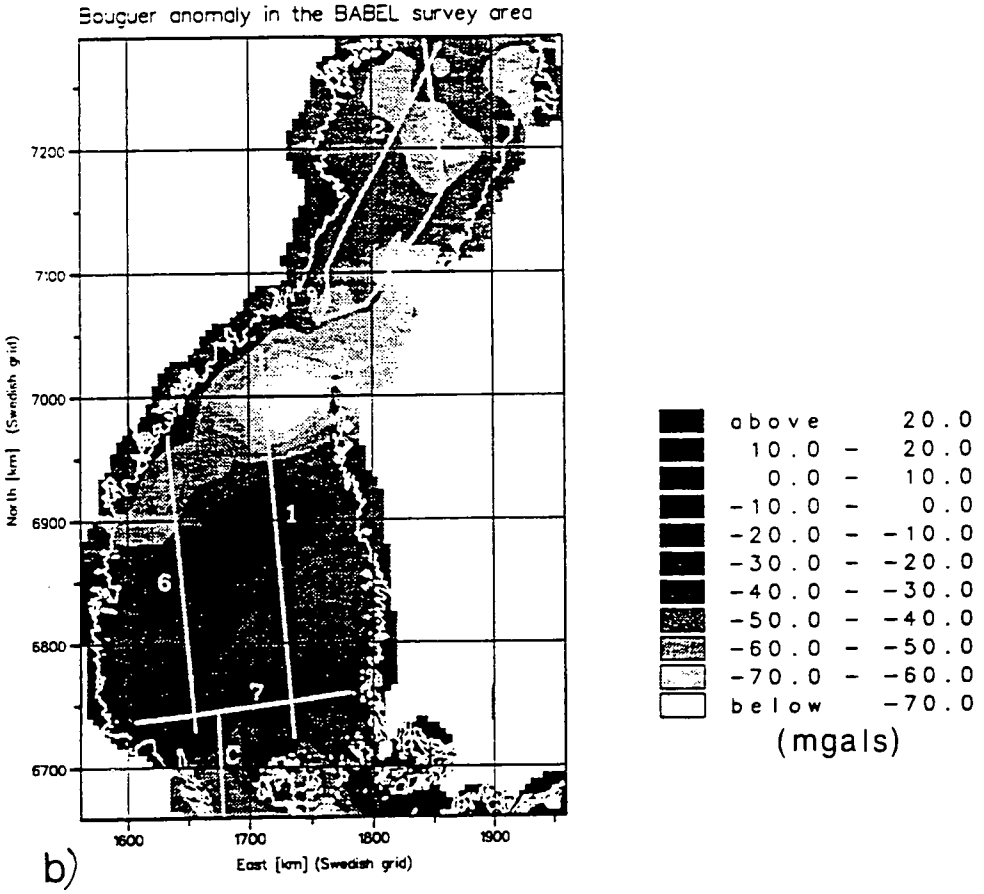

Figure 3.8 a) Postglacial uplift in Fennoscandia (Bungum *et al.*, 1980), **b)** Bouger anomalies in the Sea of Bothnia (Pedersen *et al.*, 1992).

Seasat and Geos-3 altimetry measurements, with a sample interval of 30 km (Pedersen *et al.*, 1992). Anomalies in the Sea of Bothnia run NE-SW. If the anomalies originally ran E-W, this would be consistent with the direction of displacement along the Baltic and Bothnian megashear zone suggested by Berthelsen and Marker (1986).

Within the Sea of Bothnia, two large anomalies are seen along BABEL line 1; a gravity low at the northern end of the line where the Bouger anomaly decreases to below -70 mgals and a gravity high at approximately the middle of the profile where the Bouger anomaly is greater than 0.0 mgals. Along BABEL line 6 the variation is much less. The Bouger anomaly is generally between -30 and -20 mgals. At the southern end, where line 7 crosses line 6, there is a small gravity high of -20 to -10 mgals. The gravity low seen at the northern end of line 1 appears to extend to line 6 although it becomes smaller and less pronounced (-40 to -50 mgals). The gravity high seen at the middle of line 1 does not appear to extend as far west as line 6.

The Bouger anomaly data was not available until late in this project and no gravity model has yet been constructed for line 6. Pedersen *et al.* (1992) calculated a gravity model for the line 1 data. They suggested that the gravity high at the centre of the line was caused by a large mid-crustal body with a density of $+0.12 g/cm^3$ relative to the surrounding rock. This body maps to a region of low reflectivity on the normal-incidence data for line 1. The gravity low at the northern end of the line is modelled as due to a thickening of the crust.

An aeromagnetic map of northern Europe has been compiled by Wonik and Hahn (1990) measured from an altitude of 3000 m with a contour interval of 100 nT. Unfortunately, the low level survey of Sweden has not yet been completed and it is not possible to map Sweden or the western half of the Gulf of Bothnia to this accuracy. A map of the total magnetic field intensity, with a lower accuracy, is shown in Figure 3.9a. A maximum is seen at approximately the centre of line 6. A strong maximum is also seen between line 7 and the island of Åland. This has been interpreted by Pedersen *et al.* (1992) as due to a post-orogenic granitoid pluton similar to those seen in the central Scandinavian granite-porphyry belt.

Regional gravity and magnetic surveys of Fennoscandia have revealed two types of structure, one on a crustal scale that is thought to be related to plate tectonic processes and a second type which are smaller and form circular patterns (Henkel and Eriksson, 1987). An example of a crustal scale structure is the Protogine belt in southern Sweden which forms the western limit of the Trans-Scandinavian granite-porphyry belt (Figure 3.9b). Distinct magnetic lows are seen over this feature. Two large circular structures of the second type have been identified: one in the north of the shield in the Archaean province and a second in the Svecofennides of Sweden to the south of line 6 (Figure 3.9b). The latter of these can be seen on Landsat images and in

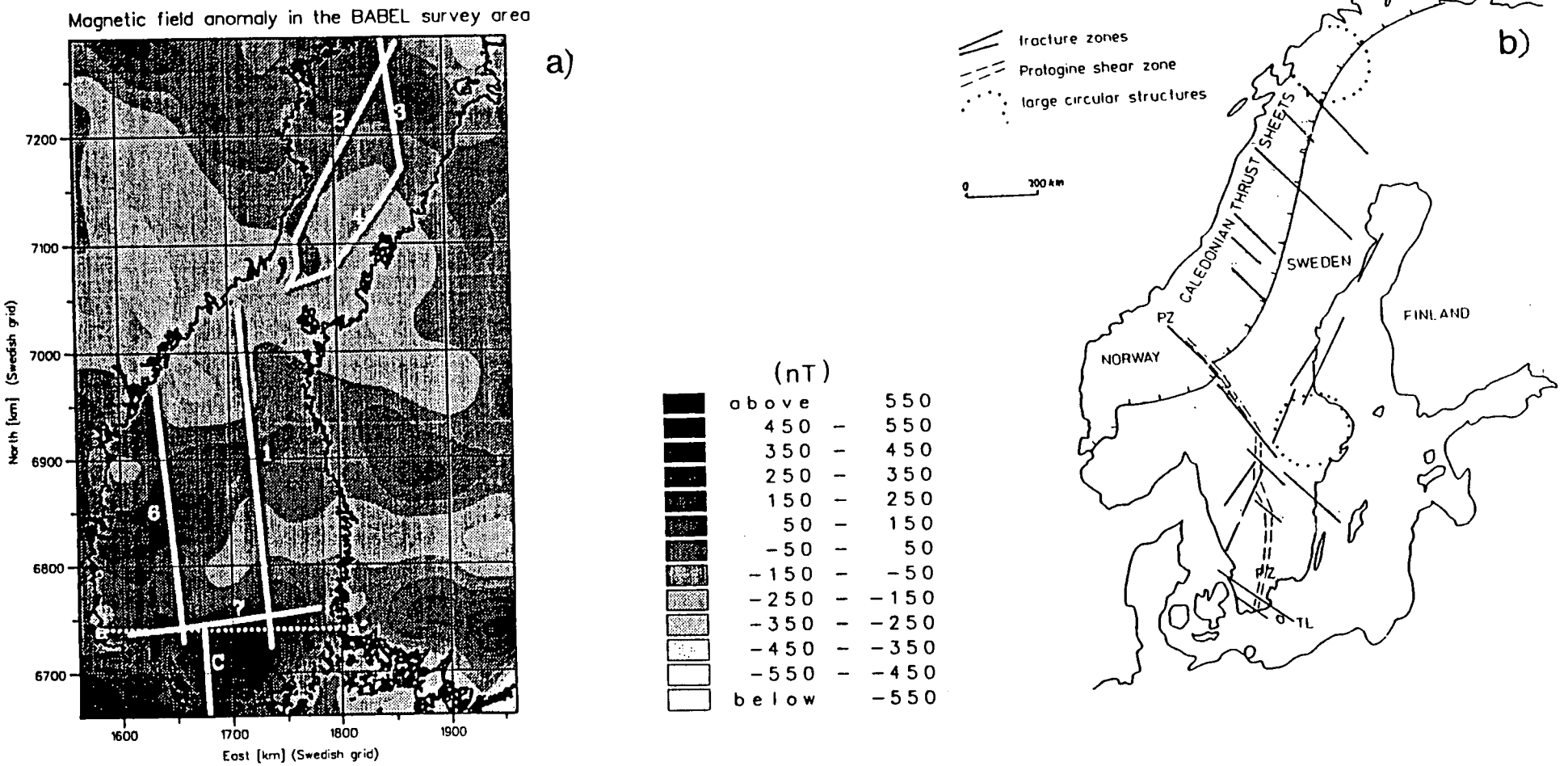

Figure 3.9 a) Magnetic anomaly map of the Sea of Bothnia (Pedersen *et al.*, 1992), **b)** Sketch map of aeromagnetic anomalies in western Fennoscandia from low altitude aeromagnetic measurements (Henkel and Eriksson, 1987). PZ - protogine shear zone, TL - Tornquist line. The southernmost circular structure has also been identified on Landsat images.

the topography of the region. These circular structures are characterised by a central gravity and magnetic high and the alignment of surrounding structures, and may be the results of large meteorite impacts in the late Precambrian (Henkel and Eriksson, 1987).

3.2.3 Geoelectric studies

The lower crust is a good conductor in most parts of the Baltic Shield while the upper crust is electrically inhomogeneous with several conductive zones which affect deep electromagnetic soundings (Hjelt, 1990). The crust can be divided into different geoelectrical blocks. In central Finland these blocks are separated by narrow, highly conductive bands within the mid-crust and the crustal conductivity increases from east to west.

Magnetotelluric, magnetovariational and frequency sounding methods have all been used to study the geoelectrical character of the Baltic Shield in Finland (Hjelt, 1987) and several crustal conductive anomalies have been identified. The surface projection of the main anomalies in Fennoscandia are shown in Figure 3.10a (Hjelt, 1992). The anomalies lie mainly to the north and east of the Sea of Bothnia. The Oulu anomaly is a zone of low resistivity that runs roughly N-S for 100 km to shore of the Bay of Bothnia. A similar low resistivity region has been found in northern Sweden: the Skellefteá anomaly and it has been suggested that the two are connected. In SE Finland there are two major anomalies: the Lake Ladoga anomaly and one associated with the Outokumpu ore belt (this ore belt is seen as a high velocity body on the BALTIC deep seismic profile, Luosto and Korhonen, 1986). A strong anomaly in the upper crust surrounds the central Finnish granite area (the Tampere Schist Belt). This anomaly is thought to change direction on the west coast of Finland (Figure 3.10a) but may continue out to sea (Hjelt, 1987). Magnetotelluric measurements were made along the FENNOLORA profile in Sweden but the spacing between these is too great to construct a reliable geoelectrical model along this line.

3.2.4 Heat flow

Surface heat-flow is a measure of the heat flow beneath the crust augmented by radiogenic heat production within the crust. The heat flow data for Fennoscandia has been interpreted by Balling (1990). Highest heat-flow densities are measured within granitic rocks which contain large amounts of heat producing elements. Figure 3.10b shows the regional variation of surface heat-flow for Fennoscandia. The oldest part of the Baltic Shield, the northern Archaean craton, has the lowest heat flow and

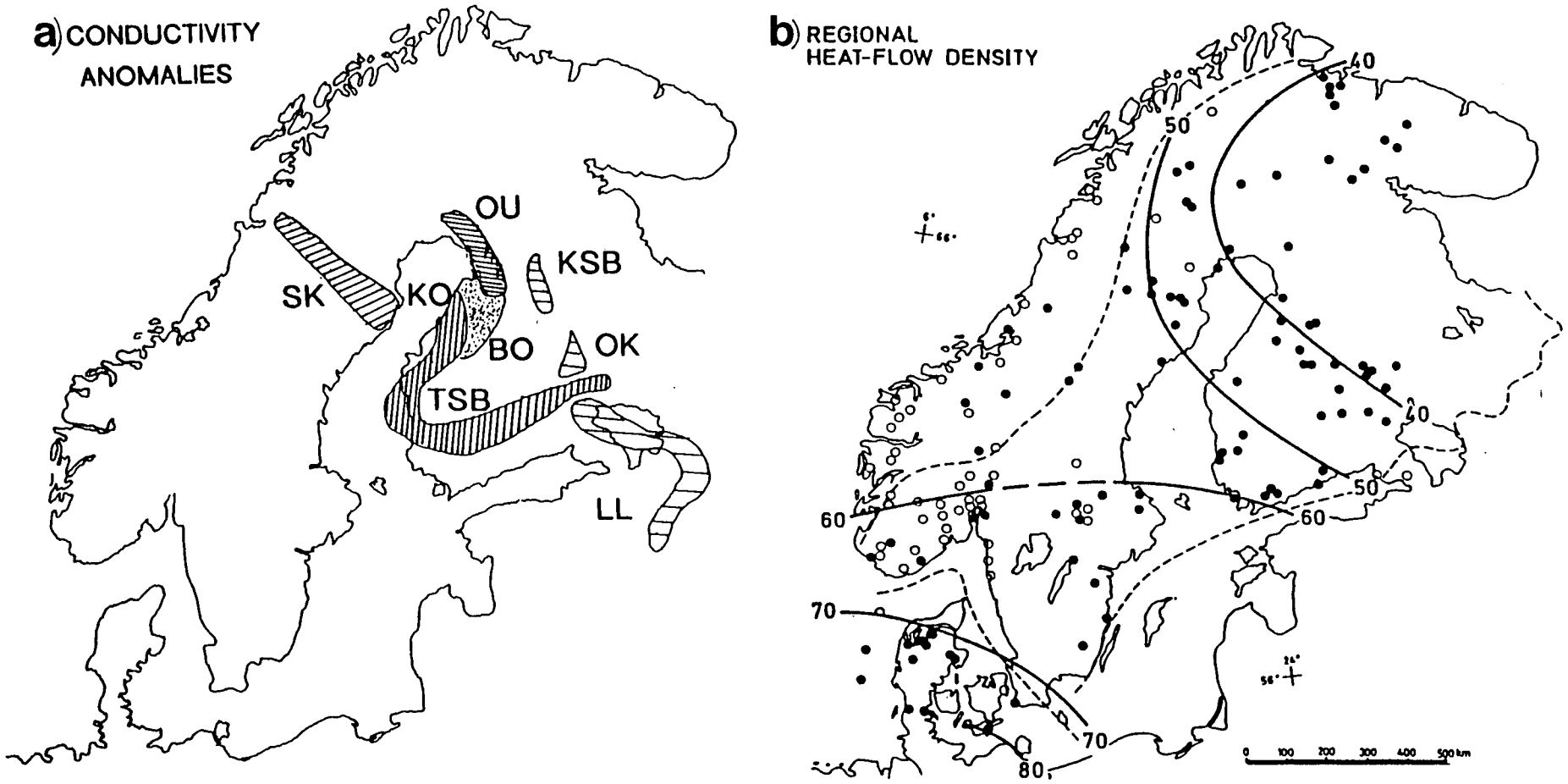

Figure 3.10 a) Horizontal projections of electrical crustal conducting anomalies in Fennoscandia (after Hjelt, 1992). Anomalies: BO - Bothnian; KO - Kokkola; OU - Oulu; SK - Skellefteå-Storavan; KSB - Kainuu Schist Belt; LL - Lake Ladoga; OK - Outukumpu; TSB - Tampere Schist Belt. **b)** Regional heat-flow density (mW/m^2) in the Fennoscandian region (Balling, 1990). Filled and open circles are the locations of observational sites.

heat-flow generally increases from the north-east to the south-west. Along BABEL line 6, the heat flow increases southwards from 50 to 60 mW/m^2. This may be the result of the transition from the central Svecofennian province of metasediments into the southern volcanic belt and to the presence of the Rapakivi granitoid intrusions to the south of the line.

3.3 Generalised structure of the Baltic Shield

The results from deep seismic surveys and other geophysical investigations have been compiled by several authors to produce a generalised model of the crustal structure of the Baltic Shield (Sellevoll, 1973, Pavlenkova, 1979, Luosto, 1990). The typical characteristics of the shield crust derived from projects prior to BABEL may be summarised as follows:

1. Due to the lack of sedimentary cover in Fennoscandia, near-surface P-wave velocities are high and the velocity rapidly reaches 6.0 km/s. In the Svecofennides, the average crustal P-wave velocity is 6.6-6.8 km/s and the crust is about 45 km thick. P-wave reflections from the Moho are weak. A high velocity layer (Vp > 7.0 km/s) is seen in the lower crust (Korhonen *et al.*, 1990).
2. Zones of reduced velocity are seen in the upper crust but are thin and of limited extent (Luosto and Korhonen, 1986).
3. Sharp discontinuities are rare within the shield crust; most boundaries are characterised by small velocity steps overlain by strong velocity gradients. Velocity inversions, if present at all, are only minor (Guggisberg *et al.*, 1991).
4. The Rapakivi granites may be associated with high velocity layers of about 6.5 km/s and high velocity bodies may also be found in the region of conductivity anomalies such as the Outokumpu anomaly (Luosto *et al.*, 1990).
5. v_p/v_s ratios are below $\sqrt{3}$ in the upper crust and above $\sqrt{3}$ in the lower crust (Hauser and Stangl, 1990, Grad and Luosto, 1987). The ratio also differs between the Svecofennian and Archaean provinces (Luosto *et al.*, 1990).
6. The average thickness of the Baltic Shield is 46 km and thins to the south. The Ladoga-Bothnian Bay zone is a region of anomalously thick crust with Moho depths of 50-55 km (Luosto, 1986).
7. The upper mantle is layered with alternating high and low (or normal) velocity layers. Subcrustal reflectors are also seen (Luosto *et al.*, 1984, Cassell and Fuchs, 1979, Luosto, 1986).

Figure 3.11 shows a Moho depth map compiled from the results from profiles in Fennoscandia (Luosto, 1990). The Rapakivi intrusion in SE Finland is seen as a

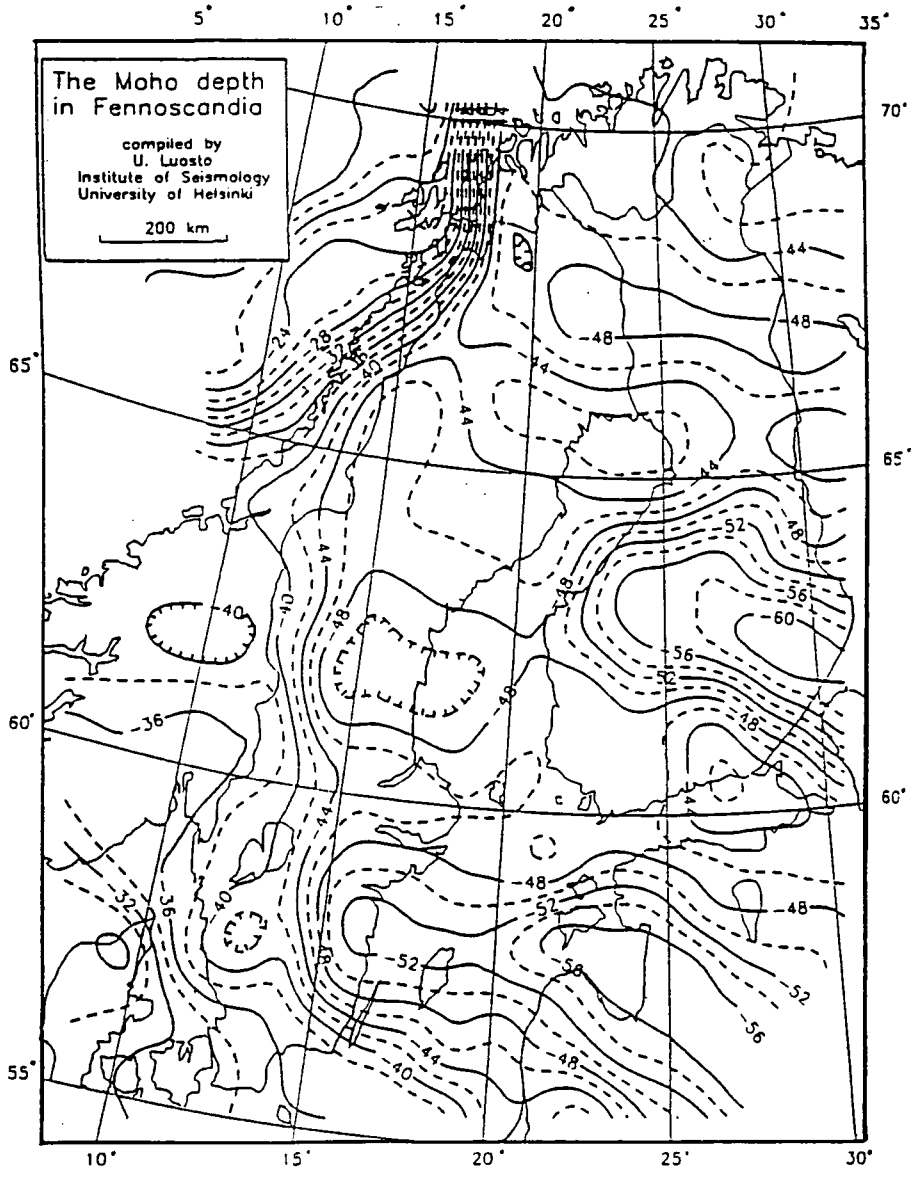

Figure 3.11 Moho depth isolines compiled from refraction profiles prior to BABEL and other geophysical studies of the Baltic studies (Luosto, 1990).

region of thin crust. The depression in the Moho beneath the Ladoga-Bothnian Bay zone appears to be related to the depression on the FENNOLORA line between shot points D and E rather than to the more northerly Skellefteá region where this zone is generally assumed to continue (Luosto, 1990). This would suggest that the crustal thickness should increase towards the middle of line 6 in a manner similar to that seen on the BALTIC and SVEKA lines. Luosto (1990) states that the connections between these regions may be artefacts of the interpolation method due to the lack of data from the sea areas between Sweden and Finland. One of the aims of the BABEL project was to provide data from this region to enable features seen in Finland to be related more accurately to those seen in Sweden.

CHAPTER IV

BABEL 1989: DATA ACQUISITION

4.1 The BABEL profiles

The BABEL project was shot between 16th September and the 8th October 1989. Over 2268 km of deep seismic profiles were recorded at normal-incidence and wide-angle by teams of Swedish, Finnish, German, Danish and British scientists. The profiles were divided into nine lines (Figure 4.1). Lines 1-7 formed the northern part of the experiment and were designed to give a three dimensional coverage of the Gulf of Bothnia. In the south, line A crossed the Tornquist zone (Europe's longest tectonic lineament), approximately perpendicular to its supposed strike, and lines B and C linked the northern and southern parts of the project.

The BIRPS[1] core group was responsible for the acquisition of the normal-incidence data while other groups recorded wide-angle data at onshore recording arrays installed around the coast of the Gulf of Bothnia and the Baltic Sea in Finland, Sweden and Denmark. Since airgun shots were expected to travel long distances (400-500 km) through the shield crust, it was decided that the onshore recording stations should, wherever possible, remain in position for the duration of the experiment, although shortages of equipment meant that this was not always feasible. The station-shot offsets along the BABEL profiles were such that the wide-angle part of the experiment imaged principally the mid and lower lithosphere.

During the northern part of the experiment, Durham University was involved in wide-angle data recording in Sweden using an array of fifteen analogue recording stations around the Swedish coast of the Sea of Bothnia. These were supplemented by two digital PDAS recorders. One PDAS was located at the centre of the analogue array and recorded continuously while the second instrument was used to record particular lines from temporary on-line sites.

The wide-angle profiles were divided into a series of independent experiments to be worked up by the individual groups involved. Durham elected to work on lines 1,

[1]British Institutions Reflection Profiling Syndicate

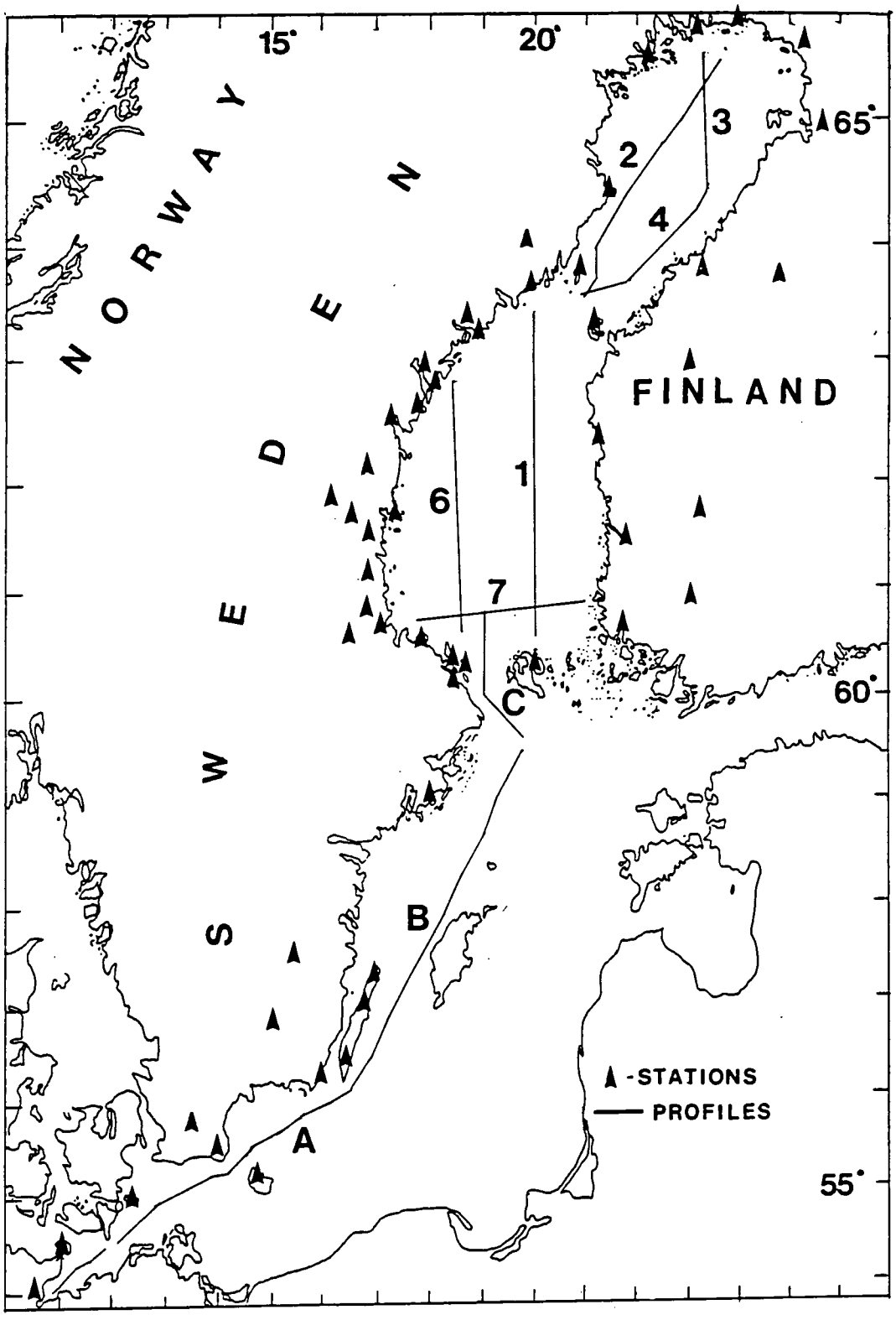

Figure 4.1. Location map of the nine BABEL profiles and the onshore recording stations.

6 and 7. Lines 1 and 6 are parallel profiles in the Sea of Bothnia and were recorded by arrays of seismic stations in Sweden and Finland (Figure 4.1). An important feature of this arrangement of lines and stations is that the mid-points of rays from the shots for line 1, recorded at stations in Sweden, lay beneath line 6 and those from line 6 into the Finnish stations lay beneath line 1. This three dimensional coverage was designed to give a network of intersecting raypaths so that lateral variations in velocity could be investigated. The third line in the Sea of Bothnia, line 7, runs approximately E-W crossing the southern end of lines 1 and 6, providing a tie between the two lines. Line 5, which would have crossed the northern end of the lines, was not shot due to a shortage of time and funds.

This thesis is concerned with the results from BABEL line 6. Lines 1 and 7 have been interpreted by Graham (1993) and Bruguier (1992) respectively and the results from these lines will be compared with those from line 6 in chapter IX.

4.2 Marine shots

The BABEL profiles were shot under the auspices of BIRPS by the S/V MINTROP, the largest ship available to PRAKLA-SEISMOS (Hanover, Germany). The airgun arrangement used is shown in Figure 4.2. The array consisted of 48 airguns in 6 strings fired at a depth of 7.5 m and giving an overall capacity of 120.6 ltr (7359 cubic inch) at 140 bar (2030 psi). Figure 4.3 shows the farfield signature and spectrum of this array measured by PRAKLA prior to the experiment. This is the acceleration response (hydrophone) rather than the velocity response (as recorded by the seismometers) but, in the absence of any preferable signature, was used as a rough approximation to the source wavelet in the synthetic seismogram modelling for line 6 (this will be discussed further in chapter VII). The initial pulse is clean and sharp with a duration of about 50 ms. The frequency content ranges from about 5 Hz to 75 Hz, although there is a significant but decreasing contribution from frequencies above 75 Hz.

The equipment proved very reliable and few shots were lost due to misfires or gun drop-outs. Weather conditions were also good during the experiment and wave noise was generally low; only two days were lost due to bad weather. Ship traffic was light and noise from other ships was only a problem in the shipping channels around Denmark (profile A). Navigation data was distributed after the project in the form of a UKOOA format tape containing shotpoint numbers, times, locations etc. Noise tests were fired approximately every 10 km and no shot was fired at this shotpoint.

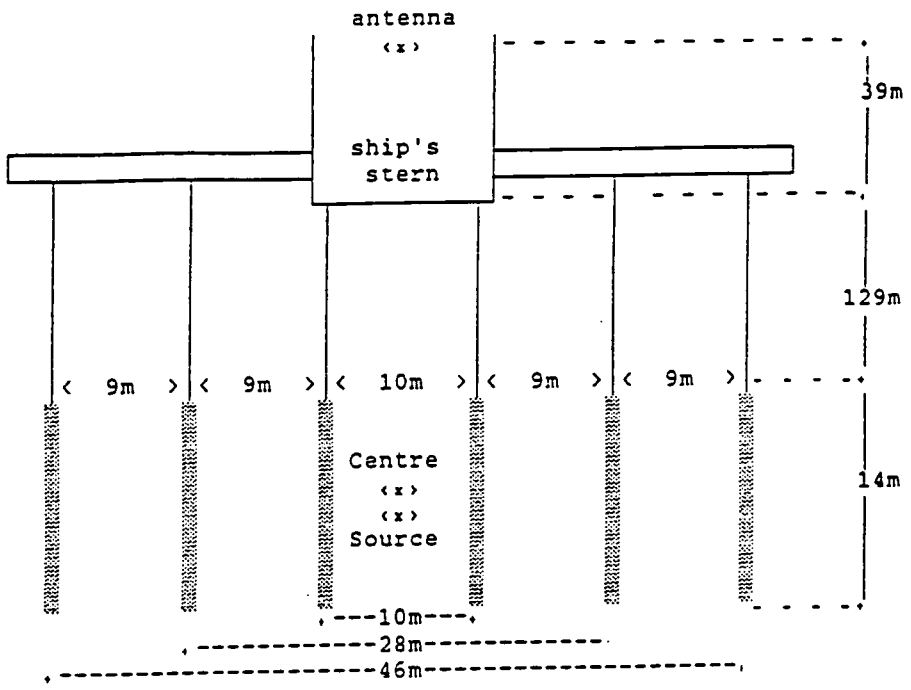

Figure 4.2. Configuration of the S/V MINTROP airgun array.

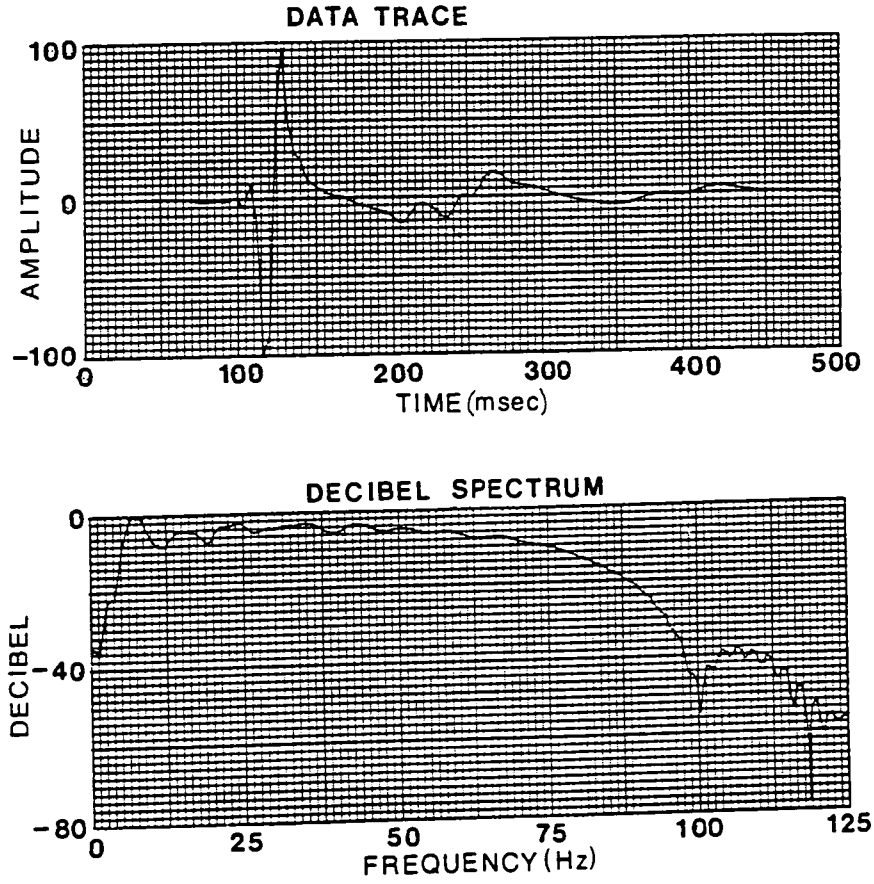

Figure 4.3. Farfield source signature and frequency spectrum (array depth: 7.5 m, hydrophone depth: 108.0 m below airgun).

Recorded shot times referred to the computer order to fire rather than to the actual release of air; the onset of the minimum phase wavelet occurred 10 ms later. Times were corrected for this delay during processing. The shot times were measured with a purpose built system designed by PRAKLA. The ship's internal clock (estimated accuracy of ±1 ms in 3 weeks) was calibrated against GPS satellites and, where possible, against the West German radio-telemetry DCF-77 time signal which transmits universal time (UTC). The shot time was written directly into the UKOOA navigation tape, precise to 1 ms. In addition, second pulses from the internal clock plus two GPS satellites were recorded on three auxiliary traces for cross checking of time drifts.

Shot locations were measured using DECCA chains combined with continuously recorded Doppler sonar and all possible transit satellite fixes to give the single 'best fit' position. The DECCA chain was the principal navigation tool but the actual navigation error should be less than the DECCA error as two chains were recorded simultaneously wherever possible. The standard DECCA error is of the order of 25 to 50 m for points along line 6.

The shots were recorded at normal-incidence using a 3 km long, 60 channel streamer towed at 15 m depth, except where shallow water conditions required the streamer depth to be decreased. A MICROMAX[2] processing system on the MINTROP produced normal-incidence brute stacks during the experiment and showed clear crustal arrivals and a much more complex crustal signature than had been expected for Shield crust (Meissner and Wever, 1990).

Line	Shot interval	Record length		Line length	Latitude	Longitude
6	62.5 m	23.5 s	SOL	40.6 km	62° 47.11′	18° 24.71′
			EOL		62° 39.06′	18° 26.47′
6A	62.5 m	23.5 s	SOL	184.5 km	62° 38.25′	18° 26.96′
			EOL		61° 03.29′	18° 36.67′
6B	62.5 m	23.5 s	SOL	15.5 km	61° 02.47′	18° 37.50′
			EOL		60° 35.00′	18° 40.00′

Table 4.1. Line coordinates for BABEL line 6 (SOL - start of line, EOL - end of line).

Line 6 was shot in three sections (6, 6A and 6B) between the 28th and 29th of September. The break between sections 6 and 6A was due to a defective depth controller. The second break was due to a power failure that led to shots 4240-4312

[2]Trademark of Advance Geophysical Corporation

being cancelled. The streamer depth was reduced to 12 m for shots 1545-1620 because of patches of shallow water and the same problem at the southern end of the line resulted in the line being truncated. Parameters for the individual line sections are shown in Table 4.1

4.3 Seismic recording stations

Over 50 land recording stations were in operation during the BABEL project. Durham was responsible for 18 of these in southern Sweden, surrounding the Sea of Bothnia, with sites varying from small islands in the Sea of Bothnia to highland areas further inland (Figure 4.4). The main coverage was provided by 10 outstations and 5 analogue Geostore base stations. Each outstation consisted of a single vertical component seismometer. These were radio-linked to the base stations where the signals were recorded, together with the universal time signal MSF (from Rugby, England) and 3-component data from seismometers located at the base station. This arrangement of base stations and radio-linked outstations had been used successfully in previous wide-angle onshore/offshore surveys such as the 1987 BIRPS/MOBIL project (West, 1990, Blundell *et al.*, 1991).

Station sites were originally chosen in August 1989 from 1:100 000 scale maps and 'line of sight' radio links between base stations and outstations were determined from reading contours between the two stations in question. Prior to the experiment, the chosen sites were surveyed by Hans Palm of Uppsala University, who checked the line of sight radio-links and arranged for access to the station sites. This proved an invaluable contribution, as the time available for installation prior to the project was limited. Base station sites had to be as accessible as possible while still fulfilling the requirements of good rock outcrops to provide good instrument coupling, undisturbed sites, and protection for the recording instruments.

The five base stations were spread over a distance of about 500 km along the shore of the Sea of Bothnia and the data tapes at these stations were changed every two days. The good coastal main roads in Sweden and the lack of traffic made the maintenance of this array possible with a single vehicle, despite the distances and the poor condition of the minor roads. A house was rented for accommodation at the middle of the Geostore array (close to BS3) and was also used as a communication centre during the project and as a permanent PDAS station (BS3P). Tapes at stations to the north and to the south of this were changed on alternate days.

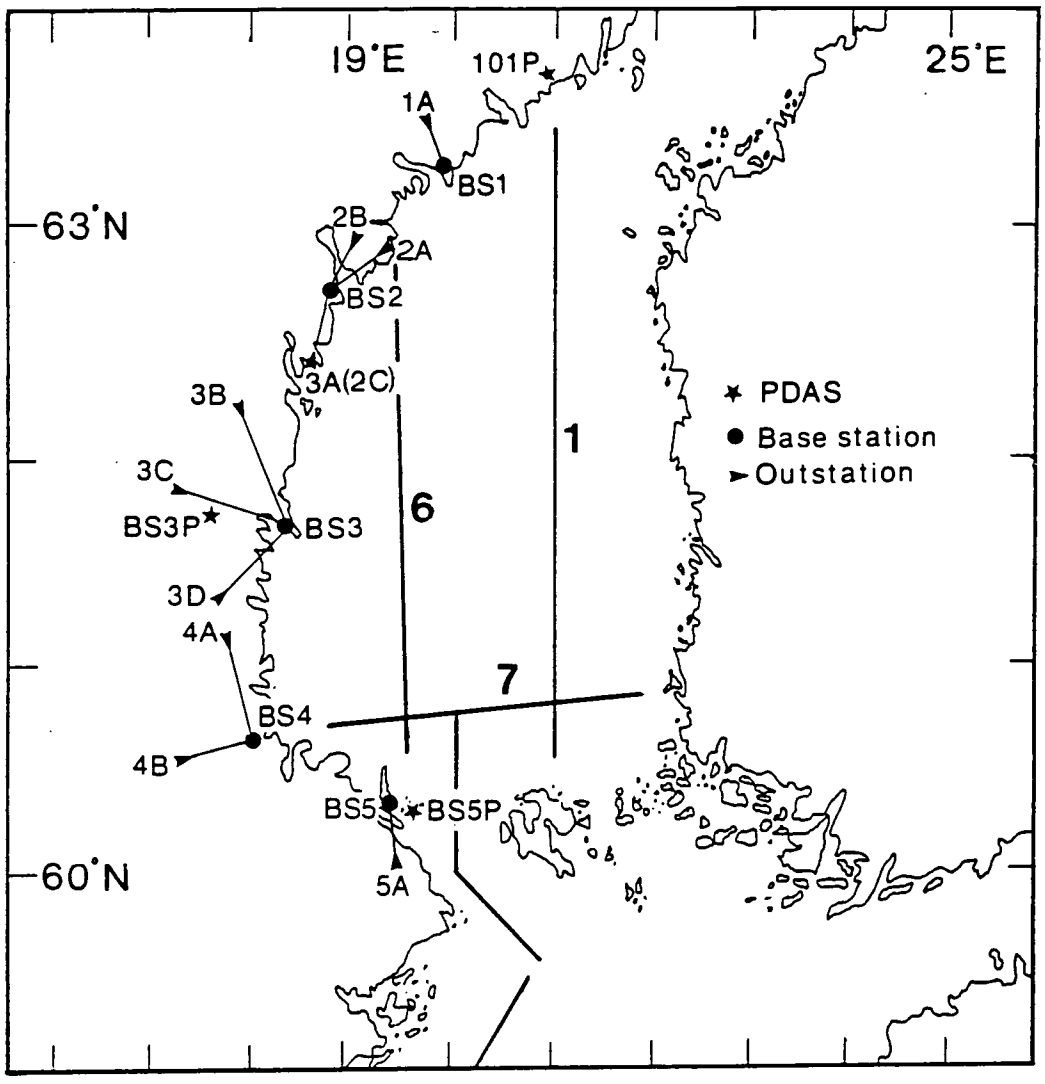

Figure 4.4. Locations of recording stations operated by Durham during the northern part of the BABEL project. Radio-links between inland recording stations and Geostore base stations are shown by lines.

Outstations were placed on hills inland where there was a line of sight link to one of the five Geostore base stations located in the low lying coastal region (in some cases long range transmissions were possible down valleys). Good rock outcrops were available at most of the outstation sites and installation was relatively simple. Most outstation sites were remote and there was little danger of the equipment being disturbed. All of the outstations were in forested areas and the motion of trees was expected to generate some low frequency seismic noise.

The Geostore recorder was placed under cover at each of the base stations in shelters varying from the basement of a house (BS1) to a tent borrowed from Uppsala University (BS3). A 3-component seismometer set was placed within the same building (if it contained a rock outcrop) or else buried outside and an aerial and receiver were erected close by. The Geostore array was unmanned, apart from visits to change data

tapes at the base stations and to replace batteries at both outstations and base stations. Figure 4.4 shows the locations of the base stations and outstations which are described below.

Base station 1 (BS1) was in the basement of a house that was unoccupied during the week and recorded a single outstation, 1A. Some noise was caused by a thermostatically controlled heater in the cellar but this was switched off for most of the experiment. BS2 was in a small shed belonging to an amateur radio group. The time signal recorded here was poor but was improved when a 10 K resistor was included in the earth line of the receiver and when a radio repeater that had been causing interference was shut down. Outstation 2A proved to be excessively noisy even after the station site was altered in an attempt to improve the ground coupling. Outstation 3A (3A(2C) in Figure 4.4) was also recorded at BS2 since the radio reception was clearer here than at BS3.

Outstations 3B, 3C and 3D were recorded at BS3. The Geostore recorder at BS3 was placed in a tent as there was no convenient shelter. During the experiment, the track leading to outstation 3C was excavated in preparation for road repairs, which made access for battery changing somewhat awkward. BS4 was sited in a farm shed which contained a large rock outcrop in one corner on which the 3-component set was positioned. Some problems were found with reception of the radio signals from 4A and 4B but this was improved by using a higher aerial pole. At BS5, located in an old blacksmiths shop on the island of Gräsö, reception of the MSF time signal was poor for most of the experiment but reception of the outstation signal (5A) was clear.

Two Geotech digital PDAS recorders were also used during the experiment. These had been adapted to give up to 15 hours of continuous unattended recording but the command software written to control this process proved unreliable. As a result it was necessary to have an operator at each PDAS station to restart the data recording if the system failed to restart automatically after off-loading to tape. One PDAS was sited in the rented house, marked BS3P in Figure 4.4, and recorded continuously during the northern part of the experiment providing digital coverage at the centre of the Geostore array. The location of BS3P, between a minor road and a large lake and near to a house, was not ideal with regards to seismic noise. Cars passing near to the recording site resulted in high amplitude bursts of noise and the data from this station was very poor. Only 2 components were recorded, vertical and east-west.

The second PDAS was used to record 3-component digital data for the lines in which Durham had particular interest. For line 1, the PDAS was sited to the north of the line at station 101P. The PDAS was left unattended during the first night but crashed shortly after being left. As a result, the southern end of line 1 was not recorded. After this, the PDAS stations were continuously manned. For line 6, the

GEOSTORE				
Station	**Location**	**Latitude**	**Longitude**	**Component**
BS1	Stubbsand	63° 13.49′	18° 57.66′	Z, EW, NS
1A	Nr Klingre	63° 27.42′	18° 42.05′	Z
BS2	Hörnön	62° 36.52′	17° 57.93′	Z, EW. NS
2A	Kåstaänget	62° 52.93′	18° 21.71′	Z
2B	Nr Milstabbana	62° 52.63′	18° 02.00′	Z
3A(2C)	Nr Sösidan	62° 24.85′	17° 41.46′	Z
BS3	Nr Amöviken	61° 41.29′	17° 23.81′	Z, EW, NS
3B	Västansjökullen	62° 08.27′	17° 05.20′	Z
3C	Klotjärnsasen	61°49.08′	16° 24.57′	Z
3D	Nr Storäsen	61° 31.19′	16° 53.48′	Z
BS4	Iggön	60° 52.42′	17° 17.46′	Z, EW. NS
4A	Nr Gullberg	61° 12.59′	16° 50.33′	Z
4B	Kungsberget	60° 45.16′	16° 30.00′	Z
BS5	Gräsö	60° 18.63′	18° 32.28′	Z, EW, NS
5A	Nr Sundsveden	60° 15.08′	18° 35.92′	Z
PDAS				
Station	**Location**	**Latitude**	**Longitude**	**Component**
BS3P	Nr Forsa	61° 41.44′	16° 55.45′	Z, EW
101P		63° 36.76′	19° 58.39′	Z, EW, NS
BS5P	Rävsten	60° 18.70′	18°36.63 ′	Z, EW, NS

Table 4.2 Location of the fifteen analogue Geostore and three digital PDAS stations run by Durham during BABEL (Z - vertical component, NS - transverse component, EW- radial component).

PDAS was moved to the southern end of the line in a rented cabin on Rävsten, a small island just off Gräsö (BS5P in Figure 4.4).

Table 4.2 shows the coordinates of all 18 recording stations and the components recorded at each station.

4.4 Equipment

4.4.1 Analogue Geostore array

The Geostore outstation/base station arrangement is shown in Figure 4.5a. A single vertical component seismometer connected to an amplifier modulator (amp mod) was used at each outstation. These were placed on a rock outcrop or in a

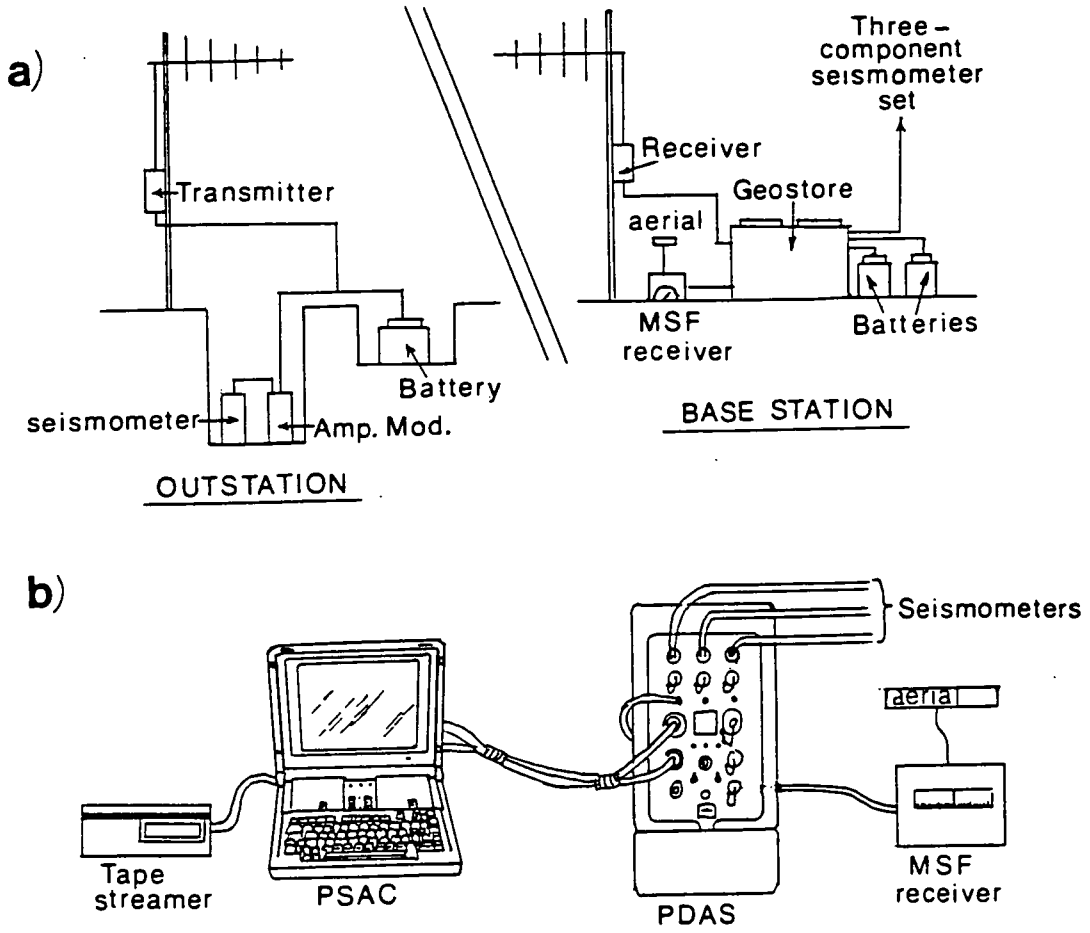

Figure 4.5. Diagram of a) the analogue Geostore recording equipment and b) the PDAS digital recorders.

shallow depression dug down to bedrock and protected, where necessary, by a large bucket, which was camouflaged with a cairn of rocks, branches, etc. A 12 volt battery, placed in a plastic bag and buried near to the seismometer pit, was used to power the amp mod and transmitter. These had to be replaced and recharged during the experiment.

The amp mod was used to amplify and frequency modulate the low-level, low-frequency signals from the seismometer. Ten gain settings were available with a gain of 1 giving a range of ±250 mV and a gain of 10, a range of ±0.25 mV. The optimum setting of the amplifier depends on the noise level at the site and the expected seismic intensity. As there was no time before the experiment to perform test recordings at the sites, it was decided to use the same settings as had been used in previous experiments. All of the gains were initially set to 7 (±2.5 mV), suitable for quiet sites. The gains of

the 3-component seismometer sets at BS2, BS3, BS4, BS5 and the vertical component at BS1 were later adjusted to 8 (±1.0 mV) prior to the shooting of line 6.

The transmitter unit was attached to a radio aerial which was erected at some distance from the seismometer to minimise the seismic noise generated by wind vibrations in the antenna system. The normal radio-frequencies for this kind of radio-link were not usable in Sweden since they are used for the mobile telephone network and so the receivers and transmitters were adjusted to use 25 kHz bands between 439.700 and 439.975 MHz. At the base station a receiver, mounted on a similar aerial, passed the outstation signals to the Geostore recorder.

The Geostore recorder is a 14 channel analogue FM. recorder and was used to record multiplexed data on ½ inch magnetic tape at 15/160 inches per second. This was one of three possible speeds and was chosen to give a data bandwidth of 31.2 Hz. Three of the 14 channels were used to record two flutter tracks and an internal Vela time code, leaving 11 data channels. One of these was used to record the external MSF time signal so that the recordings could later be calibrated to Universal time and the drift of the internal clock could be measured. The remaining data channels were used to record a three component seismometer set installed at the base station and from one to three outstations. Power was supplied by two 12 V batteries.

4.4.2 Digital PDAS recorders

The Geotech PDAS[3] recorders can record six channels of data at up to 1000 samples per second. An auxiliary channel may also be recorded (this is usually used for the external time code). There are three possible recording modes; event triggered, scheduled window or continuous. For continuous recording it is more convenient to use a mains power supply than the recorder's battery pack. The PDAS also contains an internal battery supply which is capable of preserving data for up to a year after external power loss. The PDAS is controlled by a computer known as the PSAC[4]. This can be used as a remote terminal for the PDAS when setting up parameters prior to recording or can be used to monitor the data during recording. The PDAS can communicate with any IBM compatible PC running Crosstalk software. In BABEL, the PDAS recorders were run continuously, controlled by Zenith or Toshiba laptop computers, and recorded data at a sample rate of 100 samples per second. This sample rate was chosen as an optimum value to give a bandwidth of 40 Hz while still

[3]Portable Data Acquisition System.

[4]Portable Setup and Analysis Computer

permitting a reasonable period of continuous recording before the PDAS memory was full.

The PDAS was 'milked' at 20 minute intervals to off-load demultiplexed data files to the hard disk of the PSAC. This milking interrupted data recording, losing roughly two to three minutes of data every twenty minutes. The files from the PSAC were off-loaded to high density tape at hourly intervals without interrupting recording. Each high density tape held about fifteen hours of data. A series of batch files to control the off-loading of data from the PDAS recorders had been written prior to the experiment by Dr Roger Long. Unfortunately, a problem with the interaction between the PSAC and the PDAS meant that on random occasions the PSAC failed to pass control back to the PDAS after the tape operation. This problem resulted in the loss of the southern end of line 1 and after this the PDAS stations were manned at all times.

Data files were automatically labelled with the time (according to the internal clock) at which they were recorded. Internal time is measured using a digitally compensated crystal oscillator which synchronises the internal clock to an external reference time (MSF). The maximum clock drift is less than 6 msec per 24 hour period. The internal clock was set to the local time read from the PSAC at the beginning of the experiment.

Figure 4.5b shows a block diagram of the PDAS-100 as used in BABEL. At each station, the MSF time signal, the internal clock and 3-components of seismic data were recorded. Programmable gain pre-amplifiers were set to x100 for the three seismic data channels and to x1 for the auxiliary channel (MSF). A 132 dB gainranging amplifier was common to all data channels. Three different recording formats are available on the PDAS system: 16 bit, 32 bit or 14/2 gainranged data. In BABEL, the latter of these formats was used. In this format the data are written as 2 byte integers but with a 14 bit mantissa and a 2 bit gain code; this gives the maximum dynamic range for the minimum memory consumption. Data is degainranged at the first stage of processing to give a 4 byte integer.

The PDAS creates demultiplexed, MS-DOS compatible, files with unique names and stores them on the static memory module from which they are read to the hard disk of the PSAC when the PDAS is 'milked'. The file names are made up of the following information: the file type (1 character), the channel number (1 digit), the PDAS serial number (3 digits), the sequence number (3 digits) and the Julian day as a 3 digit extension. The sequence number returns to zero for each new day. For example, file P0107042.271 is the 42nd file recorded on day 271 for the auxiliary channel, (channel 0), on PDAS 107.

4.4.3 Frequency response

The low-frequency response of the Geostore and PDAS recording systems was controlled by the seismometers. Willmore Mk III variable period seismometers were used which generate an E.M.F proportional to the ground velocity. The frequency response depends on the resonant frequency and the damping. The optimum damping is 0.7 of the critical damping, as this is where the flat part of the frequency response extends to the lower frequencies (figure 4.6a, h is the ratio of damping to the critical damping). The Willmore Mk III seismometers used in BABEL had resonant frequencies of approximately 1.5 Hz and were damped with $h \approx 0.7$.

The high frequency response depends on the various filters in the recording and playback instruments (anti-aliasing filters, etc.). The PDAS recorders contain two anti-aliasing filters: one analogue and one digital. The analogue filter is a six pole (36 dB/octave) Butterworth filter with a bandwidth of 200 Hz. The digital filter is determined by the sample rate. For a sample rate of 100 Hz (as was used for the BABEL data) there is a flat response from DC to 40 Hz, no measurable 50-60 Hz induced signal and 120 dB of alias protection (372 dB/octave of anti-aliasing filtering). The frequency response of the PDAS recording system is shown in figure 4.6b.

The analogue Geostore data was played back on a Store-14 tape system and digitised. This recording/playback system contains no anti-aliasing filter but the data is filtered when it is demodulated. The sample rate for digitising the BABEL Geostore data was chosen so that the low-pass filter used for demodulating the analogue signal also acted as an anti-aliasing filter. For a tape speed of 5/160 inches per second the filter has a bandwidth of 31.2 Hz and a roll-off of 20 dB/octave. A sample rate of 200 Hz was chosen for the BABEL data since this means that at the Nyquist frequency (100 Hz) there is 45 dB of alias protection (i.e. the amplitude of the signal has been reduced by a factor of 100). The frequency response of the recording/playback system for the Geostore data is shown in figure 4.6c.

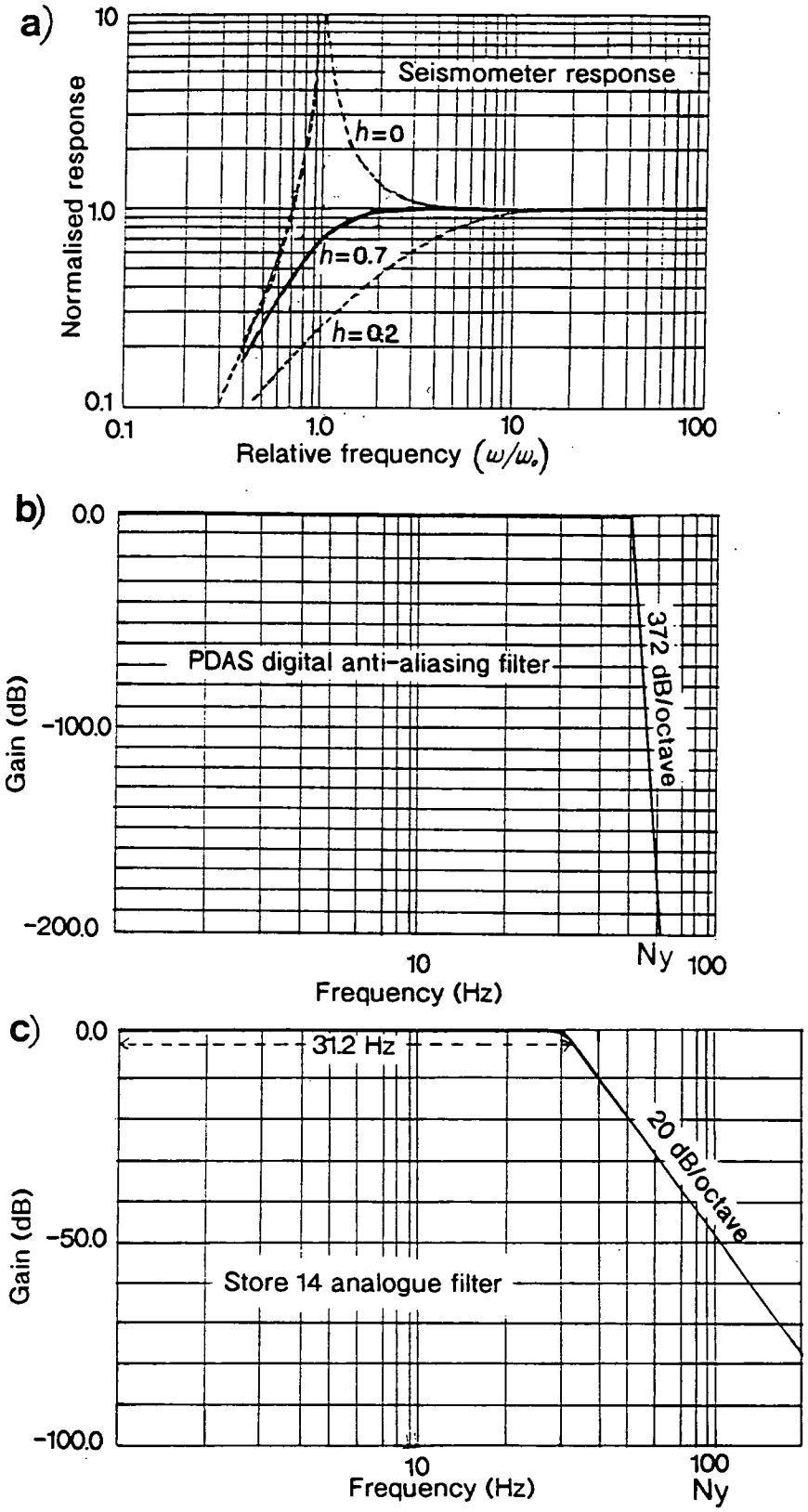

Figure 4.6 a) Normalised seismometer response curves (h is the ratio of the damping relative to the critical damping; ω_0 is the resonant frequency). b) PDAS digital anti-aliasing filter for 100 Hz sample rate. c) Analogue low pass filter used in the Store-14 to demodulate the FM data (tape speed = 15/160 Hz). Data was digitised at 200 samples per second. NY = Nyquist frequency.

CHAPTER V
DATA CONVERSION

5.1 Conversion to SEGY-WAR

To allow easy exchange of the BABEL data between the various groups involved it was suggested that all data should be written in a modified form of the standard SEGY format (Barry *et al.*, 1975). The raw field data were initially converted to a format similar to SEGY but suitable for use on the Departmental computer system. This was converted to the modified SEGY format when the data was written to tape. The stages in the conversion of the digital PDAS and analogue Geostore data are shown in Figure 5.1.

In SEGY, the data is written as a continuous file consisting of a reel identification header of 3600 bytes (40 EBCDIC card image and 400 bytes of binary code) followed by a series of traces. The traces are of variable length and the trace header (240 byte binary) contains all the information pertinent to the following trace. The format of the data is specified in the reel header and several different channels may be recorded in the same SEGY file.

The modified SEGY (SEGY-WAR) uses the empty bytes in the reel and trace headers to record information relevant to wide-angle data. These include the reduction velocity and the delay between the shot instant and the start of the trace (the long offsets in wide-angle surveys means that this delay overflows the 2 byte integer assigned to it in standard SEGY). A four character station code and a four character channel code are included in the trace header. The SEGY-WAR format defined by Dr Roger Long is listed in appendix A.

The SEGY-WAR format was further modified to make the data compatible with the computing system in the Department of Geological Sciences, Durham University (this 'internal' format will be referred to as SEGYi). SEGYi uses ASCII and 4 byte IEEE floating point values rather than the EBCDIC and IBM real*4 values defined in SEGY-WAR. Since both MS-DOS and UNIX use ASCII/IEEE (although the byte order varies), it was more convenient to write the BABEL data in this format.

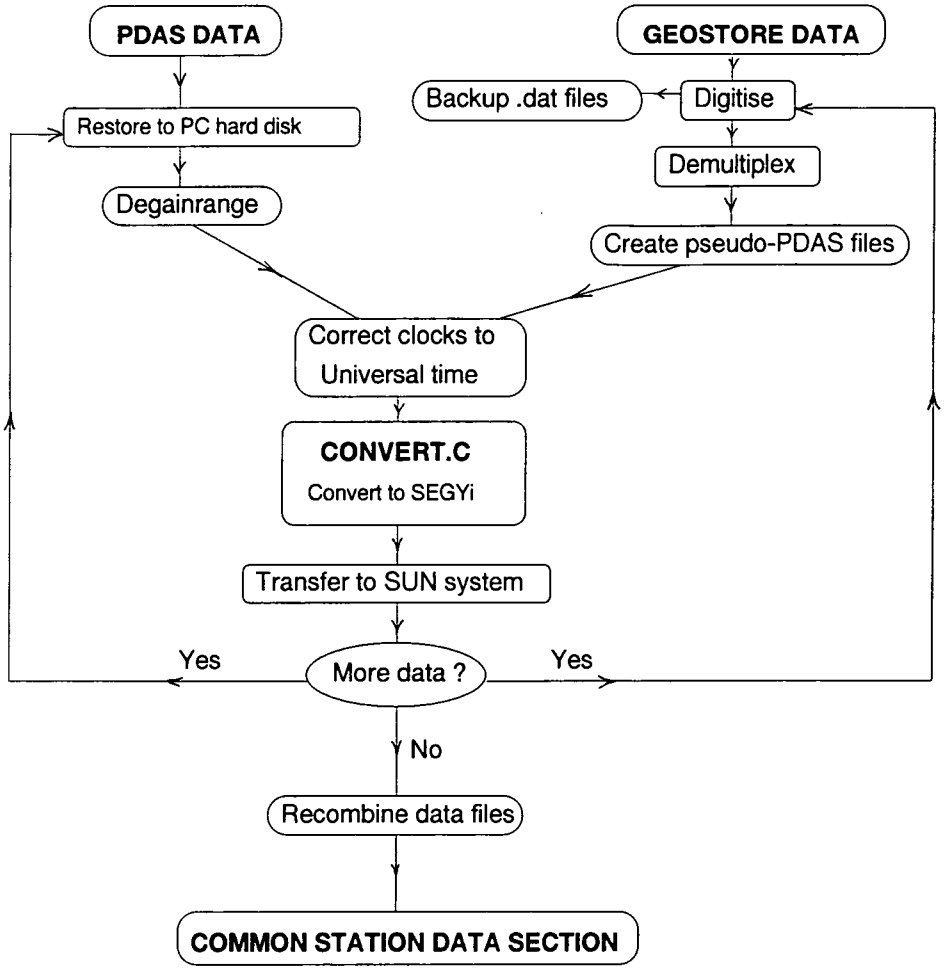

Figure 5.1. Flow chart showing the different stages in the conversion of the analogue and digital field data to SEGYi format.

All 2 byte integer header values are written as 4 byte integers or floating point numbers and only the upper case characters A-Z and the digits 0-9 are used in the headers to make conversion to SEGY-WAR easier. The SEGYi format was also compatible with software that had been written for previous projects.

During conversion, the traces for individual shots had to be extracted from the continuously recorded field data. In near-surface and normal-incidence seismic work, this is usually done by extracting a specified number of seconds of data beginning at the shot time. For wide-angle seismic data, the large station-shot offsets mean that the delay between the shot instant and the arrival of energy from that shot at the recording station may be very large. For example, for an offset of 300 km and an upper crustal velocity of 6 km/s there is a delay of 50 seconds before the first arrivals are recorded. In order to keep data sets to a manageable size, wide-angle data is often 'reduced' by adding a variable delay to the shot times, as described below.

A start time (T_S) is calculated for each trace from the event (shot) time (T_e), the station-shot offset (x) and the reduction velocity (v_r) using the formula given below:

$$T_s = T_e + \frac{x}{v_r} - T_r$$

The 'run-in' time (T_r) is subtracted to ensure that the first arrivals are not lost if the estimated reduction velocity is too low (all of these variables are recorded in the trace headers). A specified number of seconds of data are then extracted from the continuous field data beginning at T_S. All of the Durham BABEL data were reduced during the conversion to SEGYi with a reduction velocity of 6 km/s and a 'run-in' time of 6 secs. Traces of forty seconds length were extracted.

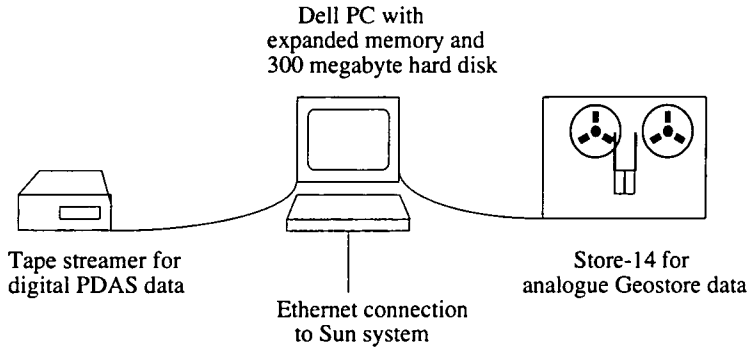

Figure 5.2. Playback system for the field data.

The program CONVERT was written to perform the extraction and conversion of traces from the BABEL field data. A listing and detailed explanation of this program is given in appendix B. CONVERT was designed to run on the PC system shown in Figure 5.2 and was written in ANSI standard C (Kernighan and Ritchie, 1988), except for a few machine specific routines. The C programming language allows the use of pointers to memory addresses, which makes it possible to label a particular position in a stream of data. The use of the ANSI standard was intended to make the program portable to other machines.

5.1.1 Conversion from PDAS format to SEGYi format

The digital PDAS data was recorded in approximately twenty minute blocks with 1-2 minutes gap between each block of data, as described in the previous chapter. Each PDAS file consists of an ASCII header of variable length, followed by binary data values. An example of the ASCII header is shown in Table 5.1. The time at which the first sample of the file was recorded is given in the header of the PDAS files. This

time is relative to the internal clock (local time). This time was corrected to universal time by manually reading the MSF channel.

Header	Description
DATASET P1107022271	Name of the PDAS File.
FILE_TYPE INTEGER	Data type (Integer = 2 byte, Long = 4 byte).
VERSION next	Sets the filename to the next sequence number.
SIGNAL MSF	Channel name (as given during set-up).
DATE 9-22-89	Date on which data was recorded.
TIME 17:59:50.50(500)	Time at which data was recorded.
INTERVAL 0.010	Sample interval in seconds.
VERT_UNITS Counts	Always counts.
HORZ_UNITS Sec	Always seconds.
COMMENT GAINRANGED	Data type.
DATA	Beginning of Binary file data.

Table 5.1. Example of an ASCII header for a gainranged PDAS data file.

The MSF signal consists of a series of binary pulses, one every second, with a burst of 100 Hz code at the minute marker (Figure 5.3). The time at a minute marker is given by the 59 preceding pulses. For both the PDAS and the Geostore stations, the clarity of the MSF time code depended on the radio reception at the recording site. At many of the stations this was poor, and signal was intermittent or else the time code was so noisy that the pulses could not be identified. As a result, it was necessary to search through the MSF data to find the patches which were reasonably legible (this will be discussed further in section 5.2).

The BABEL PDAS data was recorded in 2 byte (14/2 bit) gainranged format with a sampling rate of 100 samples per second (section 4.4.2). An option was written into the program CONVERT to degainrange the trace data during extraction but it was found to be less time consuming to degainrange files beforehand (a degainranging program, DRANGE, was supplied with the PDAS software). Degainranging converts the data from 2 byte integers into 4 byte floating point values, doubling the volume of data. As the disk partition size on the PC was limited to 32 Mbytes, it was necessary to convert the data in small sections which were later recombined on the departmental SUN system.

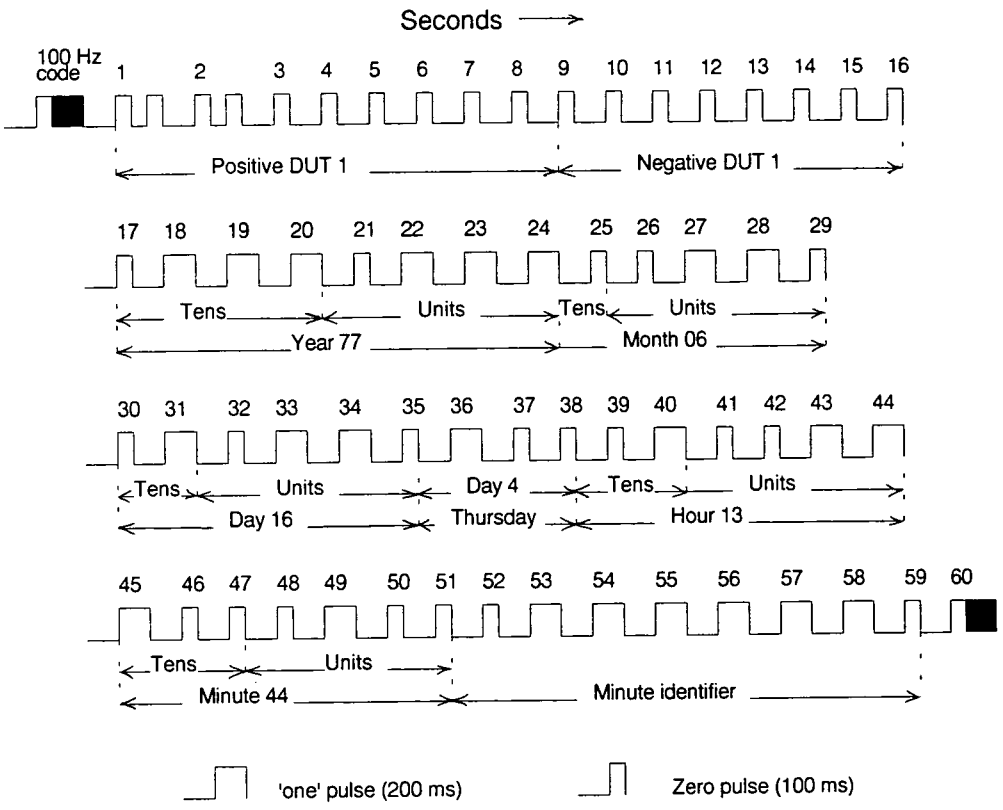

Figure 5.3. MSF radio time signal from Rugby, England. The data applies to the following minute. Bit 58 is 300 ms when BST is in force and the data is 61 minutes fast of UT. For the hour preceding changes to and from BST (0200 UTC), bit 53 is 300 ms. Day '0' is Sunday.

For each section of data converted, as many PDAS files as possible were restored from the streamer tapes to the hard disk of the PC and then degainranged. The program CONVERT reads and corrects the start time of the first PDAS file specified by the user. It then checks the list of shots to find the first shot fired after this time, calculates the reduced start time (T_S) and finds the position within the PDAS data file of the corresponding trace. Traces are then extracted from this data file, and from subsequent files for the same channel, until there are no more files or the end of the line is reached. When this occurs, the program looks for PDAS files for another channel and repeats the process.

The PDAS data may be considered as a continuous stream of data blocks with blank gaps between them. An individual trace for a particular shot may fall entirely within a data block, or within a gap, or cross from one to another (Figure 5.4).

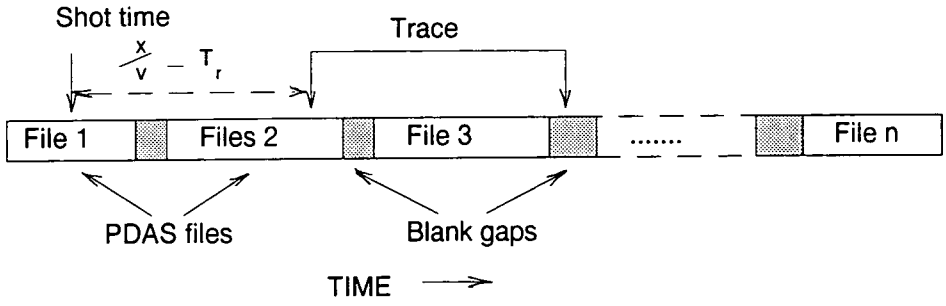

Figure 5.4. PDAS data may be considered as a continuous stream of data files (1,2,3....n) separated by blank gaps.

For the BABEL data, the gap between PDAS files was longer than the trace length and traces did not cross from one file into another. Where a trace lay partially within a data gap, the trace was padded with blank values. If the trace lay entirely in the data gap then a blank trace was written. After conversion the data was transferred from the PC to the SUN system via the ethernet.

5.1.2 Conversion from GEOSTORE format to SEGYi format

Geostore data is analogue and multiplexed and the process of converting it to SEGYi was more complicated than for the PDAS data. It was decided to digitise and demultiplex the Geostore data and to write it in the form of 'pseudo-PDAS' files. These could then be converted to SEGYi in the same manner as the PDAS data. A commercial software package, GLOBAL LAB, was used for digitisation. GLOBAL LAB is a high speed data acquisition, display and analysis software package designed to run on an IBM PC. It was run on the PC system shown in Figure 5.2 with the hard disk of the PC partitioned to give 10 disk drives (C to L). All of the drives had a capacity of 32 Mbyte, apart from drive L which was not used in the conversion process. The acquisition and conversion software was stored on drive C and drive D was used for intermediate stages in the processing, leaving seven data drives. DOS 5.0 allows disk partitions of greater than 32 Mbytes, which would have permitted the data to be converted in larger portions, but this version of DOS was not compatible with other software used during the conversion process.

The conversion of the Geostore data was divided into three stages: extraction from analogue tape, conversion to pseudo-PDAS files and conversion to SEGYi using the program CONVERT. The GLOBAL LAB package was used for high speed digitisation and for displaying data signals, time codes, etc.

In the first stage of processing, data was extracted from the analogue Geostore field tapes and digitised. The BABEL tapes were replayed on a STORE-14 tape system with a playback speed of 7½ inches per second (80 times the original recording

speed of 15/160 inches per second). The data was digitised at 80x real-time using the GLOBAL LAB package and a series of 'PROJECT_NAME.DAT' files were generated, one on each of the seven data drives (E to K). The finite time required to change from writing to one drive to writing to the next resulted in a large gap in the data, since the data was being read at 80x real-time. To prevent this, the .DAT files were pre-written on to the data drives to save time during the drive change and the system was adapted to rewind the data tape slightly before re-starting reading data for the new drive.

A nominal sampling rate of 200 samples per second was used for digitisation (this sample rate was chosen so that the filter used to demodulate the signal from the STORE-14 also acted as an anti-aliasing filter, section 4.4.3). Due to variations in the speed of both the recording and the playback instruments, the true sampling rate had to be calculated from the internal clock channel after digitisation. The size of the .DAT files was limited by the size of the data drives and the number of channels being digitised (the MSF and internal clock (IC) channels were always digitised, as these were used to calculate the start time of the pseudo-PDAS files and the sampling rate). The size of the .DAT files was further limited by the fact that the data in the pseudo-PDAS files was written in 2 byte offset binary format and had to be converted to 4 byte floating point values, doubling the disk space required. The .DAT files were copied to the SUNs and then backed up on Exabyte cassettes.

In the second stage of the processing, software written by Dr Roger Long was used to demultiplex and divide the .DAT file from a single drive into a series of pseudo-PDAS files. The length of these files was specified by the user. All files started and ended at an internal clock minute marker, except for the first and last files which differed in length from all the others. For each file, the sampling rate and the file start time were calculated from the internal clock. This sample rate was an average over the length of the file but, since the individual files were short, this was reasonably accurate. The pseudo-PDAS data was written in offset binary format. A new data type, OFFSET, was created and included in the pseudo-PDAS headers and the program CONVERT was re-written to deal with this format of data (for true PDAS files the data type is either LONG or INTEGER).

In the third step, the pseudo-PDAS files were converted to SEGYi format. The internal clock was corrected to universal time by comparing it to the MSF time code using another routine written by Dr Roger Long (this was originally designed to read the first break time for earthquake data). To read the MSF code, the minute pulse of the MSF signal was selected and the time for that pulse was read automatically according to the internal clock. The time at the pulse was then read manually from the MSF code. This was repeated at several different points for each field tape. The

variation in correction times was quite large (see section 5.2), partly due to the drift of the internal clock and partly since the MSF signal was difficult to read for many of the stations. An average of the measured values was taken (excluding obviously spurious results) and used as the clock correction in CONVERT.

Once all of the seismic data channels for the drive were converted and transferred to the SUNs, the conversion process was repeated for the next data drive. When all of the data for a particular station/line had been converted and transferred to the SUNs, the small SEGYi files created from the individual .DAT files were combined into a single SEGYi file for each channel.

5.2 Internal clock drift

The internal clocks of all recording instruments have a tendency to drift with time and this means that the difference between internal clock time and universal time may change during an experiment. This drift was measured for the BABEL recording instruments at the stations used for modelling line 6: Geostore stations BS2, BS1 and BS5 and the PDAS station BS5P (Figure 5.5). The locations of these stations are shown in Figure 4.4. For the Geostore stations (a, b, and c in Figure 5.5), the difference between the internal and external time codes was measured at roughly three hourly intervals along the field data tapes using the routine written by Dr Roger Long. All three of the stations show a linear drift with time. The occasional erratic readings occur where the MSF code was poor and are probably due to the minute marker being incorrectly selected. The gaps occur where the MSF code was unreadable.

The internal clock errors were averaged by excluding obviously erratic readings and then calculating the mean clock error during the period that line 6 was being shot (marked by dotted lines in Figure 5.5). This error was used to correct the internal clock. The use of this average value causes a cumulative error in the data. In the case of BS1, the internal clock drifted by 0.012 secs during the shooting of line 6. This means that, if the time is correct at the start of the line, then there is a time error of 12 msec over the length of line 6 (roughly 240 km). An arrival with a velocity of 6 km/s will appear to have a velocity of :-

$$\frac{240\ \text{km}}{39.988\ \text{s}} = 6.0018\ \text{km/s},$$

a 0.03% error in velocity.

For BS2, the clock drift is 0.0525 secs which gives an error in velocity of 0.13% and for BS5 the drift is 0.143 secs which results in a velocity error of 0.35%. Errors will be discussed in more detail in the next chapter.

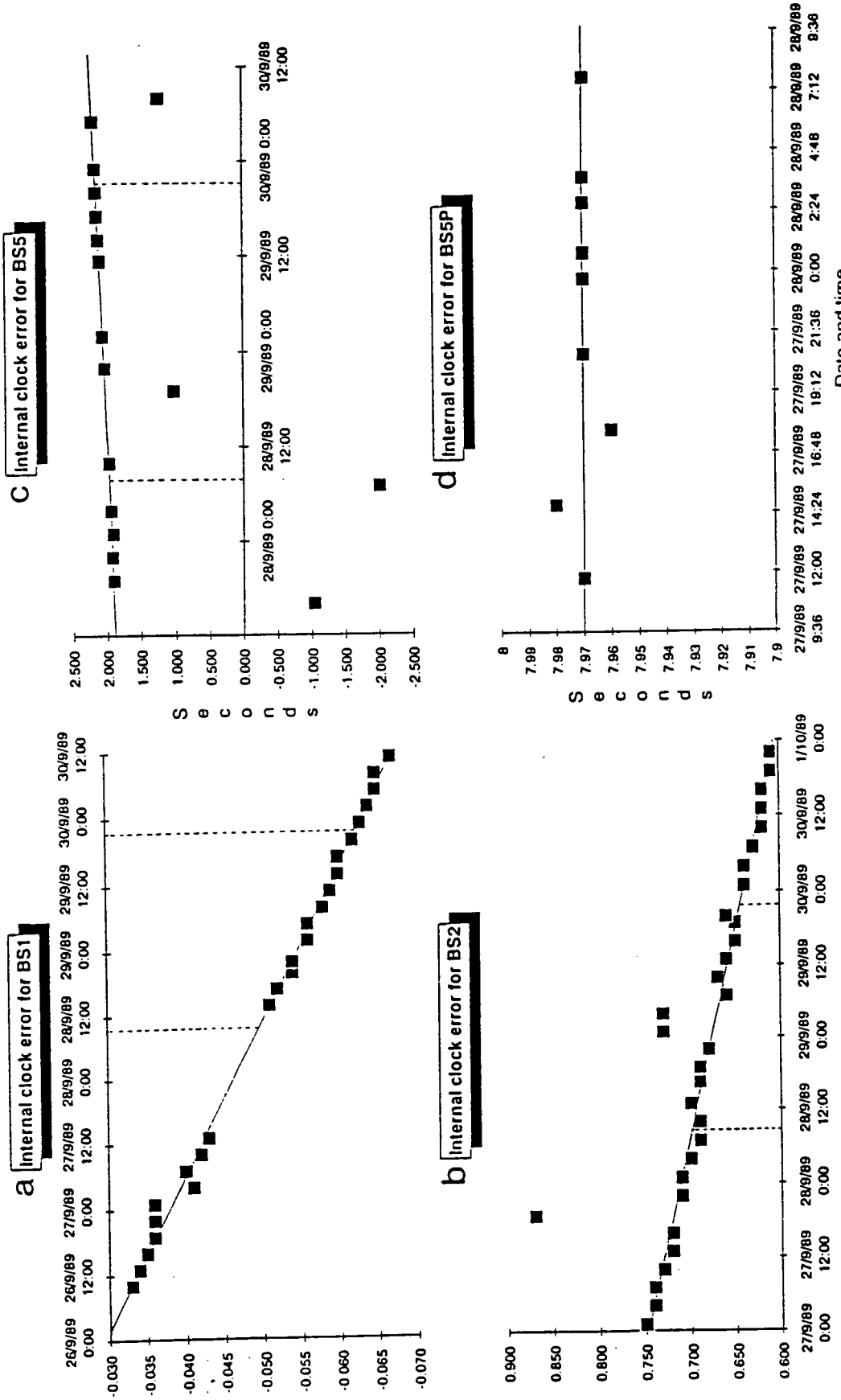

Figure 5.5. Clock drifts for the Geostore recorders at **a)** BS1, **b)** BS2, **c)** BS5 and for **d)** the PDAS recorder used at BS5P.

Dotted lines show the beginning and end of line 6.

The internal clock for the PDAS station BS5P (Figure 5.5d) shows no measurable drift over a period of 24 hours (a maximum error in the PDAS internal clock of less than 6 ms per 24 hrs is claimed by the manufacturers). The MSF code for this station was very poor and only a few MSF files were readable. When the reduced data was plotted after being converted with a time correction of 7970 ms, the first arrivals were seen to arrive much earlier than on the data sections from neighbouring stations, suggesting that this time correction was incorrect. The MSF code was re-read for all files where the signal was clear and it was found that the internal clock had 'jumped' prior to the shooting of line 6. This was not noticed originally as there were only three files with a decipherable radio time code recorded after this jump. The jump may have occurred as the result of one of the recording instrument crashes that were mentioned in the preceding chapter. The BS5P SEGYi traces were amended to correct for this error.

CHAPTER VI

THE BABEL DATA SECTIONS

6.1 Wide-angle data

6.1.1 Frequency analysis

Examples of the unfiltered frequency spectra for a single shot (line 6, shotpoint 3166) recorded at a PDAS station to the south of line 6 (BS5P) and a Geostore station to the north of the line (Z2A) are shown in Figure 6.1. The data from other stations have similar spectra. The amplitudes have been normalised so that the maximum amplitude for each spectrum is one. In order to make the later peaks in the spectrum more visible, the maximum plotted amplitude is 0.2.

Fleuh and Dickmann (1992) suggested that the frequency content of the wide-angle data recorded during BABEL fell in a limited bandwidth between frequencies of 5 and 12 Hz. This is clearly not the case with these data, where the bandwidth of the frequency content is much wider, between about 3 and 25 Hz. This again emphasises the necessity of recording as wide a bandwidth as possible for wide-angle data.

The BABEL wide-angle data recorded by Durham University were dominated by low frequency microseismic noise. This is seen as a peak in the frequency spectra in Figure 6.1 at about 1-2 Hz. The microseismic noise had to be removed by filtering before the data could be interpreted. A bandpass filter was used which also removed the high frequency noise above the frequencies of the recorded data (the cutoff values for the filter were chosen by considering the frequency spectra and by plotting test sections, section 6.1.2).

The digital anti-aliasing filter in the PDAS recorder (section 4.4.3) sharply truncates the frequency spectra for BS5P between 40 and 50 Hz and there is no noticeable signal beyond the Nyquist frequency (50 Hz,). For the Geostore data, the filter which demodulates the FM signal was used as an anti-aliasing filter (section 4.4.3). This has a much gentler roll-off than the PDAS filter and the amplitude of the frequency spectra for Z2A gradually decrease from 32 Hz onwards. The Nyquist frequency for the digitised Geostore data is 100 Hz. The shape of the PDAS and Geostore filters were shown in Figure 4.6.

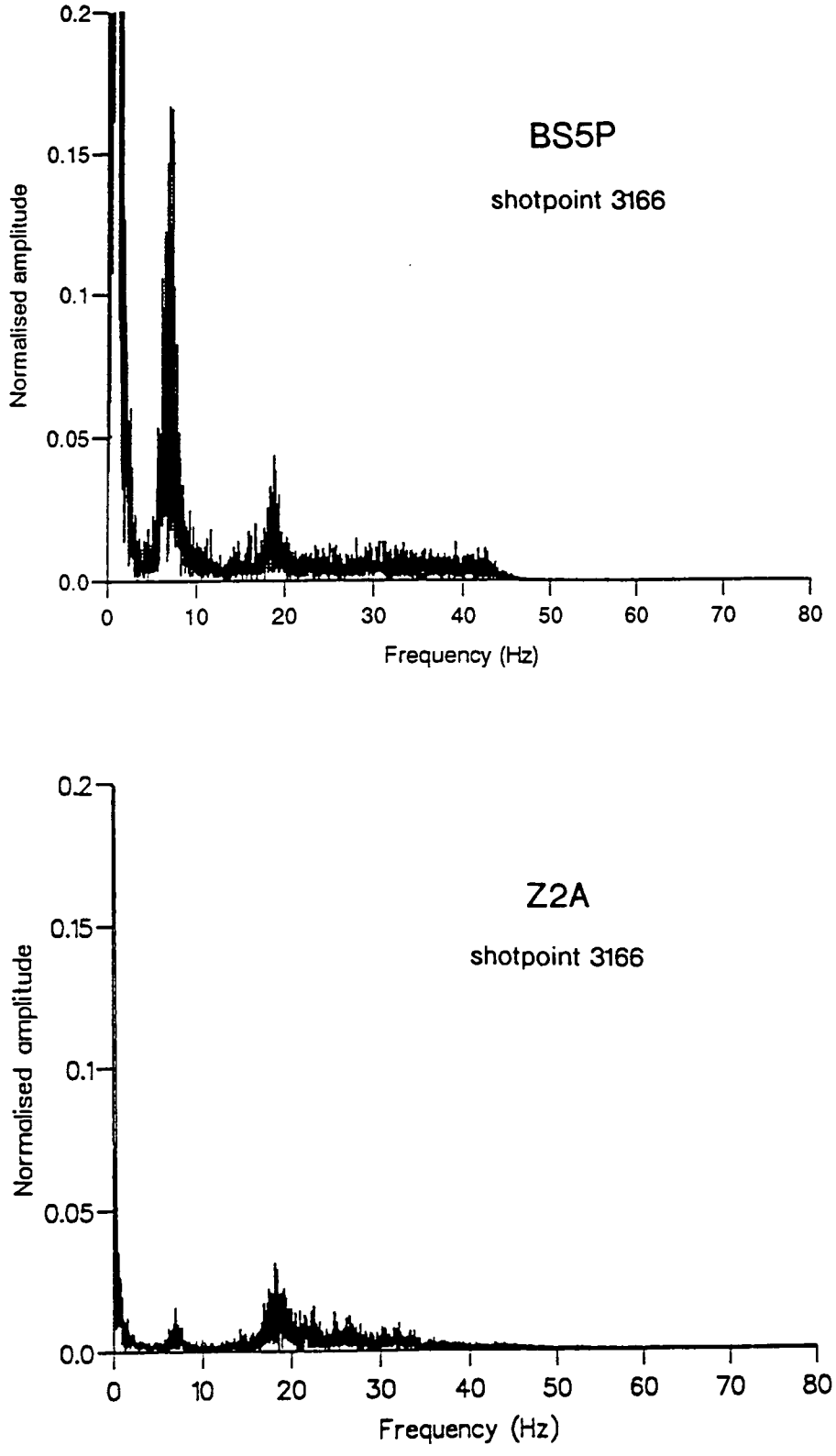

Figure 6.1. Unfiltered frequency spectra for a single shotpoint (line 6, shotpoint 3166) recorded at stations BS5P and Z2A (amplitudes have been normalised to one).

As well as the microseismic noise peak at 1-2 Hz, two other peaks are seen in both spectra, the first at about 7 Hz and the second at about 18 Hz. In the Z2A spectrum, the second peak is the higher amplitude of the two. This is only true for the data from Z2A; all of the other BABEL data show a dominant first peak. The reasons for the high amplitude of the second peak at Z2A are discussed later in this section.

Figure 6.2 shows the variation of frequency with distance for the PDAS data from the southern end of line 6 (BS5P). The frequency spectrum of each trace was calculated using a fast Fourier transform (FFT) routine, converted into SEGYi format and plotted against distance using the same routines as for the seismic data. The data has been bandpass filtered to remove the low frequency seismic noise peak so that the other peaks are more easily seen (the filter used is shown to the right of the data). The two peaks can be clearly seen and show large variations in frequency with distance. These variations show a strong correlation with the water depth, which is also shown in Figure 6.2.

There are two major factors which modify the frequency content of the source wavelet: the oscillations of the bubble pulse and the effects of resonance within the water column (the result of reverberations between the sea surface and the sea bottom). The first of these is countered by the use of tuned airgun arrays which attenuate the bubble pulses by destructive interference (the far field source signature for the airgun array used in BABEL was shown in Figure 4.3). The second factor depends upon the water depth. The frequency at which the water column resonates may be calculated as follows:

$$F_a = \frac{(2n-1)V_w}{4h} \qquad (6.1)$$

were n is an integer, V_w is the water velocity and h the water depth (Burkhardt and Vees, 1975). Immediately prior to the BABEL experiment, PRAKLA measured the average water velocity in the Gulf of Bothnia as 1450 m/s. A plot of the theoretical values of F_a against distance for n=1 and n=2 is shown in the overlay for Figure 6.2. The variation in frequency of the peaks with distance and the separation of the n=1 and n=2 values of F_a is a good match to that seen in the experimental data.

The differences between the theoretical and experimental frequencies may be due to a number of factors. The geology of the sea floor varies greatly along the line (section 2.7) and this may affect the frequency content of the downgoing wavefield. The depth of the airgun and the minor effect of the bubble pulse may also alter the frequency content from that predicted theoretically. Similar frequency spectra have been seen in the wide-angle Caledonian Suture Seismic Project, CSSP (Green, 1984)

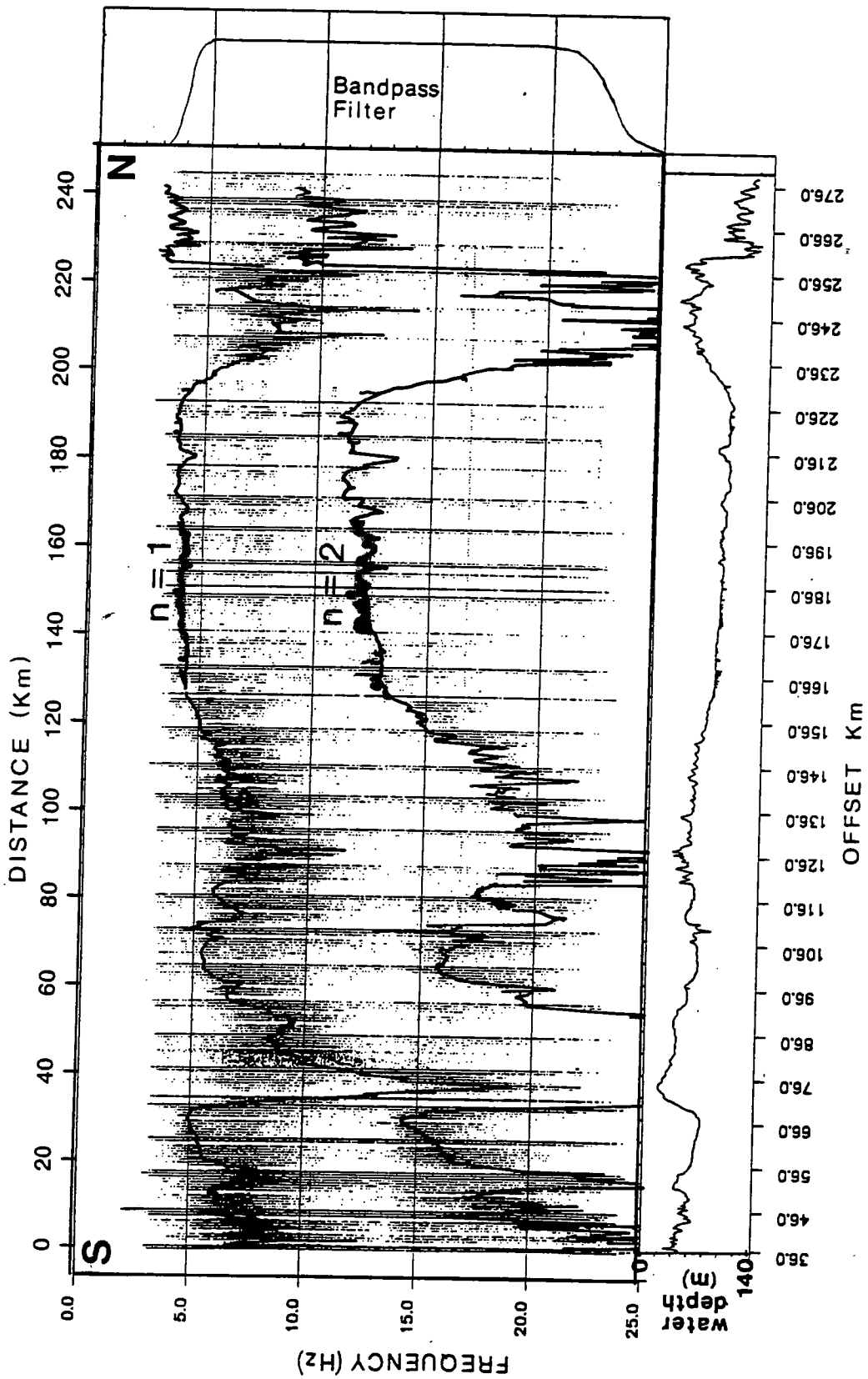

Figure 6.2. Variation of frequency content with distance for the line 6 wide-angle data recorded at station BS5P. The data has been bandpass filtered and the variation of water depth along line 6 is shown for comparison (offsets are measured from BS5P)

Resonant frequency of the water column along BABEL line 6 calculated from Fa=(2n−1)Vw/4h.
The water velocity (Vw) = 1450 m/s.

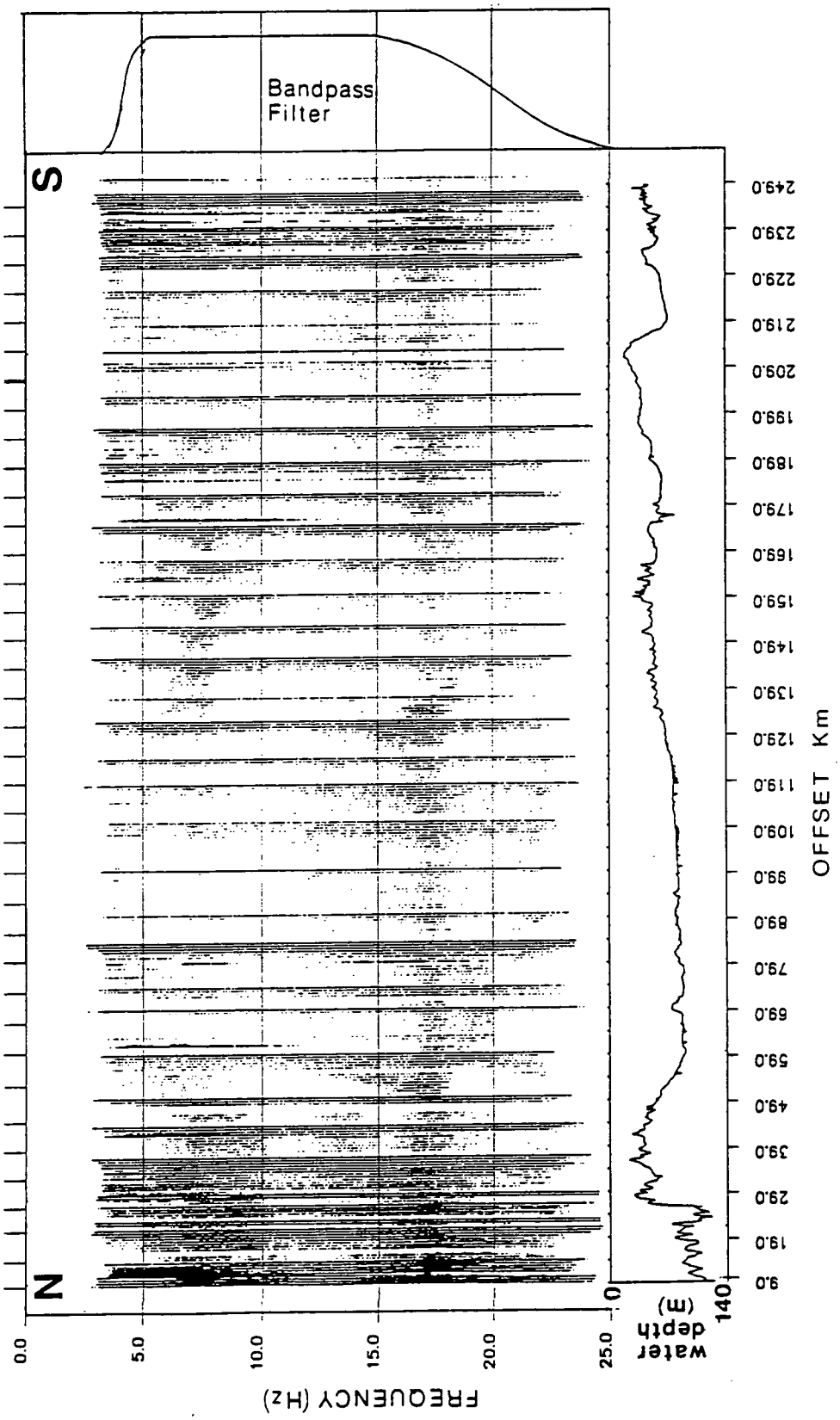

Figure 6.3. Variation of frequency content with distance for the line 6 wide-angle data from station Z2A. The data has been bandpass filtered and the variation of water depth along line 6 is shown for comparison (offsets are measured from Z2A).

and the water depth was found to be the major factor affecting the frequency content of this data.

The variation of frequency content with distance for Z2A is shown in Figure 6.3. The peaks are less clear than for the PDAS frequency section (the data is more noisy). The lower frequency peak still appears to vary with the water depth but the higher frequency peak occurs at a constant frequency across the section. This differs from the PDAS spectra and from the spectra for other Geostore recording sites where the frequency of the second peak also varied with water depth. This suggests that it is a feature of the recording site. Station Z2A was located on a badly weathered hillside (section 4.3) that may have generated high frequency noise. This may also explain why the second peak of the Z2A data is higher amplitude than the first. Since Z2A was the nearest online station to the northern end of line 6, it was important for reversing the model.

6.1.2 Filtering

The data for BS5P and Z2A were filtered with a Hanning window filter. The Hanning window filter is a bandpass filter with cosine tapered edges (Figure 6.4). The low cutoff for both PDAS and Geostore data was set at f_1= 3 Hz and f_2= 4 Hz. This cutoff was sharp in order to remove the low frequency noise while losing as little of the data as possible. For the BS5P spectra, the high frequency cutoff was set to f_3 = 20 Hz, f_4 = 25 Hz, retaining the second peak of the frequency spectra. The filtered spectra for BS5P and Z2A are shown in Figure 6.5.

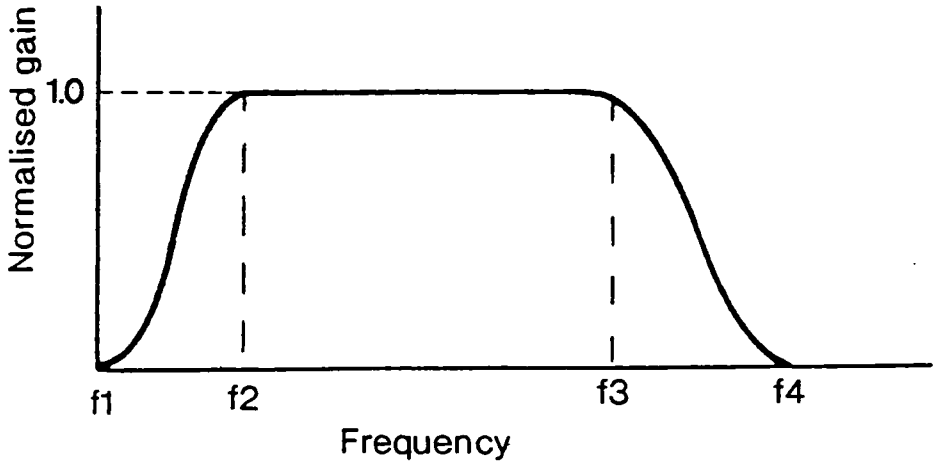

Figure 6.4. The Hanning window filter.

The high frequency cutoff for the Z2A data was varied by trial and error to find the best parameters for the data section. It was found that the clearest arrivals were seen when the amplitude of the second peak was reduced to below that of the first

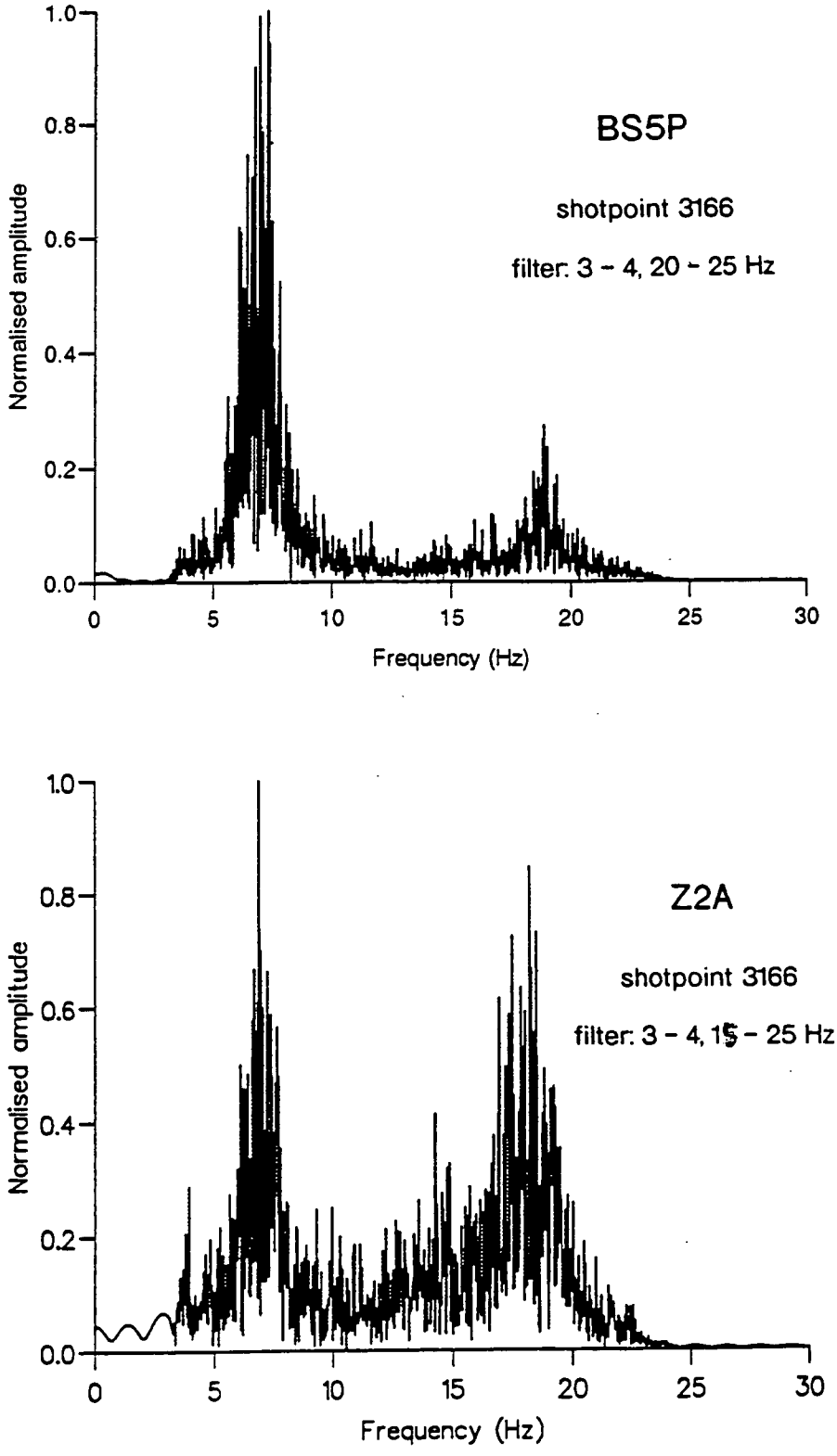

Figure 6.5. Filtered frequency spectra for the PDAS data from BS5P and the Geostore data from Z2A (the unfiltered spectra are shown in Figure 6.1).

peak (i.e. when the high frequency noise due to the station location is no longer the dominant feature of the data section). This was achieved by using a gentle taper between 15 Hz and 25 Hz. The shape of the filter used for the Z2A data is shown in Figure 6.3.

Filter parameters for the other BABEL wide-angle sections were determined by considering the frequency spectra and by plotting test sections until the optimum values were found.

6.1.3 Other wide-angle data processing

Apart from the frequency filtering described above, no other processing was applied to the data which was used to produce the line 6 model. There were three main reasons for this approach:

Firstly, although several attempts have been made to apply various processing techniques to the wide-angle data from BABEL and other similar projects, these have resulted in little or no improvement in the quality of the data. Fleuh and Dickmann (1992) have used techniques commonly used in shallow and normal-incidence seismic processing, such as trace mixing, stacking and residual statics, to improve the signal to noise ratio of wide-angle data. They found that the signal to noise ratio of the BABEL data was generally good out to offsets of more than 300 km and that it was only at offsets greater than this that these techniques improved the data quality to any appreciable extent.

Other processing methods have met with little success. Velocity filtering in the F-k domain has been shown to produce pronounced smearing of the arrivals due to the limited frequency content of the wide-angle data (Fleuh and Dickmann, 1992, Graham, 1993). Deconvolution in the Tau-p domain (Jokat and Fleuh, 1987) suppressed some of the ringing in the data but resulted in a loss of resolution. Predictive deconvolution using short operators and short prediction lengths has been unsuccessful due to the aperiodic nature of the multiples and the fact that the data is bandlimited (Fleuh and Dickmann, 1992).

Secondly, processing is aimed at selectively removing parts of the data, multiples, ringing, etc. In order to choose the processing parameters to remove the required parts of the data, it is necessary to have some idea of the origin of the various arrivals seen on the section. The complexity of the BABEL data makes it difficult to identify which phases are artefacts (such as multiples) and which are reflections or diving rays.

Thirdly, in wide-angle studies, phases which are usually removed in normal-incidence or near-surface seismic processing have been found to yield important

information on crustal structure. For example, arrivals in wide-angle data that have been identified as possible diffractions have been used to determine the subsurface position of small offsets of reflecting boundaries which would otherwise not have been modelled (Matthews, 1989, West, 1990). Similarly, peg-leg multiples in near-surface structure and P- to S- wave conversions have also been used to constrain near-surface data (Rowbotham, 1990).

Modelling the unprocessed wide-angle data provides explanations for the main arrivals seen on the sections. Processing may then be aimed at enhancing specific phases.

6.1.4 Plotting

The SEGYi data sections were plotted using software written for wide-angle data by Dr C. Prescott. This used the UNIRAS library of subroutines for the display of seismic data and was modified by Dr C. Pierce to provide a single plotting package for wide-angle and OBS seismic data. The program (DAZZLE) plots data with either equal trace spacing or against the distances specified in the trace headers. The program provides options to filter the data with a simple bandpass filter, to plot an automatic gain controlled section or to apply a reduction velocity to the data (or a different reduction velocity if the data is already reduced). The data may be plotted as wiggle traces (with either positive or negative fill) or as a variable area plot. Each trace is plotted as true amplitude relative to the rest of the section.

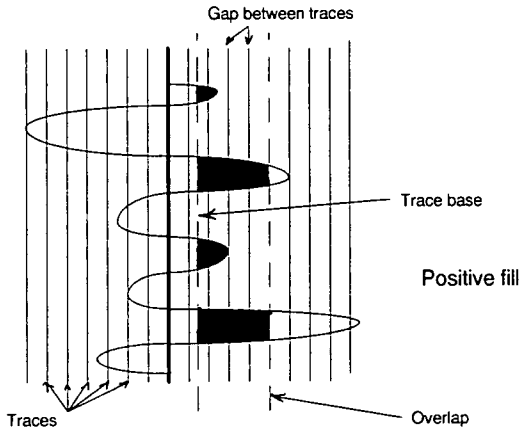

Figure 6.6. Example of the overlap and baseline parameters used in DAZZLE (for an overlap of 5 and a baseline of 0.3, positive fill).

Using the UNIRAS routines, the amplitude of each trace is calculated as follows. The maximum amplitude (T_m) of the data section is estimated by averaging the maximum amplitudes measured from every tenth data trace across the section (if

there are less than ten traces then every trace is used). The amplitude of each sample is then scaled according to this maximum and to the overlap and baseline specified by the user.

The trace spacing is found from the size of the plot to be generated. The scale for plotting each trace is set so that T_m equals the number of traces specified by the overlap. The overlap controls the saturation of the data; samples are 'clipped' when their amplitude exceeds T_m (T_m is only an estimate of the maximum amplitude). The baseline-T_m is coloured for either the positive or negative peak. When plotting variable area sections, the baseline determines the low amplitude cutoff of the data; samples with amplitudes less than this are not plotted (Figure 6.6).

The variable area option gives the clearest plots for dense data with closely spaced traces. This option was used for all the line 6 wide-angle sections.

6.1.5 Wide-angle data sections

The BABEL data has a much higher resolution than that of any previous deep seismic refraction survey of the Baltic Shield. For comparison, a section of data from BABEL line 6 (BS5P) and the parallel segment of the 1979 FENNOLORA profile (the closest profile to line 6) are shown in Figure 6.7. Both plots were recorded at sites at the southern end of the Gulf of Bothnia and are plotted on the same scale. The FENNOLORA section is a trace-normalised common-shot section with an average station spacing of about 3500 m while the BABEL section is a true-amplitude common-station section with an average shot spacing of 62.5 m. In the FENNOLORA data, only the first arrivals are easily identifiable. In the BABEL data, the increased resolution reveals a large number of complex arrivals throughout the section.

Data from five of the BABEL stations in Sweden (Figure 4.4) have been used to produce the models for line 6 presented in this work. Initial models were derived using the P- and S-wave data from the southern PDAS station (BS5P) and P-wave data from the Geostore station closest to the northern end of line 6 (Z2A). The model was then extended to include the data recorded at greater offsets from other online Geostore stations (BS5 and Z5A to the south and Z1A to the north). The data sections from these stations are shown in Figure 6.8a-h. All of the sections are true amplitude and plotted as reduced travel time against offset from the recording station (the data is reduced at 6 km/s, unless otherwise specified). Data is plotted with the northernmost trace at the righthand side.

Offsets in the data sections in Figure 6.8 vary from a minimum of about 12 km (station Z2A, Figure 6.8g) to a maximum of about 305 km (station Z1A, Figure 6.8h). In the BABEL experiment, many stations recorded clear arrivals at offsets of 350 km

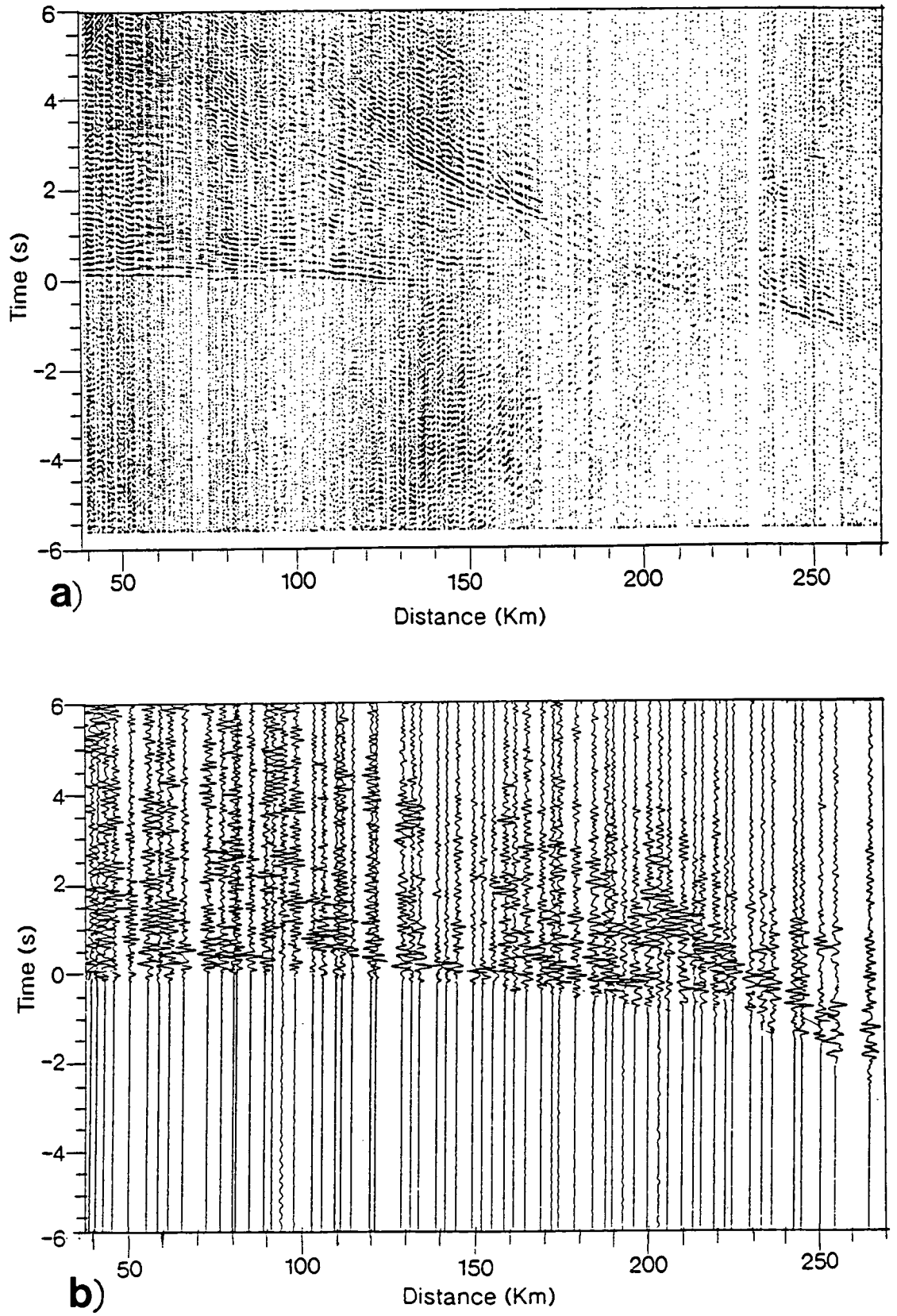

Figure 6.7. Comparison between **a)** BABEL line 6 recorded at BS5P (true amplitude) and **b)** the trace normalised section of FENNOLORA that lies parallel to line 6 (after Guggisberg et al., 1991). Both sections are reduced at 6 km/s.

or more using single seismometers. The airgun shots were also detected at distance of 500 - 700 km by using arrays of geophones (BABEL working group, 1991a). This was the maximum distance at which attempts were made to record the airgun shots and it may be possible to record arrivals at even greater offsets The good detection of arrivals at large offsets was due to a combination of quiet recording sites with good coupling to bedrock and the high Q value of the Shield crust.

i) Digital PDAS data: BS5P

Figure 6.8a shows 35 seconds of the vertical component data recorded at PDAS station BS5P. The vertical white stripes are the result of the PDAS data being recorded in twenty minute sections. This does not cause a problem as arrivals can easily be traced across the data gaps. Clear P- and S- wave arrivals can be seen. Unfortunately, the shot interval for line 6 was about 23.5 seconds and, as a result, the S-wave from the previous shot interferes with the current P-wave arrivals at offsets between 150 and 230 km. Similarly, the P-wave arrivals from the previous shot obscures the S-wave data at travel times greater than 26 secs. Since the shot interval varied slightly along the line, the arrivals from the previous shot are not coherent across the section. Attempts have been made to remove the S-wave interference by filtering in F-k space but with only limited success (Graham, 1993).

Both P- and S- wave data show a similar pattern of arrivals. The amplitude of these arrivals does not greatly exceed that of the background noise although arrivals are clearer than in previous projects on the Phanerozoic crust around Britain (Matthews, 1989, West, 1990). In most cases, it is the coherence that makes the arrivals visible against the background noise. The amplitude and phase of these arrivals change rapidly across the section. One possible explanation for this is that differences in the sea bottom geology along line 6 result in a variation in the strength of the P- to S-wave conversion at the sea bed. If this is the case, then an increase in the amplitude of the S-wave arrivals should be seen where that of the P-wave decreases. The amplitudes of the PDAS data do not seem to show this variation and do not appear to be related to changes in water depth.

Figure 6.8b shows an expanded section of the P-wave data in Figure 6.8a. The first arrivals at the smallest offset have reduced travel-times close to zero, indicating that the near surface velocities are close to 6 km/s and that there is little sedimentary cover along the line. The section appears relatively simple. Two major bands of arrivals are seen; one with an apparent velocity of about 6 km/s and the second with an apparent velocity of about 8 km/s. On a closer inspection, these bands are seen to consist of several overlapping arrivals and there are other, lower amplitude arrivals

Figure 6.8. BABEL common station sections used in modelling line 6. All sections are true amplitude. Sections are reduced with a reduction velocity of 6 km/s (unless otherwise stated) and are plotted with the southernmost trace at the left hand side of the section. The locations of the recording stations are shown in Figure 4.4:

a) Station BS5P.	Vertical component PDAS data.
b) Station BS5P.	Vertical component P-wave data.
c) Station BS5P.	Transverse component PDAS data.
d) Station BS5P.	Transverse component S-wave data (reduced at 3.5 km/s).
e) Station BS5.	Vertical component Geostore data.
f) Station Z5A.	Vertical component Geostore data.
g) Station Z2A.	Vertical component Geostore data.
h) Station Z1A.	Vertical component Geostore data.

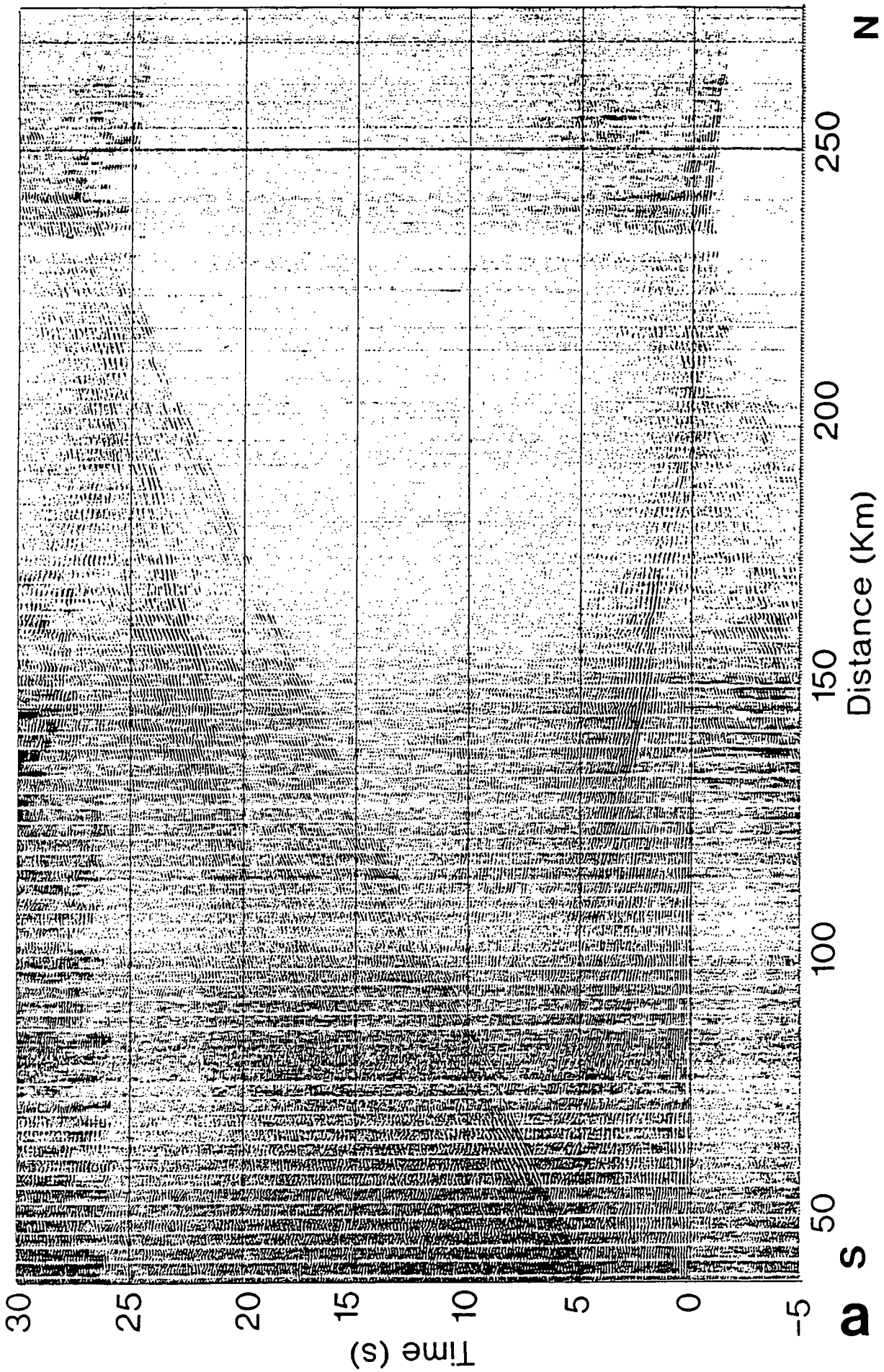
a
S
N
50
100
150
200
250
Distance (Km)
30
25
20
15
10
5
0
-5
Time (s)

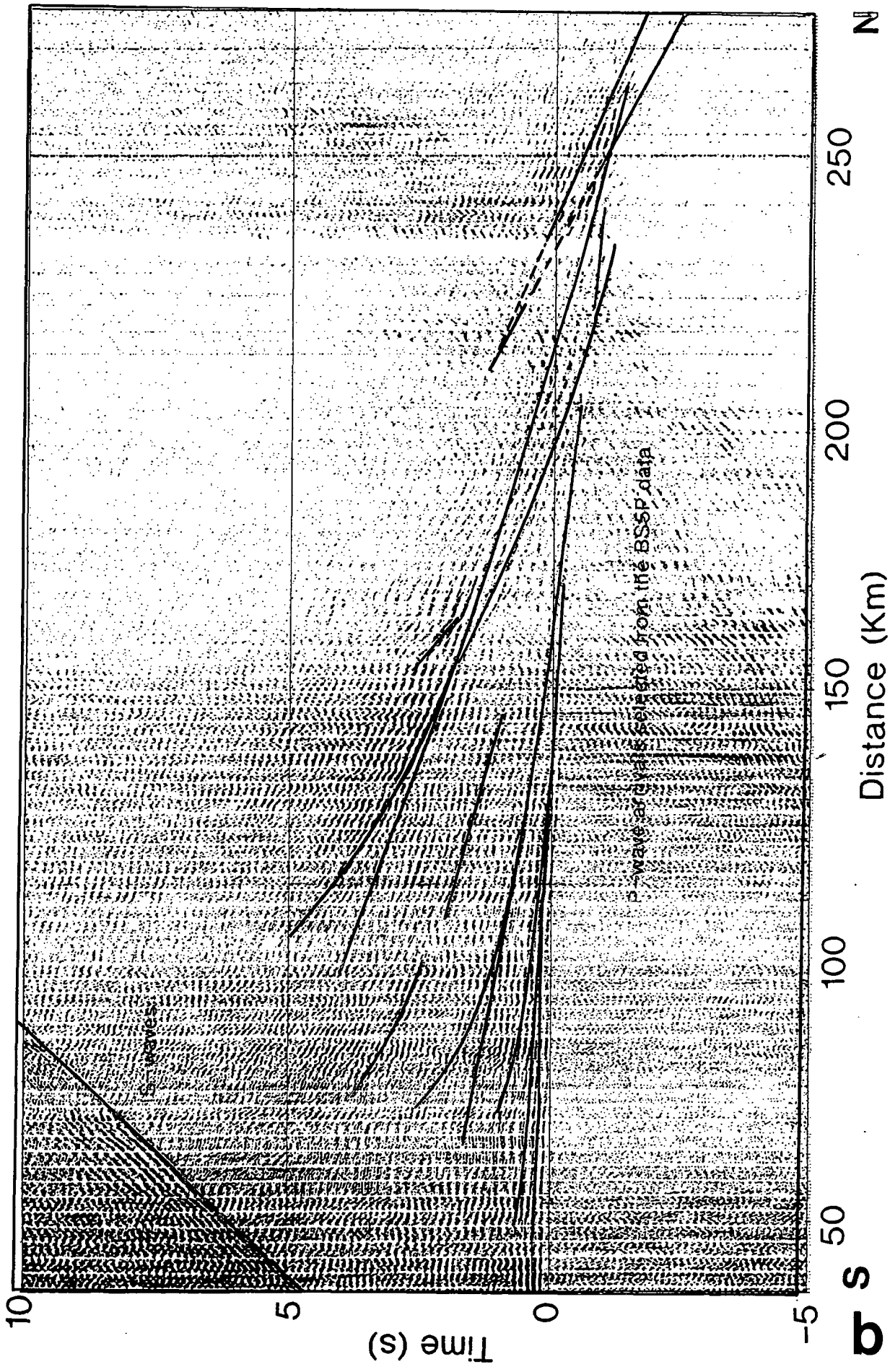
b
S
N
Distance (Km)
50
100
150
200
250
Time (s)
10
5
0
-5
p-wave arrivals picked from the BSSP data
cp waves

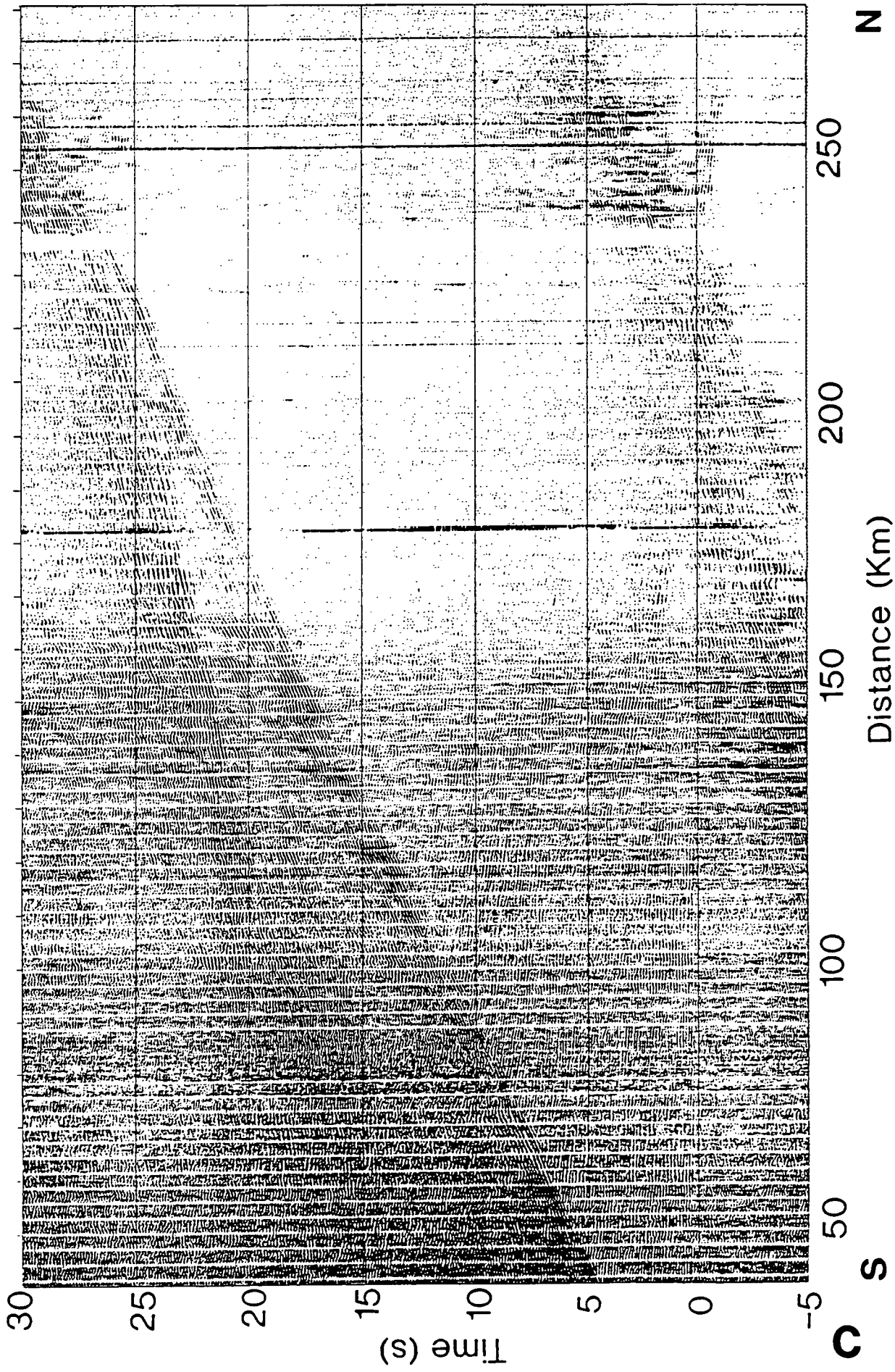
N
S
C
Distance (Km)
50
100
150
200
250
Time (s)
30
25
20
15
10
5
0
-5

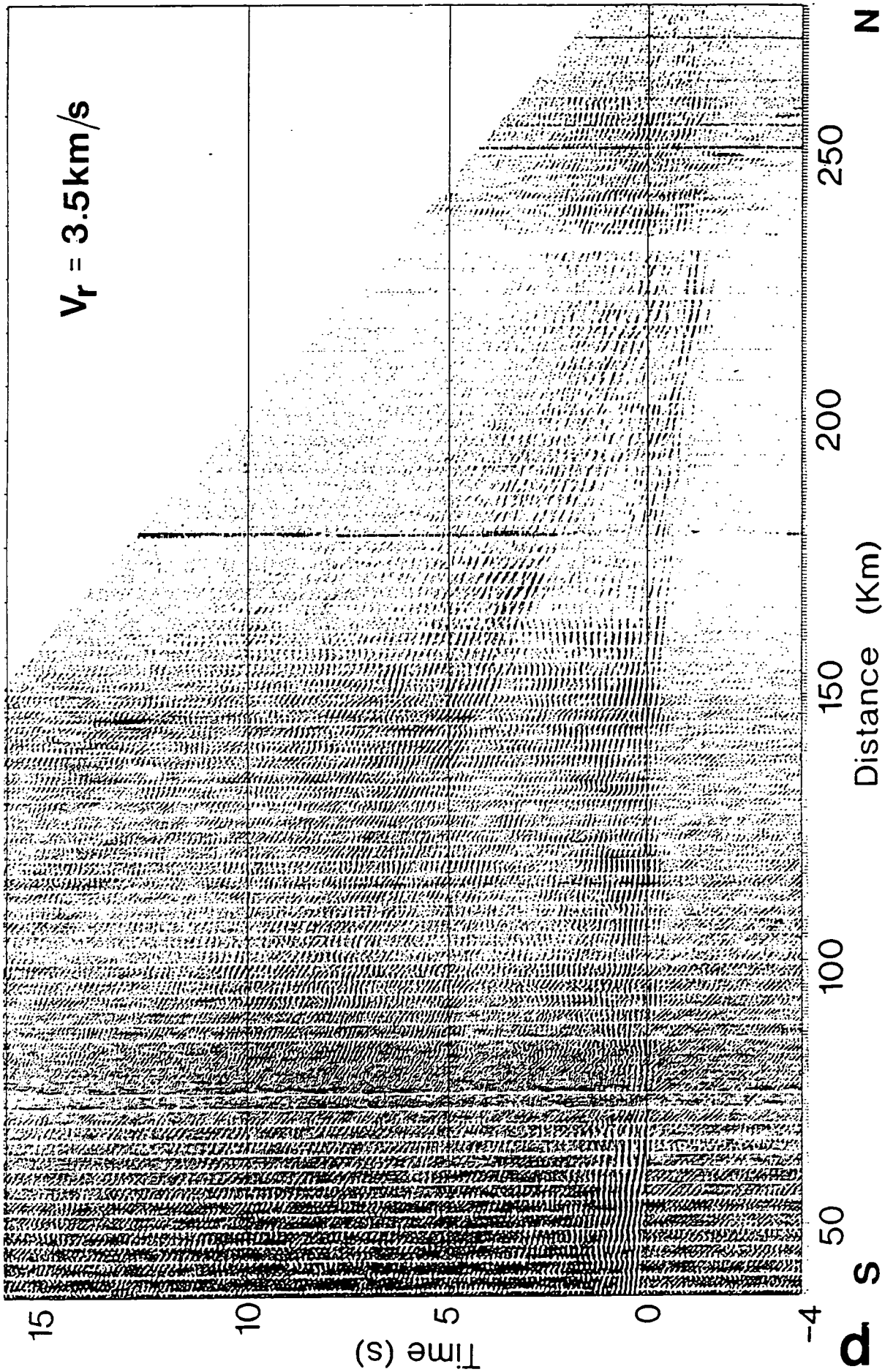
V_r = 3.5km/s
Time (s)
15
10
5
0
-4
Distance (Km)
50
100
150
200
250
S
N

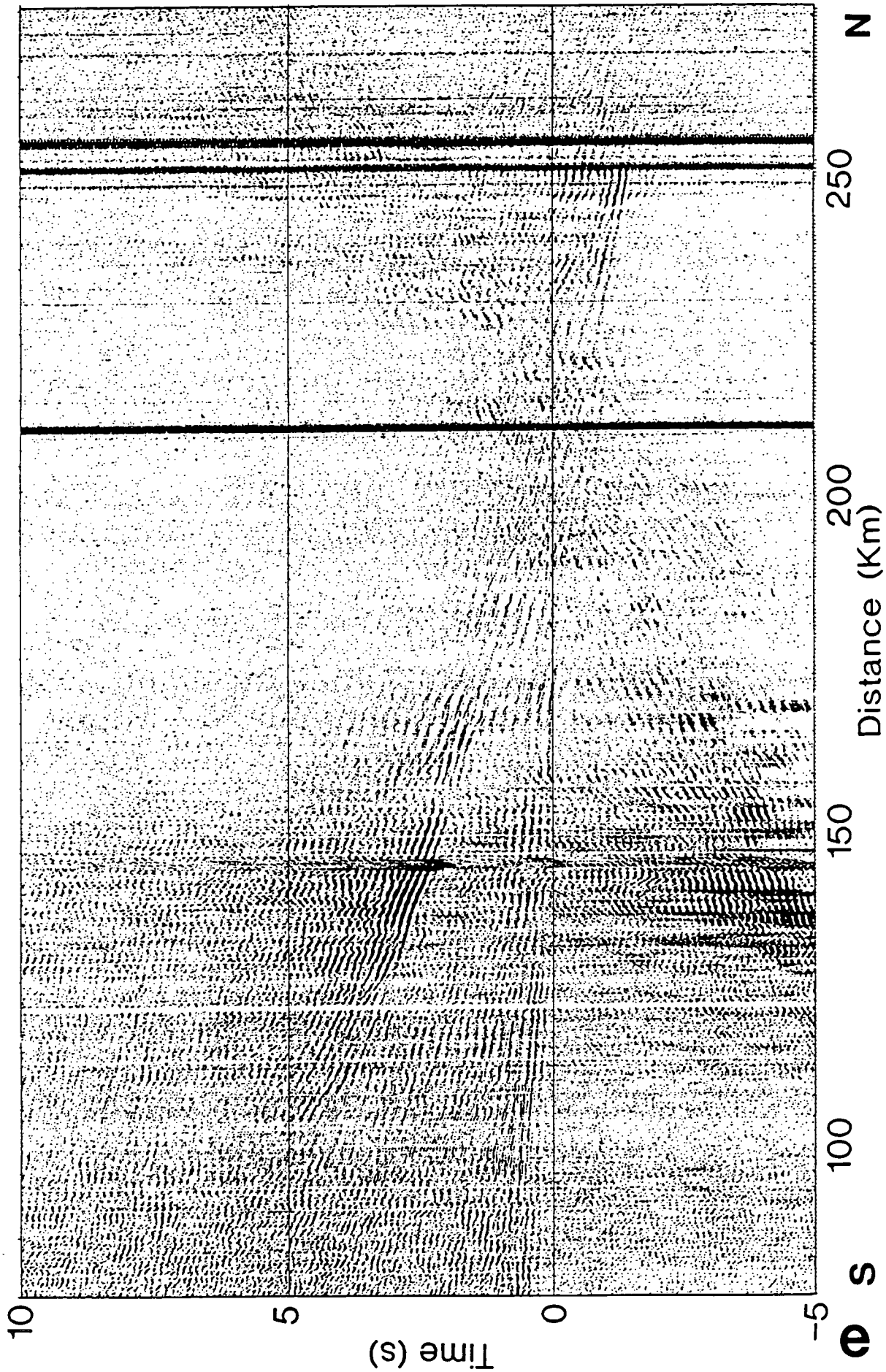
S
N
100
150
200
250
Distance (Km)
10
5
0
-5
Time (s)

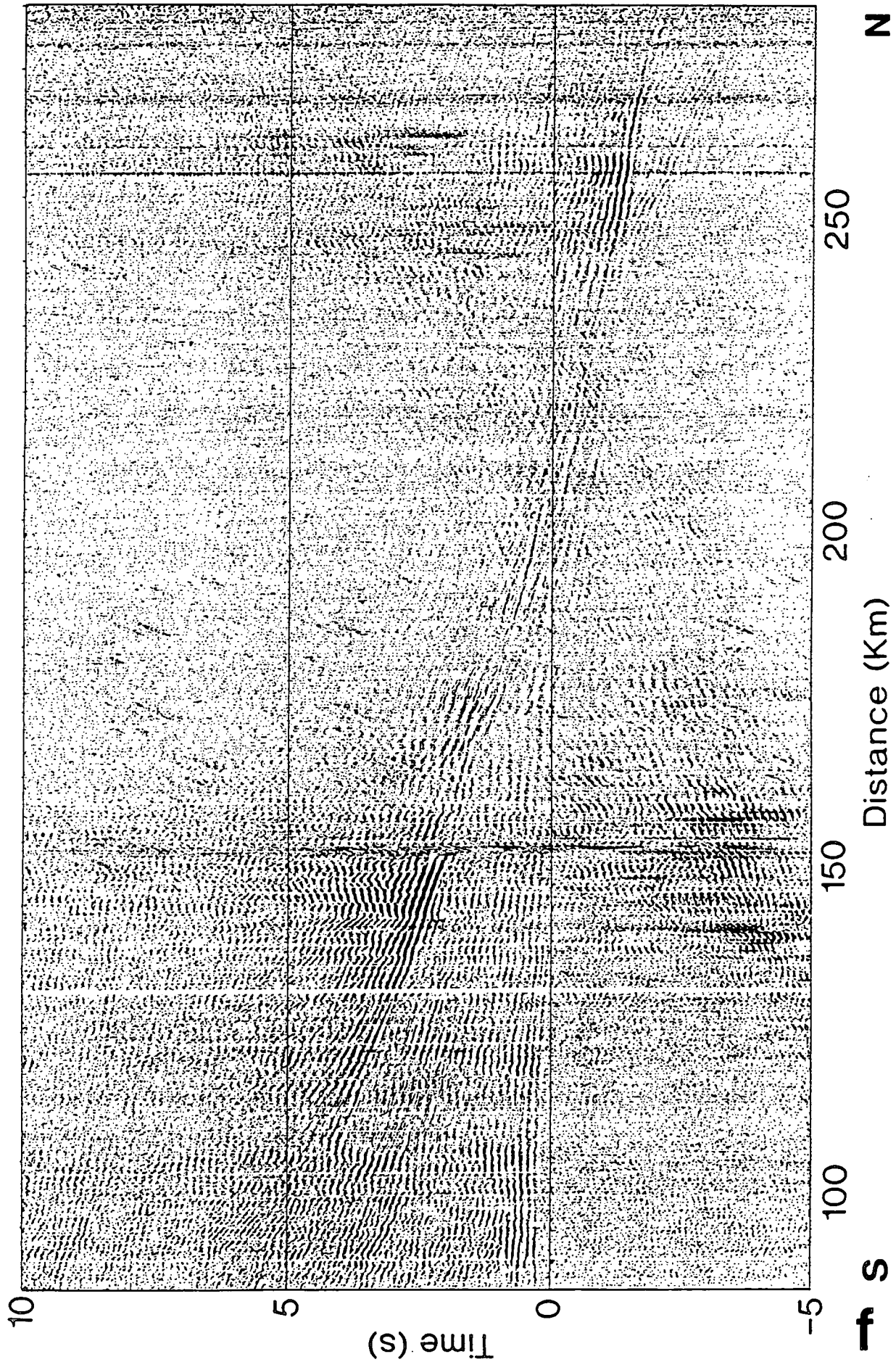
N
S
Distance (Km)
100
150
200
250
Time (s)
10
5
0
-5

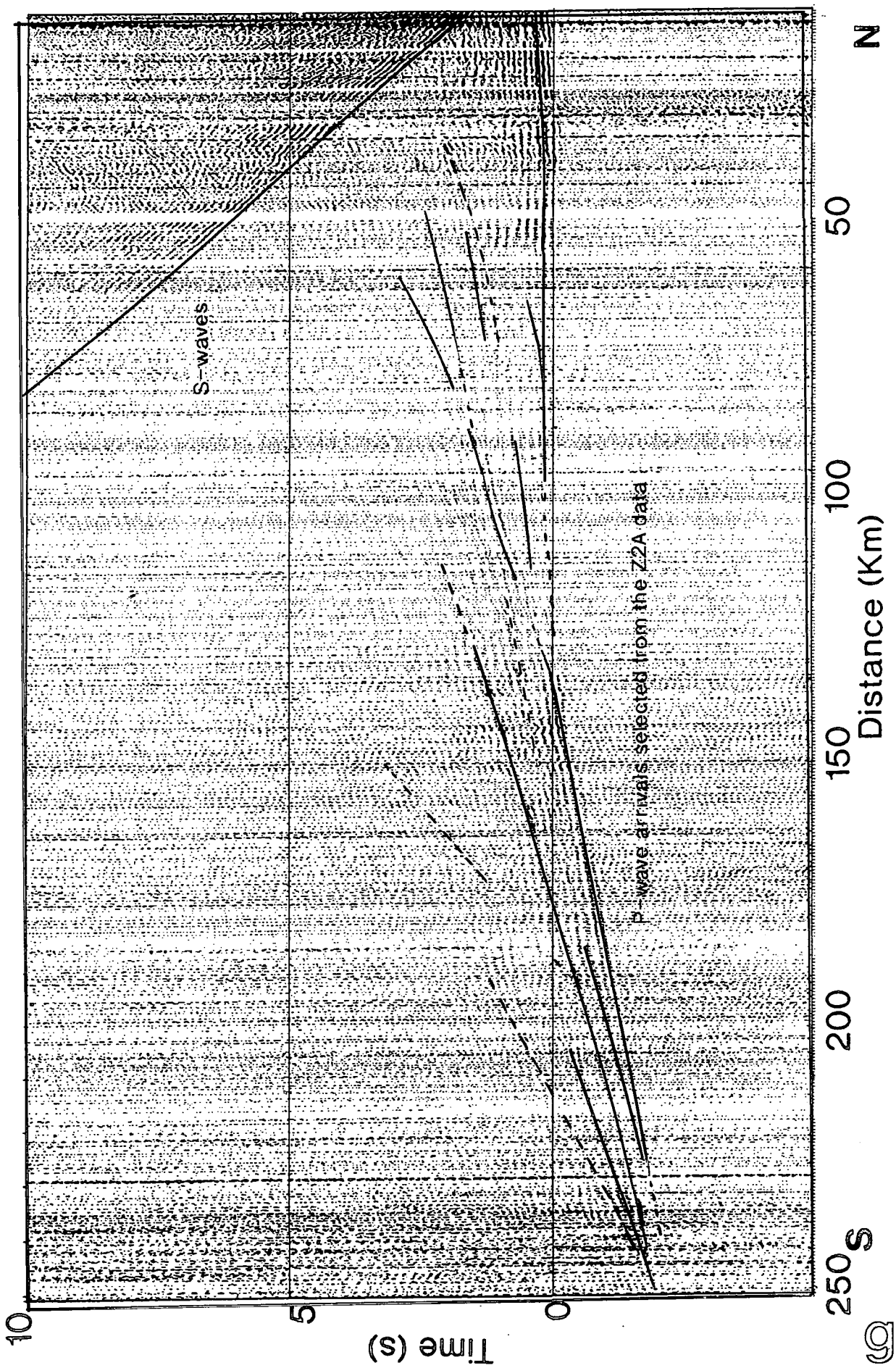
S-waves
P-wave arrivals selected from the Z2A data
Time (s)
10
5
0
250
200
150
100
50
Distance (Km)
S
N

g

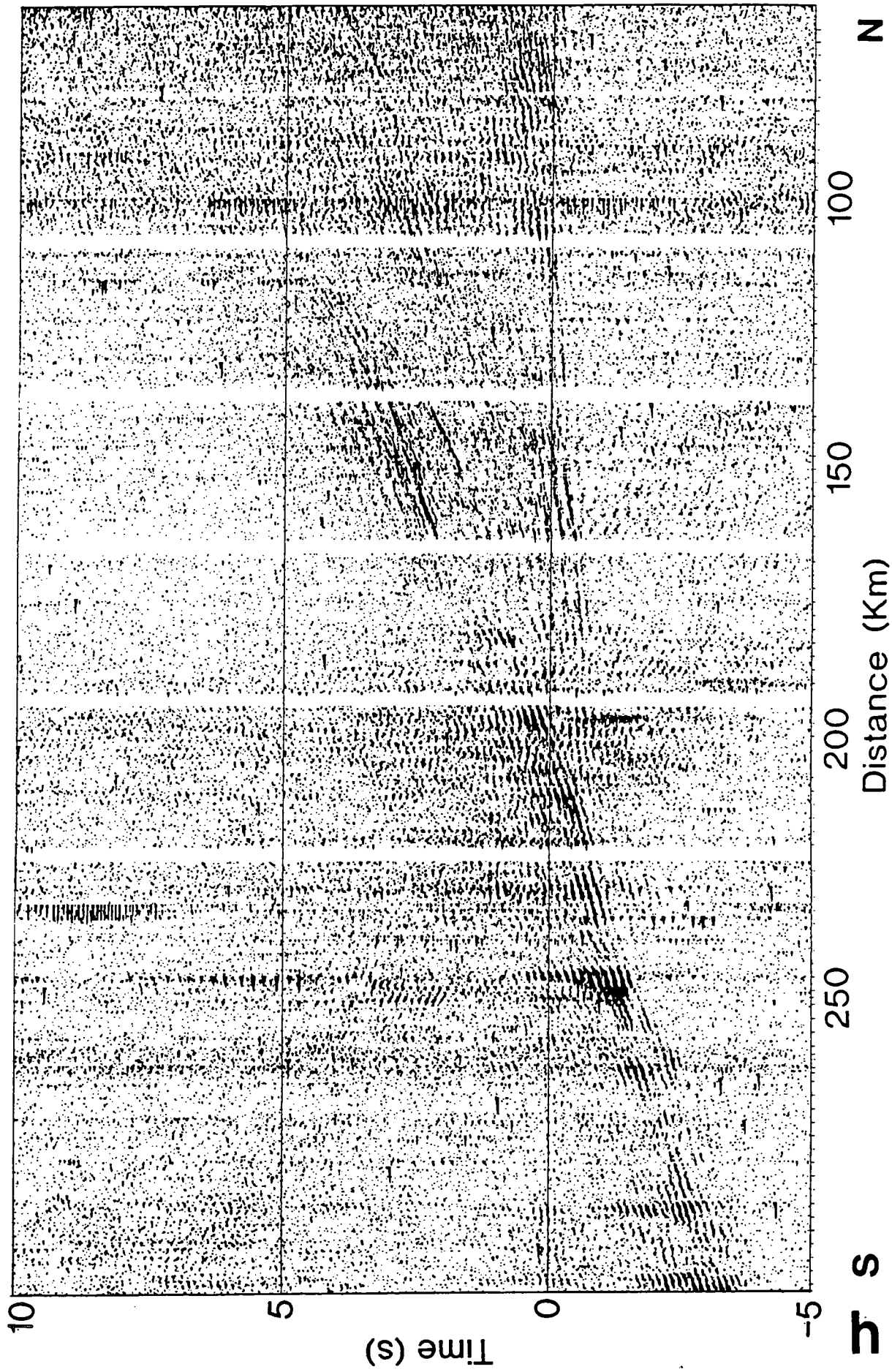
S
N
Distance (Km)
100
150
200
250
Time (s)
10
5
0
-5

with intermediate velocities between these two bands. Much of the variation in amplitude appears to be due to interference effects where these arrivals cross.

The transverse component recorded at BS5P is shown in Figure 6.8c. The section is dominated by S-waves since, although the data has not been resolved into S_H and S_V components, the seismometer was roughly in line with the S_H arrivals. The amplitudes of the S-wave arrivals are much greater than the P-wave on this transverse component and interference with the P-wave arrivals from the previous shot is minor. The S-wave data for this component was re-reduced with a reduction velocity of 3.5 km/s (Figure 6.8d).

Since the original data traces were only 40 seconds long, a slopping cutoff of the data is seen at offsets greater than 150 km. The absence of interference from the P-wave from the previous shot means that the S-wave arrivals are much clearer than for the vertical component (Figure 6.8b). The pattern of arrivals seems to be very similar to that seen in the P-wave data. Again, rapid changes in amplitude and phase are seen along what appear to be continuous arrivals.

ii) Southern online Geostore data: BS5 and Z5A

Station BS5P was situated on a small island at the south of line 6 (Figure 4.4). Two Geostore stations were located near to this; one slightly to the east (BS5) and a second further to the south (Z5A). The data for these two stations are shown in Figures 6.8e and 6.8f respectively. Both sections have been bandpass filtered and resampled to 100 samples per second to make it easier to plot them clearly at this scale. Three bands of noise are see at the northern end of the BS5 section. BS5 was located in a disused blacksmiths workshop on a small farm. and the noise may be due to traffic on the nearby farm track. At an offset of about 145 km, the data on both the BS5 and Z5A sections is distorted. This is probably due to an error in the start time or the sampling rate of one of the pseudo-PDAS files.

Both BS5 and Z5A show similar arrivals to the digital PDAS data recorded at BS5P. At near offsets, the first arrivals have a slightly greater travel time than for BS5P, suggesting lower near-surface velocities, probably due to greater sedimentary cover. On all three sections, the maximum amplitude is seen at offsets of 120-150 km, associated with an arrival with an apparent velocity of about 8 km/s. Between 170 and 230 km the amplitude of the arrivals appears to decrease, although this may be the effect of interference with the S-wave from the previous shot.

iii) Northern Geostore data: Z2A and Z1A

Figures 6.8g and 6.8h show data recorded at two Geostore stations to the north of line 6. The data recorded at Z2A (Figure 6.8g) is of much poorer quality than for the other recording sites (the reasons for this were discussed in section 6.1.1). The amplitudes of the arrivals are about the same as the background noise and there is a rapid fall off of amplitude with offset. Z2A was the closest online station at the northern end of line 6 which made it important for reversing the model.

Several different plotting methods were used in an attempt to improve the resolution of this data. The data was re-filtered with an upper limit of between 10 and 15 Hz to remove the noise due to the station location but this left only the low frequency component of the data and reduced the resolution. An AGC (automatic gain control) was applied to the data to normalise the amplitudes along each trace but this produced little improvement, since the amplitude of the noise and arrivals are approximately the same. A trace normalised section was also plotted with the maximum amplitude of each trace scaled to the same value. This removed the effects of the fall off of amplitude with distance but also removed the variations of amplitude and phase which play such an important part in the interpretation of the BABEL data. All of these sections were used to help select arrivals for station Z2A.

The next closest online station at the northern end of line 6 is BS1. This station was situated in the basement of an unoccupied house. Unfortunately, the data from this station is dominated by bursts of high frequency seismic noise which obscure the arrivals. These were probably generated by electrical appliances within the house such as the heating system and refrigerator. Some minor bursts of noise can also be seen on the data from the outstation recorded at this base station (Z1A, Figure 6.8h) which may have arisen as the result of radio interference at the base station.

Several blank vertical stripes are seen in the data section for Z1A. The Z1A data was digitised before the GLOBAL LAB macros were altered to pre-write data files to each new hard disk drive of the computer (section 5.1.2). Each of the sections between the vertical white lines corresponds to a different disk drive and the gaps are the result of changing from one drive to another. These gaps are much broader than those seen on the PDAS data and it is more difficult (although not impossible) to trace arrivals across them.

6.1.6 Selection of arrivals

The major discrepancies between different interpretations of wide-angle data arise, not as a result of different modelling packages, but as a result of the subjective

selection of arrivals by individual interpreters (Ansorge *et al.*, 1982). The high resolution of the BABEL data means that a large number of complex arrivals are seen. A combination of phase and group correlation methods (Geise, 1976) were used in an attempt to find a consistent method of selecting the major arrivals seen in the data sets.

The amplitude and phase of arrivals changes rapidly across the data sections on the scale of a few km. Short lengths of arrivals (~1-2 km) were selected, where the amplitude and phase were constant, (phase correlation) and traced on to a sheet of acetate overlying the large paper data section. These short lengths were selected according to the following criterion: they had an amplitude higher than the background noise, a realistic apparent velocity for the phase in question and were of a reasonable length (about 1 km or more). The regions in the data where the apparent velocity of the arrivals appeared to change were used as an indication of the appearance of a new arrival.

Continuous arrivals were then drawn across the section joining together phase correlated segments which appeared to have the same apparent velocity (group correlation). This assumes that the crustal structure consists of a series of roughly horizontal layers extending over large distances and that the changes in phase and amplitude along the arrivals arise as the result of localised variations in the boundary conditions which are generally ignored during modelling.

The initial model for line 6 was based on the arrivals selected in this manner from the data from BS5P to the south of line 6 and Z2A to the north of the line. These arrivals are shown in the overlays for Figures 6.8b and 6.8g.

6.1.7 Errors

The errors in the data due to the drift of the internal clock have been considered in section 5.2 and result in an error in the apparent velocity of the arrivals on the Geostore data sections of about 0.02 km/s. Other errors arise as the result of the uncertainty in the shot and station locations which leads to an error in the offset of the data. The error in the shot location was of the order of 0.05 km (section 4.2). The error in the station location was greater since locations were measured from those marked on a map during the experiment. The station error was of the order of 0.5 km. Both errors are small compared to the offsets along line 6 (30-240 km).

Further minor errors are introduced into the data by the responses of the recording instrument and of the playback system. Variations in the recording speed of the analogue recorder and of the Store-14 reduce the accuracy of the Geostore data, as does the averaging of the sampling rate for the pseudo-PDAS files.

The frequency content of the data is limited, with a maximum frequency of about 25 Hz. This reduces the accuracy with which it is possible to pick arrivals. If the dominant frequency of the data is low, of the order of 10 Hz, then the peak to peak width of the arrivals is 100 ms and the error in picking the arrival is of the order of ± 50 ms. This is equivalent to picking the arrivals to the nearest millimetre on the paper record sections. This introduces a much larger error than the errors involved in recording and processing the data, and underlines the importance of recording and retaining as much high frequency data as possible.

6.2 Normal incidence data

6.2.1 Frequency spectra

The normal-incidence data was processed by PRAKLA-SEISMOS under the guidance of BIRPS. Paper copies of the brute stacks were available soon after the project was shot but SEGY tapes of the intermediate stacks were not obtained until December 1991.

The frequency spectrum of the normal-incidence data is shown in Figure 6.9 for the same shotpoint as for the wide-angle data in Figures 6.1 and 6.5. This is the acceleration response rather than the velocity response measured for the wide-angle data. A series of peaks are seen in the spectra for the single trace and are shown more clearly in the spectrum of 60 stacked traces. The two lowest frequency peaks in the normal incidence spectra occur at the same frequencies as the two peaks seen in the wide-angle spectra (Figure 6.5). The higher frequency peaks are lost from the wide-angle data due to the filters in the recording/playback systems (section 4.4.3).

6.2.2 Crustal reflectivity patterns

One of the aims of the BABEL project was to compare the reflectivity of the Baltic Shield with that of Phanerozoic Europe. Phanerozoic crust is often considered as being separated into an unreflective upper crust and a reflective lower crust. These overlie an upper mantle that is much less reflective than the lower crust and the transition between crust and mantle is often abrupt (Matthews and Cheadle, 1986). This transition is termed the reflection Moho and is generally thought to correspond to the refraction Moho (Mooney and Brocher, 1987).

Cratonic normal-incidence crustal profiles (for example, COCORP, Latham *et al.*, 1988 and GLIMPCE, Behrendt *et al.*, 1988) typically show more diffractions than reflections. The reflectivity of the crust gradually decreases at about the depth of the

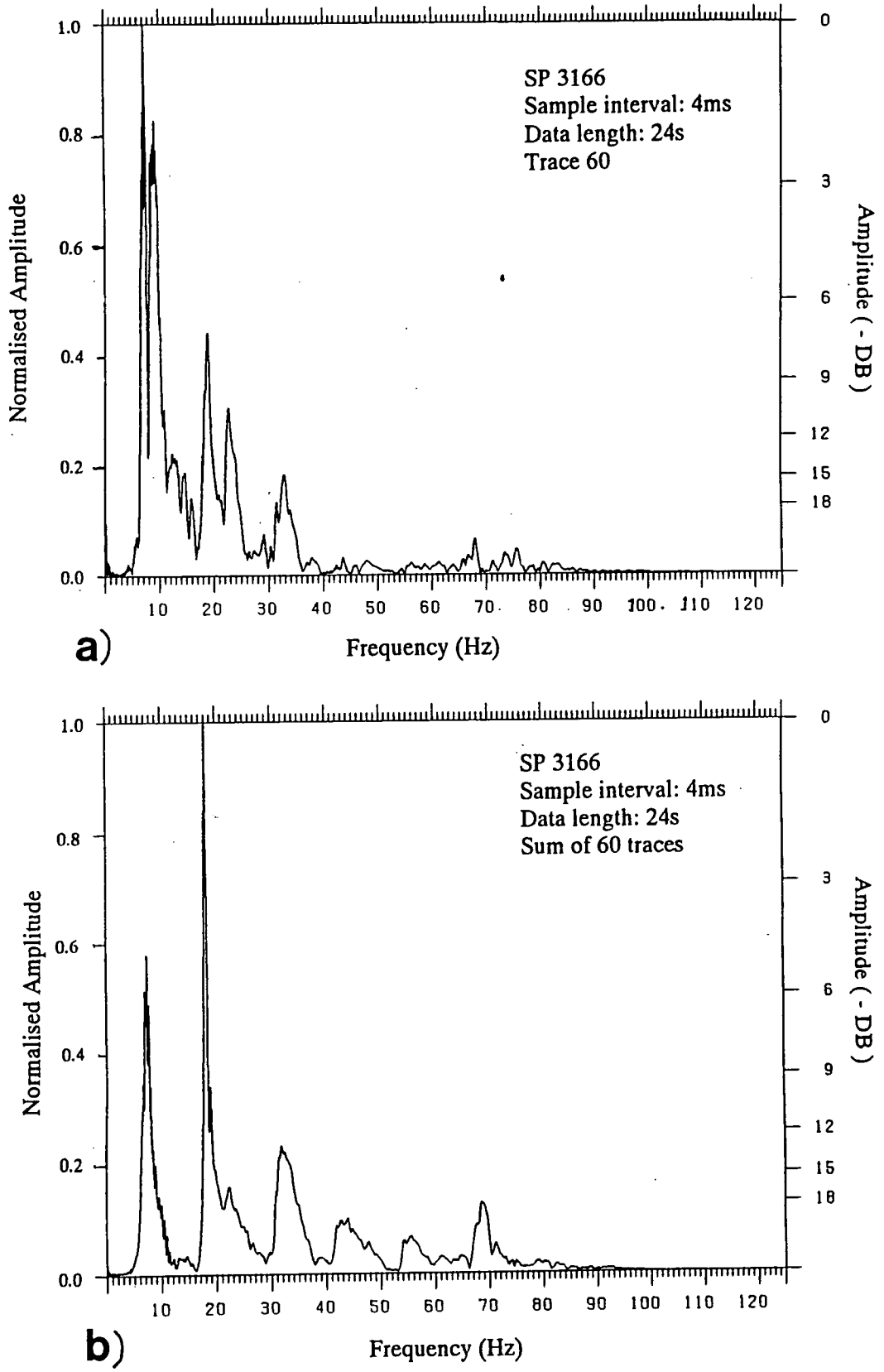

Figure 6.9. Frequency spectra of the normal-incidence data for the shotpoint used in Figures 6.1 and 6.6. **a)** for a single trace; **b)** for the sum of 60 traces.

refraction Moho but no sharp boundary is seen except in regions were Phanerozoic processes have affected Archaean crust (Brown *et al.*, 1983, Dahl-Jensen *et al.*, 1987). It has been suggested that all lower crustal reflectivity arises as the result of Phanerozoic tectonics, even in crust which predates this.

The origins of lower crustal reflectivity are disputed. Several geological explanations have been proposed. These include:

1. Pervasive igneous layering or mafic sills arising from underplating by hotspot vulcanism.
2. Horizontal foliation in gneisses, mylonites, etc., due to the effects of shear, in which existing structures are drawn into horizontal zones.
3. Layer cumulates in igneous bodies (anorthosites, gabbros, etc.).
4. Fluids trapped in the lower crust. Regions with pronounced lower crustal reflectivity often have low resistivities and Hyndman and Shearer (1989) suggest that the reflectivity and low resistivity may both be due to the presence in the lower crust of a few percent of free saline water.
5. Metasedimentary and metavolcanic layers caused by overthrusting during continental collisions (although the reflectivity may be due to subducted fluids rather than to the composition of the different layers).

There are difficulties with each of these explanations. High grade metamorphic exhumed rocks (such as granulite), which are considered to have originated in the lower crust, have a mineralogy suggesting that they formed under dry conditions and are rarely conductive or reflective. This suggests that either they are not typical of the lower crust or that they have been altered during the process of uplift (for example, by fluid exchange). Reflective lower crust is often seen in extensional areas but the most highly strained regions do not always show the greatest lower crustal reflectivity (Klemperer *et al.*, 1987, Trappe, 1989).

More recently, it has been suggested that lower crustal reflectivity may arise, not as the result of layering, but as the result of wavelength-scale velocity fluctuations. Hobbs and Levander (1992) have shown how a layered reflectivity pattern can be produced from a model as a result of processing, even though there is no horizontal layering in the model. Holliger and Levander (1992) have modelled a bimodal fractal velocity distribution based on the structure seen in an exposed piece of lower crust, the Ivrea zone in Northern Italy. This model generates a reflectivity pattern similar to that seen in normal-incidence data and has the advantage that dramatic changes in reflectivity may be modelled by relatively small variations in composition.

6.2.3 BABEL line 6 normal-incidence data

The normal-incidence data for line 6 is shown in Figure 6.10. The data has been migrated with a constant velocity of 6.5 km/s. The first 2 secs twtt show a series of closely spaced horizontal reflections. These may result from ringing due to shot generated multiples although Pedersen *et al.* (1992) have interpreted similar layering on line 1 as a sequence of metagreywackes.

Below this, the upper crust, down to a depth of about 6 s twtt, shows no distinct reflectors. This may be partly an effect of the processing of the normal-incidence data which is targeted at features in the lower crust. A lack of strong reflections in the uppermost crust has been seen on various BIRPS deep reflection profiles but its is unclear whether this is due to a predominance of sediment generated multiples or source generated noise, both of which could mask reflections in the upper crystalline crust (McBride *et al.*, 1992). At the northern end of the parallel profile (line 1, Graham, 1993), strong reflectors are seen in the upper crust. It has been suggested that these are dolerite sills, similar to those seen in nearby outcrops in Sweden and Finland (BABEL working group, 1991b). These dolerite sheets do not appear to extend across to line 6.

The lower crust shows patches of high reflectivity interspersed with regions where reflectivity is very much weaker. Bands of reflectivity are seen in the northern 15 km at about 8 km, 10 km and 13 km but no bands of reflections can be traced continuously across the section. Plutonism has played a major part in the formation of the Svecofennian crust (chapter II) and this patchwork of reflectivity in the lower crust may be the result of intracrustal intrusions.

A distinct change from reflective crust to non-reflective mantle is seen at about 16 s twtt (two-way travel time) and this boundary appears to be roughly horizontal across the section although the reflectivity contrast between the two layers varies. At distances of between 90 - 160 km, the boundary is indistinct and little energy is reflected from the lower crust. This may be a result of poor penetration of energy into the lower crust due to the overlying limestone mentioned in section 2.7 (Winterhalter, 1972), although this limestone extends beyond this region. Pedersen *et al.* (1992) modelled the gravity data for line 1 and suggested that a similar low reflectivity zone seen in the mid-crust at the northern end of the line is a post-orogenic granitoid pluton (section 3.2.2). These low reflectivity zones will be discussed in more detail in chapter IX.

The band of reflectivity seen at a twtt of 24 s is an artefact of the migration and is not seen on the unmigrated final stacks. A strong, steeply dipping reflection is seen in the mantle on both migrated and unmigrated sections, at distances of 150 - 180 km.

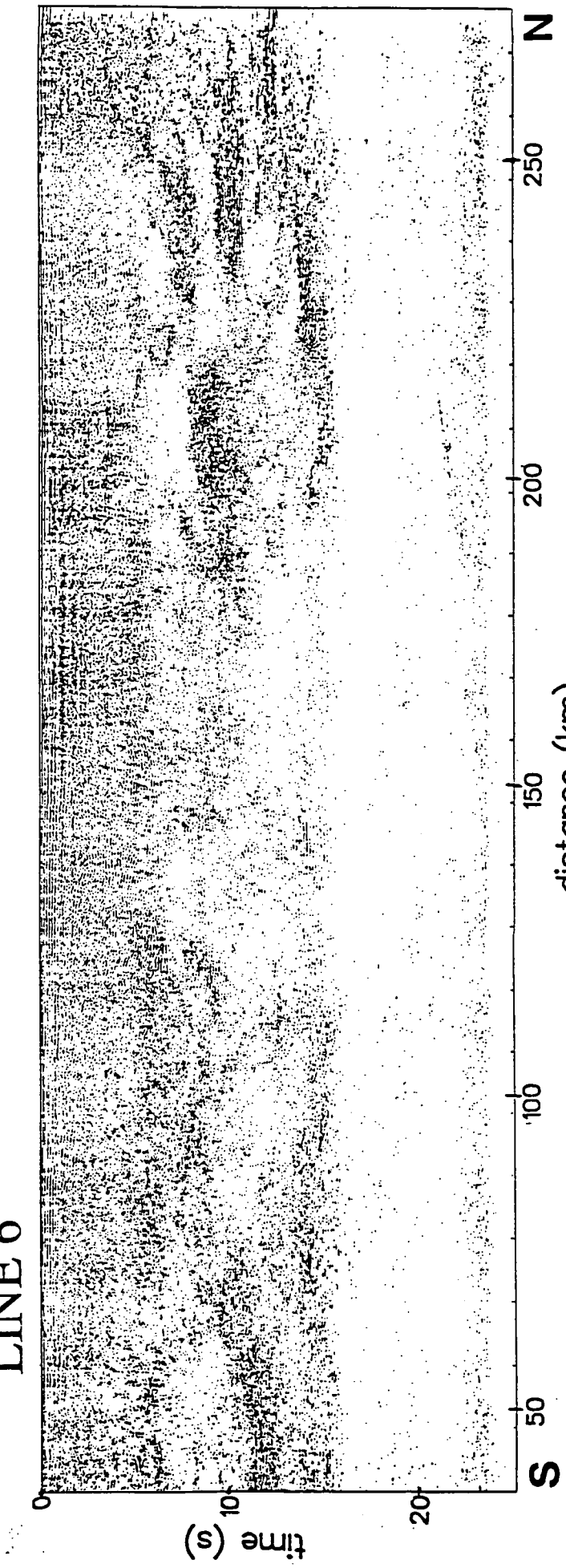

Figure 6.10. Line 6 normal-incidence data (migrated at a constant 6.5 km/s). Time is the two-way travel time in seconds and distance is measured from the southern end of the line.

A similar reflection was seen at the northern end of line 1, but much closer to the Moho. Strong reflections originating in the mantle have been seen on BIRPS profiles around the British Isles (Flack *et al.*, 1990) and interpreted as major faults or shear zones in the mantle, in this case associated with a Caledonian thrust fault. The large reflection coefficients of these reflectors may be due to a mafic layer or a partially hydrated layer within normal peridotite (compositional layering or seismic anisotropy would not produce such large reflections if olivine and pyroxene are the major minerals in the reflective zone, Warner and McGeary, 1987).

Several mantle reflectors have been seen in the Skagerrak (Lie *et al.*, 1990) which do not appear to be structurally related to the crust. These are seen at depths of about 100-110 km depth. It has been suggested that these reflectors are related to layers in the mantle rather than to overlying crustal structure. The mantle reflector seen on BABEL line 6 appears to be an isolated occurrence more typical of those seen on the BIRPS profiles than on the Skagerrak data.

The normal-incidence data was used to improve the first model for line 6 by matching the boundaries for wide-angle reflections to features seen in the normal-incidence section. This is described in more detail in chapter VIII.

CHAPTER VII

BEAM 87- GAUSSIAN BEAM RAYTRACING

7.1 Modelling wide-angle data

Unlike normal incidence sections, plots of wide-angle data do not relate directly to a depth section of the crust. Geological structure is found from wide-angle data by travel-time and waveform modelling. There are several methods for interpreting wide-angle data. The reflectivity method is the only exact method but is only applicable to 1D models. For 2D models, methods of determining this fall into two main groups; those based on direct numerical solutions of the elastodynamic equations, such as the finite difference method, the finite element method, and those which are based on asymptotic ray theory (ART). These different methods have been compared by several authors (e.g. Fuchs and Müller, 1971, Kennett and Harding, 1985, Weber, 1988).

The models for BABEL line 6 in this work were generated using a generalised ray theory method (BEAM87) where the crust is modelled as a series of homogeneous layers. Raypaths are calculated from shot to receiver through a model defined by the user and the wavefield is calculated by summing the elementary seismograms for different rays. The travel-times, amplitudes and synthetic seismograms are compared with the experimental data. The model is then improved iteratively to find the best possible fit to these parameters.

Generating synthetic seismograms from raytracing has the advantage over direct numerical methods, such as the finite difference and finite element methods, in that it is simpler and faster and requires less computing power, but the method does not give a full solution for the complete wavefield and breaks down in singular regions such as the critical region and caustic regions where the ray field is not regular. Various modifications to standard ray techniques are used to improve the accuracy and stability of raytracing packages. The most widely used of these are the WKBJ-Maslov method (Chapman, 1985) and the Gaussian beam method (Červený, 1985a). BEAM87 uses the second of these modifications.

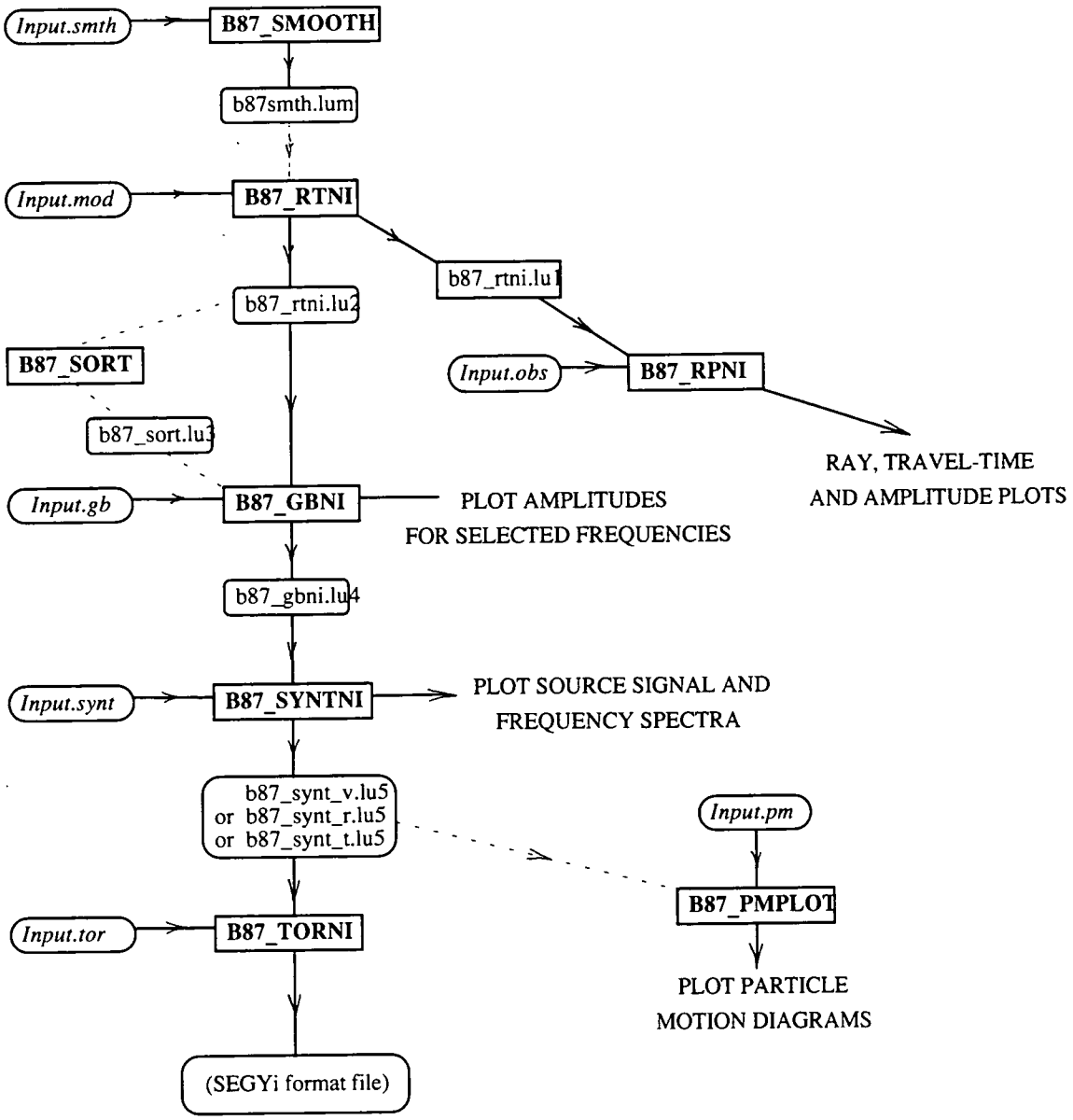

Figure 7.1. Routines in the BEAM87 raytracing package. Dotted lines mark optional routes. Formats for the input and output files are given in the BEAM87 users manual.

The BEAM87 raytracing package was written by Dr V. Červený and uses a Gaussian beam approximation to generate synthetic seismograms. This 'smears' out the raypaths, making the amplitudes of the synthetic seismograms less sensitive to approximations in the method. In computing terms it requires roughly the same CPU time and memory as its predecessor SEIS83 which used standard ray techniques. The routines in the BEAM87 package are shown in the flow chart in Figure 7.1.

7.2 Amplitude calculations along raypaths

Like most ray tracing packages, BEAM87 was originally written to model rays from a single source recorded at an array of receivers and to generate common-shot synthetic seismograms. In recent surveys, where a few land stations are used to record a large number of marine shots, the program has been used to model the reversed situation and to generate common-station synthetic sections. The kinematic properties of the rays, such as raypaths and travel-times, are perfectly reversible but the amplitudes calculated along the rays are not. Calculating amplitude from the receiver to the shot is not the same as calculating from shot to receiver.

A simple two layer model is shown in Figure 7.2. The raypath through the model is the same for a ray shot from left to right ('forward') as for a ray shot from right to left ('reversed'). The amplitude of the ray depends on the transmission coefficients (T) at the interface between layer one and layer two and the reflection coefficient (R) at the base of layer two.

For the forward ray:

$$q_f(x,y,\omega) = T_{12}^F R_{22}^F T_{21}^F p(x,y,\omega) = T^F R_{22}^F p(x,y,\omega)$$

and for the reversed ray:

$$q_r(x,y,\omega) = T_{12}^R R_{22}^R T_{21}^R p(x,y,\omega) = T^R R_{22}^R p(x,y,\omega).$$

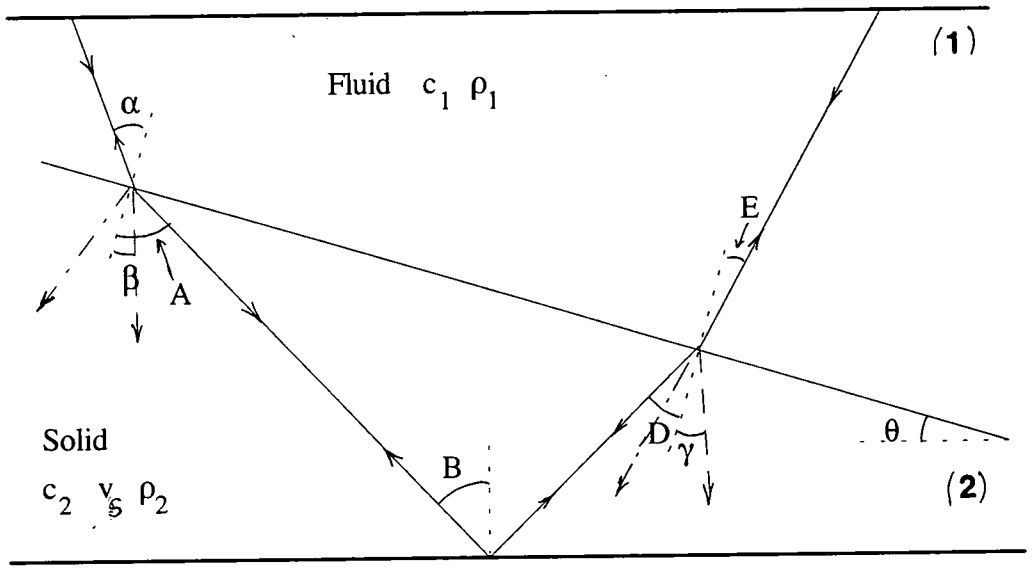

Figure 7.2: Simple two layer fluid/solid model (P-wave rays = ——; S-wave rays for forward path = — — —; S-wave for reversed path =— - — - -).

Since R_{22}^F and R_{22}^R are equal (the reflection coefficient is reversible), any difference in amplitude between the forward and reversed rays is due to the differences between T^F and T^R.

7.2.1. Simple case: a sloping fluid/solid boundary

In the simplest case, the upper layer is considered to be fluid with a P-wave velocity c_1 and a density ρ_1, while the lower layer is solid with a P-wave velocity c_2, S-wave velocity v_S and density ρ_2. The equations for downwards (T_{12}) and for upwards (T_{21}) transmission across the boundary are given below (Aki and Richards, 1980, Berkhout, 1987).

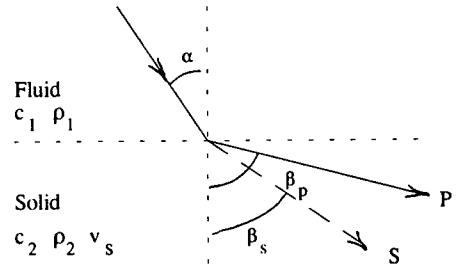

$$T_{12} = \frac{2B\rho_2 c_2 \cos\alpha}{A^+\rho_2 c_2 \cos\alpha + \rho_1 c_1 \cos\beta_p} \qquad 1.1$$

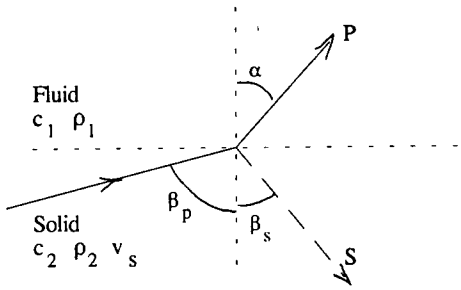

$$T_{21} = \frac{2B\rho_1 c_1 \cos\beta_p}{A^+\rho_2 c_2 \cos\alpha + \rho_1 c_1 \cos\beta_p}, \qquad 1.2$$

where $B = 1 - 2\sin^2\beta_s$ and $A^+ = (1-2\sin^2\beta_s)^2 + \left(4\frac{v_s}{c_2}\sin^2\beta_s\right)\cos\beta_p$.

The difference between T^F and T^R can be calculated for the simple model shown in Figure 7.2 as follows:

Equations 1.1 and 1.2 may be rewritten in terms of Z_α and Y_α where, for any angle α,

$Z_\alpha = 1-2\sin^2\alpha$ and $Y_\alpha = 4\frac{v_s}{c_2}\sin^2\alpha\cos\alpha$, giving

i) Forward ray

$$T^F = T_{12}^F T_{21}^F$$

$$T_{12}^{F} = \frac{2Z_{\beta}\rho_2 c_2 \cos\alpha}{\left(Z_{\beta}^2 + Y_{\beta}\cos A\right)\rho_2 c_2 \cos\alpha + \rho_1 c_1 \cos A}, \qquad 1.3$$

$$T_{21}^{F} = \frac{2Z_{\gamma}\rho_1 c_1 \cos D}{\left(Z_{\gamma}^2 + Y_{\gamma}\cos D\right)\rho_2 c_2 \cos E + \rho_1 c_1 \cos D}. \qquad 1.4$$

ii) Reversed ray

$$T^{R} = T_{12}^{R} T_{21}^{R}$$

$$T_{12}^{R} = \frac{2\,Z_{\gamma}\rho_2 c_2 \cos E}{\left(Z_{\gamma}^2 + Y_{\gamma}\cos D\right)\rho_2 c_2 \cos E + \rho_1 c_1 \cos D}, \qquad 1.5$$

$$T_{21}^{R} = \frac{2\,Z_{\beta}\rho_1 c_1 \cos A}{\left(Z_{\beta}^2 + Y_{\beta}\cos A\right)\rho_2 c_2 \cos\alpha + \rho_1 c_1 \cos A}. \qquad 1.6$$

combining equations 1.3, 1.4 and 1.5, 1.6 gives the ratio of T^F to T^R as

$$\boxed{\frac{T^F}{T^R} = \frac{T_{12}^F T_{21}^F}{T_{12}^R T_{21}^R} = \frac{\cos\alpha\,\cos D}{\cos A \cos E}} \qquad 1.7$$

Although density and velocity no longer appear in the equation, these variables control the angles at which the wave is refracted. Angles D, E and A are related to α and θ as follows:

$$\sin A = \frac{c_2}{c_1}\sin\alpha; \quad \sin E = \frac{c_1}{c_2}\sin D \text{ and } B = A - \theta; \quad B = D + \theta .$$

Therefore

$$\cos A = \left(1 - \sin^2 A\right)^{\frac{1}{2}} = \left(1 - \sin^2\left(\frac{c_2}{c_1}\sin\alpha\right)\right)^{\frac{1}{2}},$$

$$\cos D = \left(1 - \sin^2 D\right)^{\frac{1}{2}} = \left(1 - \sin^2\left(A - 2\theta\right)\right)^{\frac{1}{2}} = \left(1 - \sin^2\left(\sin^{-1}\left(\frac{c_2}{c_1}\sin\alpha\right) - 2\theta\right)\right)^{\frac{1}{2}},$$

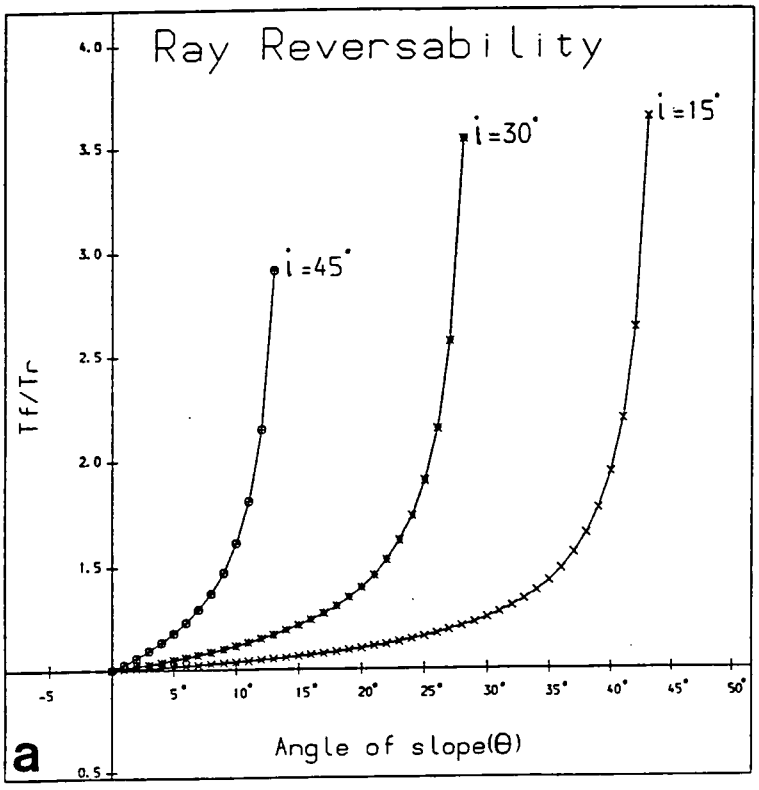

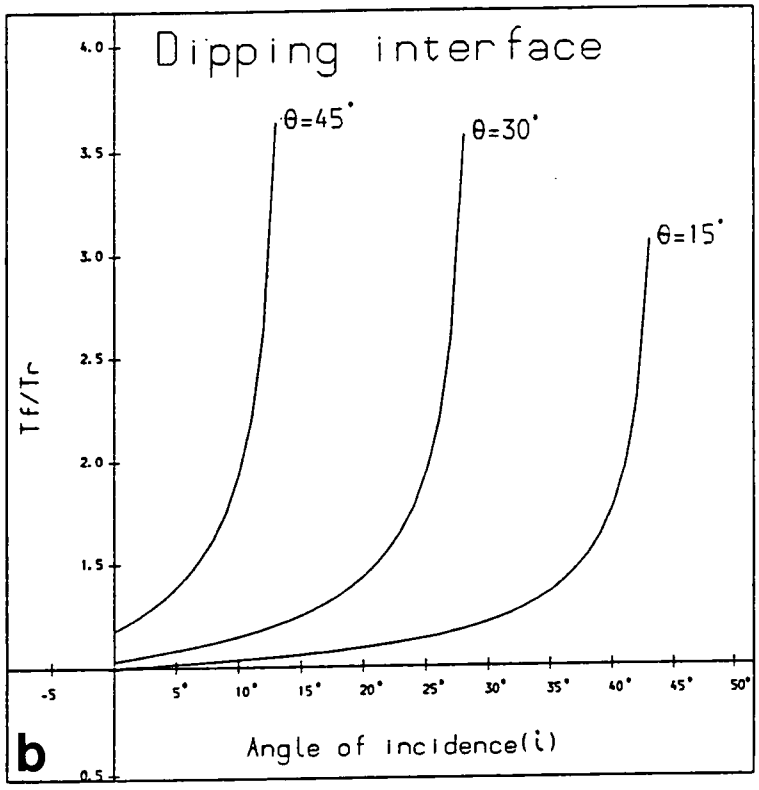

Figure 7.3. Variation of the ratio $T^F:T^R$ for a simple two layer fluid/solid model against **a)** increasing dip of the boundary (for different incident angles) and **b)** varying angle of incidence (for three different dips). V_{p1} = 6.0 km/s, V_{p2} = 7.0 km/s, ρ_1 = 2.4 g/cm^3 and ρ_2 = 3.0 g/cm^3 .

$$\cos E = \left(1 - \frac{c_1}{c_2}\sin^2 E\right)^{\frac{1}{2}} = \left(1 - \frac{c_1}{c_2}\sin^2\left(\sin^{-1}\left(\frac{c_2}{c_1}\sin\alpha\right)\right)\right)^{\frac{1}{2}}.$$

The angle of incidence of rays at the boundary between layer 1 and layer 2 (α) may be described in terms of the angle of incidence at the surface, i, and the dip of the boundary, θ; $\alpha = i + \theta$. The graphs in Figure 7.3 shows the variation of the ratio of T^F to T^R with angle of incidence i and dip of the boundary θ. For a horizontal boundary, $T^F = T^R$ for all angles of incidence. The ratio of T^F to T^R increases exponentially as it approaches the critical angle. As long as the angles of incidence of rays and the dips of boundaries within the model are moderate, the difference between T^F and T^R is small (for $i + \theta$ less than 45° the difference between T^F and T^R is less than 20%).

7.2.2 Laterally varying fluid

The ratio of T^F to T^R may be calculated in the same manner for a model where the structure beneath the shot differs from that beneath the receivers (Figure 7.4). For simplicity, the interfaces between layers are considered to be horizontal.

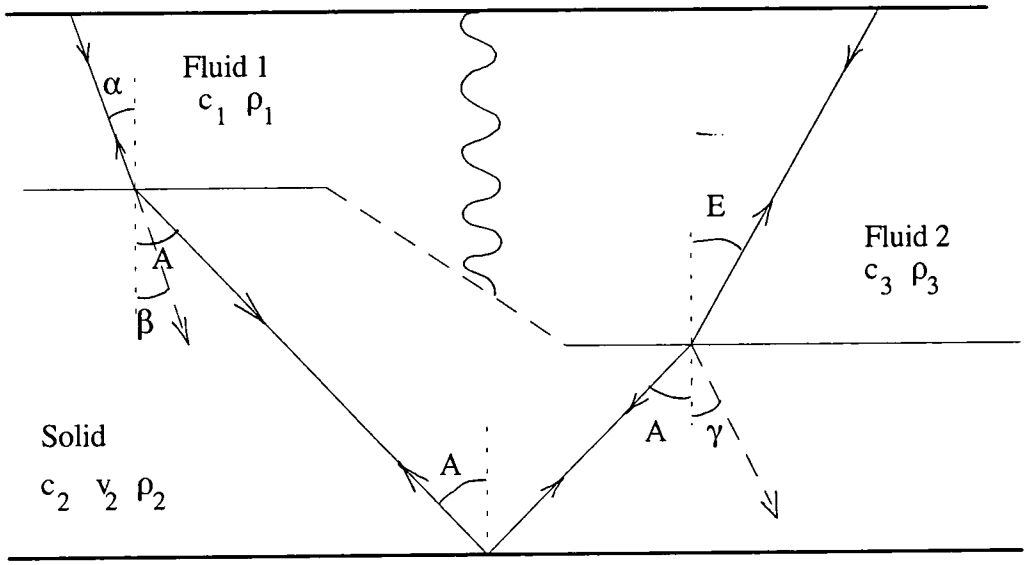

Figure 7.4: Two layer fluid/solid model with laterally varying upper medium. S-wave conversions are only shown for the forward raypath.

The difference in transmission coefficients are due to the different densities and velocities of fluid 1 and fluid 2. Using equations 1.1 and 1.2 for the raypath in Figure 7.4, the ratio of T^F to T^R becomes:

$$\frac{T^F}{T^R} = \frac{\rho_3 c_3 \cos\alpha}{\rho_1 c_1 \cos E} . \qquad 1.8$$

Again, the amplitude calculated along the ray in the forward direction differs from that in the reverse direction but differences are small where lateral velocity and density changes are small.

7.2.3. More complex cases

Similar calculations may be made for the more complex cases of a solid-solid boundary and for the effect of conversion from P to S at boundaries. In each case T^F differs from T^R but the difference is small where boundaries are roughly horizontal and where lateral velocity and density changes are small.

Examples of the amplitudes for reversed raypaths through a simple model and through a more complex model calculated using the BEAM87 raytracing package are shown in Figure 7.5 (the amplitudes are plotted on a logarithmic scale). For both models, the difference between forward and reversed amplitude for the unconverted P phase is small. Differences in amplitude are greater for the converted phases.

The error of assuming that amplitude calculations along rays are reversible is large where there are major differences in the structure beneath the shot and receiver. For the BABEL data, the shots were in a water layer and the receivers on land. The P-wave velocities beneath the shots and beneath the receiver were very different. This gives a boundary with a strong velocity contrast which rays between shot and receiver cross only once.

Figure 7.6 shows the forward and reverse amplitudes for a simple model of a water layer overlying gradational crust. The depth of the water layer has been exaggerated to make it visible in the ray diagram. The water velocity and the near surface P-wave velocity are the same as in the models for line 6 which will be discussed in the next chapter (the water velocity is 1.448 km/s and the velocity increases from 5.950 to 7.000 km/s in layer 2). The difference in the amplitudes calculated forwards and backwards along the raypath is large.

The major difference in the forward and reverse amplitudes shown in Figure 7.6 is a result of the way that the initial amplitude of the rays is chosen in the BEAM87 program. The ray-centred amplitude is unit at the source. The initial energy along the ray is different for the forward and reversed rays since the sources for them are located in media with different densities and velocities. This scaling is constant as long as all rays are from a single shot and terminate in the same layer. The angle at which the rays

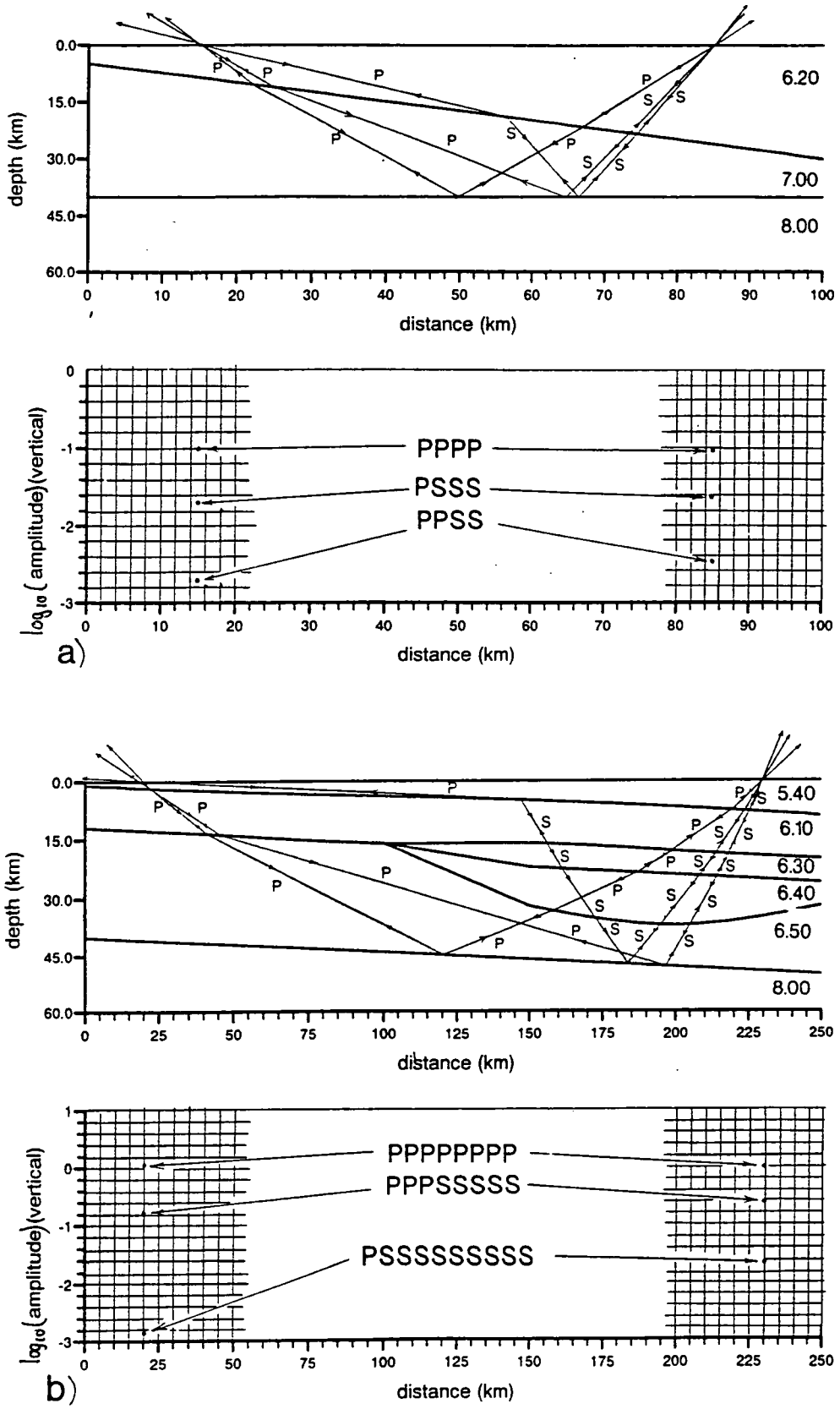

Figure 7.5 Examples of amplitudes calculated in different directions along the same raypath for **a)** a simple two layer model and **b)** a more complex model where structures differ greatly from one end of the line to the other. Layers have constant velocity (P-wave velocities in km/s are given in the Figure, S-wave velocities are calculated from $V_s = V_p/\sqrt{3}$).

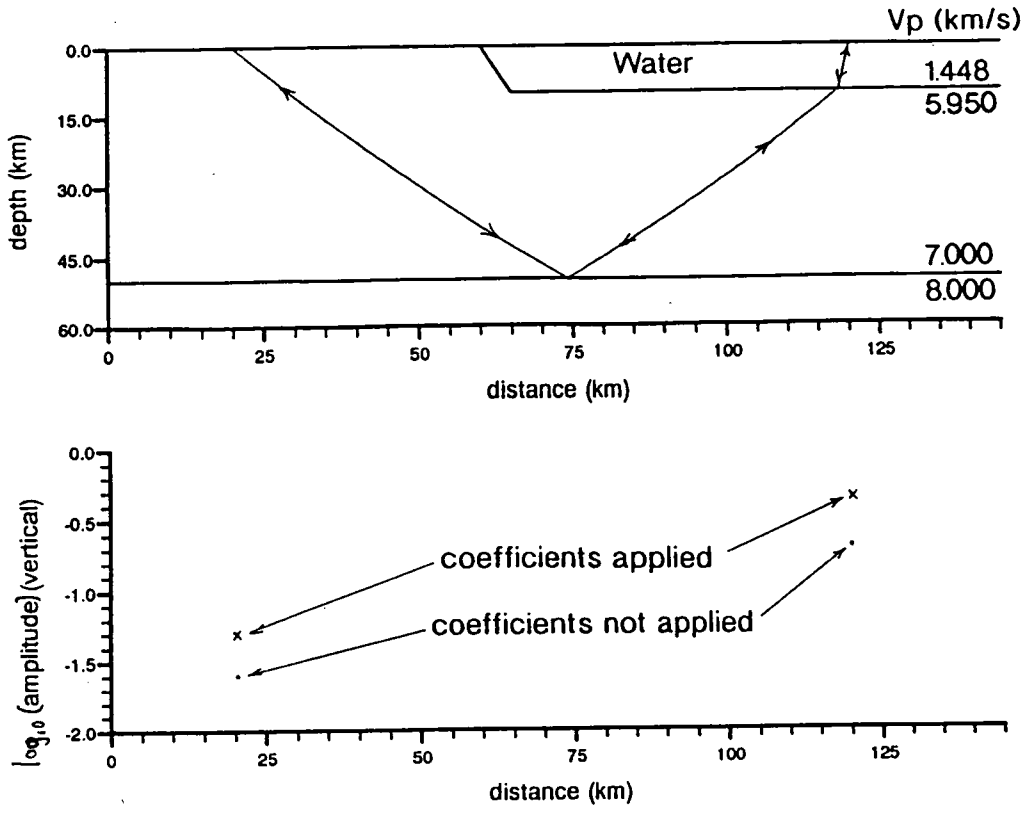

Figure 7.6 Amplitude calculations for a water layer overlying part of a gradational crust (the water depth has been exaggerated for clarity).

intersect the crust/water interface also effects the ratio of T^F to T^R. Figure 7.7 shows the variation of the ratio of T^F to T^R with incident angle θ for the velocity contrast across the water/crust boundary in the model in Figure 7.6. The variation with angle is minor.

A pair of amplitudes are plotted at each end of the rays in Figure 7.6. When the receivers are on the Earth's surface, the amplitude of the arrival depends not only on the incident wave but also on the reflected and converted waves which are generated at the free surface. BEAM87 contains an option for applying the coefficients of conversion at the endpoint of the ray which take this into account. The effect of applying this option is shown in Figure 7.8 for a diving ray and for a reflection. The coefficients of conversion decrease the amplitude of the arrivals by a uniform amount for all offsets but the scaling is different for the two arrivals. Applying these coefficients makes a major difference to the amplitude content of the synthetic seismogram.

When modelling, rays are traced in the opposite direction to the experimental arrangement and the coefficients of conversion are applied at the shots rather than at the receiver. This does not seem to make a noticeable difference to the calculated amplitudes (Figure 7.6), but further work is needed to understand the limitations of the

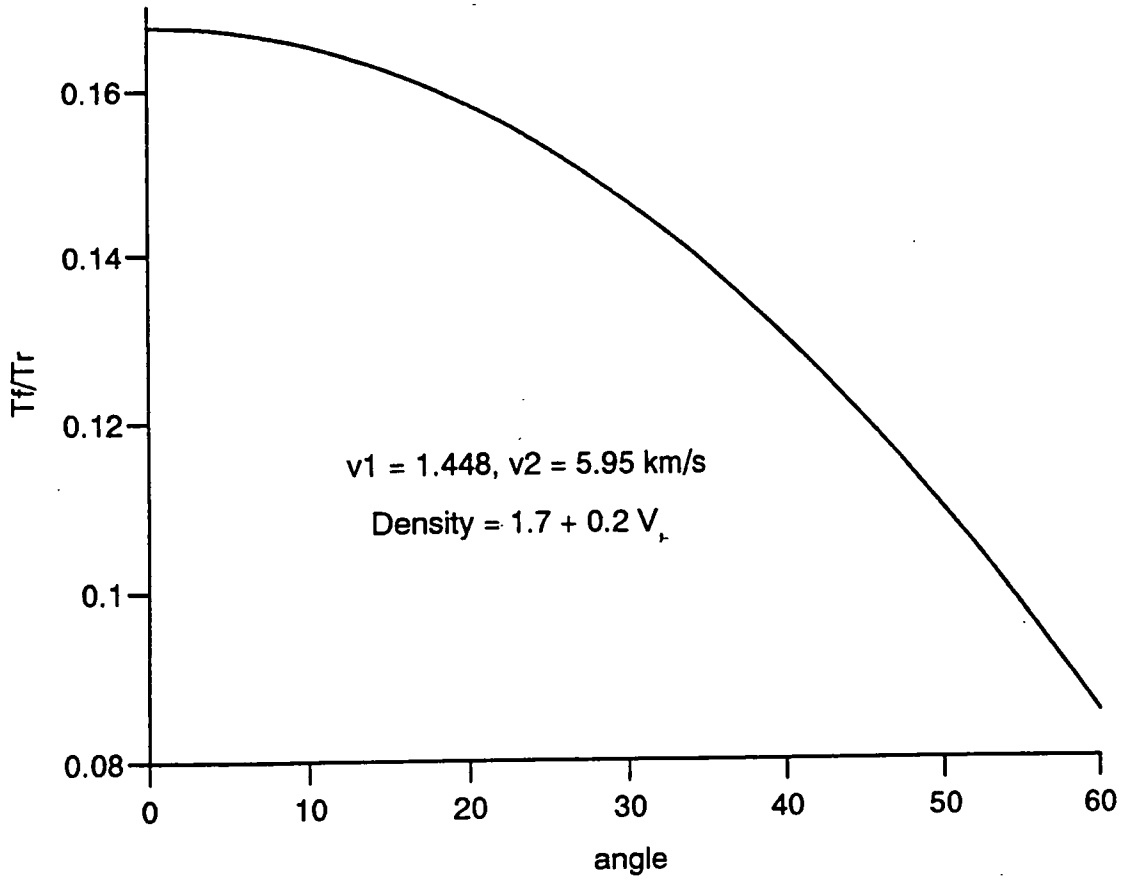

Figure 7.7. Variation of the ratio of $T^F : T^R$ with incident angle (at the boundary) for the velocity contrasts in the model in Figure 7.6.[1]

amplitude content of synthetic sections and the errors in assuming that amplitude calculations along raypaths are reversible.

As a result of the problems described above, and the fact that the amplitude content of the line 6 experimental data was complicated by interference with the previous shot, the amplitudes of the synthetic seismograms generated for line 6 have only been compared to the experimental data in the most general terms (chapter VIII, section 8.6).

[1] The values of $T^F:T^R$ are calculated from the equation derived for a laterally varying fluid (equation 1.8). The ratio of $T^F:T^R$ is not unity at zero angle as it is still assumed that the downgoing and upgoing rays pass through different media (Figure 7.4).

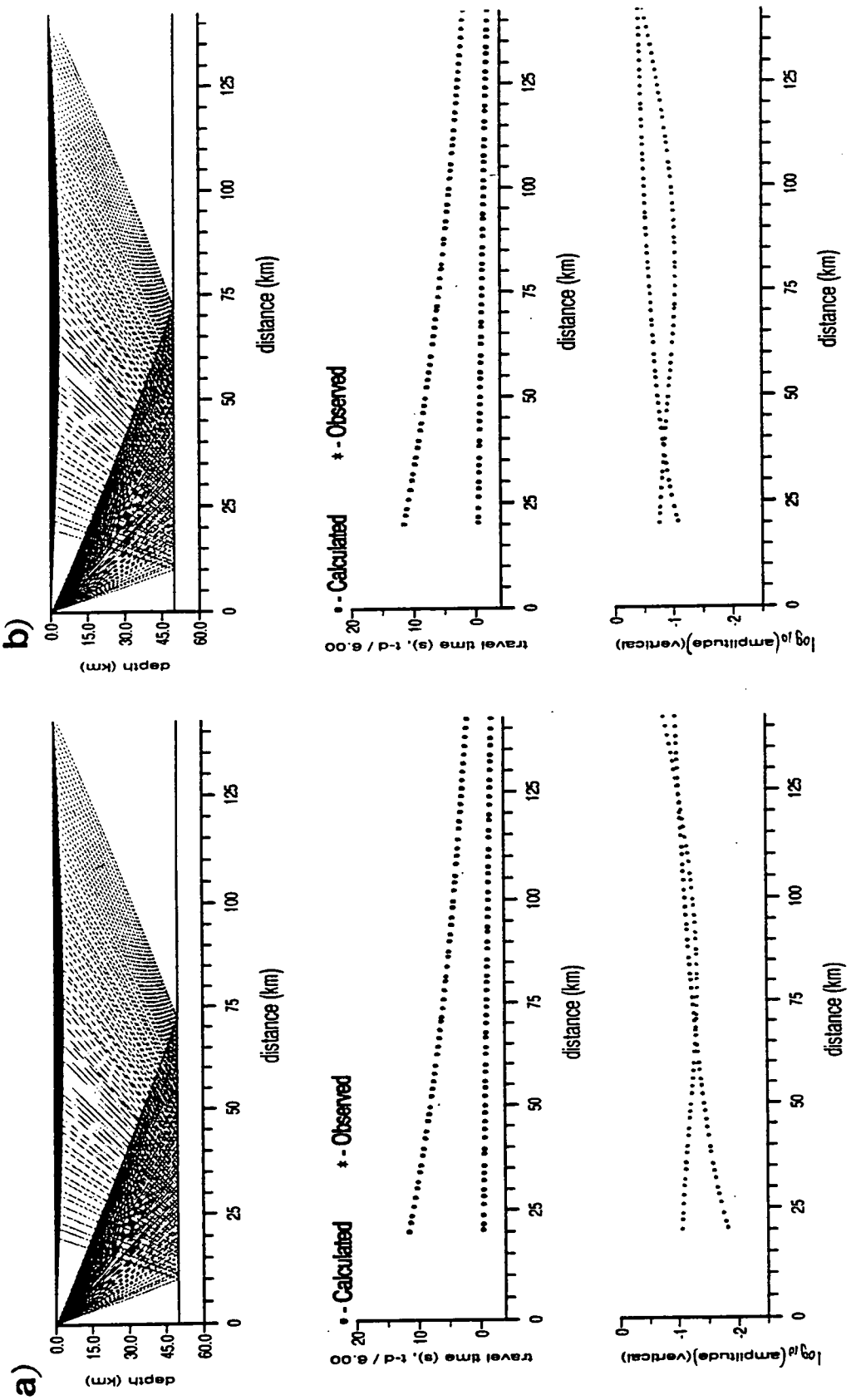

Figure 7.8. Effect of applying the coefficients of conversion to the amplitudes calculated using BEAM87 for a simple reflection and diving ray. **a)** coefficients not applied, **b)** coefficients applied.

7.3 Problems with generalised ray theory

There are three main problems of raytracing which the Gaussian beam method attempts to overcome.

i) The high-frequency approximation.

In asymptotic ray theory the seismic wavefield is represented in terms of angular frequency (ω). A high-frequency approximation is used in which terms of order ω^{-2} and higher are ignored and the wave field is represented only in terms of order ω^{-1}. This approximation is applicable only for smooth media where the dimensions of inhomogenities are larger than the dominant wavelength of the seismic waves. In terms of velocity $\underline{v}$:

$$\lambda >> \frac{\underline{v}}{|\nabla \underline{v}|}.$$

This restriction cannot be eliminated by any modification to the high-frequency asymptotic method and so it is necessary to assume that the medium is sufficiently smooth.

ii) Irregularities of the ray field.

The method fails at points where the ray field is not regular i.e. at the critical region, caustics, etc. (a caustic is a singularity caused by diving rays crossing back on themselves). Modifications (local asymptotes) may be made to the ray theory for these regions but in laterally varying media these singular regions are often complex. Shadow zones from ray methods are sharp since there is no decay of amplitude at the edges of the zone.

iii) Irregularities of the model.

The amplitudes of the high-frequency seismic waves calculated by the ray method are very sensitive to angular features of the model (such as edges of interfaces) and to fictitious oscillations in the velocity field caused by the methods of approximating velocity within the model.

7.4 The Gaussian beam method

The Gaussian beam method used in BEAM87 partially overcomes the second and third of these problems by using a beam of finite width rather than an infinitely thin

ray. A beam yields considerably better results in complex singular regions and is much less sensitive to minor details of the model (Červený, 1985a). The high frequency approximation problem is avoided by ensuring the velocity field in the model is smooth. The BEAM87 package provides a routine, B87_SMOOTH (Figure 7.1), which produces a smooth velocity field for laterally varying velocities. This routine is designed for use with the bicubic spline or piece-wise bilinear interpolation method described in section 7.4.1 Since the line 6 velocities were calculated using linear 7.4.1 ? interpolation, B87_SMOOTH was not used.

The BEAM87 routines shown in Figure 7.1 are considered individually below. These routines had to be updated from the original Fortran66 to UNIX compatible Fortran77 and from PLOTSYS to UNIRAS graphics. The routines were also modified to allow normal-incidence raytracing (coincident shots and receivers) using the same routines as for wide-angle modelling. The routines are described below in terms of a single shot and a series of receivers since this is the direction in which rays are traced in the program (i.e. the opposite direction to the experimental arrangement of BABEL).

7.4.1 B87_RTNI (raytracing)

In the raytracing routine (B87_RT), rays are traced through a model for specified elementary waves by solving a series of differential equations (the term 'elementary wave' is used for all the arrivals from a particular layer). These equations yield the ray trajectory, slowness vectors and travel-times (Červený *et al.*, 1977 and, more generally, Červený, 1985b). Amplitudes are calculated along the raypaths, correcting for geometrical spreading and for reflection and transmission at interfaces.

The model, velocity structure and elementary waves are defined by the user in the input file (*Input.mod*, Figure 7.1). Models consist of a series of roughly horizontal layers separated by interfaces. Each interface is specified by a series of coordinates (a maximum of 30 points per interface) and the coordinates of intermediate points are found by cubic spline interpolation. Interfaces can be real or fictitious or fictitious in parts (a fictitious interface gives rise to no reflection even though there may be a velocity step across the boundary). Interfaces may coincide and have sharp corner points. This makes it possible to model vanishing layers, fractures and isolated bodies.

Velocities within the model may be approximated in one of three ways: by bicubic spline interpolation, by piece-wise bilinear interpolation or by linear interpolation between isovelocity interfaces. The first two methods use a grid of velocities which cover each layer and allow 2D variations in velocity. The bicubic spline method sometimes produces small oscillations in velocity structure, even after

being smoothed, while piece-wise bilinear interpolation has been found to give rise to spurious arrivals and unstable results (Lewis, 1986, West, 1990). In the linear interpolation approximation, the interfaces are treated as velocity isoclines with the velocity in each layer defined above and below the bounding interfaces. This is the easiest method of defining velocity in the BEAM87, as well as the most stable, and was used for the line 6 models in this work.

Rays may be specified individually (including multiple and converted waves) or all direct and reflected rays may be modelled automatically. The source can lie anywhere within the model (with the exception of layers of zero thickness) and the receivers lie along the surface. Rays are traced from the source to the receivers by one of three methods: initial value raytracing, two-point raytracing or interval raytracing.

i) Initial value raytracing.

In this method, limiting angles are defined and rays are shot from the source at angles between these bounds and all rays which terminate at the surface are recorded. The method is fast and stable and it's accuracy can easily be controlled but it is not guaranteed to produce a sufficient density of ray endpoints in the vicinity of the receivers for the Gaussian beam method to work*.

ii) Two point raytracing.

Two-point raytracing produces a fully regular system of equally spaced endpoints and gives very stable results with the Gaussian beam summation. In this method, a regularly spaced array of receivers is defined by the user. Rays terminating at these receivers are found to a specified accuracy by iterative initial value raytracing. A range of initial angles can be chosen; the narrower the range, the lower the computing time. This method is recommended for raytracing to particular grid points and was used for the BABEL line 6 models presented in this thesis. As the program was run on the SUN computers it was possible to use a full 180° range of initial angles and still have a fairly short computation time.

iii) Interval raytracing

The third method, interval raytracing, is a modification of initial value raytracing. The receiver array is separated into segments with the condition that at least one ray must fall within each of these segments. This method uses initial value

---

* The wavefield at a receiver is found from the summation of the Gaussian beams centred on rays which have endpoints in the vicinity of that receiver. If the density of rays is low, then there are few beams and the results from the summation are poor.

raytracing except when this condition is not fulfilled, in which case two point raytracing is used. Interval raytracing does not produce a succession of endpoints that is monotonic with respect to the initial angle of the ray at the source. An auxiliary program, B87_SORT, is provided to re-order the endpoint records to the format required for B87_GBNI. This routine is not needed in the case of initial value or two-point raytracing.

Once the raypaths have been determined, the vertical and radial components of amplitude are computed for all of the elementary waves using standard high frequency formulae. In the case of S waves, the transverse component is also computed. All of these amplitudes are reduced so as to have unit ray-centred vertical amplitude at the point source. Slight absorption may be considered, in which case the Q values may be related to velocity or be constant for individual layers. A global absorption factor is calculated as the time integral of Q^{-1} along the raypath. For simplicity, no absorption was considered for the line 6 synthetics.

B87_RTNI is a modification of B87_RT (originally converted for use with UNIX by Dr C. Prescott). B87_RTNI provides the option of calculating normal-incidence travel-times and amplitudes using the same raytracing routines as for the wide-angle modelling. The shot and receiver are considered as coincident at the shot locations. The input file (*Input.mod,* Figure 7.1) is the same as for the wide-angle models except that the variable RMIN refers to the first shot position and RSTEP to the distance between shots. BRD(1) and BRD(2) are the limits of the normal-incidence section and should be specified (BEAM87 documentation, V. Červený, available with the program code). Rays are traced using two-point raytracing for specified elementary waves or for all possible waves. The method is considerably slower than wide-angle raytracing if calculations are made for all angles at each source position. If the source is considered as a tuned airgun array and the interfaces in the model are roughly horizontal, then it is reasonable to reduce the aperture of energy propagation from 0°-180° to 45°-135° to reduce the computation time. If the normal incidence option is not chosen then B87_RTNI behaves exactly as B87_RT.

7.4.2 B87_RPNI (Plotting of rays, travel-times and amplitudes)

B87_RPNI is a routine written to plot the output from B87_RTNI. Ray diagrams, travel-times and/or amplitudes may be plotted for each of the components (transverse, radial and vertical) of the elementary waves specified in *Input.obs*. Travel-times measured from the experimental data may be plotted in the same frame as the modelled travel-times for iterative modelling. Experimental travel-times are entered in

non-reduced form and are reduced in the same way as the calculated travel-times, using the reduction velocity given in *Input.obs*. Experimental amplitudes can be included and compared to those calculated from the model (if no experimental amplitudes are to be included, then the decadic logarithms of amplitude are plotted rather than the true amplitude). Amplitudes were not modelled in this way for line 6 because of the problems of interference in the experimental data and because of the errors in the theoretical amplitudes which result from tracing rays in the reversed direction (section 7.2.3).

For complex models there may be a large number of elementary waves. This makes it very difficult to identify which amplitudes correspond to which travel-time branch. To overcome this problem the original routine B87_RAYPL (converted for use with UNIRAS by Dr C. Prescott), was rewritten with the option of plotting each elementary wave in a different colour. The travel-time plots were also altered so that calculated travel-times could be plotted either as dots or as lines (which are thinner and may be matched with greater accuracy to the experimental values) or as a combination of the two. The routine was also altered to plot the results of normal incidence raytracing.

7.4.3 B87_GBNI (Gaussian beam method)

In B87_GBNI, the frequency response at a specified series of receivers along the Earth's surface is calculated by the summation of Gaussian beams (or by raytracing methods for situations where the Gaussian beam method is not appropriate). The routine includes various source radiation patterns and dissipation effects which may be altered without having to repeat the time-consuming raytracing.

In the Gaussian beam method, the wavefield concentrated close to a ray is found by solving the parabolic wave equation (Schrodinger's equation). The solutions decrease exponentially with the square of distance from the centre ray, giving a Gaussian profile - hence the name Gaussian beams (Figure 7.9). Asymptotic ray theory depends on two terms which vary along the raypath; one related to amplitude which varies gradually and a more rapidly varying phase related term. In the Gaussian beam modification, the phase term is altered so that the phase delay now varies perpendicular to the central ray, as does the Gaussian amplitude profile (Kennett and Harding, 1985). The response at a particular receiver is found by a weighted summation of the contributions from a set of overlapping beams (Figure 7.9). To get a reasonable result from this method, several overlapping beams are required; the more beams, the better the result, which is why a sufficient density of rays is desired from the raytracing (Červený, 1983).

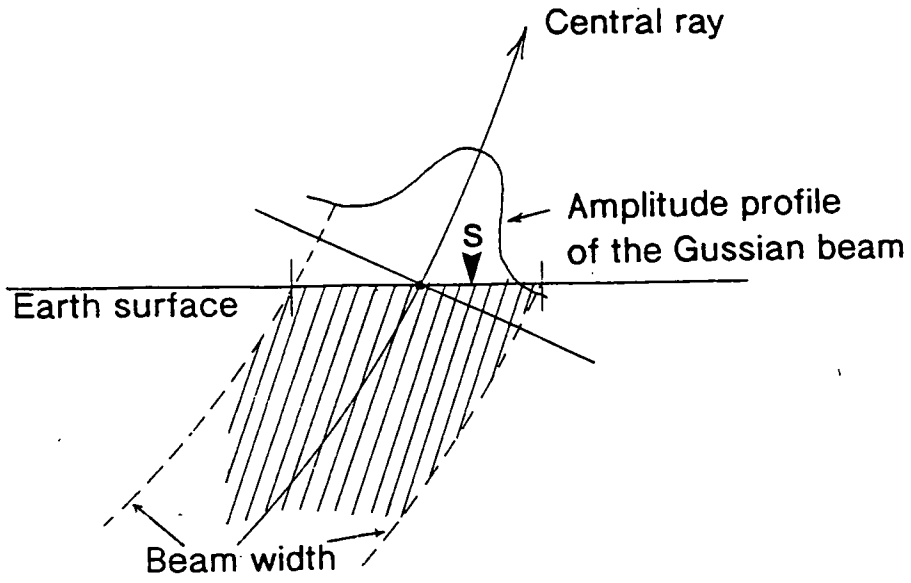

Figure 7.9. Amplitude profile of a Gaussian beam and the surface region (shaded) within which a receiver (s) will obtain a contribution from this beam (after Weber, 1988).

As well as the number of beams, the final seismogram depends on two initial parameters chosen to describe the beams. These define the width of the beam and the curvature of the phase front and vary along the ray due to spreading, reflection and transmission. The initial choice of these parameters is very important (Červený, 1985a, Weber, 1988).

BEAM87 uses the paraxial ray approximation in which the travel-time along the central ray of the beam is real but becomes a complex variable away from this ray. The Gaussian beam can be considered as a bundle of rays which are defined by a complex valued travel-time field (Červený, 1985a). The Gaussian beams in BEAM87 are specified by the real and imaginary parts of the second derivative of the travel-time field (M) perpendicular to the ray, chosen either at the end or the beginning of the ray:

$$M = M_{re} + \mathrm{i}M_{im} \ .$$

The real part of M, (M_{re}) is related to the curvature of the phase front k, of the Gaussian beam by

$$k = v \times M_{re}.$$

where v is the velocity. The imaginary part of M, (M_{im}) is related to the half width of the beam, L

$$L = \sqrt{\frac{1}{\pi \times M_{im}}}.$$

The possible initial values for M_{re} and M_{im} are given in the documentation for the BEAM87 package (V. Červeny). All of the choices may fail in the case of strong lateral inhomogenities and generate spurious arrivals. The most stable selection of parameters is with the variable MBEAM=1 and this has been used for all of the line 6 synthetic sections. For MBEAM=1, M_{re} is automatically calculated so that the second derivative of the time-travel field along the Earth's surface is zero in the vicinity of the endpoint of the ray (the effective plane phase front choice). M_{im} is found from:

$$M_{im} = sh3 \times \left| M_{re} - \frac{p2}{q2} \right|$$

where *sh*3 is defined by the user in the input file *Input.gb* (Figure 7.1) and *p*2 and *q*2 are elements of the ray propagation matrix. The method is most stable where sh3 = 1 which minimises the error due to the beams not extending infinitely (this setting was used for the line 6 synthetic sections). The beams are truncated at distances from the central ray where the amplitude falls below *AMAX* × *ACC*, where *AMAX* is the amplitude at the ray and *ACC* is a parameter specified by the user (the default value for *ACC* used for the line 6 synthetics is 0.01). A limit is also applied by the user on the maximum travel-time above which beams are not included in the summation process.

The radiation pattern of the source for P- and S-waves may either be read into the program or computed. The line 6 synthetics have been generated using a radiation pattern that is isotropic, with unit amplitude at unit distance from the source (the amplitude does not depend on the initial angle). The media may be perfectly elastic or a dissipation model may be used. The dissipation model greatly increases the computing time and was not used to calculate the amplitudes for the line 6 synthetics. B87_GBNI also contains an option for plotting amplitude verses distance curves for various frequencies.

B87_GBNI was altered to allow normal-incidence synthetics to be generated. Each shotpoint is considered separately. If there is only one shot and one receiver then there is usually only one ray for each elementary wave and Gaussian beam summation cannot be used (this could be overcome by defining sufficient receivers in the immediate vicinity of the shotpoint to provide a dense coverage of rays but for modelling line 6, a single receiver was defined and the Gaussian beam method was not used). Frequency responses for the normal-incidence data are calculated by the same method as for SEIS83 and other non-modified ART packages. Calculations are performed for all sources in the file B87_rtni.lu2. The input file for normal-incidence modelling (coincident source and receiver) is basically the same as for the single-shot multiple-receiver case. The variable MEP (number of receivers) should be set to 1, RMIN is the first shot position (as in B87_RTNI) and RSTEP is the source spacing.

As there is only one receiver position for each shot, no plots of amplitude versus distance are generated.

7.4.4 B87_SYNTNI (Synthetic seismogram generation)

B87_SYNTNI generates synthetic seismograms which are normalised so that the maximum amplitude of each trace = 1. For each receiver, the synthetic seismogram consists of the sum of all of the seismograms for all elementary waves whose rays reach the station within a specified time window. There are three methods of performing the summation: by the direct summation of wave packets, by convolution or by a frequency domain approach. The first of these methods is time consuming and the second is not very efficient when considering complex travel-times as in the Gaussian beam method (Červený, 1985a).

B87_SYNTNI uses a frequency domain approach where the frequency responses of elementary waves are combined to give a single frequency response. The frequency response is multiplied by the spectrum of the source-time function (Červený, 1985b) and the synthetic seismogram is found by an inverse Fourier transformation. This approach is rapid because of the use of the Fast Fourier algorithm and also allows the inclusion of frequency related effects such as dissipation, thin subsurface layering, etc.

The input signal used in BEAM87 for calculating the synthetic seismograms may be entered via a table of points in the input file, *Input.synt,* or one of the source-time functions included in the program may be used (these are listed in the documentation included with the BEAM87 code). For the line 6 synthetics, the far-field source signature supplied by PRAKLA-SEISMOS (Figure 4.3) was digitised and used as the input signal. This will be referred to as the Mintrop signal. The frequency content of the Mintrop signal is very different to that of the experimental wide-angle and normal-incidence data which show distinct peaks. These are thought to arise as the result of resonance of the water layer (section 6.1.1). The frequency content of the experimental data varies with shotpoint (as a result of the variation in water depth). It was decided to use the Mintrop signal as a constant source signature and to include peg-leg multiples in the water layer of the model to make the frequency content close to that of the experimental data.

Since the Gaussian beam method is a high-frequency approximation, the very low frequencies must be filtered out. A double cosine filter (similar to the Hanning window filter used for the experimental data) is included in B87_SYNTNI and was applied to the Mintrop signal. The limits used for this filter were similar to those of the

bandpass filter applied to most of the experimental data: a low cutoff of 2.5-3 Hz and a high cutoff of 25-30 Hz (the filter for the Z2A data differed from this, section 6.1.1).

Synthetic seismograms may be computed for the vertical, transverse and radial components. These may be used with the routine B87_PMPLOT to plot particle motion diagrams. The normal-incidence synthetic sections are calculated in the same way as for single shots. B87_SYNTNI has been modified to read in the source information for each new seismogram and to write this out to the file b87_synt_(component).lu5. The input file, *Input.synt*, is the same as for the single shot case.

7.4.5 Synthetic seismogram plotting

The synthetic seismic sections are plotted in the same way as the experimental data using the program DAZZLE, described in the previous chapter. Since DAZZLE plots SEGYi data, a new routine, B87_TORNI, was written to convert from the output in b87_synt_(comp).lu5 to SEGYi. Both normal incidence and wide-angle synthetic sections may be converted and B87_TORNI also provides the option of reducing wide-angle data with a specified reduction velocity.

CHAPTER VIII

RESULTS FROM RAYTRACING - A TRADITIONAL APPROACH

8.1 Introduction

As the resolution of wide-angle data has increased, interpretation has become increasingly complex. In low resolution data, such as the FENNOLORA data (with a station spacing of about 3.5 km), few arrivals can be identified and the nature of these seem constant along the travel-time branches. In the BABEL data (with a shot spacing of 0.0625 km), many more arrivals are seen, with rapid changes in amplitude along what appear to be continuous arrivals. When selecting arrivals from the experimental BABEL data, continuous arrivals were picked across the section, where possible, and the small scale amplitude and phase changes were ignored (section 6.1.6). Arrivals with unusually high apparent velocity were also seen throughout the datasets.

Interpretation methods for wide-angle data have traditionally been based on the hypothesis that the earth's crust consists of a series of roughly horizontal, laterally continuous layers, the properties of which change with depth. The line 6 wide-angle data was modelled with the BEAM87 package described in the previous chapter. This was written to model a horizontally layered crust. As modelling progressed, it became clear that models of this sort could not explain the complexity of the BABEL wide-angle data nor the patchy reflectivity of the normal-incidence data. It was decided to continue modelling line 6 using a 'traditional' approach (ignoring the rapid changes in amplitude and phase) to find the gross structure of the crust and then to investigate smaller scale crustal structures which could give rise to the rapid variations in amplitude (these alternative structures will be discussed in chapter X).

In traditional raytracing, wide-angle arrivals are modelled as a series of reflections and diving rays in a layered crust (the underlying mantle may also be layered). The line 6 modelling differed from the traditional approach in two important respects;

1. The normal-incidence data was used to constrain the model by raytracing normal-incidence arrivals through the model and comparing their two-way travel-times to the reflections seen on the normal-incidence data.
2. The arrivals with high apparent velocity seen in the experimental wide-angle data were modelled as 'diffraction-type' arrivals.

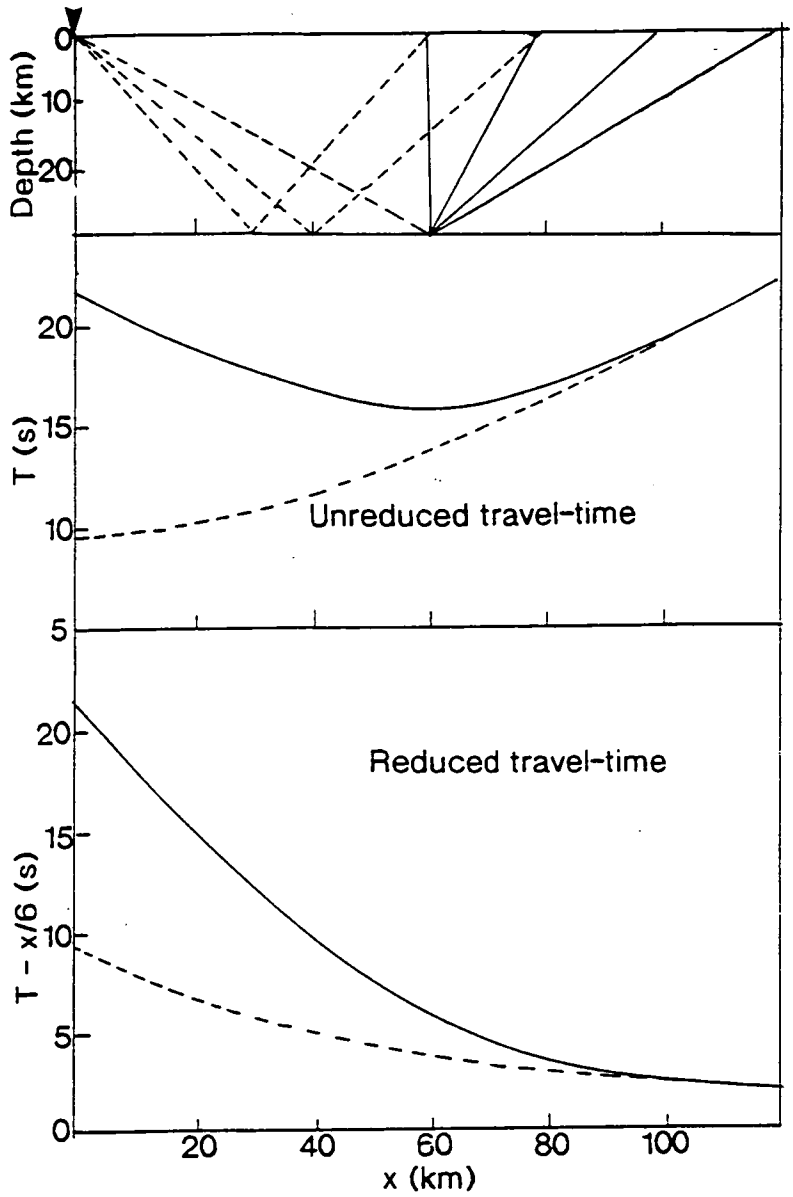

Figure 8.1. Reduced and unreduced travel-time curves for a reflection and for a diffraction.

8.2 Diffraction-type arrivals

The high apparent velocity arrivals seen in the BABEL data were similar in character and reduced travel-time to arrivals which had been observed and modelled in the 1987 MOBIL project (Matthews, 1989, West, 1990, Blundell *et al.*, 1991). It was suggested that these arrivals in the MOBIL data were some form of diffraction. The reduced and unreduced travel-time curves for a diffraction and a reflection are shown in Figure 8.1. In the unreduced plot, the apparent velocity of the diffraction is infinite at the offset of the diffractor. In the reduced plot, the travel-time curve of the

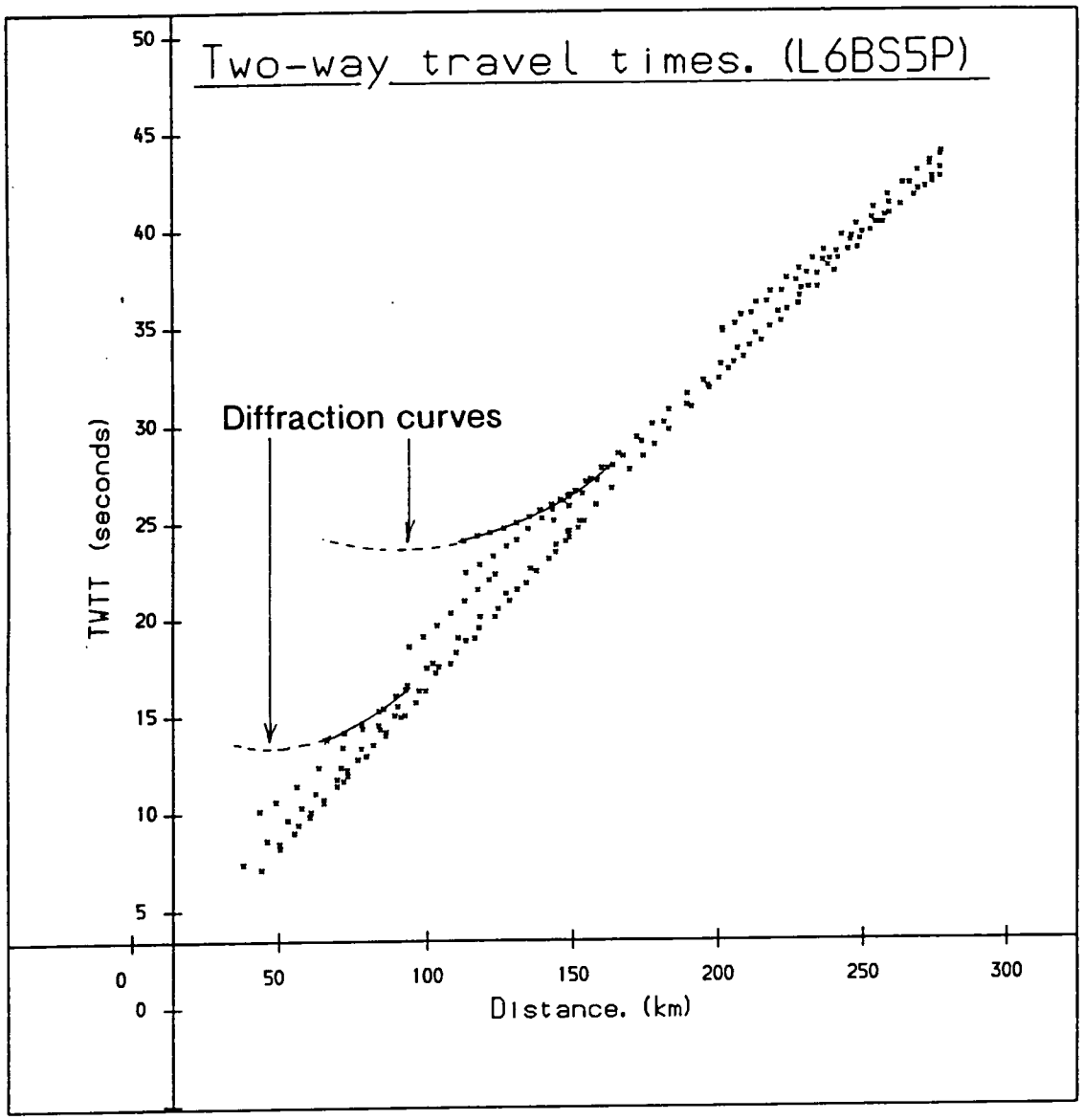

Figure 8.2. Unreduced travel-time curves for the digitised arrivals from station BS5P.

diffraction and the reflection are similar but the diffraction curve steepens more rapidly than the reflection.

It is difficult to pick 'diffractions' from experimental data for two main reasons. Firstly, the 'diffraction' usually branches off from another arrival (often a reflection) and the amplitude of the diffraction falls off rapidly as the two arrivals diverge (highest amplitudes are seen where the two intersect). Secondly, the reduced travel-time curve of the diffraction is steep, with an anomalously high apparent velocity, and is often ignored as an artefact. The near-horizontal segments of the reduced travel-time curves are easier to pick because they appear more coherent against the background noise. As

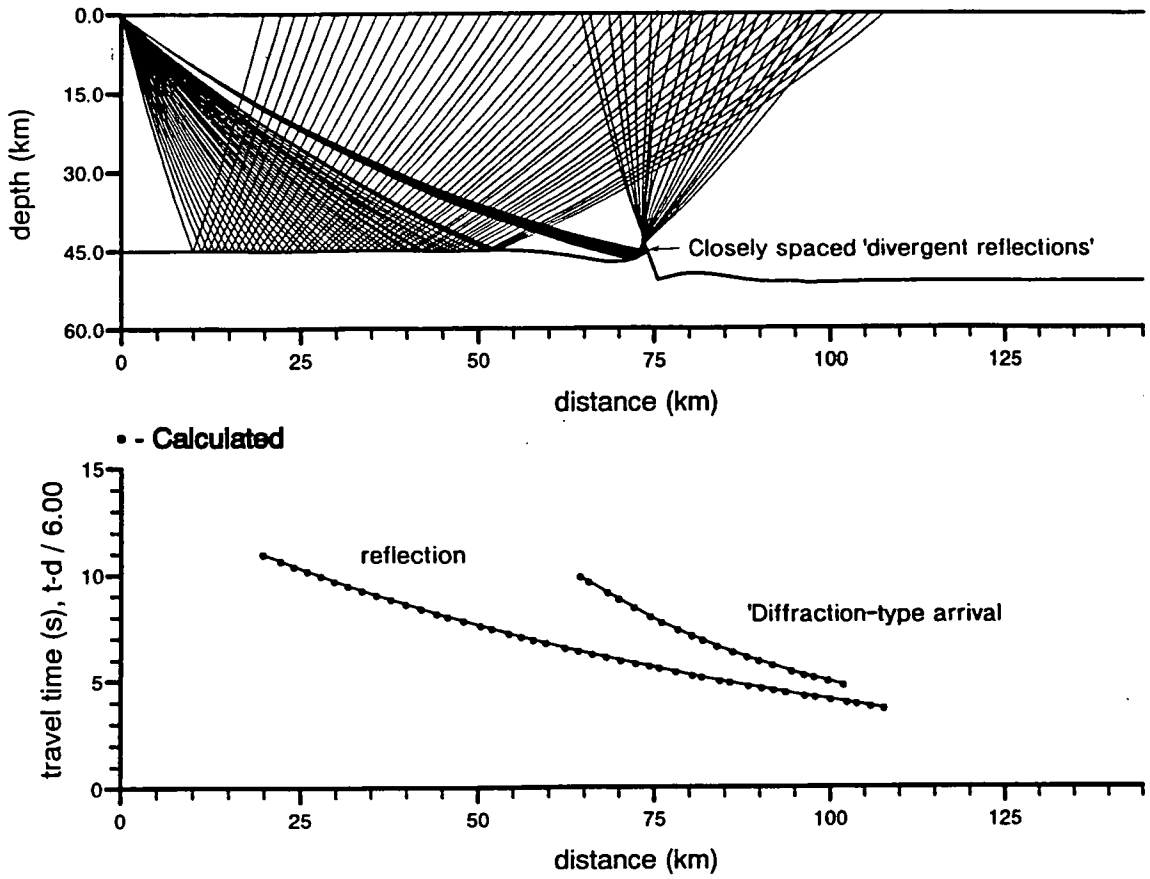

Figure 8.3. An example of a raytraced divergent reflection.

the arrival becomes steeper and interferes with other arrivals it becomes less easy to pick.

Figure 8.2 shows an unreduced plot of the digitised arrivals picked from the reduced data section from BABEL station BS5P. Two of the arrivals show a higher curvature than the others. These curves are an approximate fit to theoretical curves for diffractions (solid lines in Figure 8.2) generated by diffractors at a distance (measured from BS5P) of about 90 and 55 km respectively. The locations of these diffractors are only approximate as it has not been possible to pick the minimum of the diffraction curves from the experimental data due to the problems of interference and coherency discussed above.

Ray tracing cannot model true point diffractions but 'diffraction type' arrivals may be modelled as divergent reflections from a tightly curved part of a boundary (Figure 8.3). The reduced travel-time curve of the 'diffraction-type' arrivals seen in the experimental data approximates to this kind of divergent reflection as well as to a diffraction. Tight curvature of reflecting boundaries may be caused by faults cutting reflecting interfaces (similar to the roll over of reflectors into faults that is seen shallow seismics) and by the limbs of folds, to give but two examples.

It is not easy to model tightly curved boundaries with BEAM87 as it is necessary to closely constrain the shape of the interface to prevent the cubic spline approximation from generating wild oscillations of the boundaries (only 30 pts are allowed for defining each interface). The shapes of features included in the line 6 model to generate divergent reflections are determined mainly by the restrictions of the modelling package.

On closer inspection of the BABEL wide-angle data for line 6, other possible diffraction arrivals can be seen throughout the section (this will be discussed further in the next chapter). Only the major diffraction-type arrivals that were originally picked from the BS5P and Z2A data have been modelled in the line 6 model. The way in which these diffractions were modelled will be described later in this chapter.

8.3 Modelling BABEL line 6

The BEAM87 raytracing package can be used for synthetic seismogram modelling or to model travel-times and amplitudes which have been measured from experimental data. Modelling travel-times requires little computation time but only uses part of the available information. Modelling synthetic seismograms allows amplitudes to be modelled as well as travel-times but generating synthetic seismograms with BEAM87 is a time consuming process and not really suitable for iterative modelling.

There are also other problems with synthetic seismogram modelling. Rays are traced in the opposite direction to the experimental situation because BEAM87 was designed to model single shots and multiple receivers (the resulting errors in amplitudes were discussed in section 7.2). The synthetic sections do not show the complexity of the experimental data (for example, the rapid changes in phase across the section). These small scale amplitude and phase variations were ignored when the arrivals were picked from the experimental data and are not included in the model. The experimental data is also affected by interference with arrivals from the previous shot. This makes it difficult to compare the synthetic and experimental sections directly.

The model for BABEL line 6 presented in this chapter was produced by iterative travel-time modelling. Beginning with a model consisting of a series of horizontal constant-velocity layers, theoretical travel-times were calculated and compared with those measured from the experimental data. Velocity gradients and boundary depths were then altered iteratively to improve the match between the calculated and observed travel-times. As further data sets were included in the model and the density of crossing rays increased, the model became more constrained.

The first model for line 6 was derived from the P-wave and S-wave data from the PDAS station BS5P. This model was reversed using the Geostore data from Z2A at the northern end of the profile*. These are the closest online stations to the north and south of line 6. The boundaries from the reversed model and the S-wave data from the transverse component recorded at BS5P were used to find the P- to S- wave velocity ratio. The model was constrained using the normal-incidence data from line 6.

During the iterative modelling, a variety of models were tried and discarded for each boundary and the experimental data was re-interpreted as ideas about the possible crustal structure developed. The results from each model were compared with the experimental travel-times from stations Z2A and BS5P and to the normal-incidence data and the simplest model (with reasonable crustal velocities and thicknesses) was chosen. Plots of calculated amplitude generated by B87_RTNI were used as a rough check on the amplitude of each modelled arrival. Synthetic seismograms were calculated at various stages during the modelling and were compared to the data sections.

The details of travel-time modelling for the different wide-angle datasets and the normal-incidence data are given below. The final model for BABEL line 6 is described in section 8.5 and synthetic seismograms from this model are compared to the experimental data for stations BS5P, Z2A and to the normal incidence data in section 8.6. As a check on the accuracy of the final model, travel-times were calculated for stations BS5, Z5A and Z1A (Figure 4.4) and compared to the experimental data recorded at these stations. The results from this are described in section 8.7.

8.4 Travel-time modelling

All of the BEAM87 models generated for line 6 shared the following features: The velocity structure in the model was defined by linear interpolation between isovelocity interfaces. These interfaces may also be reflectors. Fictitious interfaces (from which no reflection is generated) have not been used where there is a velocity step between layers, except for the mantle reflectors (section 8.5.6). No absorption was considered and densities (ρ) in the individual layers were calculated automatically using the BEAM87 option (BEAM87 manual, Červený) where density is approximated from the P-wave velocity of the layer using the relation:

$$\rho = 1.7 + 0.2 v_p .$$

* The PDAS data was converted in to SEGYi format within a year of the survey being shot, the Geostore data took a further year.

Two-point ray tracing was used for a grid of 400 points and with 20 iterations for each ray (the maximum values permitted in BEAM87). The accuracy of the endpoint of the ray was set to within ±0.025 km of the receiver position and the accuracy of the integration of the ray tracing system was 0.0002 (see the BEAM87 manual for further details of these parameters).

The end points of the rays for line 6 terminate in the water layer. Coefficients of conversion may be applied at the endpoint of the ray unless the surface layer is liquid. Since applying the coefficients of conversions makes a major difference to the amplitudes in synthetic sections (section 7.2), the water layer was defined in the BEAM87 model as a solid layer with a P-wave velocity equal to that of water. When modelling the S-wave data, the rays within this layer where explicitly defined as P rather than S. In the experimental situation, S-waves are generated by conversion at the sea floor; in the model the rays are traced from receiver to shot and the ray within the water layer forms the last segment of the raypath.

All distances in the models were measured from station BS5P, as this was the first station to be modelled.

8.4.1 Reversed model: P-wave data from BS5P and Z2A

The initial model for line 6 was derived from the vertical component P-wave data from a single station at the southern end of the line. Structure within the model was therefore limited to the southern section; the layers to the north through which no rays passed were left as horizontal. This model was improved by incorporating the S-wave data from the transverse component recorded at BS5P. In BEAM87, S-wave layer velocities may be calculated from the P-wave layer velocities using the ratio of P-wave to S-wave velocity (v_p/v_s) which is specified for each layer by the user. Boundary positions and v_p/v_s ratios within the model were altered to give the best fit to both the P-wave and the S-wave experimental travel times.

Crustal structure for the northern part of the line was found by modelling the data from station Z2A, while ensuring that the changes in the model did not affect the fit of the BS5P data. Where this was not possible, the BS5P data was remodelled. As well as the Z2A and BS5P data, S-wave and normal-incidence data were used to produce the final model for line 6 (sections 8.4.2 and 8.4.3); this model is shown in Figure 8.4. Ray diagrams and reduced travel-time fits at BS5P and Z2A are shown in Figure 8.5a to f for the different arrivals from the final model.

The rays in Figure 8.5 are plotted at 10 km intervals for clarity (a spacing of 2 km or less was used during modelling). Offsets in the model are measured from BS5P. As a result of the way that station offsets are defined in BEAM87, it was not possible

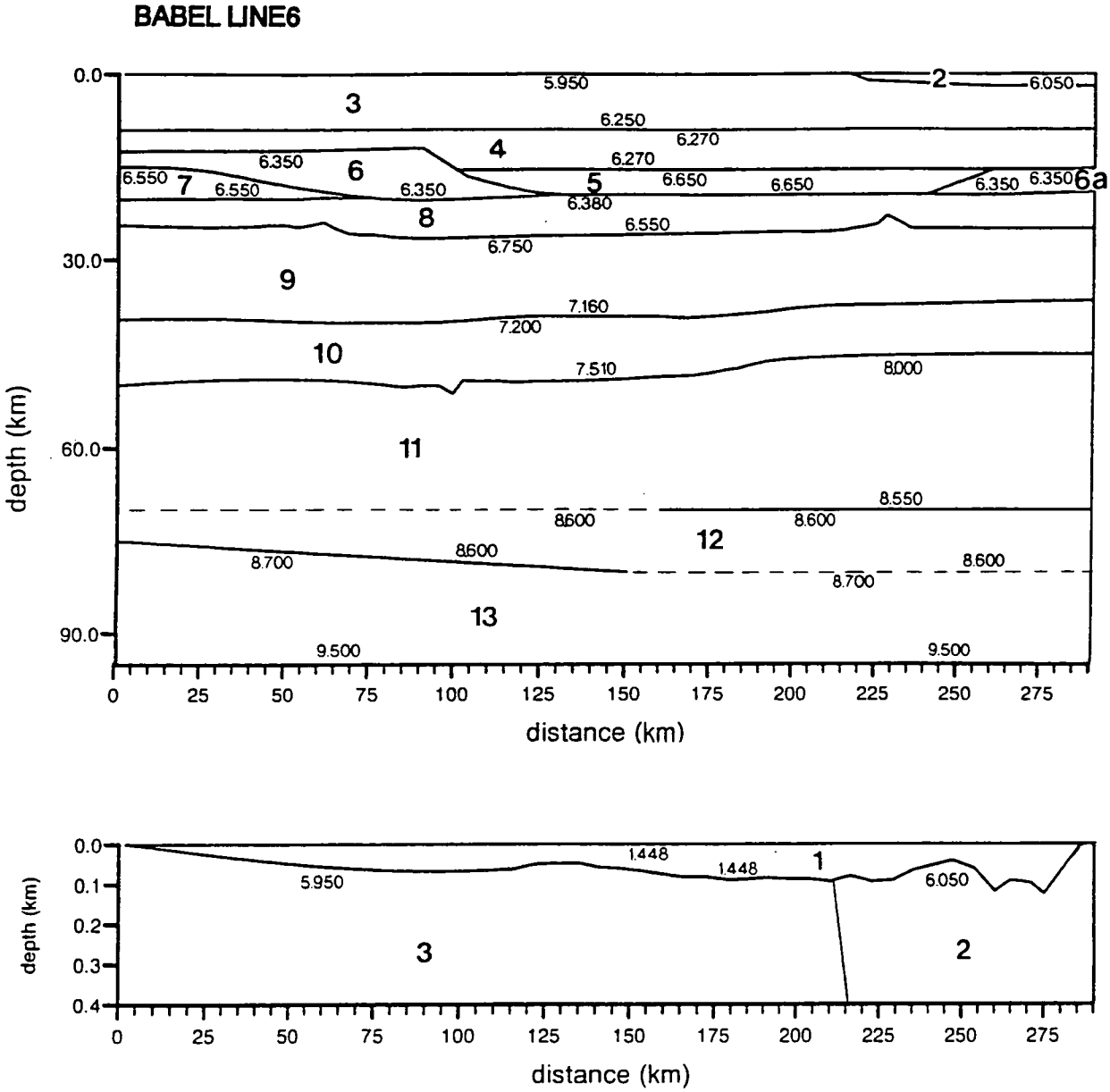

Figure 8.4. BABEL line 6 final model. Layers are numbered 1 to 13. Other numbers give the P-wave velocities above and below the interfaces. Dotted lines mark the portions of interfaces which are fictitious (there is a velocity step across these boundaries but no reflections are seen). An expanded section of the upper 400 m of the model showing the water layer 1 is given below the main model.

to define a minimum offset for the endpoints of rays from station Z2A (i.e. to define the distance from Z2A to the northern end of line 6). Rays from Z2A are traced to endpoints from zero offset outwards. The offset between BS5P and Z2A at the opposite end of the line is 287.065 km.

8.4.2 S-wave modelling

The S-waves arrivals from the transverse component recorded at station BS5P were modelled to find the S-wave velocity in each of the layers. For each layer, the v_p/v_s ratio was adjusted to find the best fit to the digitised S-wave arrivals, while keeping the same boundary positions as in the reversed P-wave model.

The results of this modelling are shown in Figure 8.6. Each elementary wave is plotted in a different colour. The fit to the experimental data is poorer than for the P-wave arrivals from the reversed model. The method used to model the S-wave arrivals assumes that the v_p/v_s ratio is constant within the layers and that the S-wave arrivals are sensitive to the same structures as the P-waves. The poor fit of the later arrivals suggests that the situation is more complex. Altering the original model, found from BS5P P-wave and S-wave data, to include the Z2A data from the far end of the line has degraded the best fit of the modelled S-wave arrivals to the experimental data.

8.4.3 Normal-incidence data

The two-way travel times (twtt) for normal-incidence arrivals from the line 6 models were calculated using the modified BEAM87 package at various stages during the modelling. In the lower crust, it was found that the normal-incidence reflections from the wide-angle model often coincided with the boundaries between the reflective and non-reflective crust in the normal-incidence data, although the reflections from the model were more extensive. The boundaries between these patches were therefore used as a guide to the position of the reflecting interfaces in the line 6 model.

Figure 8.7 shows the vertical two-way travel times (twtt) calculated by ray tracing through the line 6 model, overlaid on the experimental normal-incidence data*. Distances are measured from the southern end of line 6. The arrivals from the model are generally continuous along the length of the line while the normal-incidence data

---

* Unfortunately, the only available small paper copy of the normal incidence data was a migrated section and so the data section in Figure 8.7 has been migrated with a constant velocity of 6.5 km/s while the travel-times have not (Durham did not receiver a SEGY tape of the normal-incidence final stack until late in this project and there has not been time to play this data out).

Figure 8.5: Ray diagrams and travel-time fits for stations BS5P and Z2A. Rays for BS5P (southern end) are given in the upper part of each figure and those from Z2A (northern end of the line) are given in the lower part. For clarity, the endpoints of the rays are spaced at 10 km interval. All distances are measured from BS5P. The raytraced arrivals for the following layers are shown:

a) layers 1, 2, 3 and 4;

b) layers 5, 6 and 7;

c) layer 8;

d) layer 9;

e) layer 10 ('Moho');

f) layers 11 and 12.

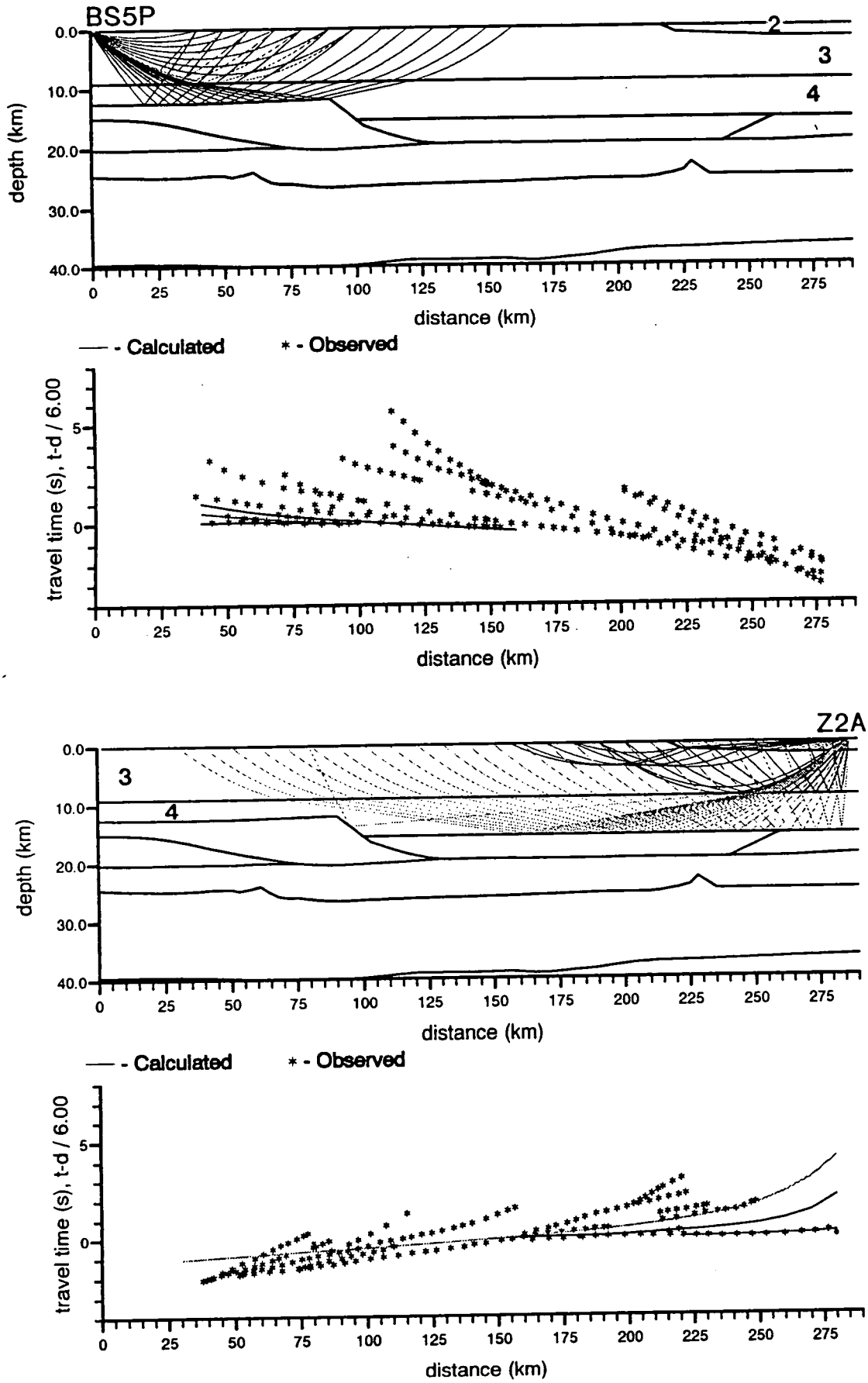
BS5P
2
3
4
depth (km)
0.0
10.0
20.0
30.0
40.0
0
25
50
75
100
125
150
175
200
225
250
275
distance (km)
— - Calculated
* - Observed
travel time (s), t-d / 6.00
5
0
distance (km)
Z2A
3
4
depth (km)
distance (km)
— - Calculated
* - Observed
travel time (s), t-d / 6.00
distance (km)

a

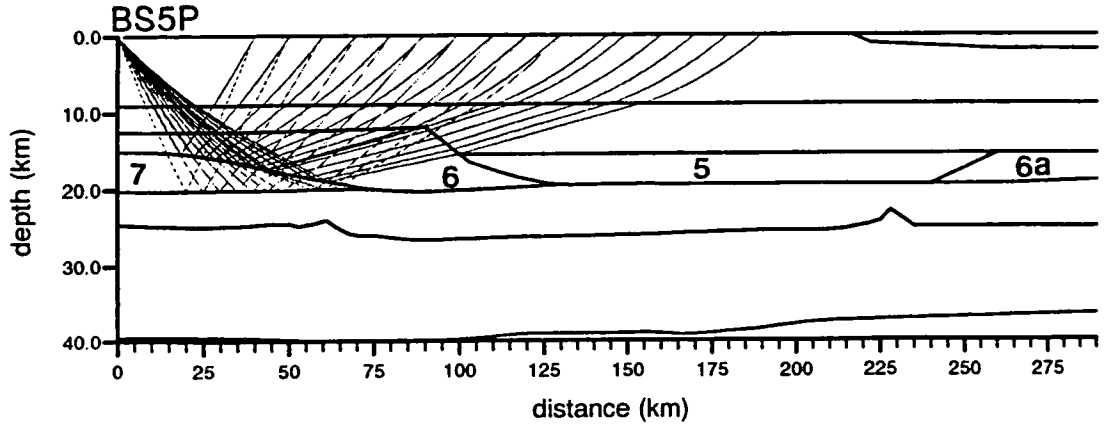
BS5P
depth (km)
0.0
10.0
20.0
30.0
40.0
7
6
5
6a
0
25
50
75
100
125
150
175
200
225
250
275
distance (km)

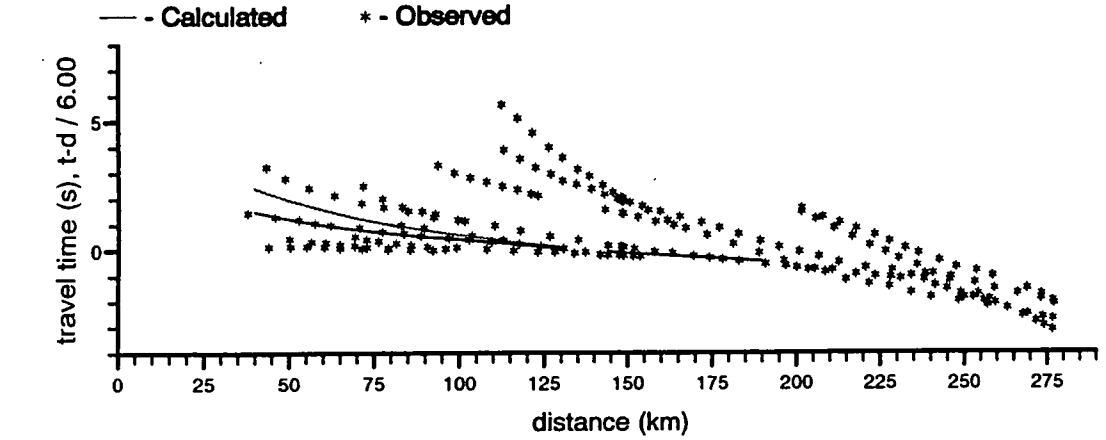
— - Calculated
* - Observed
travel time (s), t-d / 6.00
5
0
0
25
50
75
100
125
150
175
200
225
250
275
distance (km)

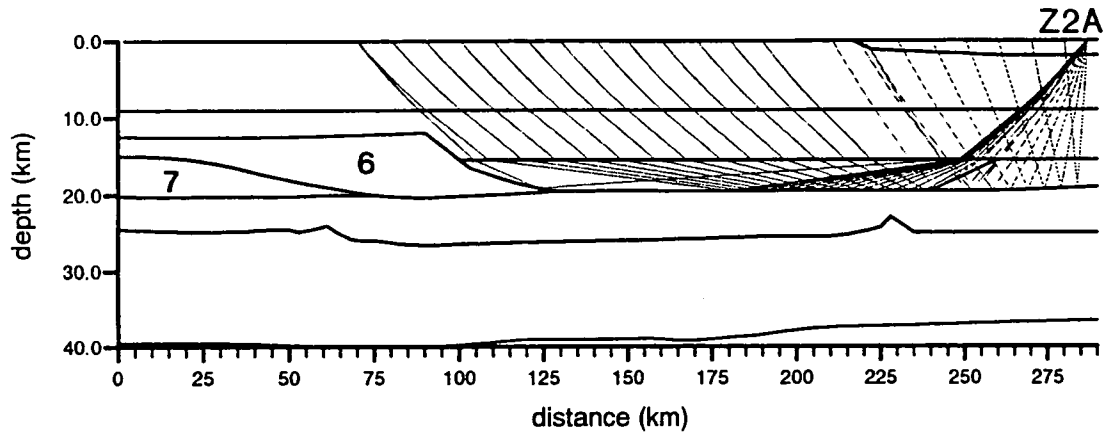
Z2A
depth (km)
0.0
10.0
20.0
30.0
40.0
6
7
0
25
50
75
100
125
150
175
200
225
250
275
distance (km)

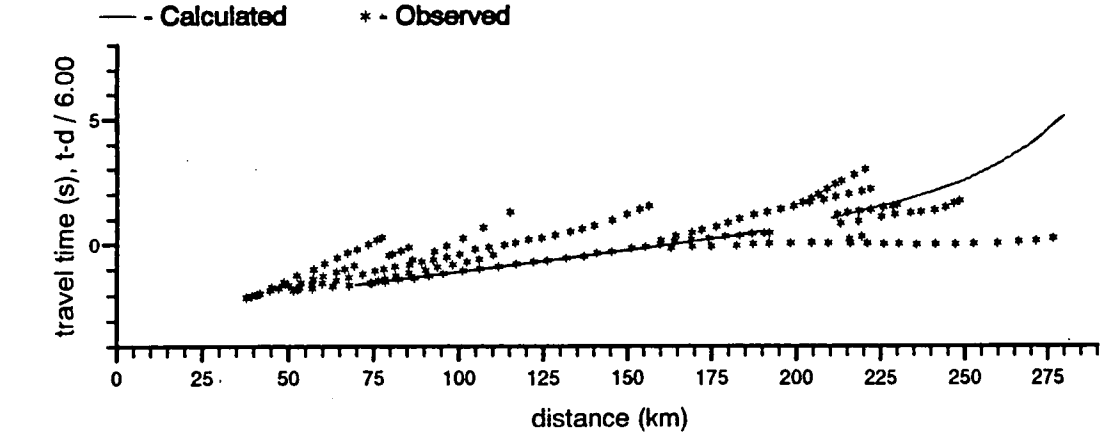
— - Calculated
* - Observed
travel time (s), t-d / 6.00
5
0
0
25
50
75
100
125
150
175
200
225
250
275
distance (km)

b

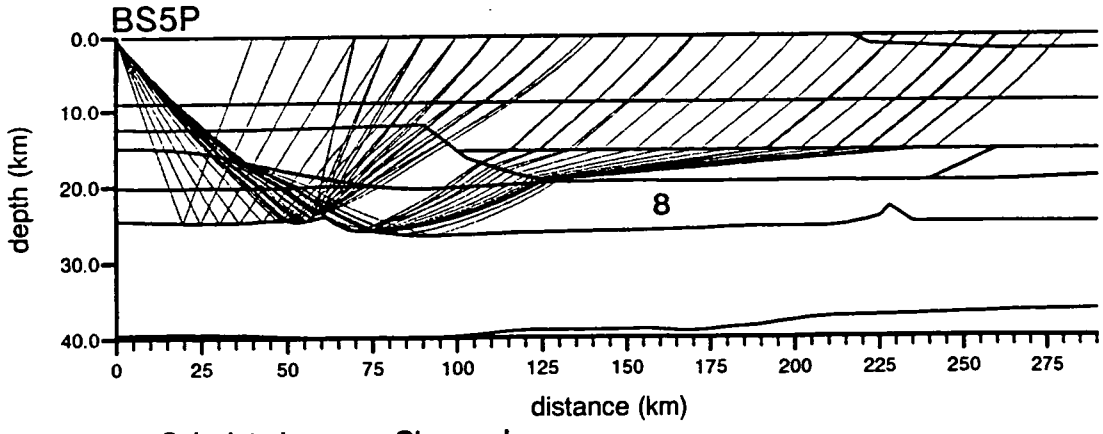
BS5P
depth (km)
0.0
10.0
20.0
30.0
40.0
8
0
25
50
75
100
125
150
175
200
225
250
275
distance (km)

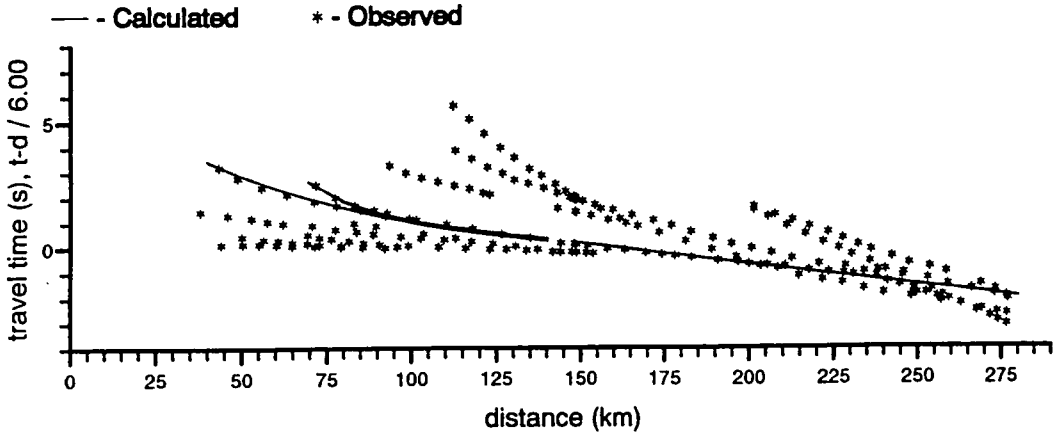
— - Calculated
* - Observed
travel time (s), t-d / 6.00
5
0
0
25
50
75
100
125
150
175
200
225
250
275
distance (km)

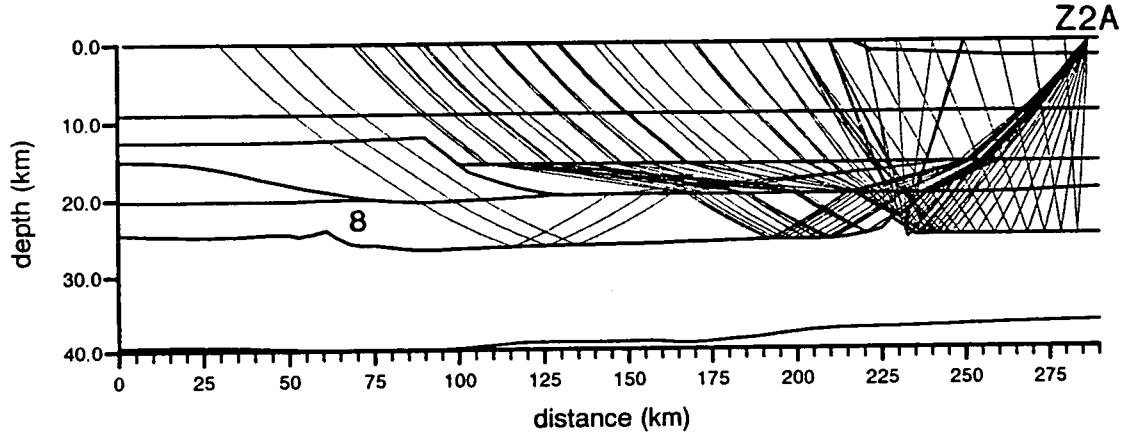
Z2A
depth (km)
0.0
10.0
20.0
30.0
40.0
8
0
25
50
75
100
125
150
175
200
225
250
275
distance (km)

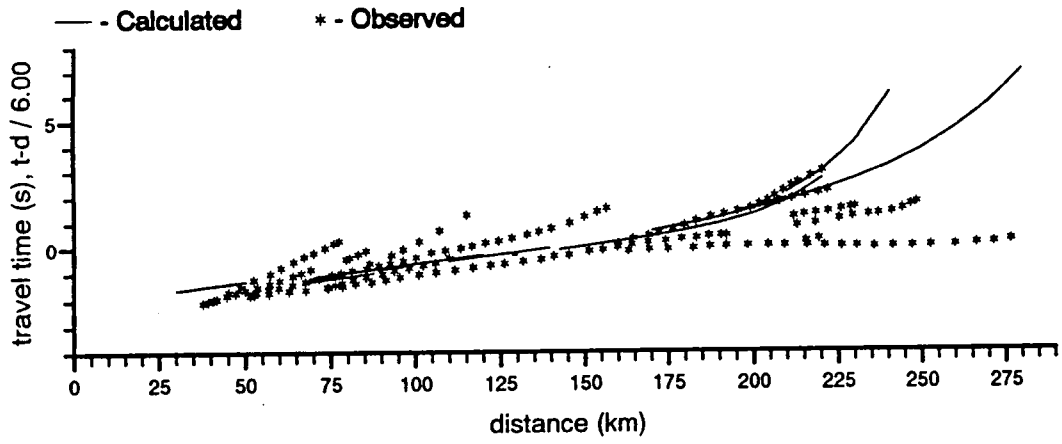
— - Calculated
* - Observed
travel time (s), t-d / 6.00
5
0
0
25
50
75
100
125
150
175
200
225
250
275
distance (km)

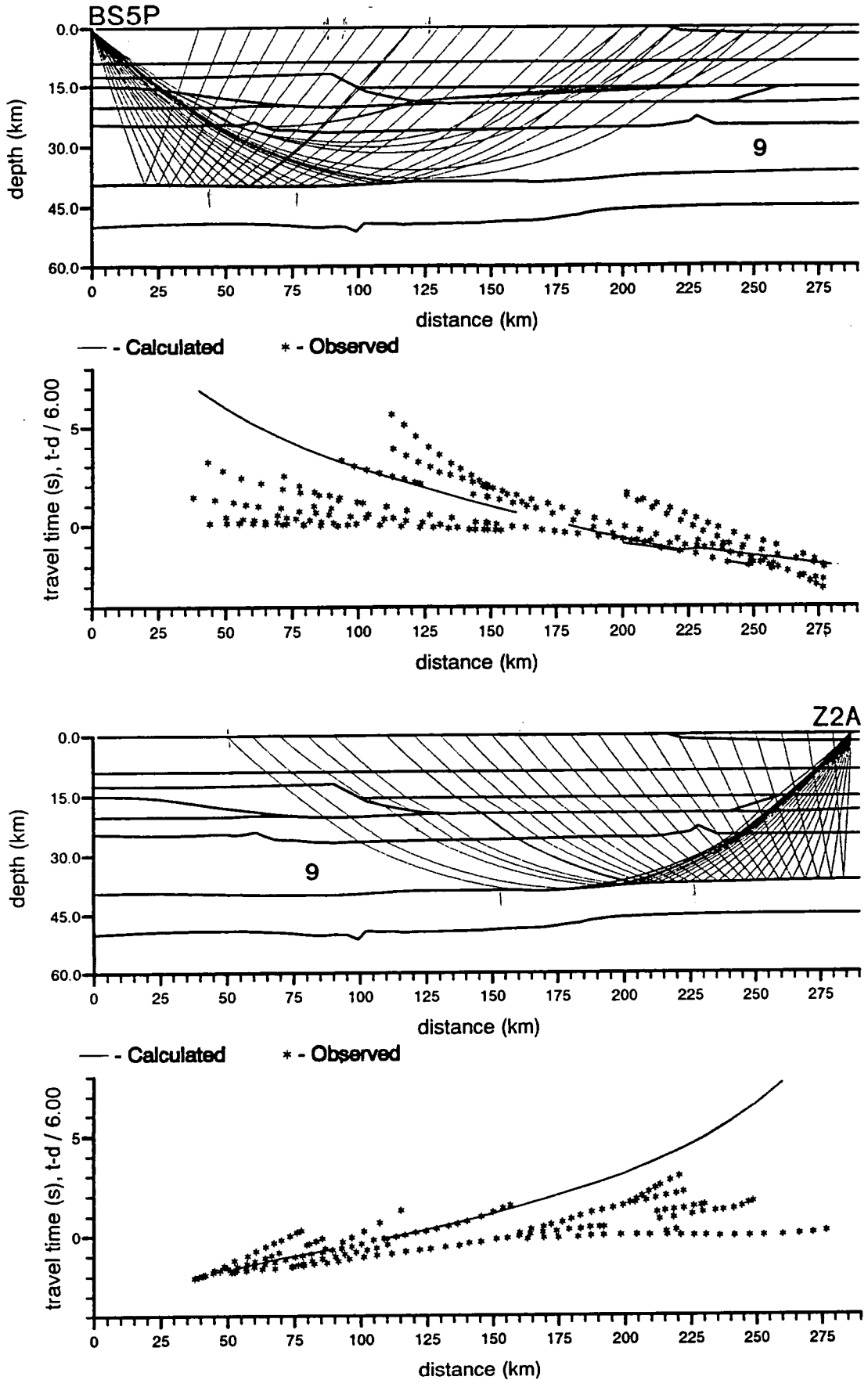
BS5P
depth (km)
0.0
15.0
30.0
45.0
60.0
9
0 25 50 75 100 125 150 175 200 225 250 275
distance (km)
— - Calculated
* - Observed
travel time (s), t-d / 6.00
5
0
0 25 50 75 100 125 150 175 200 225 250 275
distance (km)
Z2A
depth (km)
0.0
15.0
30.0
45.0
60.0
9
0 25 50 75 100 125 150 175 200 225 250 275
distance (km)
— - Calculated
* - Observed
travel time (s), t-d / 6.00
5
0
0 25 50 75 100 125 150 175 200 225 250 275
distance (km)

d

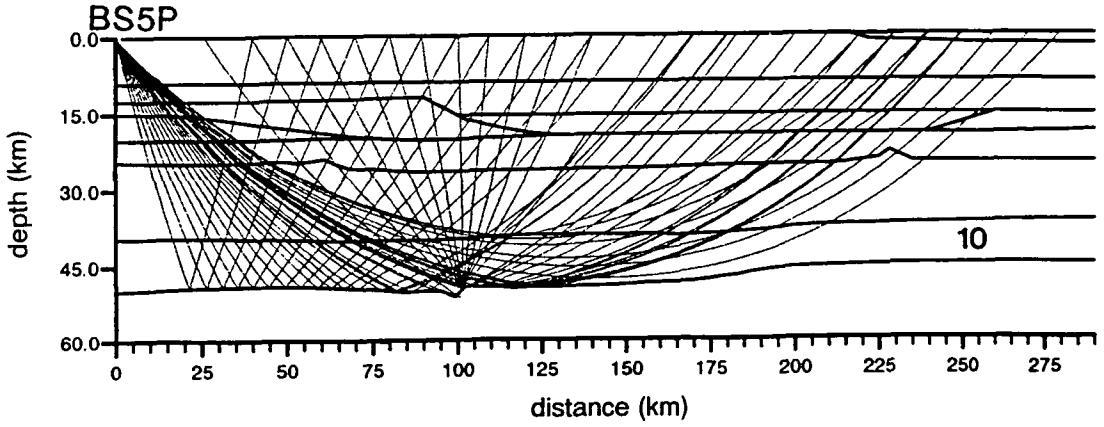
BS5P
depth (km)
0.0
15.0
30.0
45.0
60.0
10
0
25
50
75
100
125
150
175
200
225
250
275
distance (km)

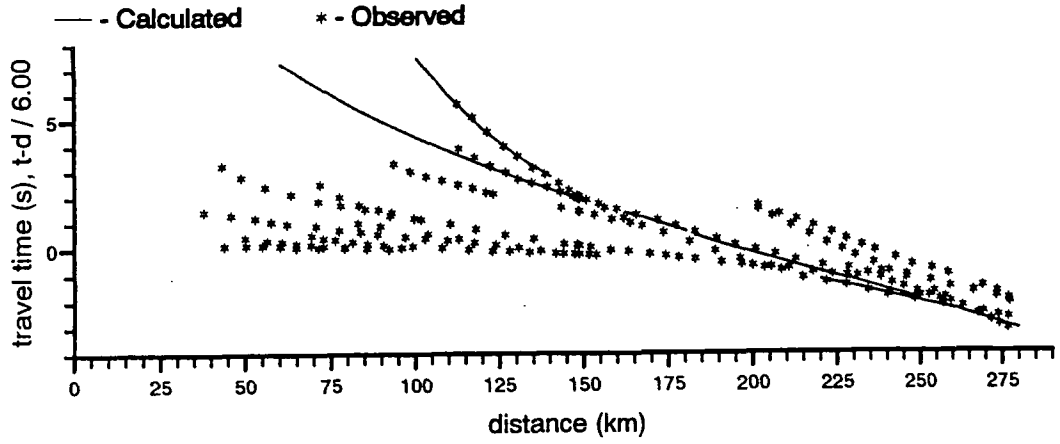
— - Calculated
* - Observed
travel time (s), t-d / 6.00
5
0
0
25
50
75
100
125
150
175
200
225
250
275
distance (km)

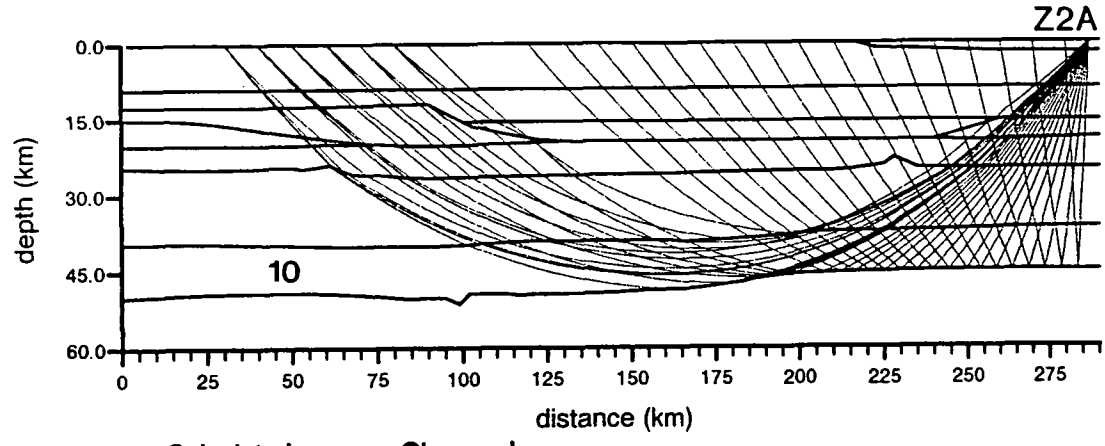
Z2A
depth (km)
0.0
15.0
30.0
45.0
60.0
10
0
25
50
75
100
125
150
175
200
225
250
275
distance (km)

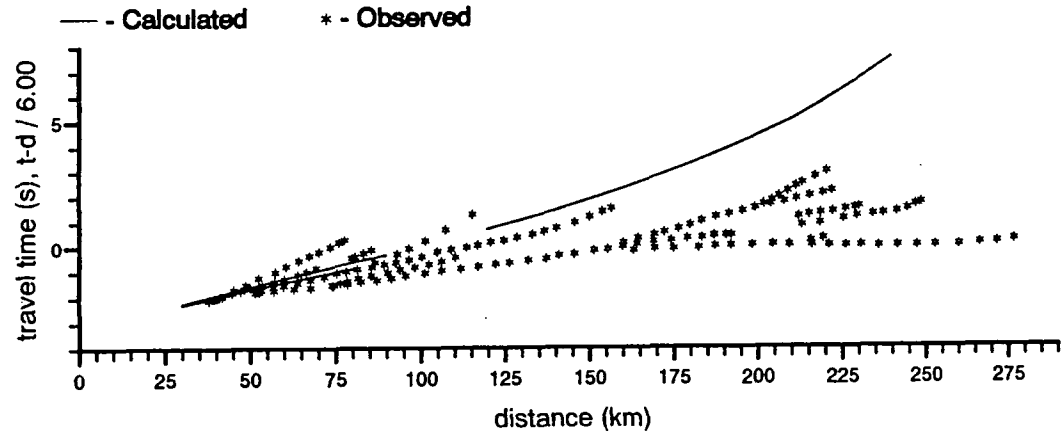
— - Calculated
* - Observed
travel time (s), t-d / 6.00
5
0
0
25
50
75
100
125
150
175
200
225
250
275
distance (km)

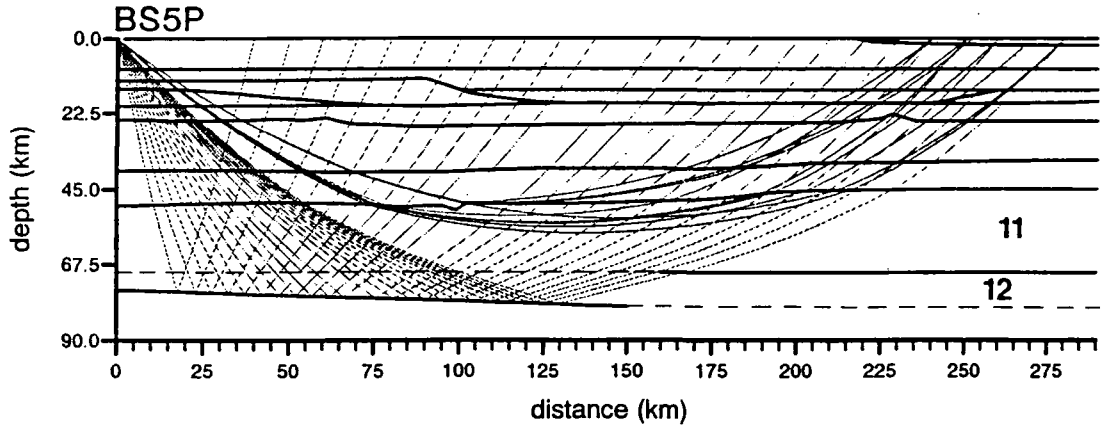
BS5P
depth (km)
0.0
22.5
45.0
67.5
90.0
11
12
0
25
50
75
100
125
150
175
200
225
250
275
distance (km)

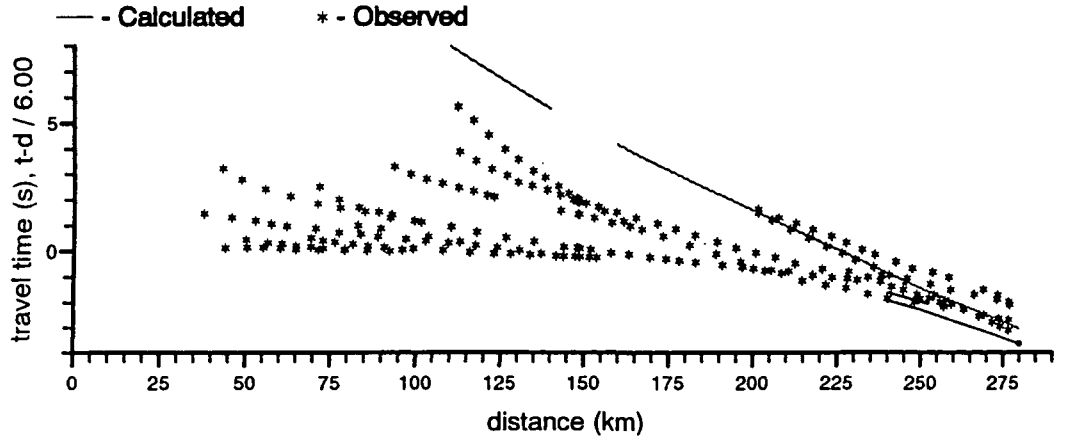
— - Calculated
* - Observed
travel time (s), t-d / 6.00
5
0
0
25
50
75
100
125
150
175
200
225
250
275
distance (km)

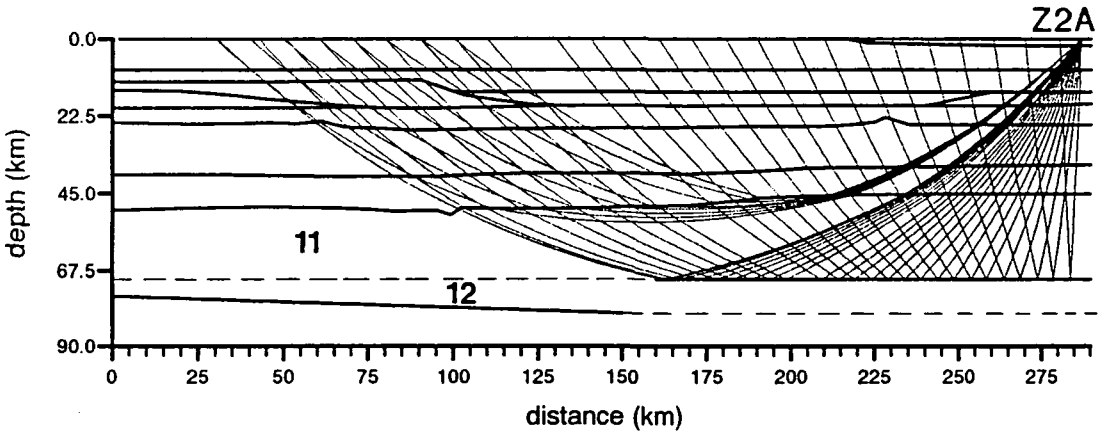
Z2A
depth (km)
0.0
22.5
45.0
67.5
90.0
11
12
0
25
50
75
100
125
150
175
200
225
250
275
distance (km)

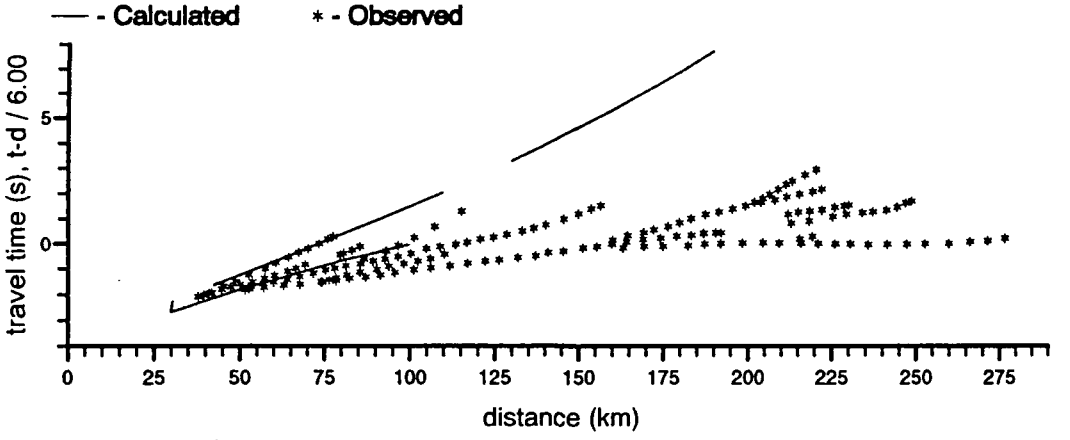
— - Calculated
* - Observed
travel time (s), t-d / 6.00
5
0
0
25
50
75
100
125
150
175
200
225
250
275
distance (km)

f

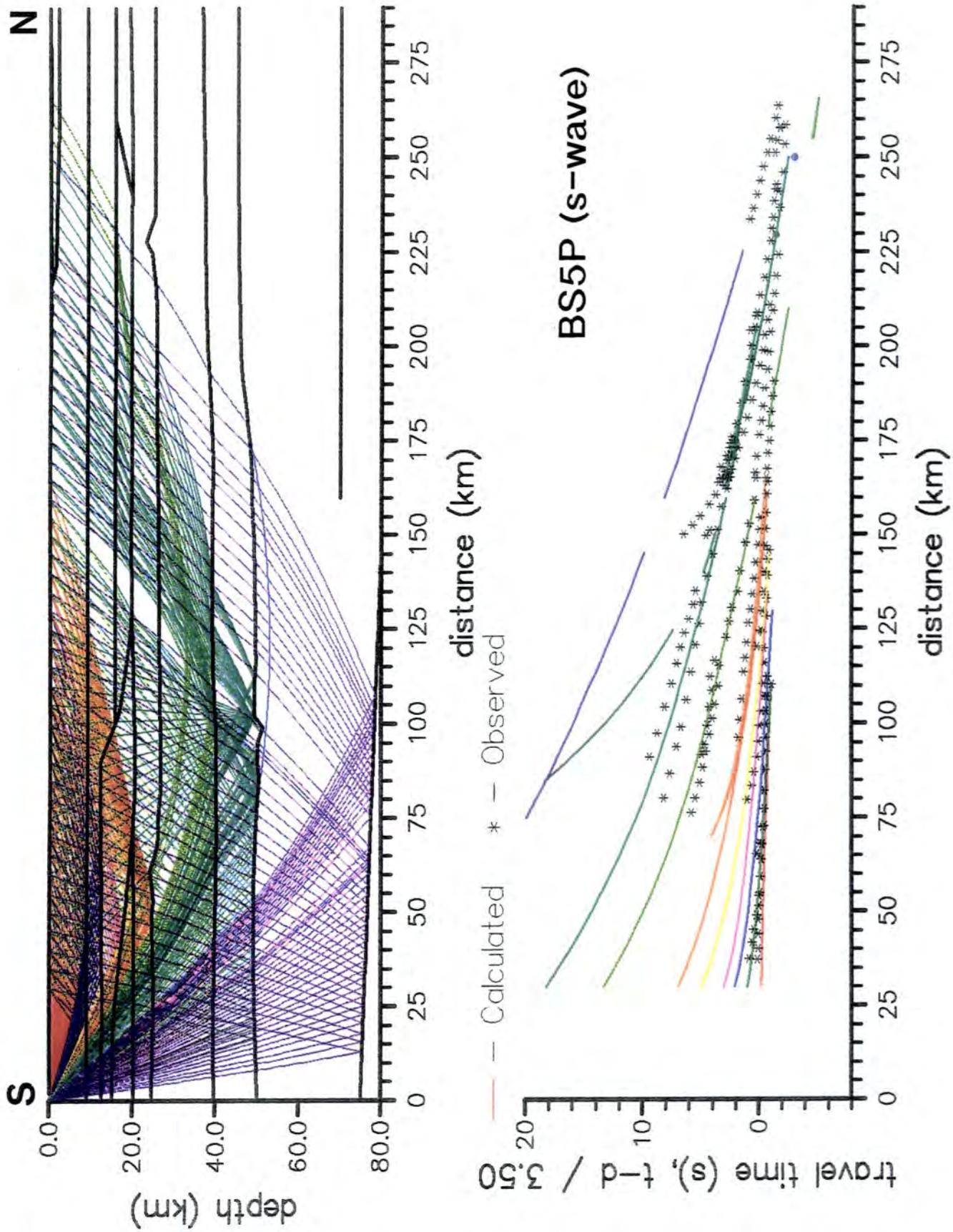

Figure 8.6. Fit of S-wave arrivals calculated from the line 6 model to the experimental arrivals picked from the transverse component of data recorded at BS5P.

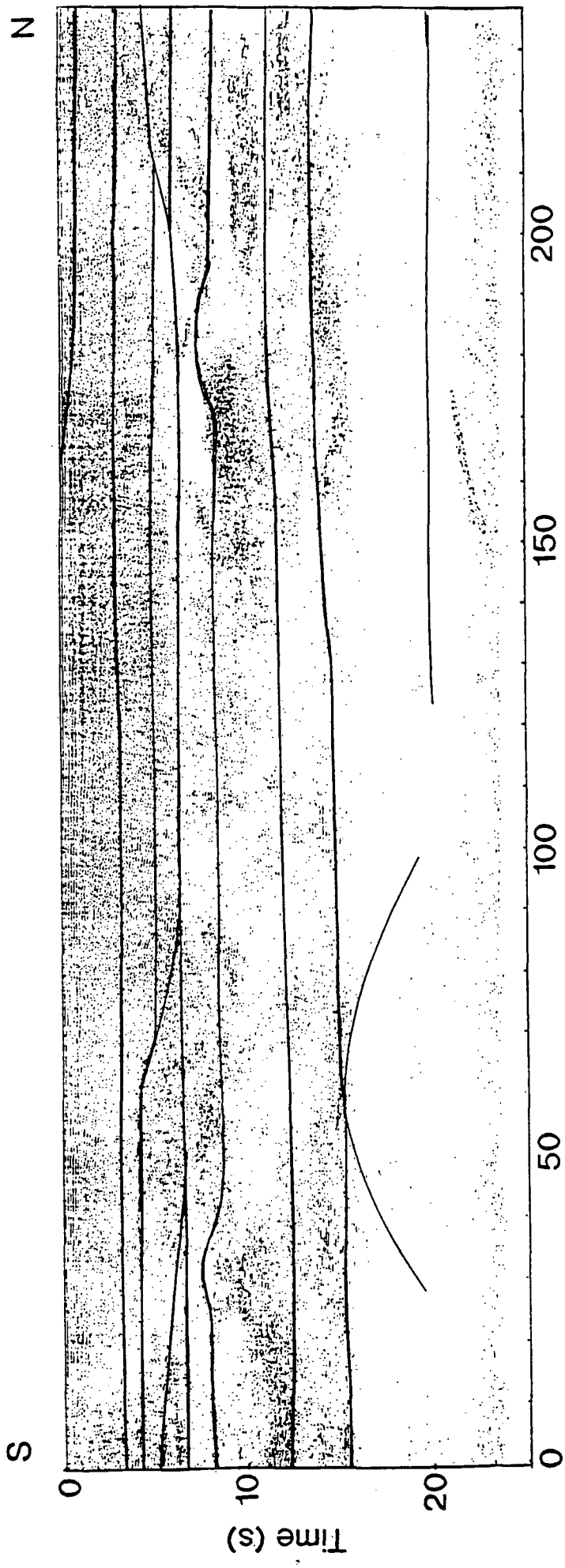

Figure 8.7. The two-way travel-times of arrivals calculated from the line 6 model superimposed on to the normal-incidence data for line 6.

consists of reflective and non-reflective patches. The modelled arrivals appear to generally coincide with the edges of the reflectivity packages rather than to any continuous normal-incidence reflectors but are more extensive. The possible reasons for this will be discussed in more detail in the next two chapters.

8.5 The line 6 model

The reversed model derived from the P-wave data from BS5P and Z2A consists of 13 layers (Figure 8.4) and is considered in detail below. Not all of the layers are continuous across the model (for example, layer 6 is divided into two segments, 6 and 6a, by layer 5). There is no evidence of the division into upper and lower crust that has been proposed for some of the previous profiles in the Baltic Shield (chapter III). For convenience, the model is discussed in terms of an 'upper crust' (layers above about 15 km), a 'mid-crust' where structures are more complex (15-20 km), a 'lower crust' (20-40 km) and a Moho and sub-Moho region. The P-wave velocities in the model are shown above and below each interface in Figure 8.4.

8.5.1 Upper crust (layers 1, 2, 3 and 4)

Layer 1 is the water layer corresponding to the Sea of Bothnia. The water depths in the Gulf of Bothnia are shallow and modelling the water layer makes little difference to the travel-times of arrivals. The frequency content of the BABEL data appeared to be related to the water depth (section 6.1.1) and layer 1 was included so that multiples in the water could be modelled in the synthetic seismograms (the delay between an arrival and its multiple in the water layer is small, of the order of 0.05 s, and these are not seen as separate arrivals in the reduced travel-time plots).

Layer 1 is not visible in Figure 8.4 since the water depths are very small compared to the thickness of the crust. An enlargement of the upper 0.4 km is shown beneath the model. The velocity in the water layer was set at 1.448 km/s (the average water velocity measure by PRAKLA in the Sea of Bothnia prior to the experiment). Water depths in the model are taken from the depths measured during the experiment (Figure 2.10) and extrapolated to zero thickness at the coast. Much of the detailed variation of water depth is lost as a result of the limited number of points provided to define each interface in BEAM87 but the major changes in depth to the north of the line are retained.

To the north of the model, in the near surface, there is a 75 km long, 2 km thick, high velocity layer. This is required to model the high apparent velocity of the first arrivals seen in the Z2A data from about 275 to 225 km (Figure 8.5a). The

velocity in this layer is 6.05 km/s. No such high apparent velocity first arrival is seen at BS5P. This indicates that this layer is only present at the northern end of the line.

The velocity of the first arrival at BS5P is about 6 km/s. At an offset of 75 km, this arrival is overtaken by an arrival with a higher apparent velocity (Vp ≈ 6.25 km/s). These arrivals are modelled as a diving wave and reflection from layer 3. No diving ray from layer 3 is seen in the Z2A data as a result of the near-surface high velocity layer. The reflection from the base of layer 3 forms the first arrival at Z2A between 225 and 160 km (Figure 8.5a).

At offsets greater than 100 km, the arrivals from layer 3 at BS5P are overtaken by another arrival which forms the first arrival out to offsets of 160 km. This arrival has an apparent velocity similar to that of the reflection from the base of layer 3 but longer reduced travel-times, suggesting that it is from a reflector lower in the crust. This is modelled as a reflection from a boundary at 12.5 km depth (the base of layer 4 at the southern end of the model). In the data from Z2A, an arrival with a similar velocity was seen but with longer travel-times, suggesting that this boundary deepens to the north of the line. This arrival is modelled as a reflection from the northern part of the base of layer 4 (15 km depth).

No reflection is seen in the BS5P data at offsets greater than 160 km. This may be explained by a sudden change in the depth of the boundary at the base of layer 4. No arrival has been identified in the experimental data from a boundary related to such a depth change. In the line 6 model, the change in depth from 12.5 to 15.0 km is modelled as a steep slope between offsets of 100 and 110 km. No arrival is modelled from this and the shape of the boundary in this region is arbitrary (a single ray from Z2A hits the slope). The BEAM87 model is a simplification of the crustal structure and it may be that these two reflectors (the northern and southern parts of the base of layer 4) are separate features.

8.5.2 Mid crust (layers 5, 6 and 7)

At a distance of 160 km, the apparent velocity of the first arrivals in the Z2A data increases sharply to about 6.65 km/s (Figure 8.5b). This high velocity could be due to a reflection from a steeply dipping interface or the result of a high velocity layer. Neither of these features where found during the initial modelling of the BS5P data which showed structures in the model to be generally horizontal. Attempts were made to include a steeply dipping interface in the model with little success (either the reflection produced was not as extensive as that seen in the data or else it made it impossible to model some of the other arrivals seen in the data).

The arrival was finally modelled using a 4 km thick high-velocity layer between offsets of 110 and 250 km, layer 5 (Figure 8.4). This layer has a velocity of 6.65 km/s. The horizontal length of the layer was determined by the extent of the arrival seen in the Z2A data and by the fact that no arrival from this layer was identified in the BS5P data. The shape of the ends of the layer are arbitrary, since no arrivals are seen from these in either the experimental or raytraced sections (the ends of the layer were modelled as wedges only because the easiest way to join vanishing layers with BEAM87 is to slope the two together).

A second body (layer 7) was introduced at the southern end of the line (at offsets less than 75 km) to explain two arrivals seen on the BS5P data which had reduced travel-times indicating they were from reflectors in the mid-crust. These are modelled as reflections from the upper and lower boundaries of layer 7. This layer does not affect the Z2A arrivals since few rays from Z2A reach it (only those from the Moho or below and these only pass through the thinnest part, Figure 8.5f and e).

Layer 6 and 6a (Figure 8.4) are part of the same layer in the BEAM87 model and have a common velocity and density. The velocity in this layer was determined by the reflection seen at BS5P from the upper boundary of layer 7. Layer 6 and 6a are modelled as part of the same layer for simplicity (modelling the high velocity layer in the middle of the layer 6 involves joining and separating four different interfaces and it is complicated to further increase the number of boundaries, the base of layer 5 already involves specifying three different boundaries as coincident). An arrival is seen in the Z2A data which could be a reflection from the base of 6a. The modelled arrival from 6a matches the general reduced travel-time of this arrival but not its apparent velocity, suggesting that layer 6 and 6a are separate. Again, it was not possible to model the apparent velocity of the arrival seen at Z2A with a dipping layer while modelling the arrivals from beneath this layer.

The high velocity layers in the upper and middle crust (layers 2, 5 and 7) do not seem to be particularly related to regions of either high or low reflectivity on the normal-incidence section (Figure 8.7). The northern part of layer 5, at offsets greater than 100 km, is mainly transparent but between 60 and 90 km offset (where layer 5 peters out to the south) the crust is highly reflective. As mentioned previously, the shape of the ends of layer 5 are not defined from the experimental data. Layer 2 is in the upper section of the normal-incidence data where the reflectivity patterns may be masked by sediment-generated multiples and shot-generated noise (section 6.2.3). Layer 7, at the southern end of the line relates to mainly reflective crust in the normal-incidence data but becomes less reflective as it thins.

8.5.3 Lower crust (layers 8 and 9)

The first arrivals seen in the BS5P data between offsets of 160 and 215 km are modelled as reflections from a reflector at about 25 km depth (the base of layer 8, Figure 8.5c). The high velocity layer (layer 5) increases the offsets at which this reflection is seen. A second arrival branches off the reflection at an offset of about 95 km. This was identified on the unreduced travel-time plot as a possible diffraction (section 8.2). A diffraction-type arrival is seen in the Z2A data at a distance of about 205 km. This also branches off an arrival modelled as a reflection from a boundary at 25 km depth.

These diffraction-type arrivals were modelled by including two small 'steps' on the interface at the base of layer 8, one at 60 km and one at 230 km. The position of the southernmost of these roughly agrees with that predicted from the travel-time curve for BS5P in Figure 8.2 (differences between the two positions may be due to the problems of modelling 'divergent reflections' rather than diffractions and the difficulties of extrapolating the unreduced travel-time curve).

At the southern end of the model, the 'step' is associated with a increase in depth of the interface from south to north of about 1 km. There is no change in depth either side of the northern step. The location of these steps is more accurate than their shape; they are modelled as the smallest feature that will give rise to a diffraction-type arrival under the restrictions of the BEAM87 program (the limited number of defining points, etc.).

Layer 9 is included in the model to explain the arrival seen between 160 and 50 km in the experimental data for Z2A (Figure 8.5d). The reflection from the base of this layer matches the short arrival seen between 100 and 125 km offset in the BS5P data, although this reflection extends further than the arrival seen in the data. It was not possible to limit the extent of the reflection to match the arrival seen in the BS5P data without impairing the match to the Z2A arrival.

In the normal-incidence data (Figure 8.7), the reflections from layers 8 and 9 generally separate reflective and non-reflective patches of crust, although the modelled arrivals are continuous across the section while the reflective patches are localised. For example, at offsets of 150 to 180 km, the reflection at about 9 seconds twtt (from the boundary between layers 8 and 9) separates a non-reflective patch of crust from the highly reflective region beneath it. The possible reasons for this will be discussed in the next two chapters.

The steps on the boundary between layers 8 and 9 strongly effect the arrivals that are modelled from lower layers. The step in the interface at the base of layer 8 focuses a group of rays from BS5P into the high velocity layer. This step also causes a

shadow zone in the diving ray in layer 9. Since the shape of the steps is the result of attempting to force the ray tracing program to simulate diffractions, their effect on later arrivals (such as focusing and shadow zones) is probably artificial.

8.5.4 The Moho (base of layer 10)

The high amplitude arrivals seen in the BS5P data occur mainly in two bands. The first band consists of the first arrivals in the data out to distances of about 150 km and has been modelled as a series of reflections from the upper crust. The second band has an apparent velocity of about 8 km/s and is the first arrival at offsets greater than 215 km (arrivals between these two bands are lower in amplitude). This second band of arrivals has been modelled as a reflection from a depth of about 50 km, as diving rays in the overlying layer and as a diffraction-type arrival (Figure 8.5e, layer 10).

The reflection has been interpreted as originating from the base of the crust (the 'wide-angle Moho'). The first arrivals at offsets between 225 and 280 km are modelled as diving rays in layer 10. The second 'diffraction' identified from the unreduced travel-time plot (section 8.2) branches off the Moho reflection at an offset of about 150 km. This has been modelled as a diffraction-type arrival from a small step on the Moho at an offset of about 95 km.

No strong reflection from the base of layer 10 was identified in the Z2A data. This may be partly due to difficulties in identifying later arrivals at Z2A because of the poor quality of the experimental data (section 6.1.5). The best fit of arrivals from layer 10 to the Z2A data is shown in Figure 8.5e. No experimental arrival was picked which could correspond to a reflection between offsets of 200 - 280 km.

For BS5P, the diving ray beneath the Moho could not be fitted to any of the picked arrivals (Figure 8.5f). On the FENNOLORA profile, the Pn arrival was only seen at offsets greater than 300 km. The velocity beneath the Moho was found by modelling the first arrival seen at a distance of between 30 and 50 km in the Z2A data (Figure 8.5f). The sub-Moho velocity is therefore very poorly constrained.

8.5.5 The Moho trench model

One of the features common to many of the previous Scandinavian deep seismic refraction profiles is a 'trench' like depression of the Moho. On the easternmost lines, BALTIC (Luosto *et al.* 1990) and SVEKA (Grad and Luosto, 1987), this is thought to be associated with the Ladoga-Bothnian Bay tectonic zone. On FENNOLORA a similar depression is seen between shotpoints D and E (the segment

parallel to line 6). Luosto (1990) suggested that these three trenches may be connected across the Sea of Bothnia.

Attempts were made to include a similar Moho depression in the model for line 6 and to see if this could improve the fit to the experimental data. Figures 8.8 and 8.9 show the best fit to the Z2A and BS5P data where such a Moho depression or trench is introduced (the structures and velocities in the crust above this interface are the same as those previously described). Reflections are modelled from the interface on either side of the trench and from the steep sides. The depth of the trench is arbitrary since no arrival which could be modelled as a reflection from the base of the trench was identified in the experimental data. The depth has been chosen as the shallowest which prevents a modelled diving ray beneath the Moho occurring ahead of the experimental arrivals in the BS5P data.

The southern edge of the modelled trench is 20 km to the north of the Moho step which models the diffraction-type arrival seen branching off the Moho reflection in the BS5P data. Between these two points, the Moho shallows slightly. The reflection from the northern edge of the trench partly matches the steeply dipping arrival seen in the BS5P data at large offsets (Figure 8.9). The Z2A arrivals from the trench show a similar pattern to the experimental data but the apparent velocities appear to be too low. The diving rays for Z2A beneath the Moho show a pattern similar to that of the reflected arrivals (Figure 8.8). It is not possible to determine the correct depth of the Moho boundary at distances greater than 190 km from the Z2A data since, as mentioned in the previous section, no arrivals were picked from this part of the data.

S-wave arrivals were calculated for the Moho trench model and compared to the experimental data. The ray diagrams and reduced travel-time plots for these two models are shown in Figure 8.10. The horizontal Moho model gives a better fit to the experimental data than the Moho trench model at offsets of 150 to 200 km. The 'diffraction' arrival from the step on the Moho does not match any of the picked S-wave arrivals. An arrival with a similar travel-time curve to that of the 'diffraction' is seen in the picks from the experimental data at an offset of about 175 km (D in Figure 8.10). This arrival has not been modelled and may arises at shallower depths and cross the Moho reflection.

The normal-incidence reflection from the Moho trench model overlain on the normal-incidence data is shown in Figure 8.11 For both this, and for the normal-incidence arrival from the horizontal Moho (Figure 8.7), the reflection from the southern part of the Moho (distances less than 150 km) coincides with the change in reflectivity at the base of the crust. At the northern end of the line, the reflection from the horizontal Moho model coincides with the upper boundary of a highly reflective

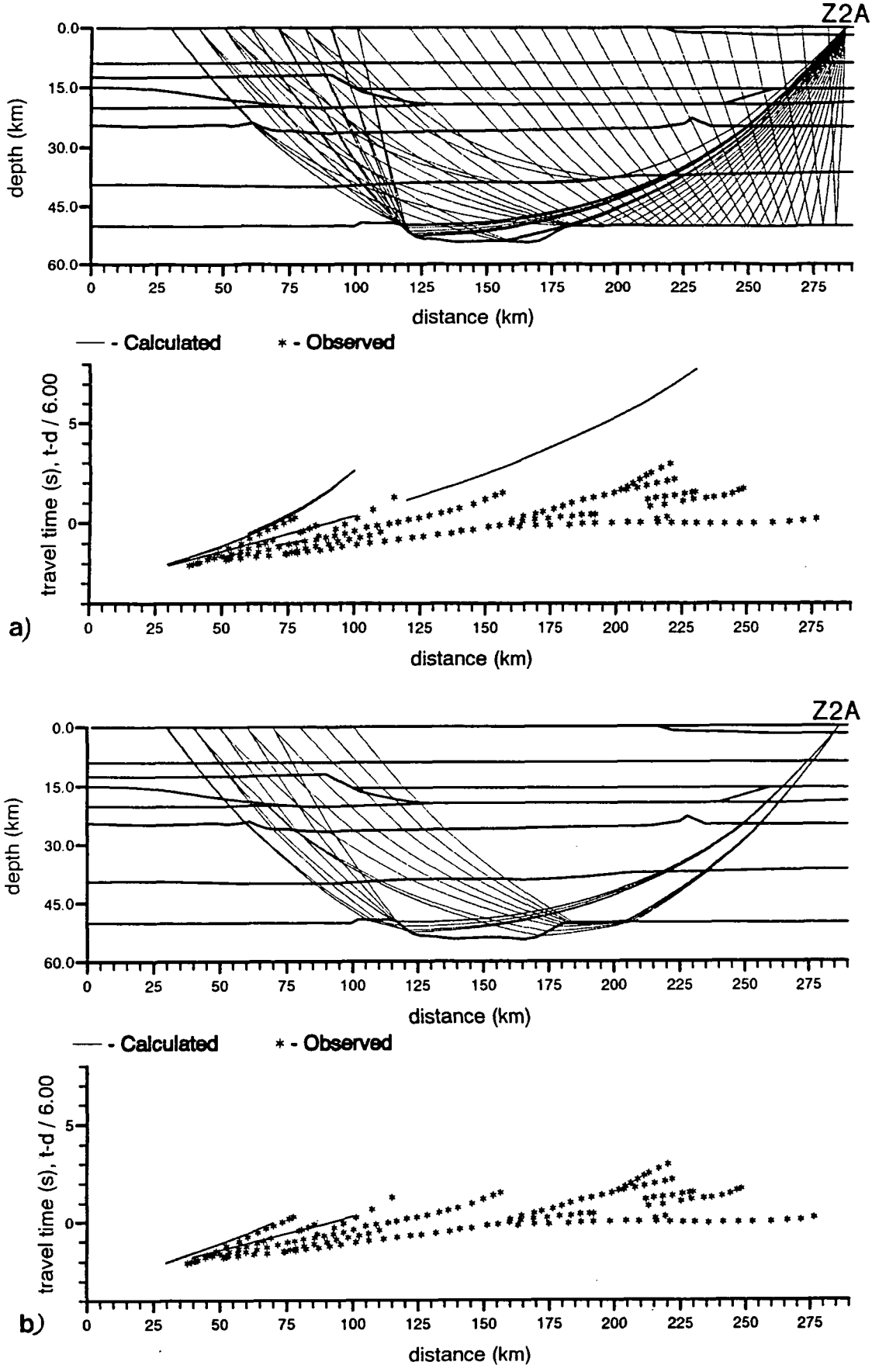

Figure 8.8. Modelled arrivals from the Moho trench for Z2A. **a)** reflections from the Moho; **b)** diving rays beneath the Moho.

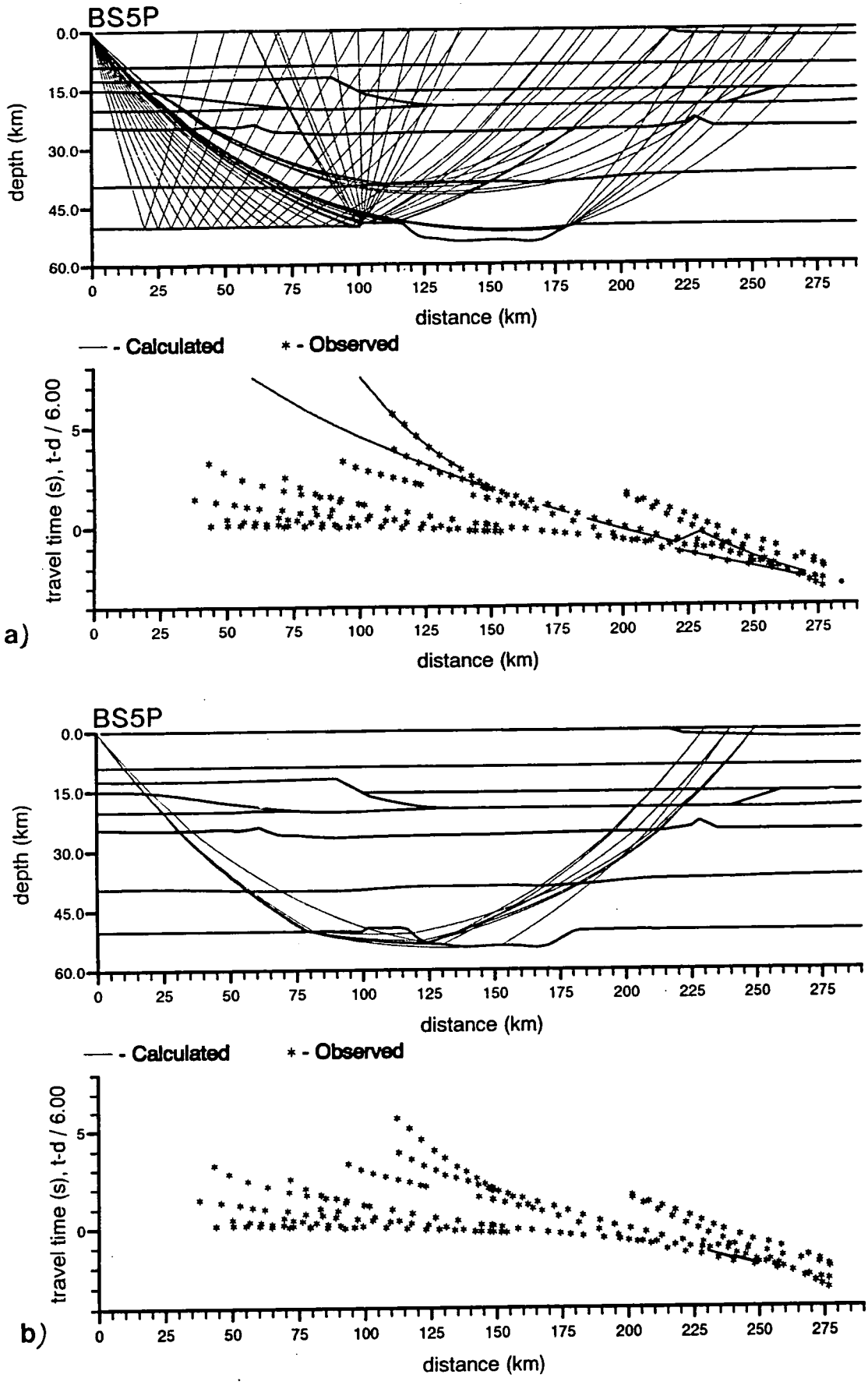

Figure 8.9. Modelled arrivals from the Moho trench for BS5P. **a)** reflections from the Moho; **b)** diving rays beneath the Moho.

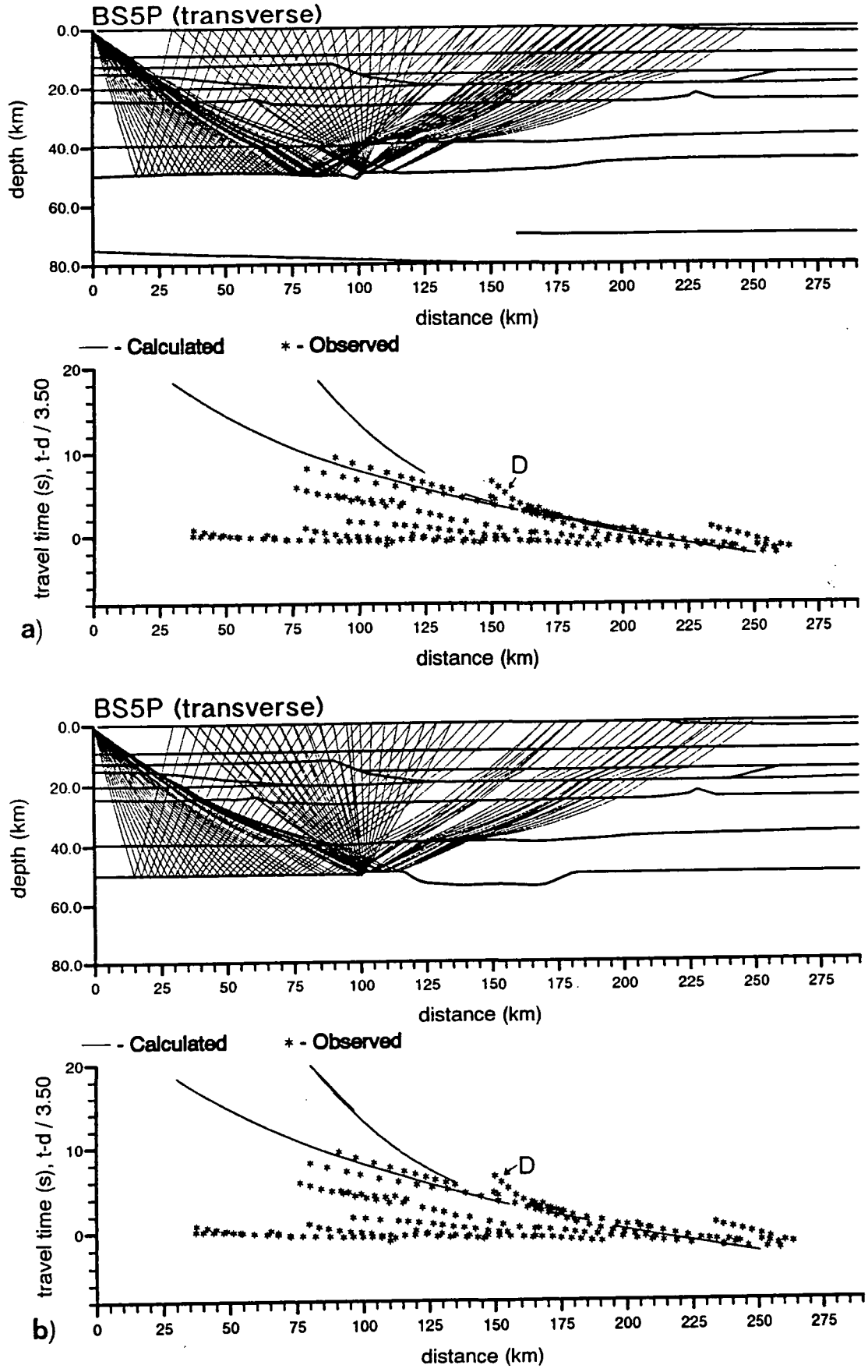

Figure 8.10. Comparison of S-wave reflections from the horizontal Moho and from the Moho trench.

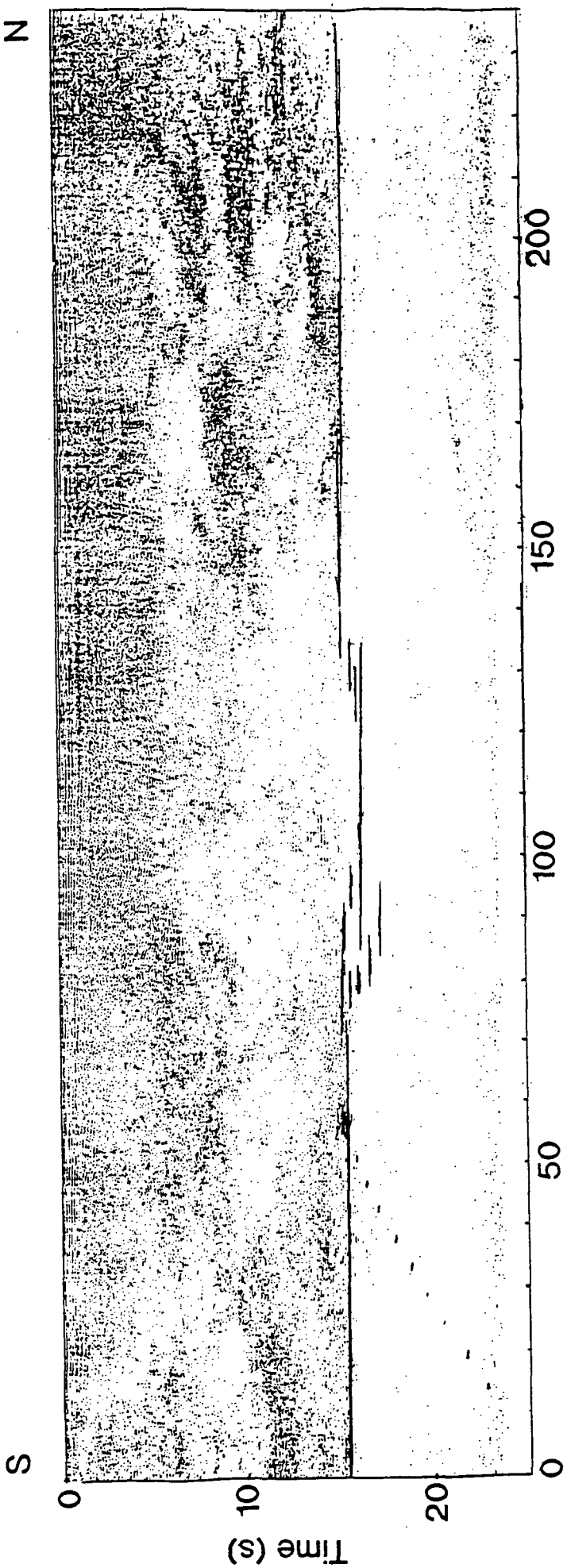

Figure 8.11. The two-way travel-times calculated from the Moho trench model superimposed on to the migrated normal-incidence data for line 6.

layer; the base of the reflective crust appears to be 2 seconds below this at 16 s twtt. In the Moho trench model, the Moho reflection at the northern end of the line coincides with the transition from high to low reflectivity.

The modelled trench is much shorter and shallower than that modelled for the other refraction profiles in the Baltic Shield (for example, the trench for FENNOLORA modelled by Guggisberg *et al.* (1991) was 10 km deep and over 100 km wide). Several other Moho structures suggested by the results of previous surveys were also tried (for example a double Moho as seen on the BALTIC profile (Luosto *et al.*, 1990)). The horizontal Moho model is the simplest structure and was used as the final line 6 model in the absence of any clear evidence in favour of a trench on the Moho.

8.5.6 Mantle reflectors

Several of the arrivals with high apparent velocities (8.5-9.0 km/s) and long travel-times that were picked from the experimental data are not accounted for by the crustal structure described so far. It is suggested that they are due to mantle features (reflections from the upper mantle have been seen on several previous refraction studies of the Baltic Shield (Lund, 1979, Luosto *et al.*, 1984, Luosto, 1986). The line 6 mantle arrivals have not been modelled in detail. Examples of how these arrivals could be modelled as reflections from boundaries in the mantle are shown in Figure 8.5f. Attempts were made to model these as crustal arrivals from steeply sloping boundaries (such as from the edge of the proposed Moho trench, Figure 8.8 and 8.9) or as diffraction-type arrivals from diffractors at large offsets but could not explain both the apparent velocity of the arrival and the shape of the reduced travel-time curve.

8.5.7 P- and S-wave velocities

A program was written to construct series of 1D vertical velocity profiles from the BEAM87 model at 2.5 km intervals and to plot these to give a 3D representation of the variation of velocity against depth with offset along line 6. The P-wave and S-wave velocity structures of the line 6 model are shown in Figure 8.12 (offsets are measured from BS5P, as in the model).

The P-wave velocity variation with depth (Figure 8.12a) is generally gradational with only small changes in velocity across the interfaces between layers. With the exception of the high velocity layers that have been described previously,

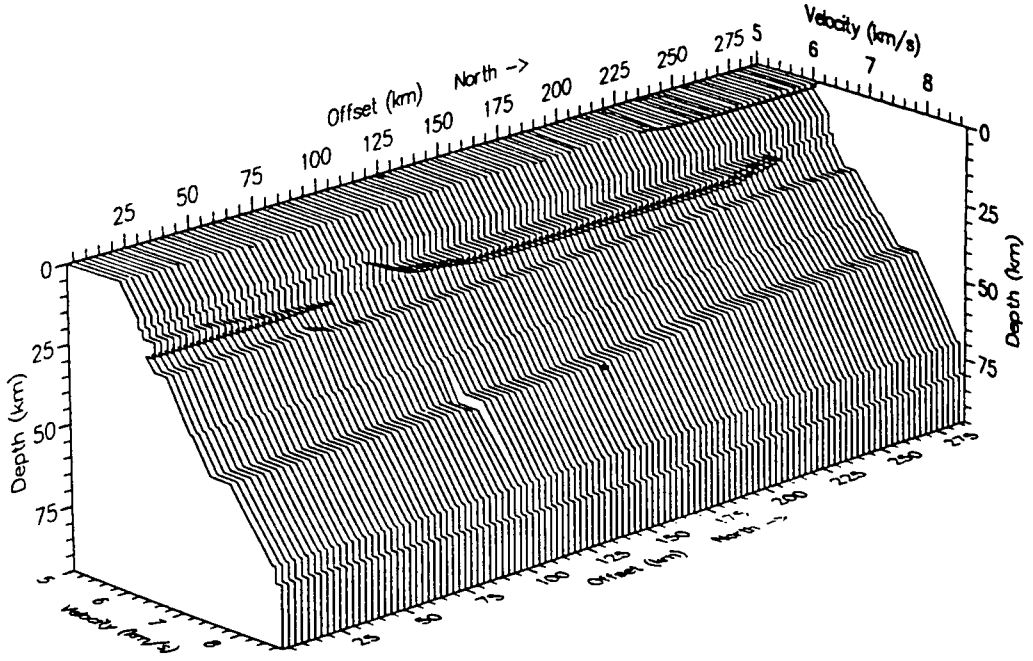

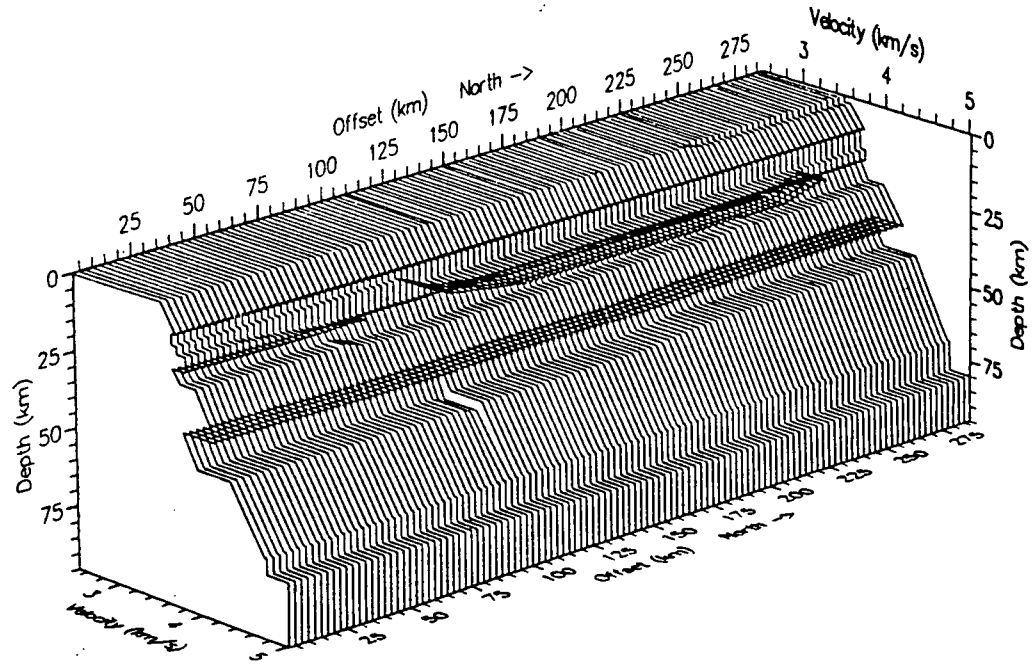

Figure 8.12. 3D representation of the P- and S-wave velocities in the line 6 model (velocity profiles are plotted at 2.5 km intervals).

the model consists of laterally homogeneous layers. The largest velocity step occurs at the Moho. This velocity step is not defined by the data from line 6 as no diving rays beneath the Moho were identified in the experimental data. The high amplitude of the wide-angle Moho reflection suggests that the velocity increase across this boundary is large. The step on the Moho at offset of about 100 km is clearly shown.

The S-wave velocities derived using the P-wave model boundaries are shown in Figure 8.12b. There is a general increase in velocity with depth, although several low velocity zones are seen and the changes in velocity across the layer boundaries are greater than for the P-waves. Layer 2 (Figure 8.4) has a high P-wave velocity but a relatively low S-wave velocity. The S-wave model has not yet been reversed since Z2A was a single vertical component station (data from the transverse component at either BS2 or BS1 should be used to reverse the S-wave model as part of the further work on this data, since the control over the S-wave velocity at the north end of the line is poor). The other high velocity layers in the P-wave data have high S-wave velocities.

Figure 8.13 shows the P-wave and S-wave velocities and Poissons ratio at offsets of 50, 150 and 250 km (layer numbers are shown next to the P-wave velocity profile). Poissons ratio (σ) is calculated from:

$$\sigma = \frac{\left(\left(\frac{v_p}{v_s}\right)^2 - 2\right)}{2\left(\left(\frac{v_p}{v_s}\right)^2 - 1\right)} .$$

In crustal rocks, the ratio of P-wave to S-wave velocities approximates as $\sqrt{3}$ (σ = ¼). In several previous deep refraction projects in the Baltic Shield where S-wave data has been modelled, this ratio has been used to divide the models into upper and lower crust, the upper crust having ratios < $\sqrt{3}$ and the lower crust ratios > $\sqrt{3}$ (Grad and Luosto, 1987, Hauser and Sangel, 1990). The boundary between upper and lower crust in the Baltic Shield is usually at a depth of about 20 - 25 km, where the P-wave velocity increases from about 6.3 to 6.5 km/s (chapter III).

For the line 6 model, the v_p/v_s ratio is less than or equal to $\sqrt{3}$ for all of the crustal layers except layer 10 (below 40 km). Ratios in layer 10 and in the upper mantle are greater than $\sqrt{3}$. The P- to S- ratios may indicate a separation into lower and upper lithosphere (rather than into upper and lower crust) but further modelling on the S-wave velocities in the lower crust is needed before this is clear.

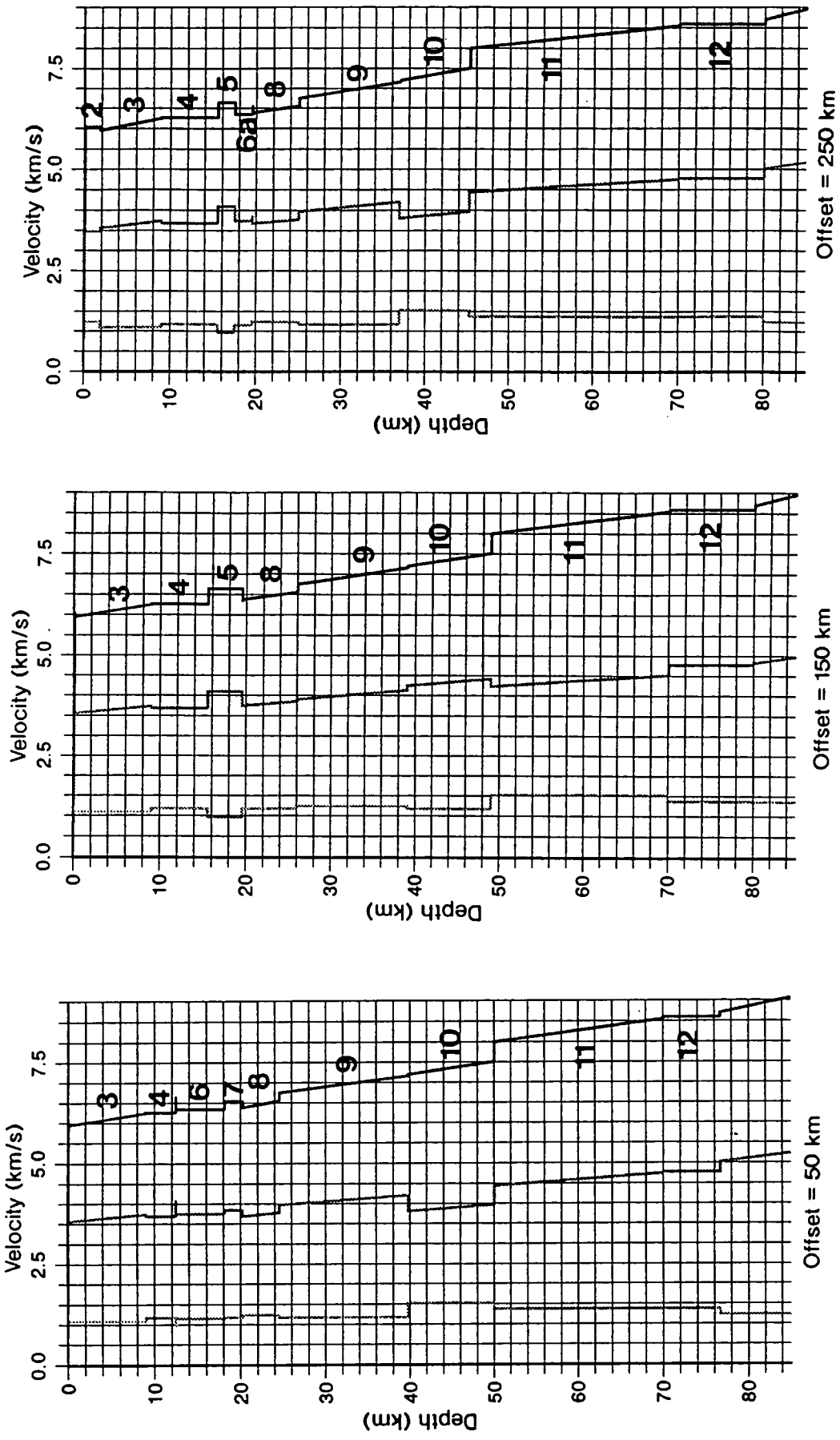

Figure 8.13. 1D velocity profiles through the line 6 model at offsets of 50, 150 and 250 km.
Numbers refer to the layers in the model (see Figure 8.4).

8.6 Synthetic seismogram modelling

The source signature used for the BEAM87 synthetics was the Mintrop signal (section 7.4.4). Since the frequency spectra of the experimental wide-angle data suggested that the first multiple in the water layer was important in controlling the frequency content of the data, the first peg-leg multiple in the water layer was included in the calculation of the synthetics.

Figure 8.14 shows the difference made to the synthetic seismogram by including the water layer multiple. The upper section (Figure 8.14a) is generated from the elementary waves (the term 'elementary wave' refers to the arrivals from a particular layer, section 7.4.1) and the lower (Figure 8.14b) from the elementary waves and their multiple in the water layer. The main amplitude changes appear to be due to interference effects (e.g. in Figure 8.14b the amplitude of the first arrivals is low between 150-180 km offset, as a result of interference between two arrivals with similar apparent velocities). Since arrivals often cross at steep angles, the changes from constructive to destructive interference can occur over short distances.

In the lower section (Figure 8.14b), constructive interference between arrivals and multiples has increased the maximum amplitude on the traces so that low amplitude arrivals are less visible. The change in amplitude along the arrivals is also more rapid. A 'gap' is seen in the first arrivals at offsets of 145 to 170 km. The marked differences between the two synthetic sections, and the improved match of the synthetic including the water multiple to the experimental data, stresses the importance of using the correct source signature when generating synthetic seismograms.

Figures 8.15 and 8.16 show the experimental data and the BEAM87 synthetic seismograms from the line 6 model (with no Moho trench) for BS5P and Z2A respectively. Distances in the figures are measured as offsets from the station in question (the separation of Z2A and BS5P was 287.065 km).

8.6.1 BS5P

For both the synthetic and experimental data for BS5P (Figure 8.15), the first arrival has the highest amplitude out to offsets of about 130 km, although the synthetic seismogram does not show the short scale (on a scale of a few km) variations in amplitude seen in the experimental data. Between 130 and 180 km, the first arrivals in the experimental data are very low amplitude. At offsets of 160 to 230 km, interference with the S-wave from the previous shot distorts the P-wave arrivals but between 130 and 160 km there is a low amplitude 'gap' in the first arrivals (labelled 1 in Figure 8.15).

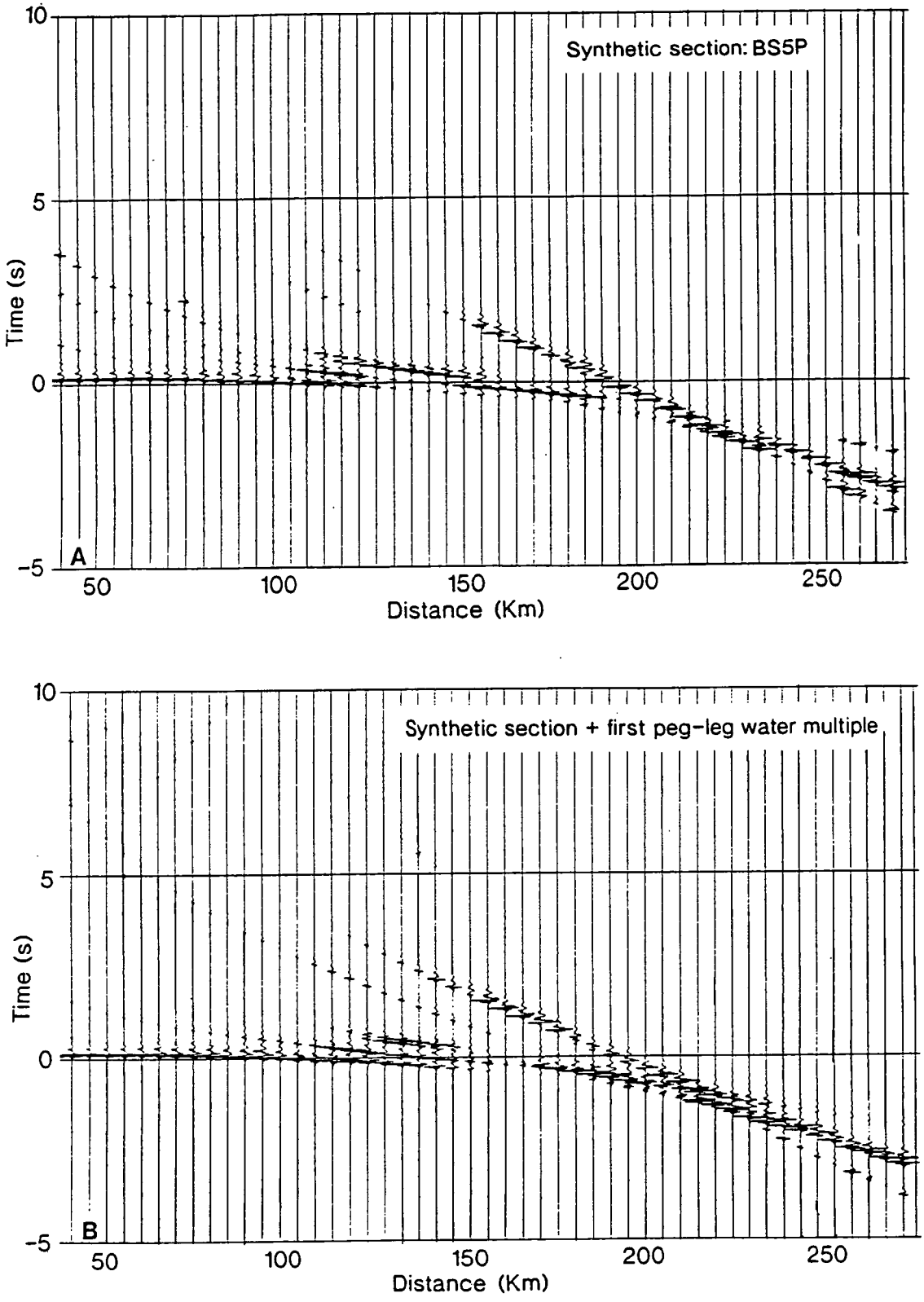

Figure 8.14. Comparison between the synthetic seismograms for station BS5P for **a)** all elementary waves and **b)** elementary waves plus their first peg-leg water multiple. Both sections have been trace normalised.

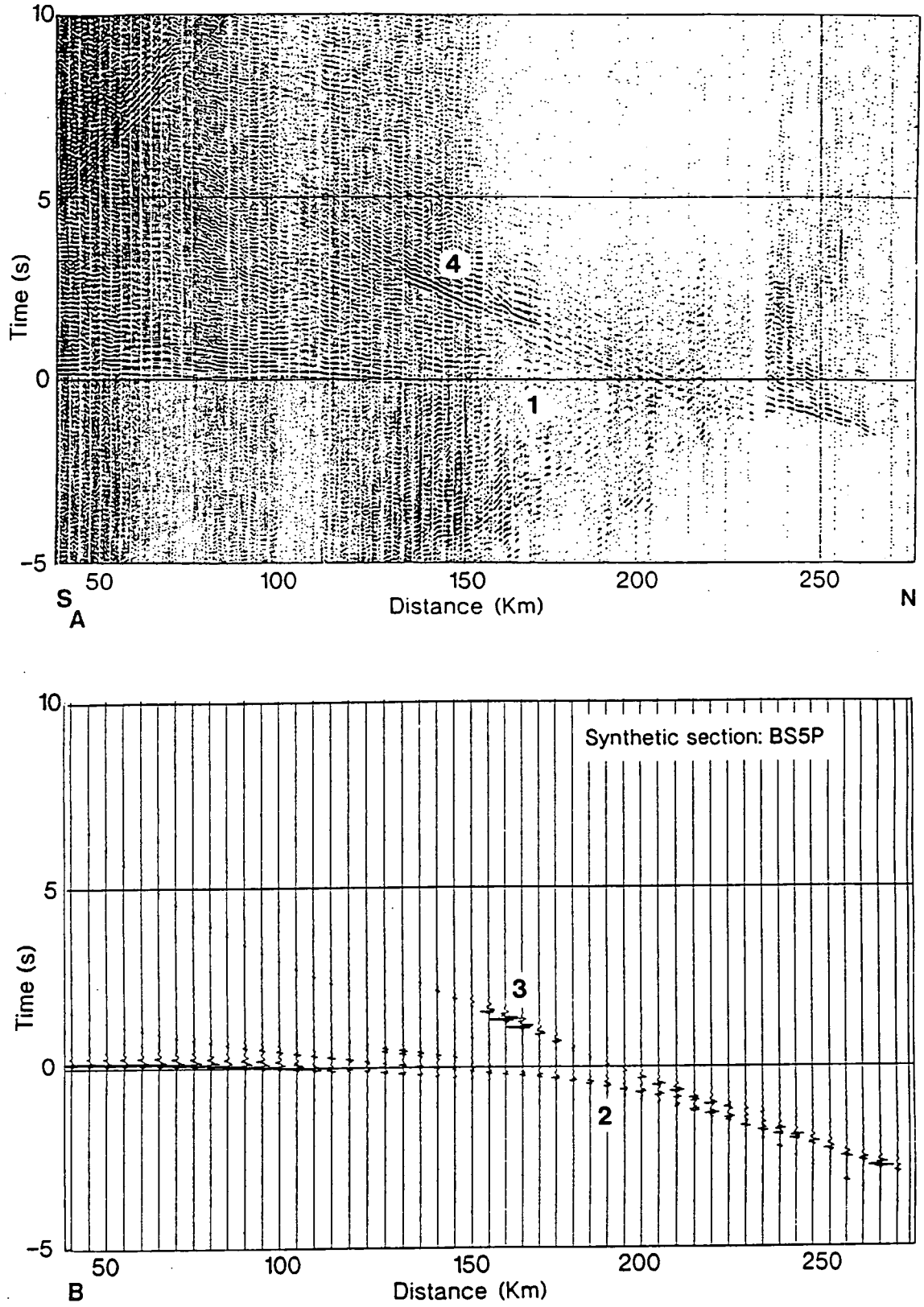

Figure 8.15 a) Experimental data from BS5P and **b)** BEAM87 synthetic section from the model shown in Figure 8.4. Distances are given as offset from station BS5P and both sections are reduced at 6 km/s and plotted on the same scale.

In the synthetic section, the amplitude of the first arrivals decreases between 130 and 160 km but less abruptly than in the experimental data and to a lesser extent. Between 170 and 200 km, a strong first arrival is seen at travel times of about 0 to -1 secs travel-time in the synthetic (labelled 2 in Figure 8.15) but has much lower amplitude in the experimental data. This may be again partly due to the problems of the S-wave interference described in chapter VI.

The 'diffraction' arrivals are not clearly seen in the synthetic section because of their low amplitude. The difference between calculated and observed amplitude may be due to the fact that these are not true diffractions (true diffractions cannot be modelled by raytracing). The point on the reflected arrival where the diffracted branch splits off has a high amplitude in both the synthetic and experimental data (for example, the section of the Moho reflection in the synthetic between 150 to 175 km, labelled 3 in Figure 8.15).

Between 130 and 160 km, the highest amplitude arrival on the experimental data section is seen at travel-times of 3 - 4 secs (labelled 4 in Figure 8.15). On the synthetic section, the amplitudes of the corresponding arrival are much lower. This may be due to the calculated amplitude of the first arrivals at these offsets being incorrect which will affect the amplitude of later arrivals.

At an offset of 240 km there is a gap in the PDAS data caused by an instrument crash, after which there appears to be a step in the travel-time of the first arrivals. This could be the result of a jump in the PDAS internal clock but no such change has been found from checking the internal and universal time (UT) (the radio time code is very poor for this part of the line (section 5.2)). If the step in travel-time is not due to a timing problem, it indicates that there is a lateral change in structure which is not included in the model and hence is not seen in the synthetic section.

8.6.2 Z2A

The synthetic section for Z2A at the northern end of line 6 is shown in Figure 8.16. It is difficult to compare the experimental amplitudes with the synthetic since the experimental data quality is poor (section 6.1.1). The synthetic section shows several differences to the experimental data. The amplitude of the first arrivals in the experimental data falls off rapidly with distance out to 60 km. In the synthetic, this fall off is not seen, although the amplitude of the first arrivals decreases between offsets of 70 to 80 km (labelled 1 in Figure 8.16). The main errors in the synthetic section amplitudes are the strength of the reflection from the boundary between layer 4 and layer 5 (labelled 2 in Figure 8.16) and the low amplitude of the reflection from the

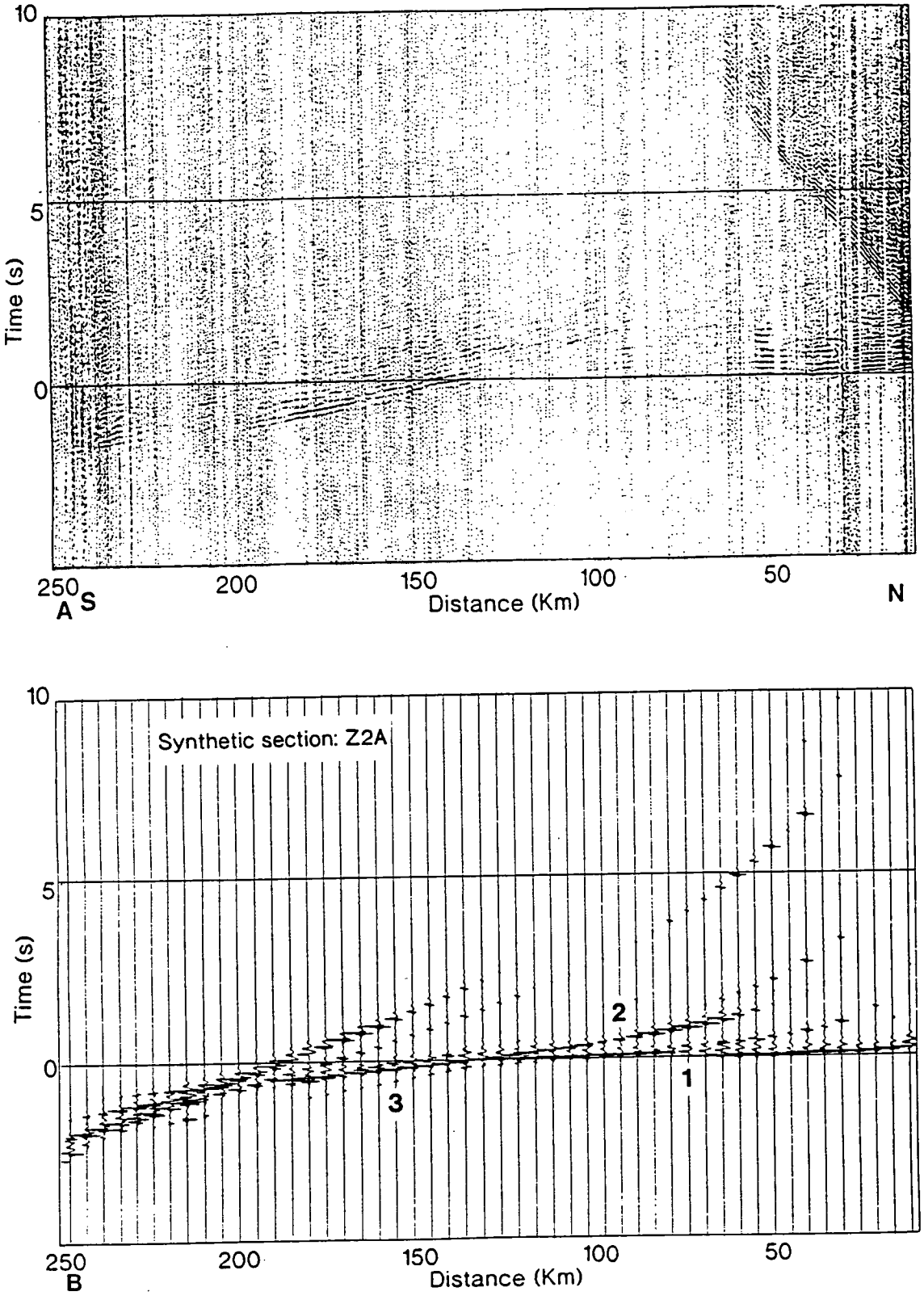

Figure 8.16 a) Experimental data from Z2A and **b)** BEAM87 synthetic section from the model shown in Figure 8.4. Distances are given as offset from station Z2A and both sections are reduced at 6 km/s and plotted on the same scale.

boundary between layer 5 and layer 8 which forms the first arrival at offsets between 130 and 200 km (labelled 3 in Figure 8.16).

The match of the modelled amplitudes to the experimental data is much poorer for Z2A than for BS5P. Line 6 was initially modelled from the data at BS5P and then reversed using the data from station Z2A. To model the Z2A data, structure was introduced at the northern end of the model, using the boundaries and velocity contrasts that had been modelled for BS5P (taking care not to distort the fit of the model to the first dataset). If there are major lateral changes along the line which have not been modelled, the velocity structure at the northern and the southern ends of the line may be very different. Ray tracing using linear interpolation between isovelocity interfaces assumes that the crust consists of a series of layers which are reasonably continuous across the model.

For both Z2A and BS5P, the experimental data is much more complex than the synthetic section. This is partly due to the fact that only the major wide-angle arrivals are modelled in the synthetic and partly because the experimental data is affected by other factors such as interference with previous arrivals, the recording locations and the ambient noise. In particular, the synthetic sections do not show the short scale amplitude variations seen in the experimental data (these were ignored during the original selection of arrivals, section 6.1.6). This will be discussed further in chapter IX.

8.6.3 Normal-incidence synthetic section

Figure 8.17 shows the comparison between the experimental normal-incidence data and the synthetic normal-incidence section generated from the line 6 model. BEAM87 was not originally designed to model normal-incidence data and occasionally fails to calculate an arrival from a boundary where one would be expected. These are shown as blank portions of the synthetic traces. Strong reflections are seen on the synthetic due to constructive interference where the high velocity zones thin and pinch out (for example, where layer 5 thins and disappears at 100 km offset and about 5 seconds twtt).

The strong reflection from the high velocity layer at the northern end of the line (layer 2) obscures the reflections from the lower crust below. In the experimental data, the reflections from the lower crust at the northern end of the line are complex and have the highest amplitudes on the section. This suggests that the velocity contrast between layer 2 and 3 is incorrect. In the experimental data, the transition from the reflective crust to the non-reflective mantle appears to be horizontal across the section and there is no indication of a thickening of the crust between 90 and 130 km offset predicted by the trench model.

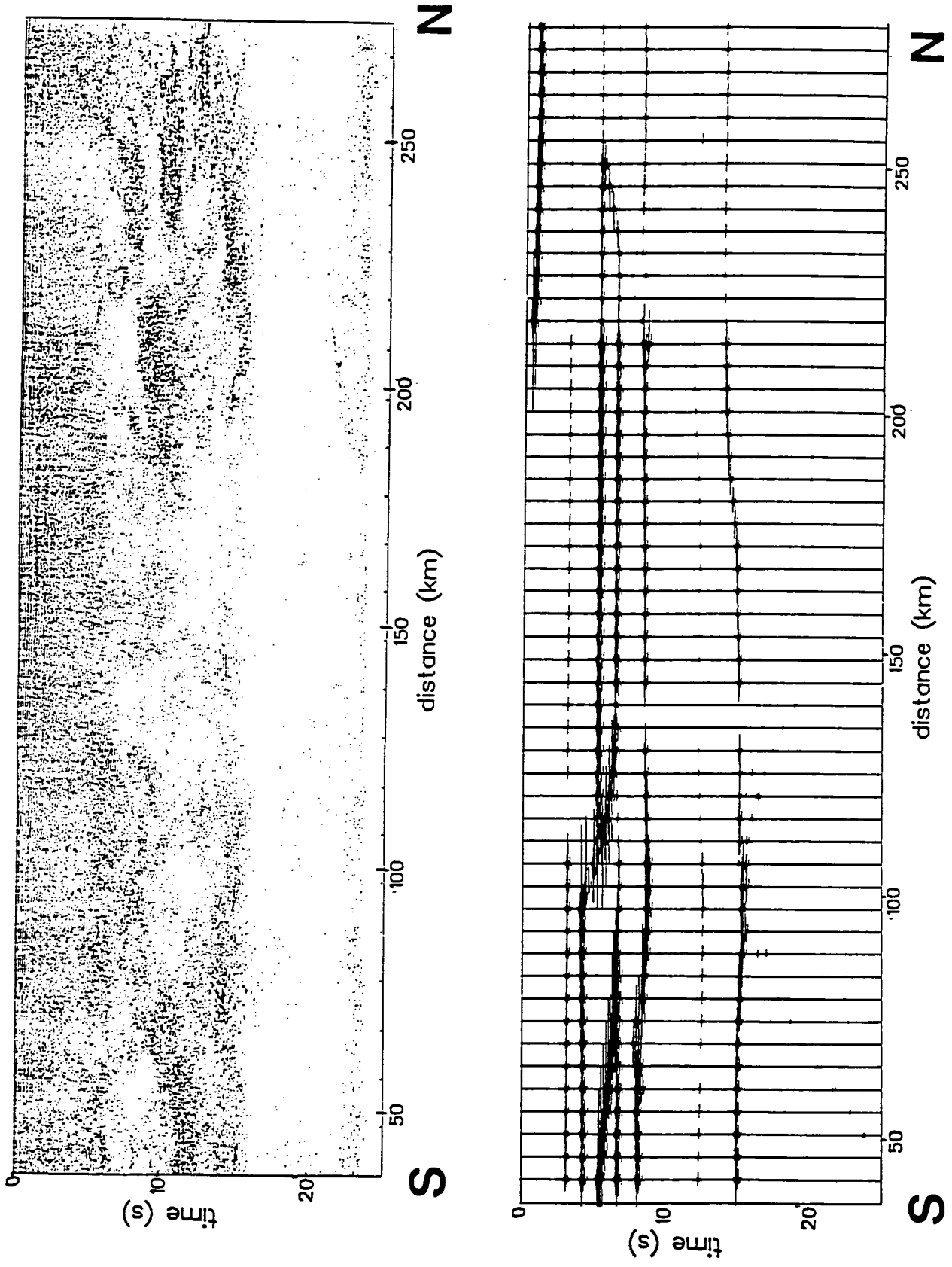

Figure 8.17. Comparison between **a)** the line 6 normal incidence data and **b)** the synthetic normal incidence section generated from the line 6 model.

8.7 Comparisons of the results from the line 6 model with the experimental data from BS5, Z5A and Z1A

BS5P and Z2A are the closest stations to the ends of BABEL line 6 and are approximately online. The next closest stations, Z1A in the north and Z5A and BS5 in the south, are slightly further offline (but still within 0.2° of longitude of the ends of line 6). Unfortunately there was not time during this work to fully model the experimental data from Z1A, Z5A and BS5 in the same manner as the data from BS5P and Z2A. Instead, rays were traced through the line 6 model for stations Z1A, Z5A and BS5 (the model boundaries were extended horizontally since these stations are at greater offsets) and the computed arrivals were compared to the experimental data to see if the line 6 model was able to explain the main features of these data (arrivals were also computed for the Moho trench model). This approach does not take into account the crustal structure beneath these stations or the fact that they are further offline than BS5P and Z2A. The results are discussed below for the different stations.

8.7.1 BS5

Figure 8.18 shows the fit of the ray-traced arrivals from the line 6 model to those digitised from the vertical component of the experimental data recorded at BS5. The match of arrival time to the first arrivals is good out to offsets of 100 km. Between 130 and 170 km, the first arrivals from the model are too early. The modelled reflections from the high velocity layer at the southern end of the line (layer 7) and from layer 8 are a poor fit to the data.

The Moho reflection is a good fit to the arrival seen in the experimental data but the 'diffracted' branch from the step on the Moho of the model does not match any of the picked arrivals. An arrival with a similar apparent velocity is seen in the experimental data, branching off from the Moho reflection at about 170 km offset (a similar arrival was seen in the S-wave data from BS5P). This suggests that either the diffraction producing feature is striking NNW to SSE and the 'diffraction' seen at BS5 comes from a different part of the feature (at a greater offset) than that seen in the BS5P data or there is a second diffractor to the north of the modelled one. The fact that a diffraction-type arrival was seen in the S-wave data from BS5P at greater offsets than the one generated from the model suggests that there may be a second 'diffractor'.

The travel-time fit for arrivals from the horizontal and trench Moho models are shown in Figure 8.19. Both reflections from the Moho and the diving ray into the upper mantle (Pn) are modelled. Neither structure is a noticeably better match to the experimental data. The diving ray from beneath the horizontal Moho has a similar

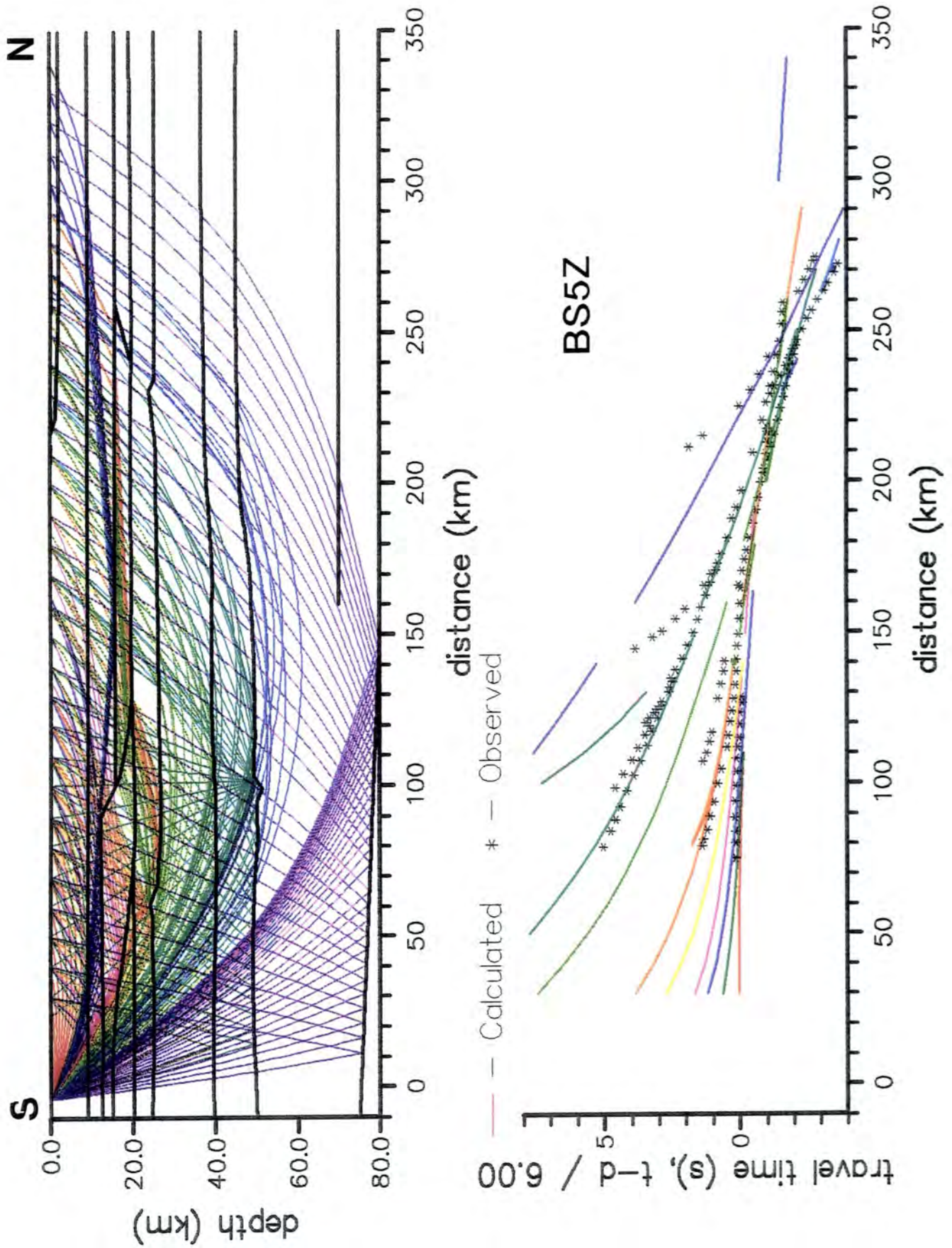

Figure 8.18. Ray diagram and travel-times from the line 6 model compared to the arrivals picked from the experimental data for station BS5.

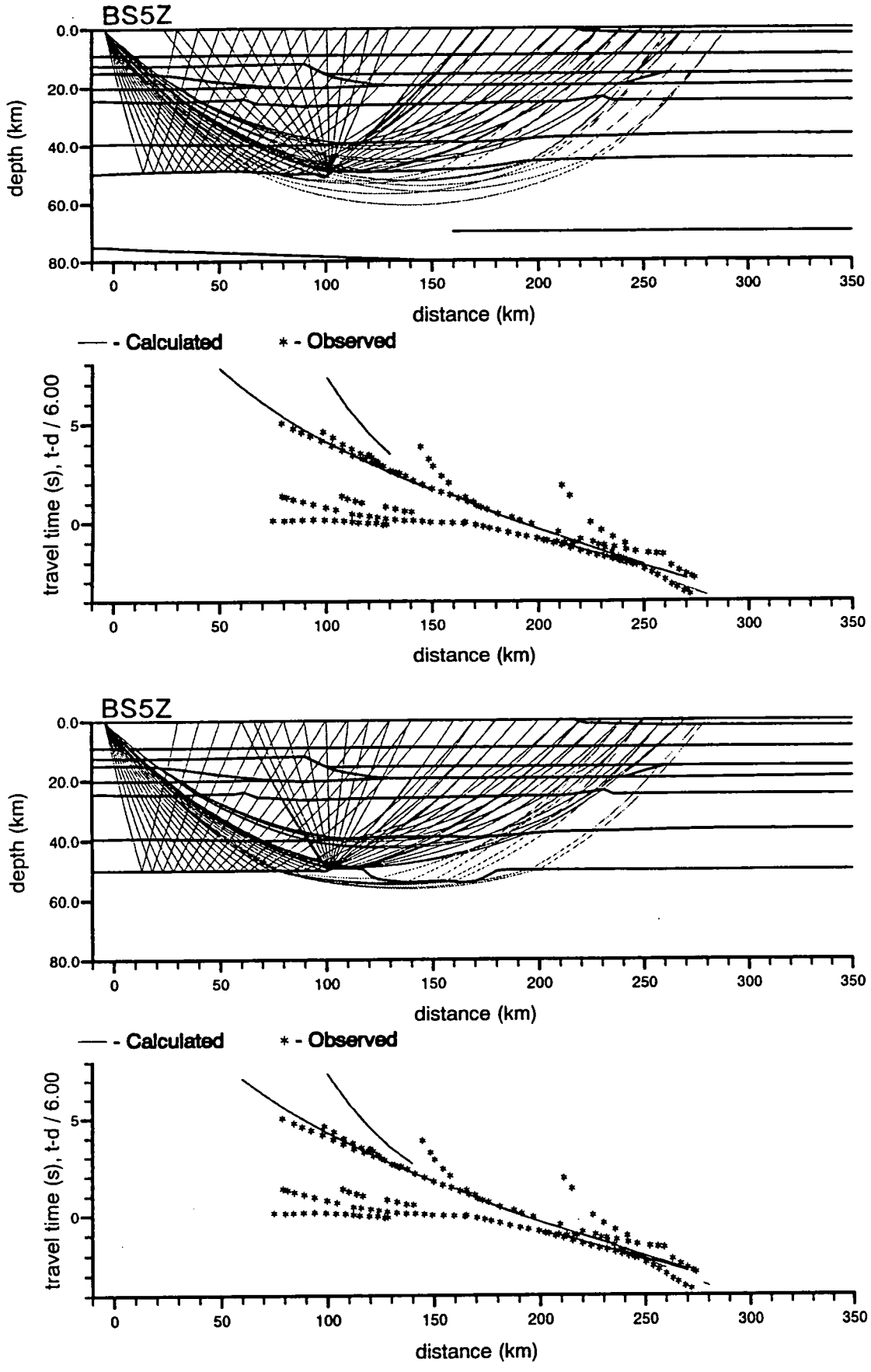

Figure 8.19. Ray diagrams and travel-time plots for the two proposed Moho structures (horizontal and trench models) compared to the experimental data from BS5.

travel-time to the arrival seen in the experimental data but a much lower apparent velocity.

8.7.2 Z5A

Station Z5A is the furthest south of all the stations that have been included in this work. The travel-time fit for this station is shown in Figure 8.20. Again, a possible diffraction is seen in the experimental data branching off from the Moho reflection to the north of the 'diffraction' from the model. This may be from the same feature as the arrival seen in the BS5 data.

The Pn arrival from the model is a close match to that seen in the experimental data, although its apparent velocity is still too low. The Pn arrival is shown more clearly in Figure 8.21 for the two proposed Moho structures. For the horizontal Moho, this arrival matches that digitised from the experimental data, forming the first arrival between offsets of 245-265 km. For the trench model, the Pn arrival is broken up by the trench into several segments none of which match the digitised arrivals at offsets of 245 -265 km. This is further evidence against the existence of a trench on the Moho.

8.7.3 Z1A

Station Z1A lies to the north of line 6 and it recorded data from this line at the greatest offsets of any of the Durham stations. The ray diagrams and travel-time fit for arrivals from this model are shown in Figure 8.22.

The arrivals from the upper crust of the model are a good fit to the experimental data but the modelled arrivals from the lower crust and from the mantle reflectors do not explain the pattern of arrivals seen in the experimental data. The first arrival from the model (a reflection from layer 2) occurs earlier than the experimental arrival, suggesting that layer 2 may not extend this far north. The modelled Moho reflection for Z1A has approximately the same apparent velocity as the highest amplitude arrival in the experimental data but its travel-times are roughly 2 seconds less. This may be due to an increase in the thickness of the crust to the north of line 6.

The experimental arrival with the greatest travel-times between 160 and 220 km offset has a surprisingly low apparent velocity for its position on the travel-time plot. This may be the result of a steeply dipping boundary. Further modelling is needed to explain the arrivals recorded at this station.

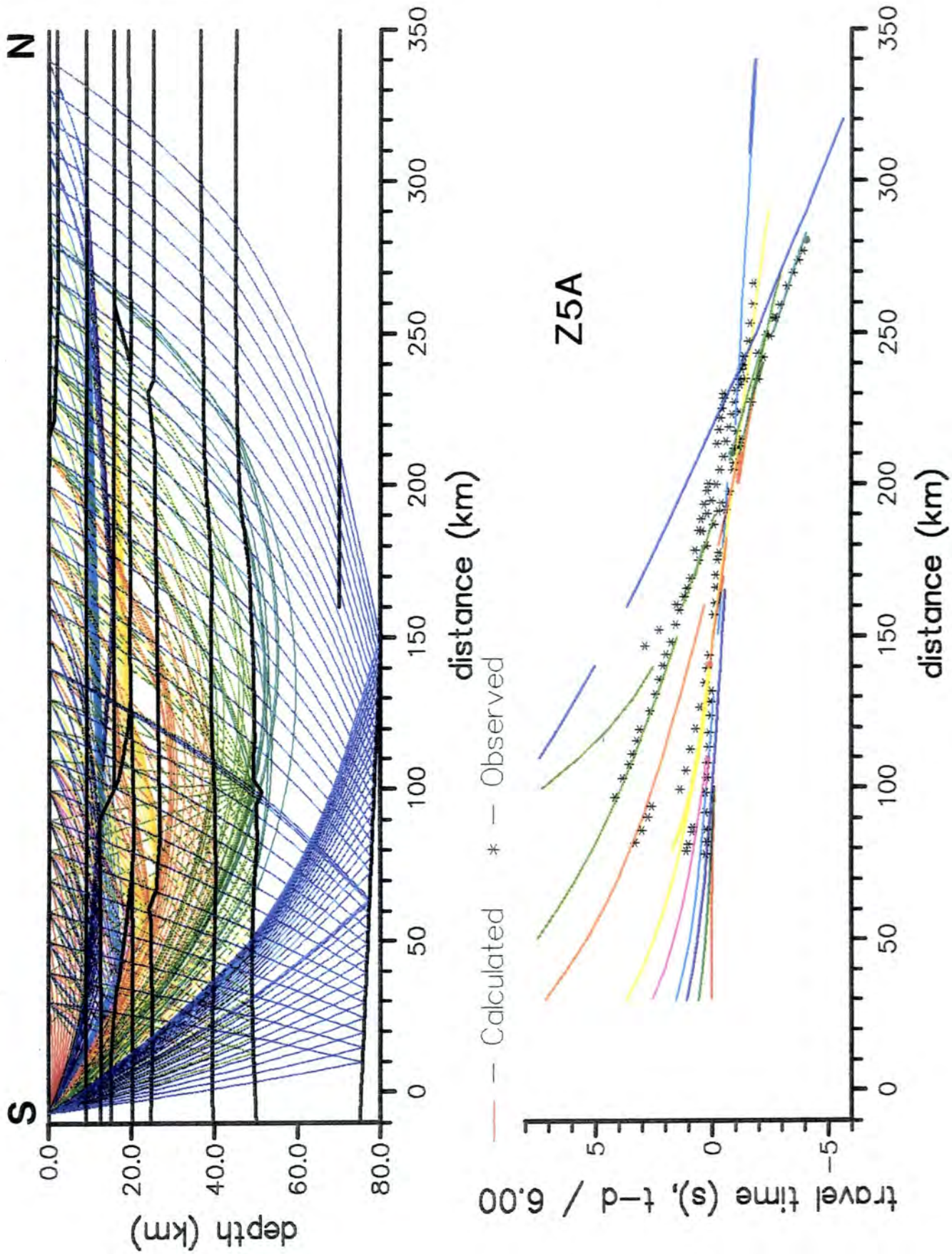

Figure 8.20. Ray diagram and travel-times from the line 6 model compared to the arrivals picked from experimental data for station Z5A.

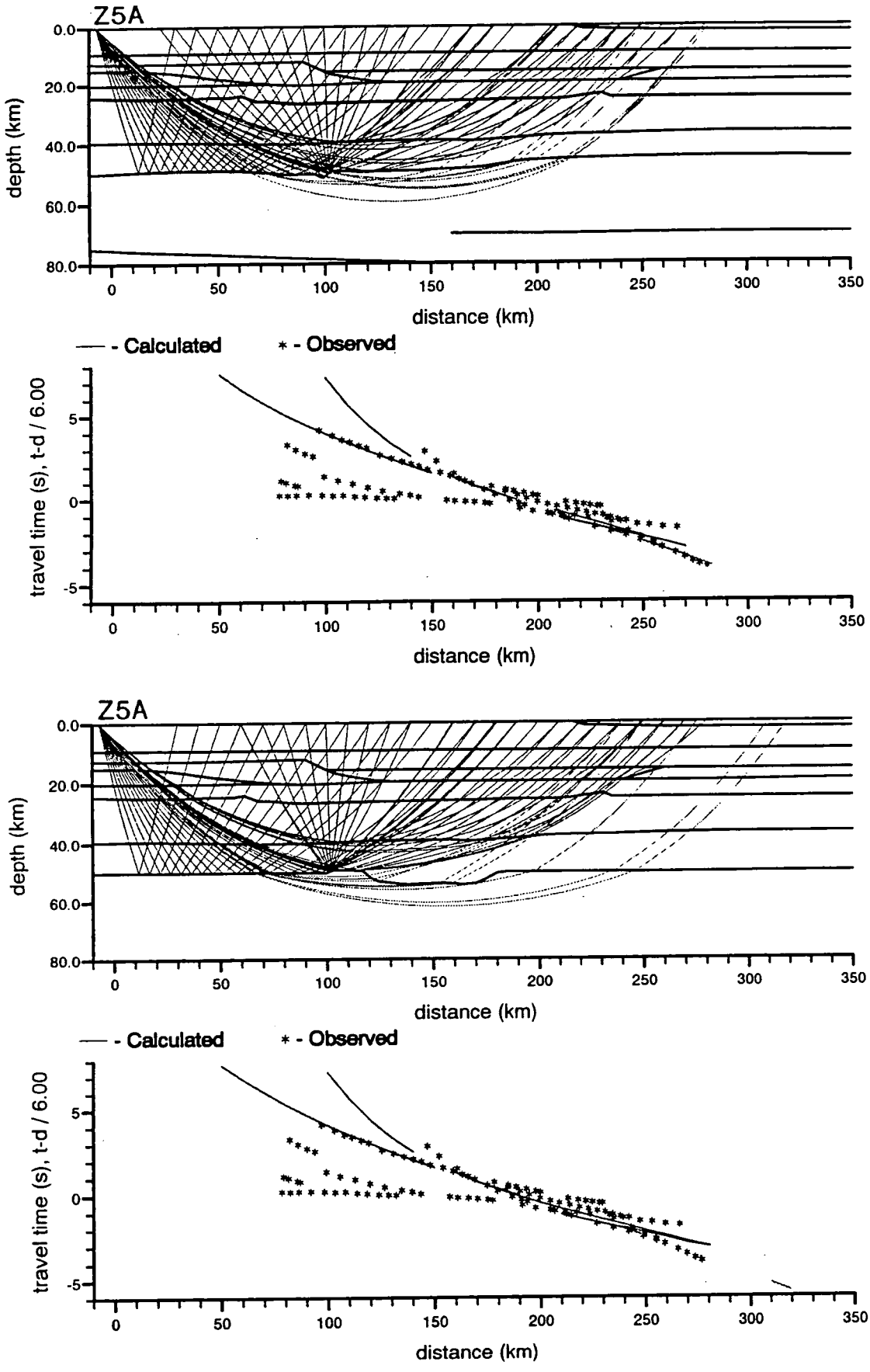

Figure 8.21. Ray diagrams and travel-time plots for the two proposed Moho structures (horizontal and trench models) compared to the experimental data from Z5A.

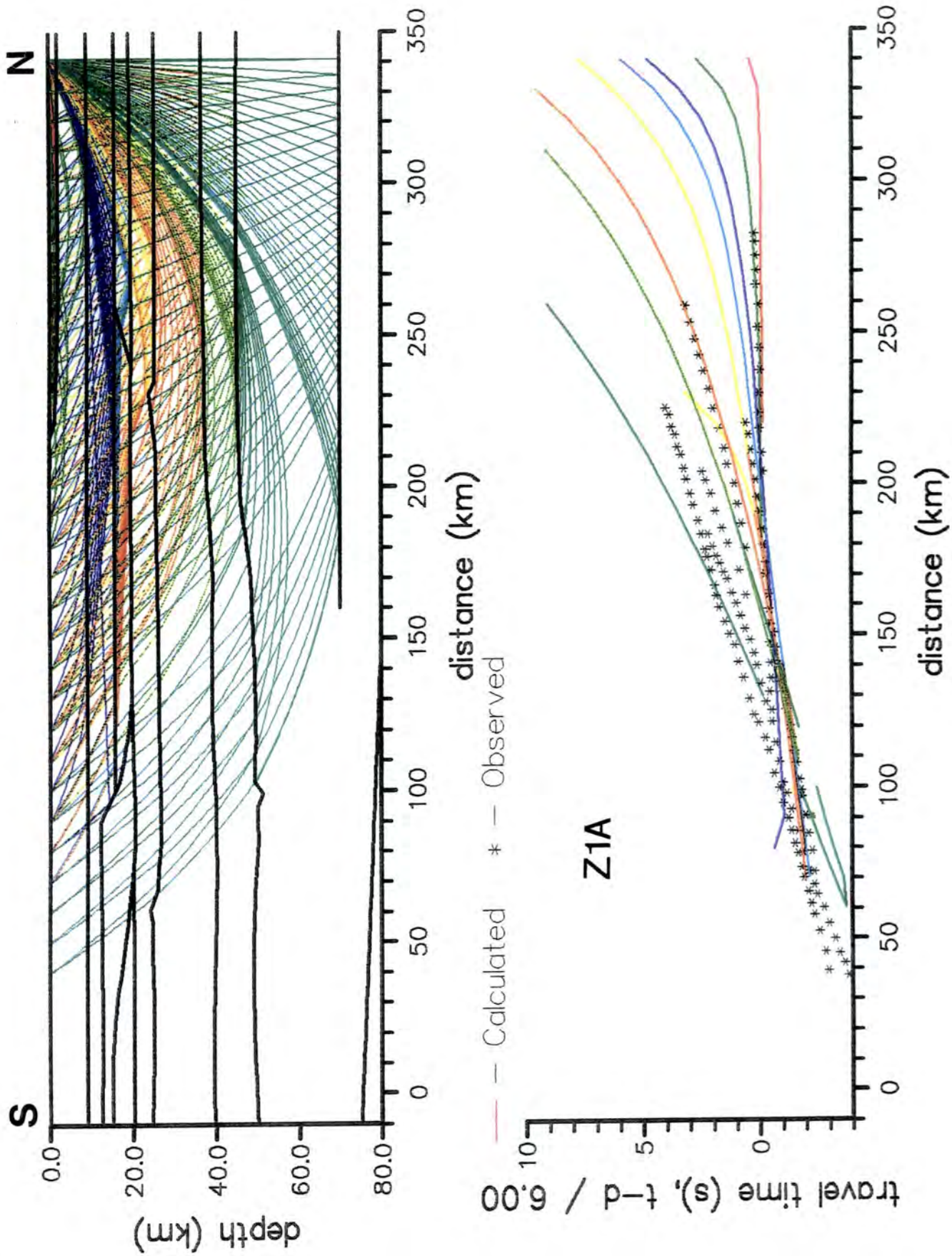

Figure 8.22. Ray diagram and travel-times from the line 6 model compared to the arrivals picked from the experimental data for station Z1A.

8.8 Summary

The main features of the line 6 model (Figure 8.4) found from modelling the wide-angle and normal-incidence data are summarised below:

Near-surface velocities are high (Vp = 5.95 km/s) and rapidly increase to 6.25 km/s at a depth of 9 km. At the northern end of the model, there is a high velocity layer (Vp = 6.05 km/s) at the surface. This layer is not seen in the Z1A data, suggesting that it is of limited extent. Two other high velocity layers are seen in the upper crust (above about 30 km depth) of the model; one in the middle of the line which is about 8 km thick (layer 5) and one at the southern end of the model (layer 7). The velocity in both of these layers is 6.65 km/s and the velocities of the surrounding layers is between 6.2 and 6.4 km/s.

At about 25 km depth, two steps (at about 60 and 225 km offset) are seen on an otherwise horizontal boundary (the base of layer 8). These give rise to the diffraction-type arrivals seen in the BS5P and Z2A data and may be related to some kind of crustal fault (this will be discussed in the next chapter). The shape of these features is controlled by the restrictions of the BEAM87 modelling package. Velocities beneath this boundary increase to 7.51 km/s at the base of layer 10 (about 50 km depth). The interface at the base of layer 10 is interpreted as the crust-mantle boundary. The velocity beneath this interface is poorly defined. A sharp undulation or step on this interface models the diffraction-type arrival seen in the BS5P data.

Including a Moho trench similar to that seen on previous deep seismic refraction profiles worsens the match of the modelled arrivals to the experimental data. The normal-incidence data shows an apparently horizontal crust-mantle boundary although this is deeper than the modelled Moho at offsets greater than 200 km. There is no evidence for a mid-crustal discontinuity separating the crust into upper and lower sections and the v_p/v_s ratios suggest a separation into an upper and lower lithosphere rather than upper and lower crust. Arrivals with high apparent velocities and long travel-times may be explained as mantle reflectors.

The model for line 6 was found from a traditional raytracing approach (with the exception of the diffraction-type arrivals and the normal-incidence modelling). The line 6 model is compared to models from the other BABEL profiles in the Sea of Bothnia and to the previous deep seismic profiles in the Svecofennides in the next chapter. The possible geological interpretations are also discussed.

CHAPTER IX

INTERPRETATION OF THE LINE 6 MODEL

9.1 Comparison to previous Deep Seismic refraction profiles

The results from the deep seismic profiles in the Svecofennian region of the Baltic Shield prior to the BABEL experiment were described in chapter III (these were combined to give a generalised structure for the Baltic Shield, the main features of which are listed in section 3.3). The majority of these are land profiles, running roughly parallel to BABEL lines 1 and 6 but two of the profiles (the Sylen-Porvoo and Blue Road profiles) run roughly east-west across the Sea of Bothnia and lie close to, but do not cross, line 6. The Blue Road profile passes to the north of line 6 while the Sylen-Porvoo profile runs eastwards from a point slightly to the northeast of the intersection of line 7 and line 6. The models for these lines were described in sections 3.1.1 and 3.1.2 respectively. Velocity profiles through the Sylen-Porvoo and Blue Road models at their closest point to BABEL line 6 are shown in Figure 9.1 a and b.

FENNOLORA is the closest land profile to line 6. The resolution of the data from this line is much poorer than for line 6 (section 6.1.5) because of the large shot spacing. Figure 9.2 shows the section of the FENNOLORA model (Guggisberg *et al.*, 1991) for the part of the line neighbouring line 6. The line 6 model described in the previous chapter is plotted on the same scale for comparison.

As with the previous projects, the near-surface velocities in the line 6 model are high (Vp = 5.95 km/s, except at the southern end), indicating that the sedimentary cover is thin. Similar velocities (5.75 - 5.95 km/s) are seen in the near-surface of the FENNOLORA model (Figure 9.2), suggesting that the sedimentary cover in the Sea of Bothnia does not differ greatly to that onshore. The Blue Road velocity profile shows a near surface velocity of 5.8 km/s, while the Sylen-Porvoo near-surface velocity is 6.0 km/s (Figure 9.1). In the models for these lines, the near-surface velocities are the same for the onland and offshore segments. To the north of shot point D, the near-surface velocity in the FENNOLORA model is similar to that seen in the high velocity layer (layer 2) at the northern end of the line 6 model.

Zones of reduced velocity interspersed by higher velocity layers were seen in the upper crust beneath the FENNOLORA profile. Examples of these can be seen in the southern half of the section of the FENNOLORA model (Figure 9.2) between

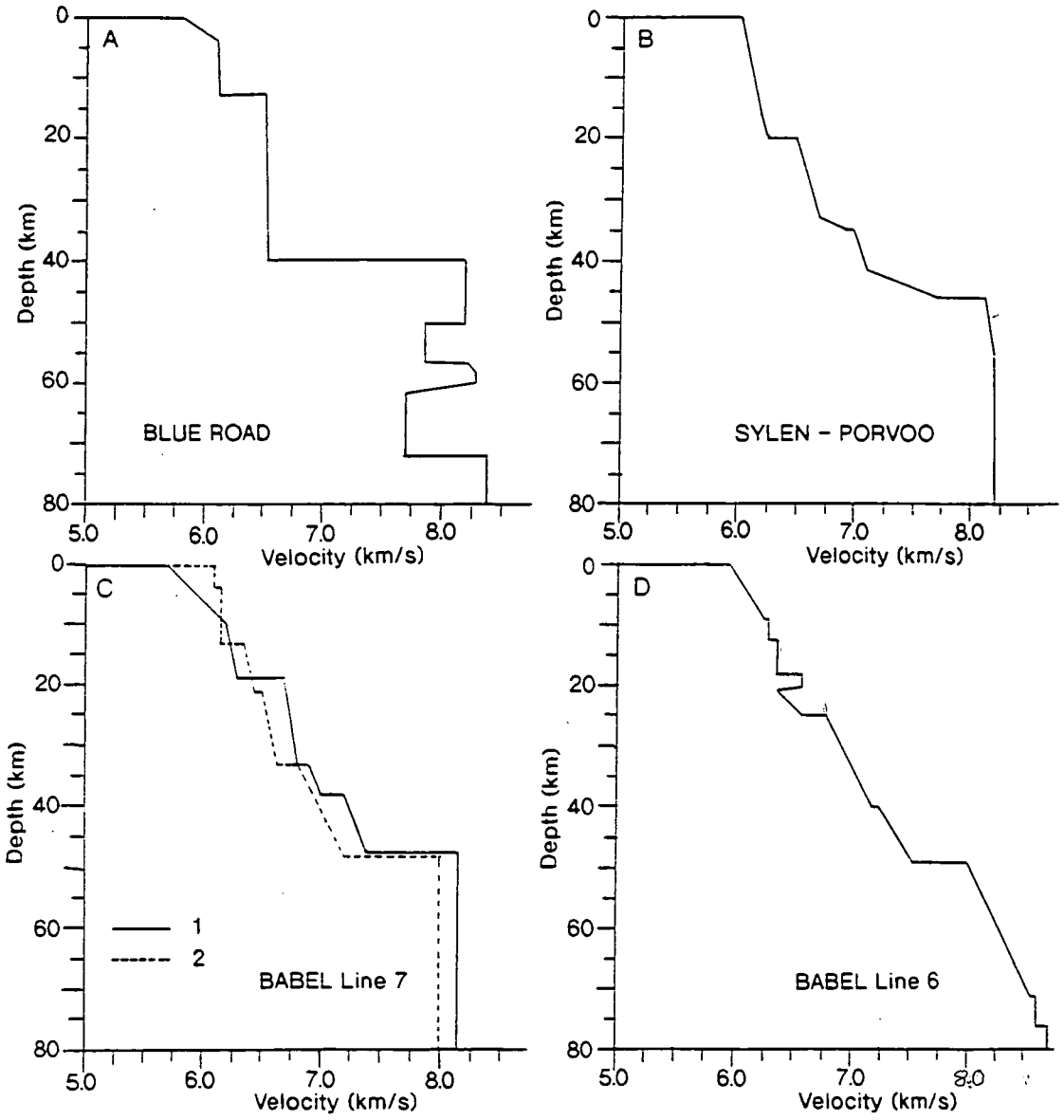

Figure 9.1. Velocity profiles of deep seismic refraction profiles which cross or end near to BABEL line 6. **a)** BLUE ROAD profile, shotpoint 5W (Cassell and Fuchs, 1979); **b)** SYLEN-PORVOO line, west end (Luosto, 1986); **c)** BABEL line 7, velocity profile at the intersection with line 6: 1. Heikkinen and Luosto (1992); 2. Bruguier (1992); **d)** Velocity profile through BABEL line 6 at the intersection with line 7.

offsets of 0 and 200 km. Luosto and Korhonen (1986) describe these reduced velocity zones as 'of limited extent'. The length of these low velocity layers is limited relative to the length of the FENNOLORA profile (Figure 9.3) but many of these 'limited' layers are longer than line 6.

The average crustal velocity for the line 6 model is 6.65 km/s which falls within the range of average crustal velocities found from previous projects (an average crustal velocity of 6.6 km/s was found for the Sylen-Porvoo line that almost reaches line 6 at its western end (Luosto, 1986)). The average crustal thickness of the Baltic Shield is

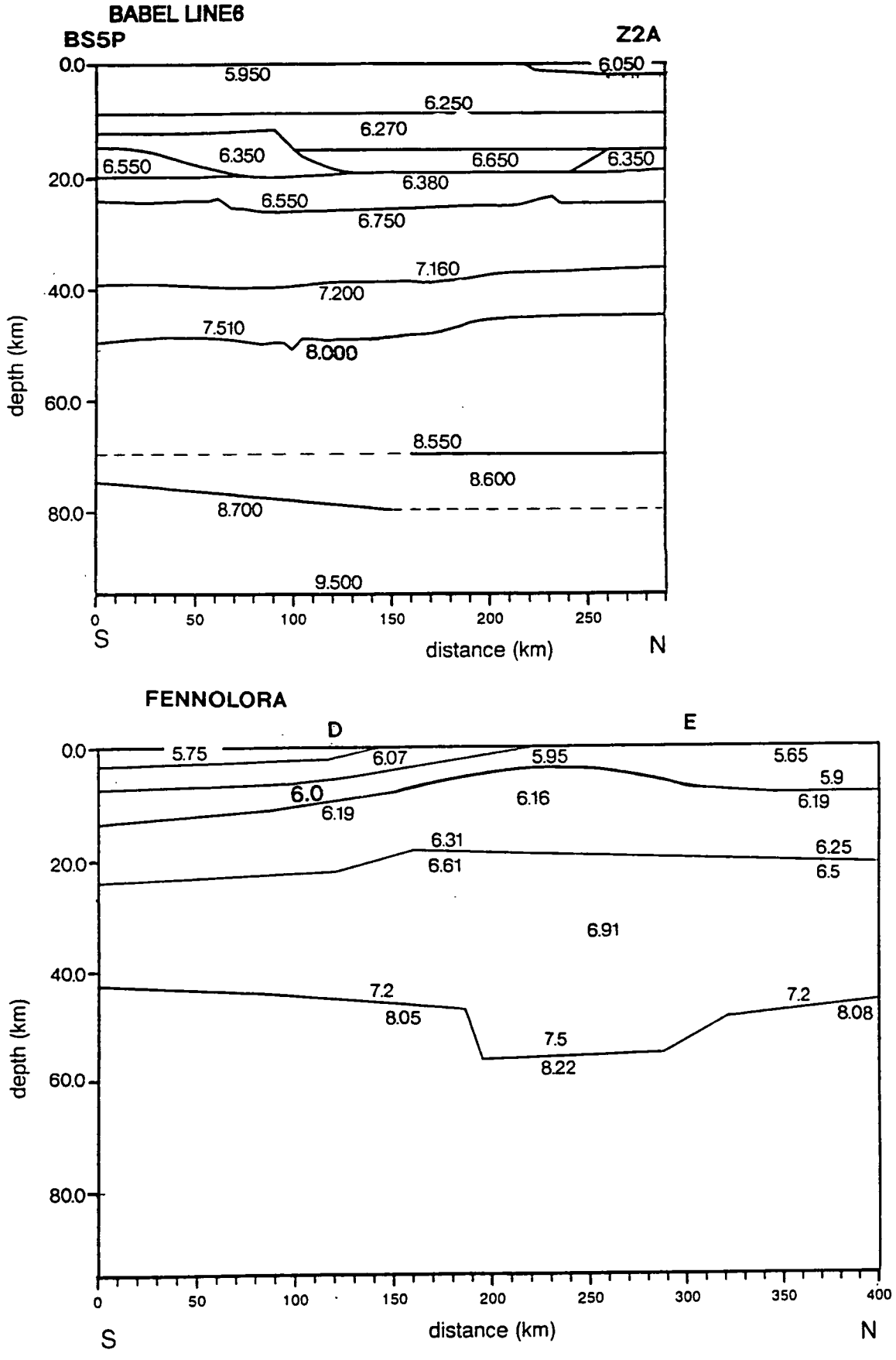

Figure 9.2. Comparison of the BABEL line 6 model presented in this work to the model for the section of the FENNOLORA profile that runs sub-parallel to line 6 (after Guggisberg *et al.*, 1991). Both models are drawn to the same scale.

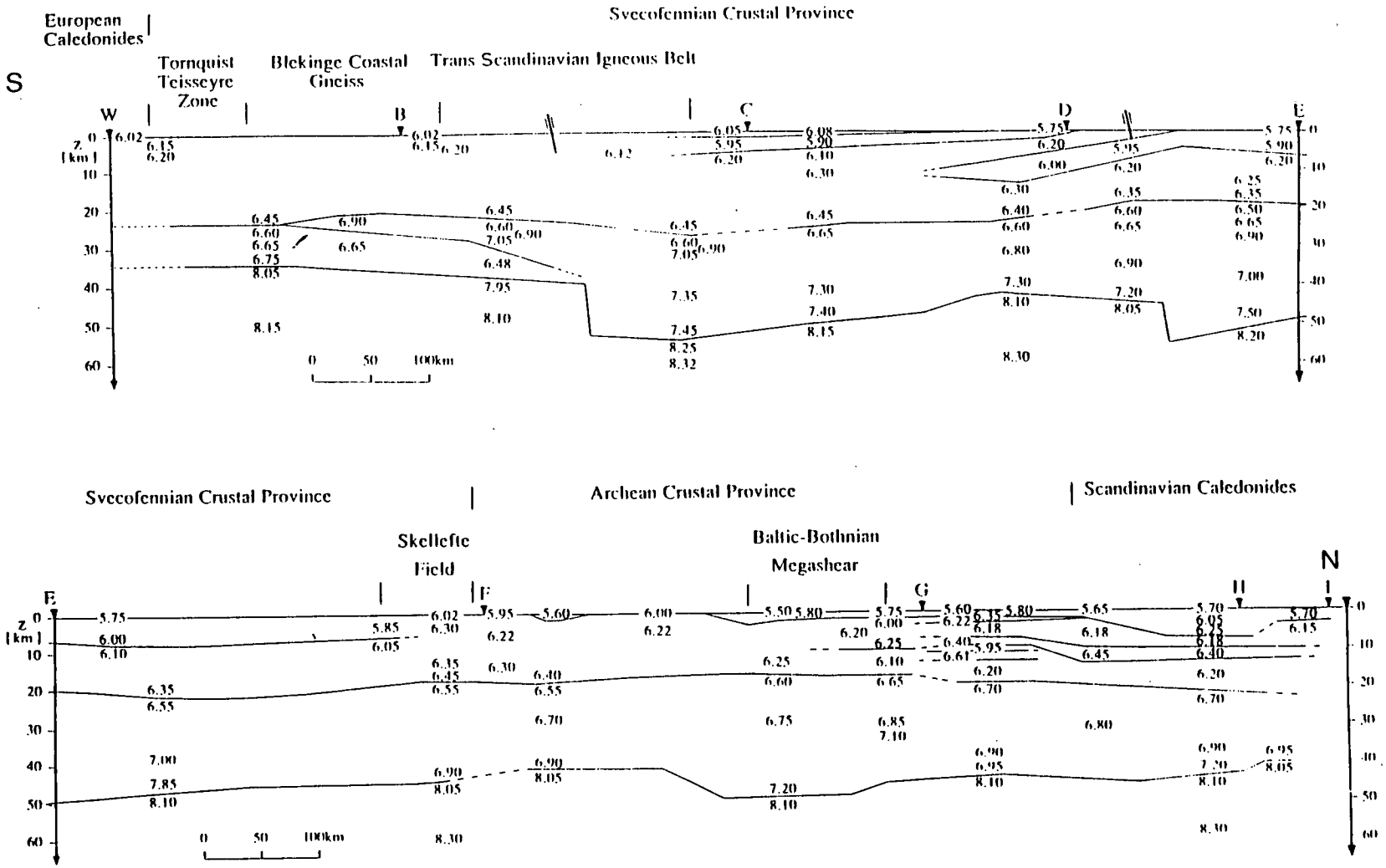

Figure 9.3. Raytraced model for the FENNOLORA profile (Guggisberg *et al.*, 1991). BABEL line 6 lies almost parallel to the section between shot points D and E.

about 46 km. The BABEL line 6 model shows a thicker crust than this (about 49 km) although the crust thins to the north of the line (to about 47 km). On the section of FENNOLORA shown in Figure 9.2, the crustal thickness varies from 42 to 58 km.

A velocity profile through the line 6 model at its intersection with line 7 is shown in Figure 9.1d. The velocities in the line 6 model generally increase gradationally with depth and velocity discontinuities in the model are small. Similar gradational velocities, and a lack of sharp velocity discontinuities, have been found for the FENNOLORA profile and for models from studies of other Shield crust (Guggisberg *et al.*, 1991). For FENNOLORA, zones with strong velocity gradients were found overlying the small velocity discontinuities. Similar zones are shown in the velocity profile for the Sylen-Porvoo line (Figure 9.1b). These zones are not seen in the model for line 6 where changes in velocity gradient are associated with velocity discontinuities.

There is no evidence of a distinct separation into lower and upper crust in the BABEL line 6 model although the crustal structure becomes less complex below about 20 km depth. In several of the previous profiles in the Baltic Shield, an increase in velocity from about 6.3 to 6.6 km/s is seen across a mid-crustal boundary at a depth of about 20 km. In the line 6 model, no such boundary was found and the velocity increases gradationally from 6.38 km/s to 6.55 km/s between 20 and 25 km depth. It has also been suggested that the upper and lower crust have different v_p/v_s ratios (Grad and Luosto, 1987, Hauser and Sangl, 1990). This was not the case for line 6 (section 8.3.7).

High velocity layers, with velocities similar to those of layers 5 and 7 in the line 6 model, have been seen in the upper crust of other refraction profiles. On the BALTIC profile it was suggested that these might be related to intrusions, such as the Rapakivi granite, or to ore bodies, such as the Outokumpu formation (Luosto *et al.*, 1990). Mantle features have been modelled for several of the previous refraction profiles (e.g.. the mantle reflectors in the Blue Road model (Figure 9.1a)). Arrivals from the mantle have generally been explained as the result of alternating high and low velocity layers, although reflectors similar to those modelled for line 6 have also been seen (Luosto, 1986).

Figure 9.4 shows the velocity variation with offset and depth for the SVEKA and BALTIC profiles and for BABEL line 6 (Figure 9.4b shows the line 6 Moho trench which was considered in section 8.3.5). Trenches are seen on the Moho for both the BALTIC and SVEKA models. The trench in the BALTIC model is about 10 km deep and about 250 km wide. In the SVEKA model, the trench is shallower with gently dipping sides. A pronounced depression is seen in the mid crustal layer at about 28 km depth. The proposed Moho trench for line 6 is a much shallower and shorter

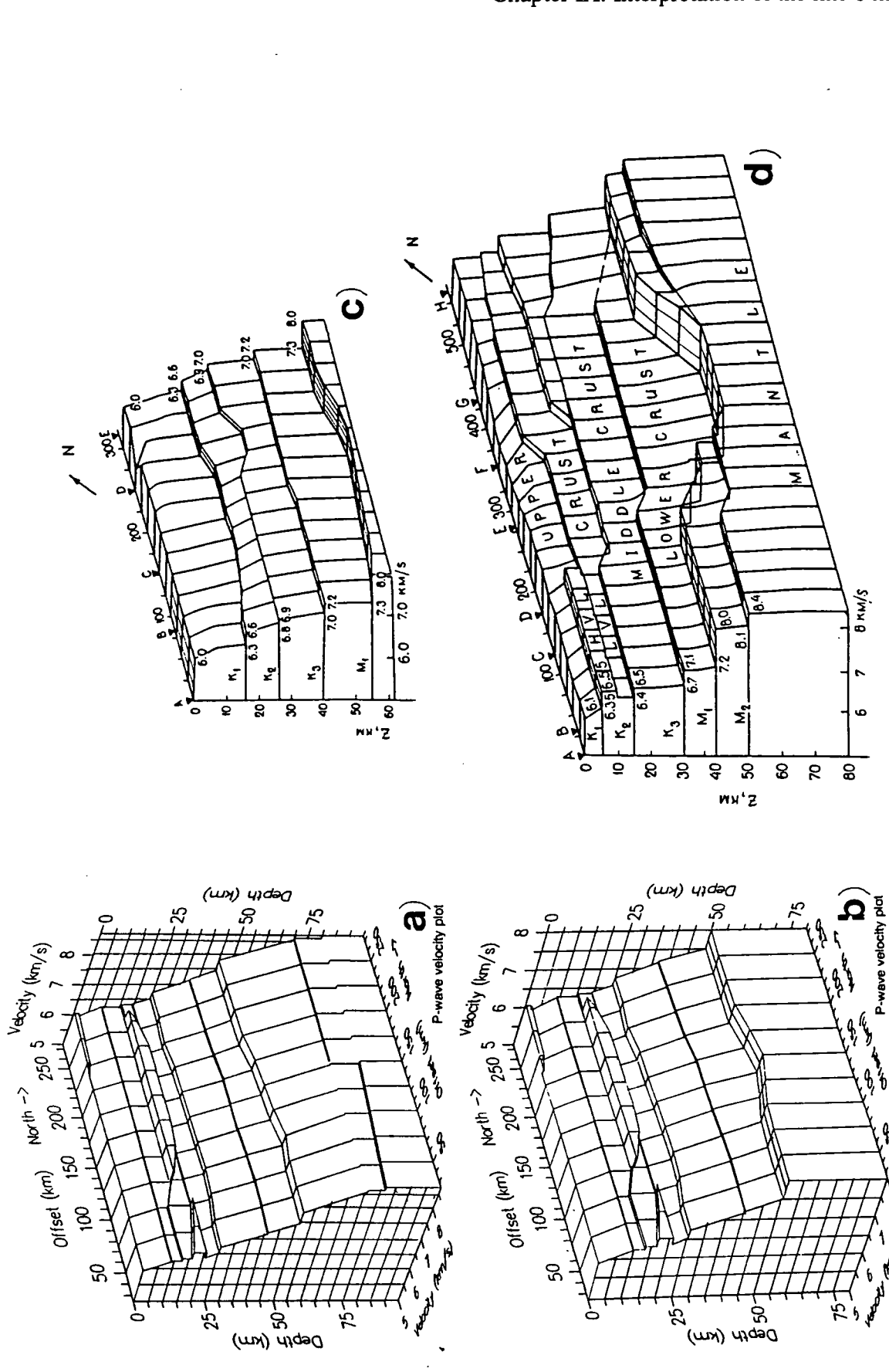

Figure 9.4 Velocity variation with offset and depth for **a)** the BABEL line 6 model, **b)** crustal structure for the BABEL line 6 Moho trench, **c)** the SVEKA profile and **d)** the BALTIC profile. In the line 6 models, only the parts of the mantle interfaces which were modelled as reflectors have been shown.

feature than that seen on the BALTIC profile and no corresponding features are seen in the overlying crust.

Luosto (1990) suggested that the trenches on the BALTIC and SVEKA models could be related to that seen on the FENNOLORA line between shotpoints D and E. If this were the case then a similar feature would be expected on the line 6 model. No clear evidence for such a feature was found and the modelled trench is further south and smaller and shallower than that proposed by Luosto (1990). The implications of this on the trends of geological structures in the Baltic Shield will be discussed later in this chapter.

9.2 Geophysical interpretation: gravity and magnetics

The gravity and magnetic data along line 6 (section 3.2.2) have not been modelled (detailed gravity and magnetic maps of the region were not available until late in 1992). Pedersen *et al.* (1992) have produced simple models from the Bouger anomaly map for line 1 (Figure 3.8b). The northern half of the normal-incidence data for line 1 is shown in Figure 9.5a overlain with the outlines of the high density bodies suggested from gravity modelling. The gravity high seen towards the northern end of line 1 in Figure 3.8b was modelled by Pedersen *et al.* (1992) as a high density body in the mid-crust (labelled LR in Figure 9.5a). This body corresponds to a region of low reflectivity in the line 1 normal-incidence data and was interpreted as a dioritic pluton (bodies with similar densities have been seen on land). The overlying layered sequence was interpreted as a series of metagreywackes.

The gravity high seen on line 1 does not reach line 6 (section 3.2.2) suggesting that the dioritic pluton does not extend this far to the east. No large transparent body similar to that seen on line 1 is seen in the mid-crust of the line 6 normal-incidence data (Figure 9.5a and 9.5b). At the southern end of line 6, where the line intersects line 7, a second gravity high is seen (Figure 3.8b, Pedersen *et al.*, 1992). This is smaller in size than the anomaly seen on line 1. At the southern end of the line 6 normal incidence data, a transparent zone can be seen between about 8 and 12 secs twtt (labelled LR in Figure 9.5b); a similar zone is tentatively identified on the line 7 normal incidence data (labelled LR in Figure 9.5c). The zone is underlain by a band of highly reflective crust similar to that underlying the transparent body in the line 1 normal incidence data. This may be another pluton. No wide-angle reflections from the base of this second body have been identified and modelled for line 6, although wide-angle reflections were modelled from the top of it.

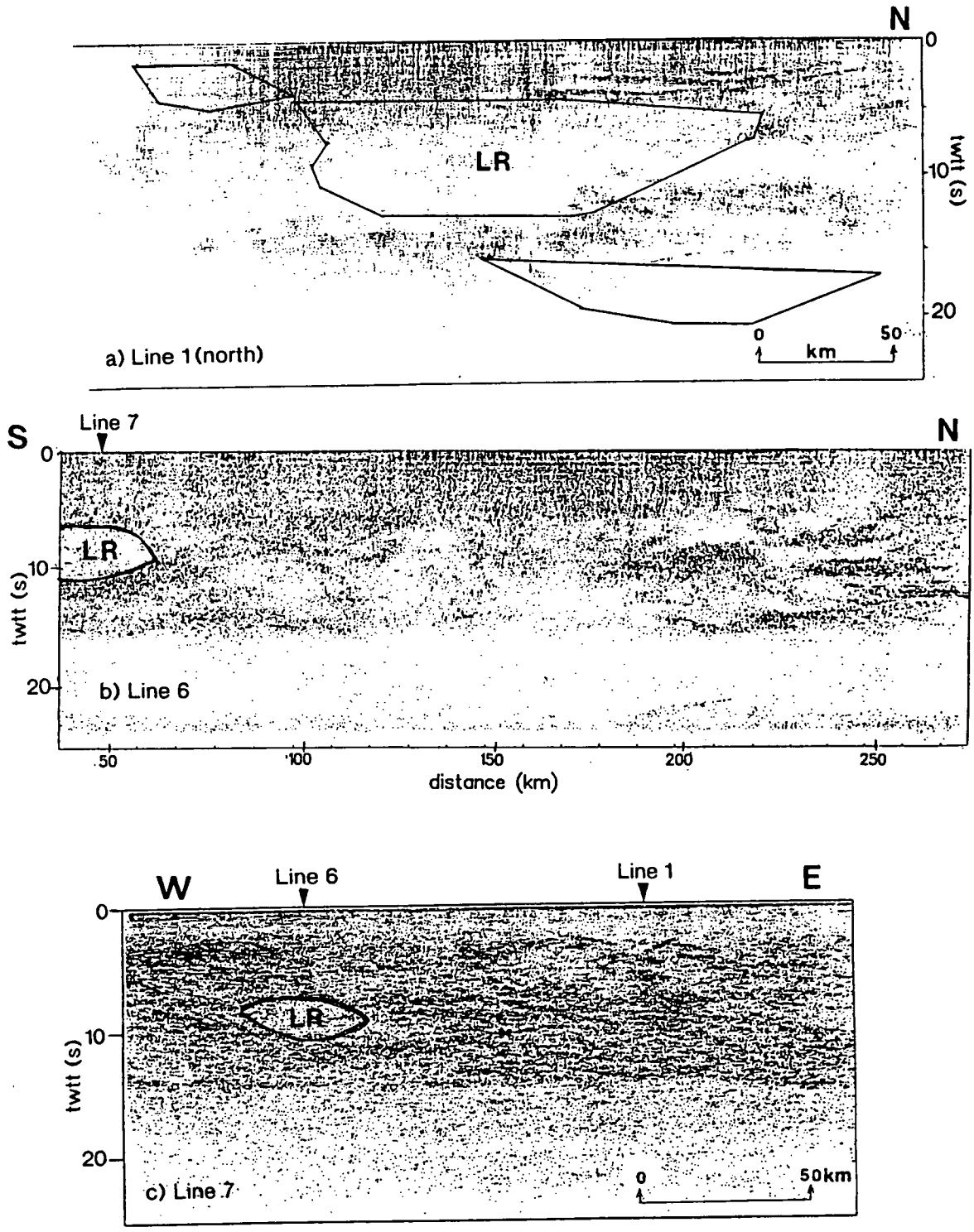

Figure 9.5 a) Normal-incidence data for northern half of BABEL line 1 and the boundaries of bodies found from gravity modelling (Pedersen *et al.*, 1992), **b)** Normal-incidence data for BABEL line 6, **c)** Normal-incidence data for BABEL line 7. LR = region of low reflectivity.

A gravity low is seen at the northern end of lines 1 and 6. On line 1, this was interpreted by gravity modelling as the result of 2-3 km of crustal thickening (Pedersen *et al.*, 1992). The gravity low is < -70 mgals at the northern end of line 1. At the northern end of line 6 the low is smaller (~50 mgals) suggesting that the thickening of the crust is less. In the line 6 model the crust appears to thin to the north rather than thicken. The Moho at the northern end of the model for line 6 is poorly constrained from the wide-angle data and corresponds to the upper boundary of a band of highly reflective crust in the normal-incidence data. The transition from reflective to non-reflective lithosphere that is usually explained as the crust-mantle transition in normal-incidence data, occurs 2-3 km below this and it may be that the crust is thicker than has been modelled. The position of the Moho at the northern end of the line 6 model is poorly constrained by the modelled datasets from Z2A and BS5P (chapter VIII). The results from the Z1A data suggest that the crust may thicken to the north of the model (section 8.5.3).

The Moho trench that was proposed as an alternative to the horizontal Moho in the line 6 model lies too far south to explain the gravity low at the northern end of line 6. The gravity anomaly resulting from this trench can be estimated using the slab formula:

$$\Delta g = 2\pi G\rho t \ .$$

where t is the thickness of the slab, G, the universal gravitational constant and ρ the density contrast. For the line 6 model, the proposed trench was about 2 km deep. Using the density contrast for the upper mantle of $+0.4 g/cm^3$ relative to the crust (as suggested by Pedersen *et al.*, 1992 for line 1), the gravity anomaly due to the trench would be of the order of 30 mgals. This is not seen in the Bouger anomaly map (Figure 3.8b).

The magnetic anomaly map shows a maximum just to the west of the middle of line 6 (Figure 3.9a). A strong maximum is also seen close to the middle of line 7 and is interpreted by Pedersen *et al.* (1992) as a granitic pluton of a different generation than the Rapakivi granites seen on Åland (these are generally much less magnetic than the modelled body). This granitic pluton corresponds to a transparent zone in the upper crust of the normal-incidence data from BABEL line 7. No obvious transparent zone is seen in the upper crust near the centre of the BABEL line 6 normal-incidence data which could be related to the magnetic anomaly seen just to the west of the line. The line 6 raytraced model contains a high velocity layer (layer 5) in the middle of the model which may be associated with the body causing this anomaly.

9.3 Comparison to other BABEL profiles

Of the BABEL lines, only line 7 crosses line 6. Line 1 runs parallel to line 6 in the eastern part of the Sea of Bothnia. The wide-angle reflection data from lines 1 and 7 have been modelled independently by other members of the BABEL working group. Models for line 1 (Graham, 1993) and for line 7 (Bruguier, 1992) are shown in Figure 9.6. Alternative models for lines 1 and 7 proposed by Heikkinen and Luosto (1992) are shown in Figures 9.7. No models have yet been produced for the northern end of line C which crosses line 7 between lines 6 and 1.

The two models for line 7 and the model for line 1 proposed by Heikkinen and Luosto (1992) are traditional raytraced models, consisting of a series of roughly horizontal layers. The structure for line 1 suggested by Graham (1993) is more unusual. Both of the line 1 models show trenches in the northern half of the line. This may be related to the crustal thickening that was proposed by Pedersen *et al.* (1992) to account for the gravity low in this region

Crustal velocities in the line 1 model in Figure 9.7 are similar to those seen in the line 6 model (Figure 9.9b). A low velocity layer with a velocity of about 5.95 km/s is seen in the upper crust of the line 1 model, overlain by a layer with a velocity of about 6.0 km/s. These are similar to the velocities in the northern part of the line 6 model where high velocity layer 2 overlies the lower velocity layer 3. The other high velocity layers in the upper crust of the line 6 model are not seen in the Heikkinen and Luosto (1992) line 1 model. The upper crust of the line 1 model in Figure 9.6 (Graham, 1993) is more complex but no high velocity layers are modelled. Neither of the line 1 models show a body corresponding to the dioritic pluton proposed by Pedersen *et al.* (1992).

Velocity profiles through the line 7 models in Figure 9.6 and 9.7 at their intersection with BABEL line 6 are shown in Figure 9.11c (the vertical velocity profile through line 6 at this point is shown in Figure 9.11d). The crust for line 6 is about 2 km thicker than for either of the line 7 models (the crust/mantle boundary at the intersection of the two lines is not defined in the line 6 model by the wide-angle arrivals but is for line 7). For both line 7 models, the increase of velocity with depth is basically gradational although the Bruguier model contains an inverted velocity zone between 5 and 15 km depth. This is not seen in the other line 7 model or in the line 6 model.

A strong reflector is seen in the line 6 model and in the Heikkinen and Luosto line 7 model at about 20 km depth (in the line 6 model this is the upper boundary of layer 7). A reflector at about 38 km is also seen in both of these models, although the velocity contrast across this boundary is larger in the line 7 model. Both line 7 models show a reflecting boundary at about 34 km that is not modelled for line 6. This is

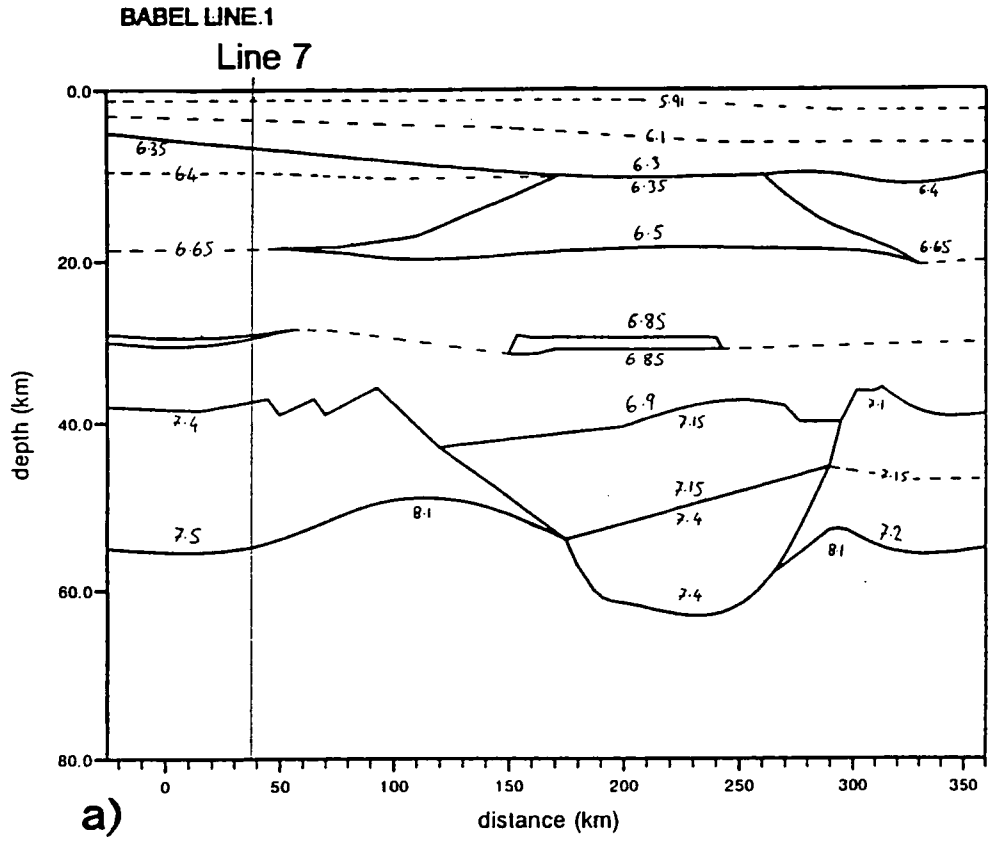

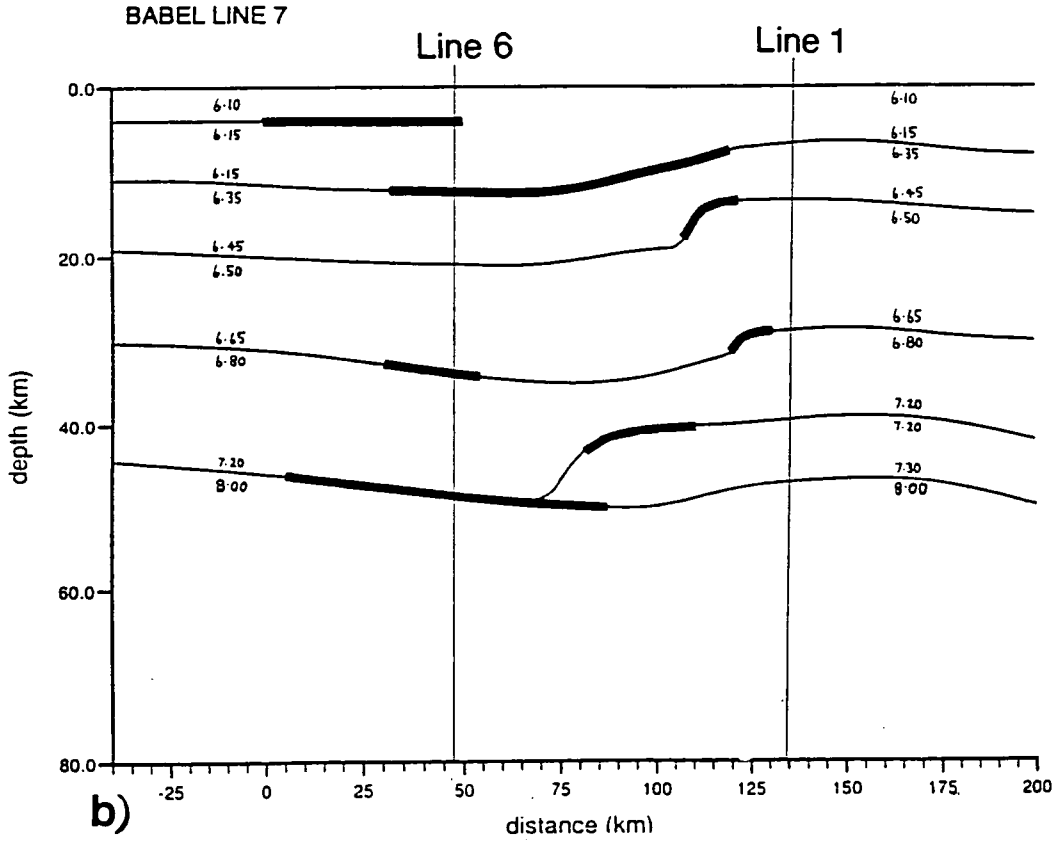

Figure 9.6 a) Crustal structure along line 1 according to Graham (1993); **b)** Crustal structure along line 7 according to Bruguier (1992).

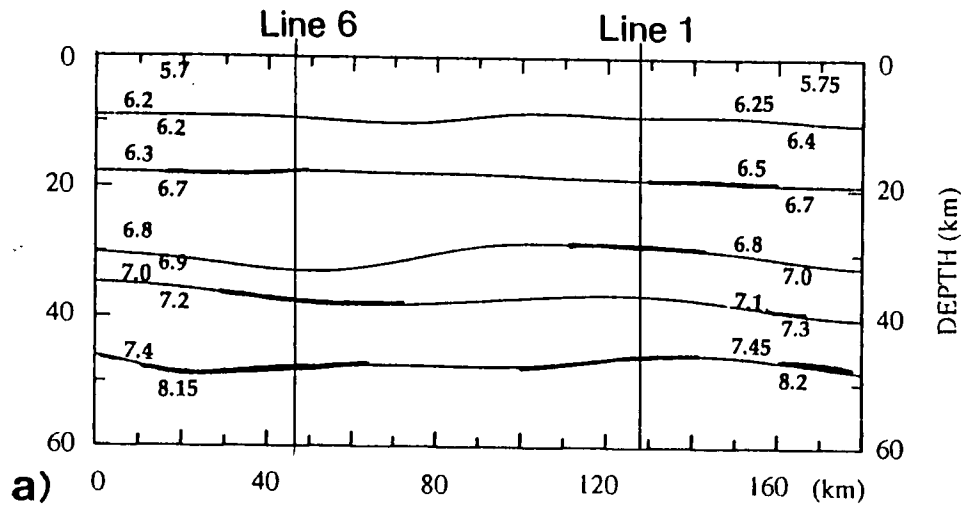

Figure 9.7 Crustal structure along **a)** BABEL line 7 and **b)** BABEL line 1 according to Heikkinen and Luosto (1992).

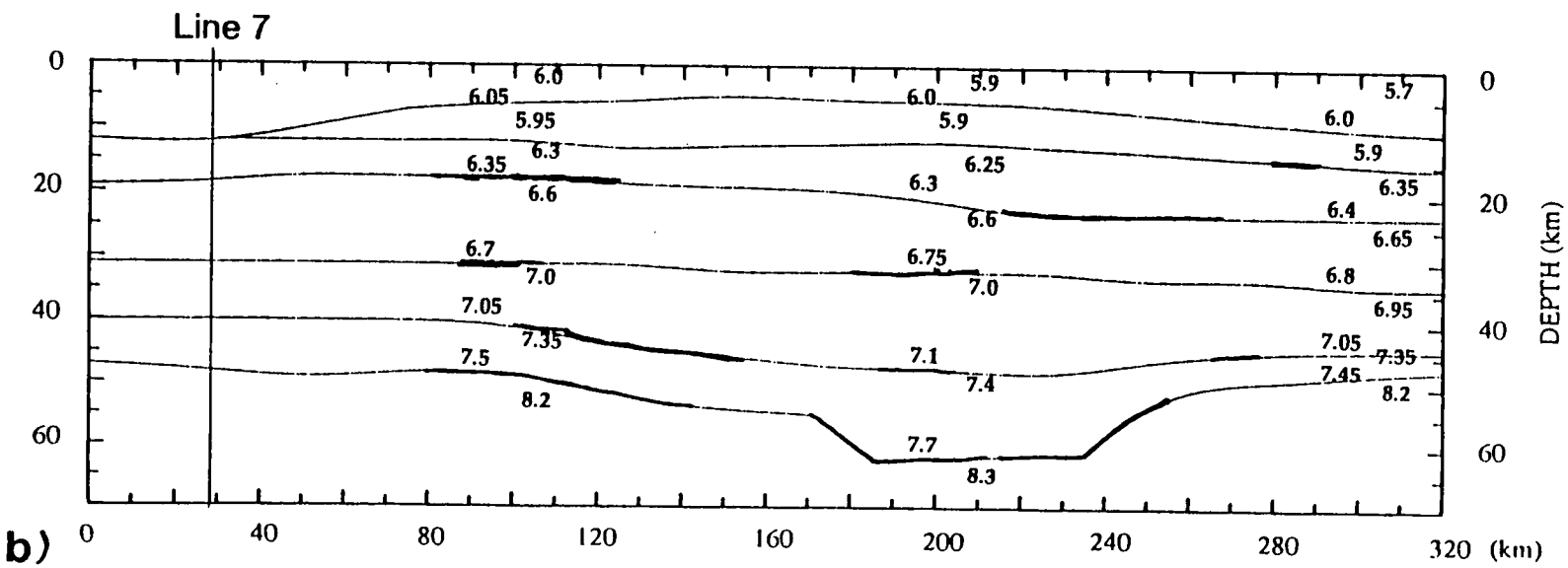

roughly the depth of the base of the transparent body seen in the normal-incidence data at the intersection of lines 6 and 7 which it was tentatively suggested might be a pluton (section 9.2).

9.4 Tectonic interpretation

One of the aims of BABEL was to answer various geological questions about the evolution and structure of the Baltic Shield. A cartoon of a possible tectonic interpretation for the line 6 model is shown in Figure 9.8. The elements of this cartoon and their relevance to the geological questions posed in the introduction to this thesis are discussed below.

9.4.1 Jotnian dolerite sills

One of the most noticeable features of the line 1 normal-incidence data are strong sub-horizontal reflectors which are seen at about 3-4 s twtt at the northern end of the line (Figure 9.5a). These have been explained as dolerite sills (BABEL working group, 1991b). An outcrop of 1.2 - 1.25 Ga sills are seen in Sweden and Finland and dolerite sills intruded into granite in the Siljan area have similar reflection characteristics to those seen on line 1 (Juhlin, 1990). Fracture zones in granitic rock also result in strong reflections but show different reflection characteristics to dolerite sills (Juhlin, 1992).

No strong reflectors comparable to those seen on line 1 are seen in the upper crust of the line 6 normal-incidence data (Figure 9.5b). Beunk *et al.* (1992) have suggested that short length reflectors, with similar reflection characteristics to that of the line 1 sills, may be identified at the northern end of the line 6 normal-incidence data. These reflectors are shown in Figure 9.10a and those seen on line 1 are shown in Figure 9.10b. Although the character of the reflectors on lines 1 and 6 are similar, they differ greatly in form and extent, suggesting that they are not part of the same feature.

Graham has attempted to include the dolerite sills in the raytraced model for line 1 since these sills are such a dominant feature of the line 1 normal-incidence data (Graham *et al.*, 1992). Reflections from these were modelled to explain the first arrivals on the wide-angle data from the north of line 1 (Graham, 1993). No wide-angle arrivals were identified on line 6 from the proposed sills. Modelling these sills with BEAM87 is awkward as they are thin and of limited lateral extent. Beunk *et al.* (1992) estimate that the thickness of these sills is between 0.1 and 0.5 km; the sills discussed by Juhlin, (1990) range from 5 - 60 m in thickness.

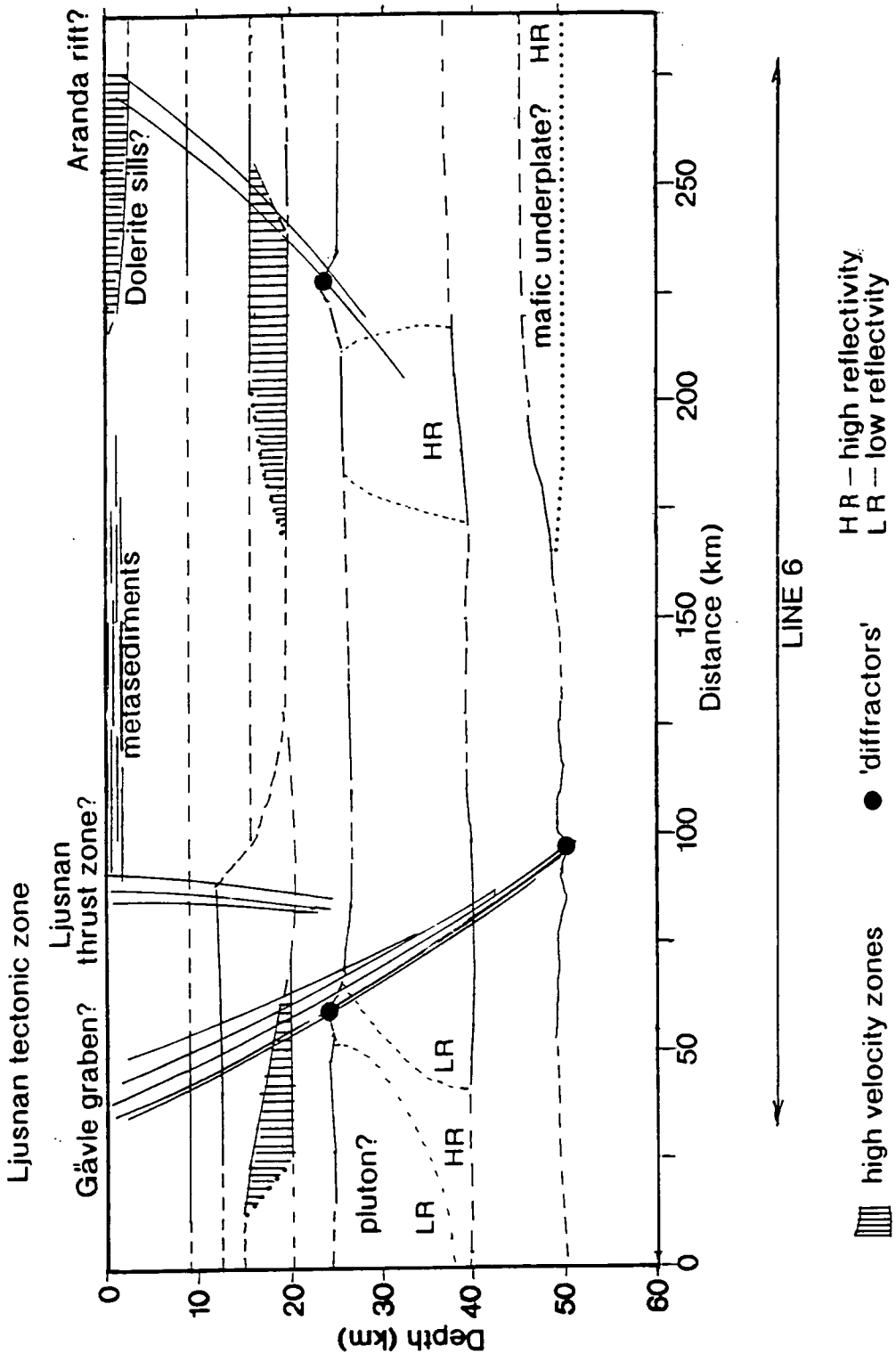

Figure 9.8. Cartoon of the structure of the crust along BABEL line 6.

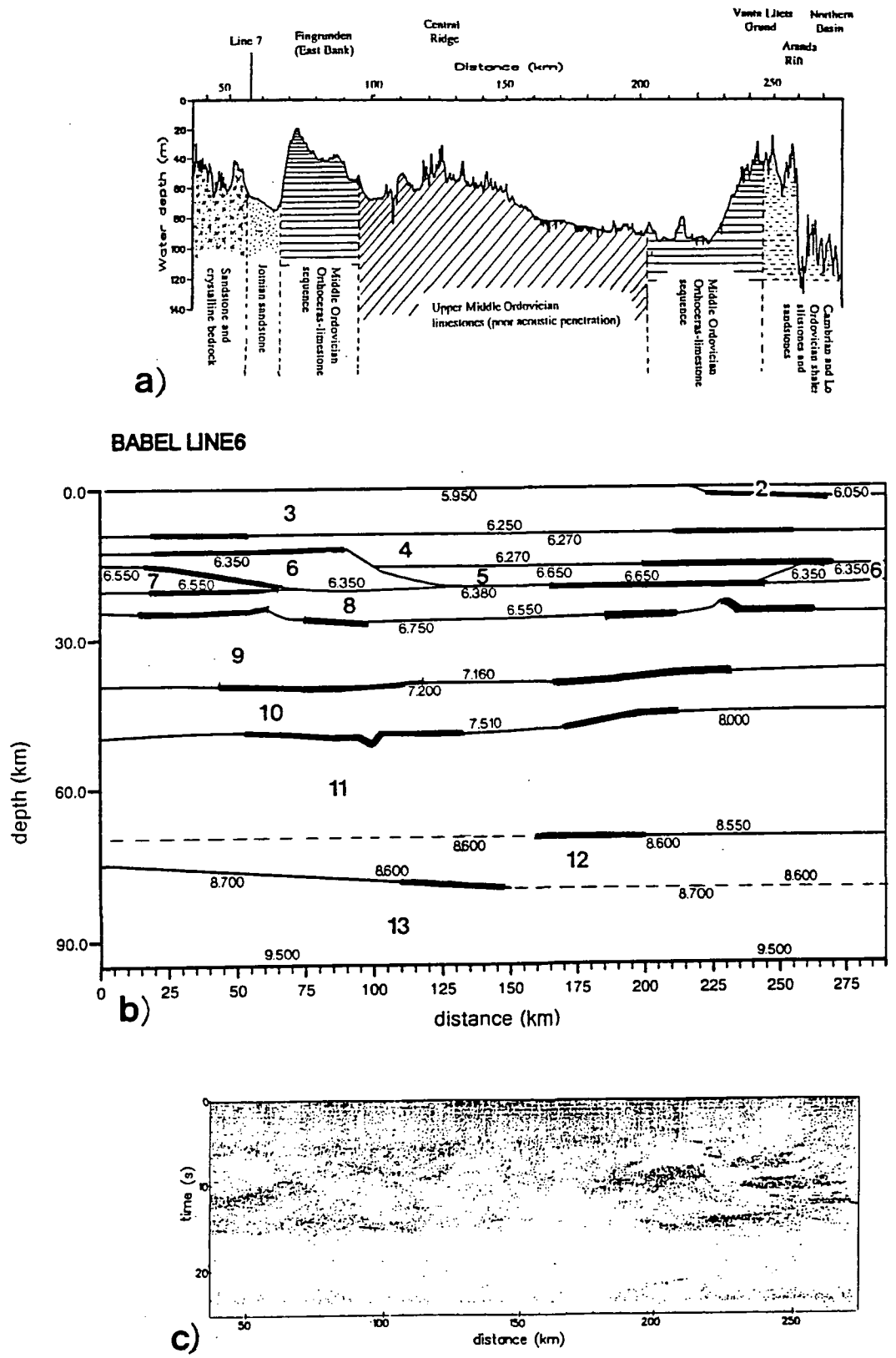

Figure 9.9 a) Variation in water depth and surface geology along line 6. **b)** Raytraced model for line 6. The bold lines are parts of the reflecting boundaries which are defined by wide-angle arrivals. **c)** Normal-incidence data for line 6. All Figures are plotted on the same distance scale.

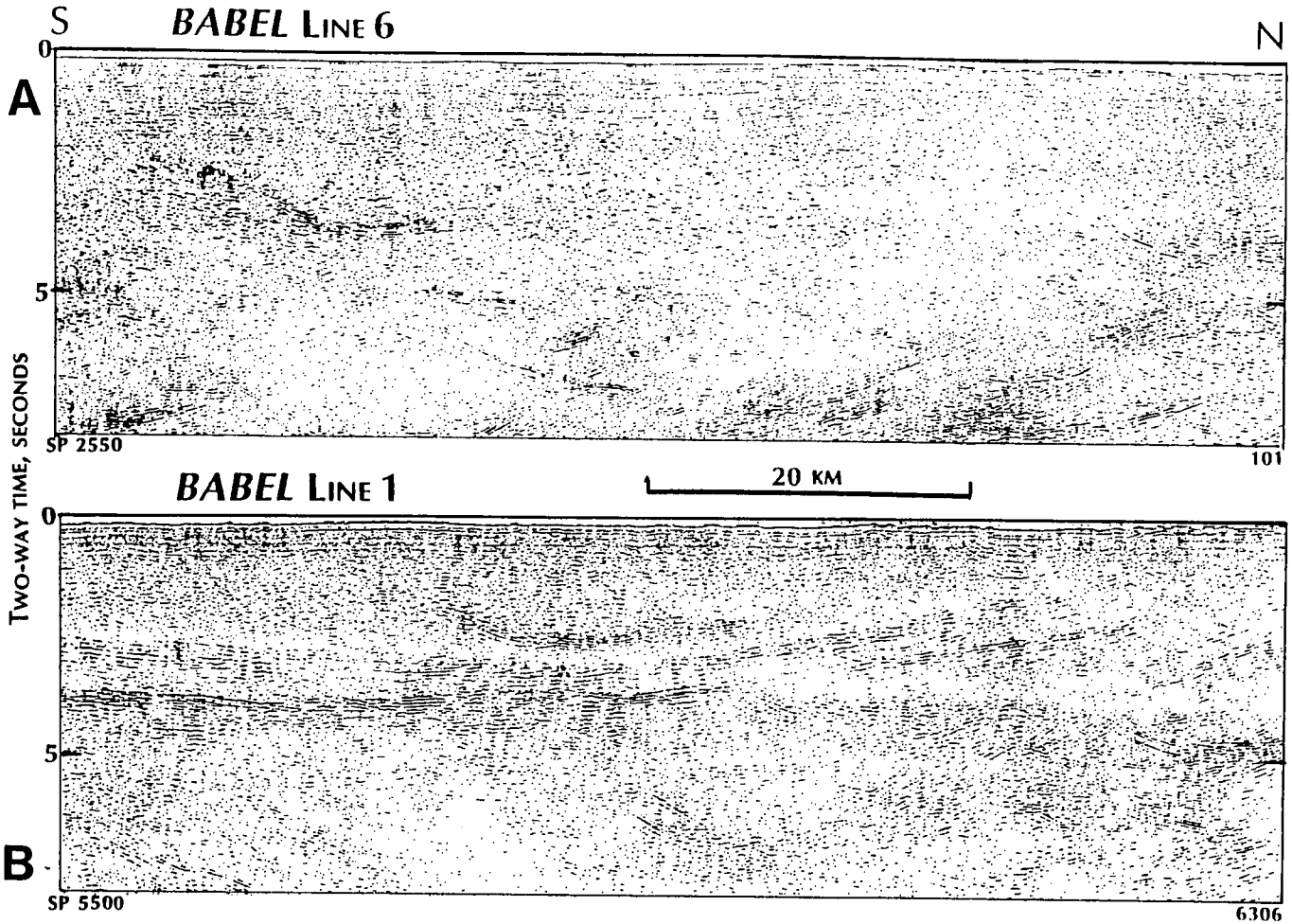

Figure 9.10 a) Possible dolerite sills in the upper crust of BABEL line 6, **b)** Northern end of BABEL line 1 showing the reflection characteristics of the Jotnian dolerite sills. Migrated at 6.5 km/s (BABEL working group, 1993a).

Comparing the raytraced arrivals from the line 6 model to the data from stations Z1A and Z2A (section 8.7) suggest that the high velocity layer at the surface (layer 2) extends over a distance of 100 km (if the high velocity layer extends further than this the modelled first arrivals at Z1A are too early, section 8.7.3). Layer 2 of the model also gives a strong normal-incidence reflection that is not seen in the experimental data (section 8.6.3). It may be that the high apparent velocity first arrival is due to shallow dolerite sills. Further work is needed to attempt to include these in the line 6 model.

9.4.2 Southern and central Svecofennian provinces

Along line 1, the reflectivity is weaker beneath the central Svecofennian province of metasedimentary and granite rocks than beneath the southern metavolcanic arc rocks (Heikkinen and Luosto, 1992). On the line 6 normal incidence data, the highest reflectivity is seen at the northern end of the line, in part of the central Svecofennian province. No division into central and southern provinces is evident. Gaál (1986) suggests that the boundaries between the different provinces may have been obscured by post-orogenic intrusions (section 2.3.2).

In the middle of line 6, the lower crust is almost non-reflective and there are no strong Moho reflections. Beunk *et al.* (1992) suggested that non-reflective lower crust on line B might be due to an intensely deformed zone with steep structures and abundant amphibolites. Continuous wide-angle arrivals (modelled as reflections from horizontal boundaries) are seen from the patch of non-reflective lower crust and no steeply dipping structures have been modelled from this region. On the normal-incidence data for line 6, weak reflections can be seen which appear to show the reflection Moho continuing horizontally through this region. This suggests that the apparent low reflectivity may be the result of poor penetration of energy to the lower crust at normal-incidence due to the overlying limestone (Winterhalter, 1972, section 6.2.3) rather than to crustal structure.

9.4.3 Reflectivity patterns

Most normal-incidence profiles in cratonic areas show low reflectivity and numerous diffractions (BABEL, 1991b). For line 6, the reflectivity pattern is very complex with bands and layering in the lower crust and diffractions. Nelson (1991) proposes that cratonic regions evolve as the result of episodic intrusions of the crust by mafic magmas and that this is the cause of the extensive dike swarms seen in Precambrian Shields. Nelson also suggests that these dike swarms are the result of

anorogenic magmatism associated with extensive underplating of the continental crust (anorogenic magmatism has been widespread in the Baltic Shield (Andersson, 1991)). This underplating would also explain the thick, high velocity, lower crust that is often seen in cratonic regions. Underplating thickens the crust by the addition of new mafic material but the maximum Moho depth may be limited to about 50 km by the gabbro/eclogite phase transition. The voluminous injections into the overlying crust disrupts the pre-existing lithological layering and destroys pre-existing reflectivity patterns. The patchy nature of lower crustal normal-incidence reflectivity on BABEL line 6 could be the result of the partial destruction of initial reflectivity patterns by intrusions.

The tectonic origins of most Precambrian dike swarms are poorly understood. Another hypothesis is that they originate as the result of the transition of the Shield across a mantle upwelling. A transition of the Baltic Shield over a hot spot was proposed by Pesonen *et al.* (1989) from the results of palaeomagnetic measurements. This was interpreted as affecting the southern part of the Svecofennides and could explain why the northernmost part of normal-incidence data for line 6 has the highest reflectivity (less of the original reflectivity has been destroyed by intrusions).

There is no clear evidence of underplating in the line 6 model. At the northern end of the line 6 model, the Moho shallows and coincides with the upper boundary of a highly reflective layer in the normal-incidence data (section 8.3.5). It may be that this highly reflective layer is the result of some sort of underplating. The overlying dolerite sills in the upper crust may have been intruded when this layer was added to the crust.. Beunk *et al.* (1992) have interpreted highly reflective lower crust on BABEL lines C and 7 as a possible mafic underplate.

Whatever the cause of the anorogenic intrusions, they would be expected to obliterate all but the largest orogenic structures (such as suture zones). A possible suture zone has been identified on the BABEL profiles in the Bay of Bothnia (lines 2, 3 and 4, BABEL working group, 1991b). No major orogenic features have been identified for line 6. This agrees with the description of the evolution of the Svecofennides given in chapter II.

9.4.4 High velocity layers and intrusions

Guggisberg *et al.* (1991) explained the thin low velocity zones in the FENNOLORA model as granites and granitoids embedded in gneiss and metasediments enriched by mica (granites which are seen at the surface near shotpoint E have low seismic velocities). No low velocity zones were modelled for line 6 but several high velocity layers were found with P-wave velocities of about 6.5 km/s. High

velocity bodies were seen on the BALTIC profile in Finland (section 3.1.5). These were explained by Luosto and Korhonen (1986) as being associated with the Rapakivi granites and with the Outokumpu ore formation. The Outokumpu is a strong geoelectrical anomaly and no similar anomaly is seen in the vicinity of line 6. This suggests that the high velocity layers may be related to intrusions similar to the Rapakivi granites.

The parts of the line 6 model boundaries defined from the wide-angle reflections are shown in Figure 9.9b. Figure 9.11 shows the normal-incidence arrivals from the segments of the boundaries in Figure 9.9b superimposed on the normal-incidence data for line 6. Some of these segments appear related to reflectors on the normal-incidence data (such as the arrival labelled 1 in Figure 9.11) and some occur where there is no noticeable feature on the normal-incidence data (i.e. arrival labelled 2 in Figure 9.11).

The majority of the wide-angle arrivals appear to originate from the boundaries between reflective and non-reflective patches. If the pattern of reflective and non-reflective zones results from intrusions, as has been suggested by several authors (e.g. BABEL working group, 1991b, Pedersen *et al.*, 1992 and Beunk *et al.*, 1992), then it appears that wide-angle arrivals are coming from the boundaries of these bodies rather than from any laterally continuous interfaces. For example, at offsets around 50 km wide-angle reflections are seen from the edges of a transparent patch (labelled 3 in Figure 9.11) while at the northern end of the line at similar depths wide-angle reflections are seen from the edges of a highly reflective patch (labelled 4 in Figure 9.11). The reflective and non-reflective patches may correspond to different kinds of intrusive material, since the mafic underplate described by Beunk *et al.* (1992) for line B is highly reflective while the dioritic pluton suggested by Pedersen *et al.* (1992) for line 1 is non-reflective.

9.4.5 Archaean basement and mantle reflectors

There is no indication in the results from line 6 of the Archaean basement underlying the Svecofennides that was suggested by Welin (1987). On the northern BABEL lines, Archaean basement shows reflectors which dip in a different direction to the rocks of the Karelides and Svecofennides (BABEL working group, 1991b).

The mantle reflectors in the line 6 model do not correspond to any features in the mantle of the normal incidence data (section 8.3.6) although a reflector is seen in the normal-incidence data at offset of about 150 to 170 km. Further modelling is needed for the arrivals seen on the line 6 wide-angle and normal-incidence data from beneath the Moho.

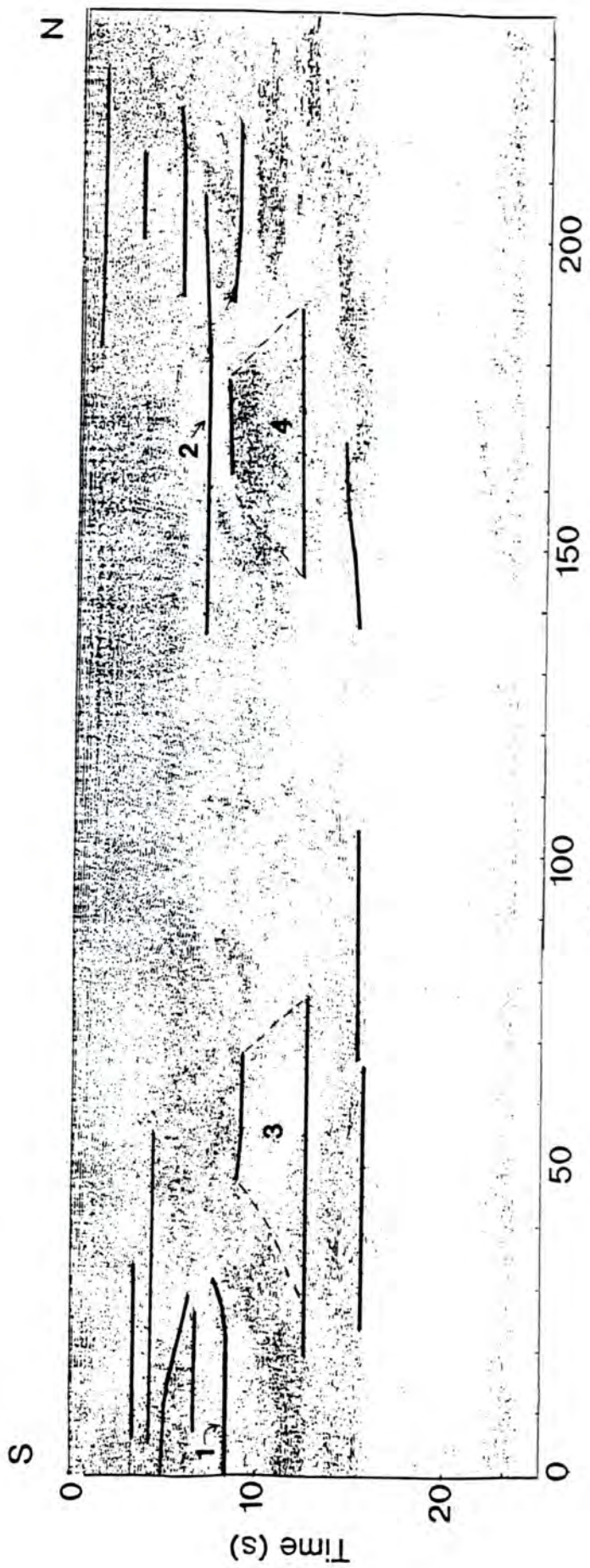

Figure 9.11. Normal-incidence arrivals from the line 6 raytraced model superimposed on the normal-incidence data. The bold lines are reflections from the parts of the boundaries which are defined by the wide-angle arrivals.

9.4.6 Baltic-Bothnian shear zone

A major shear zone was proposed by Berthelsen and Marker (1986) (the Baltic-Bothnian shear zone (BBZ), section 2.3.3) running mid-way between lines 1 and 6 and crossing line 7. If this exists, then geological and tectonic structures that were once continuous across the Sea of Bothnia should have been displaced dextrally by about 125 km. No indication of the Baltic-Bothnian shear zone is seen in the line 7 model of Heikkinen and Luosto (1992, Figure 9.7a) but the line 7 model according to Bruguier (1992, Figure 9.6b) shows several large displacements of otherwise horizontal layers which may be related to the shear zone.

Figure 9.12 shows the relative position of crustal features on lines 1, 6, 7 and on the FENNOLORA profile. The Moho depressions seen on line 1 and on FENNOLORA, and the trench that was suggested as a possibility for the line 6 model, are projected on to the surface as shaded regions. If the trenches on line 1 and line 6 were part of the same feature then the displacement of this would be of the order of that proposed by Berthelsen and Marker for the Baltic and Bothnian shear zone. The gravity data from the region suggests that this is not the case, since the thickened crust along line 1 is related to a gravity low which extends as far as line 6 but to the north of the line 6 trench.

The Jotnian sills post-date the proposed last movement of the Baltic- Bothnian shear zone (Berthelsen and Marker, 1986). Jotnian dolerite sills are seen on line 1 and it is suggested that the high velocity near-surface layer on line 6 may be related to a similar feature (9.4.1). On the map in Figure 9.12, these two features lie at roughly the same latitudes. The high velocity layer on line 6 does not appear to be related to the high velocity layer on the FENNOLORA profile.

9.4.7 Relation of surface faults to crustal structures

Guggisberg *et al.* (1991) suggested that the depression of the Moho seen between shotpoints D and E on the FENNOLORA profile was related to a major surface thrust zone (the Ljusnan thrust zone, Figure 9.12). They proposed that this structure might have formed by a process similar to 'crocodile tectonics' (Meissner *et al.* 1991) and that the upper crust has ridden up over the southern block while the lower crust has been pushed down in to the uppermost mantle (Figure 9.13). Shearing is proposed to have occurred in the middle crust, explaining why there have been no major depth changes here.

This thrust zone has not been traced offshore. If it were extended then it would cross line 6 in the region of the 'diffractor' (glitch) on the Moho. The 'diffractors'

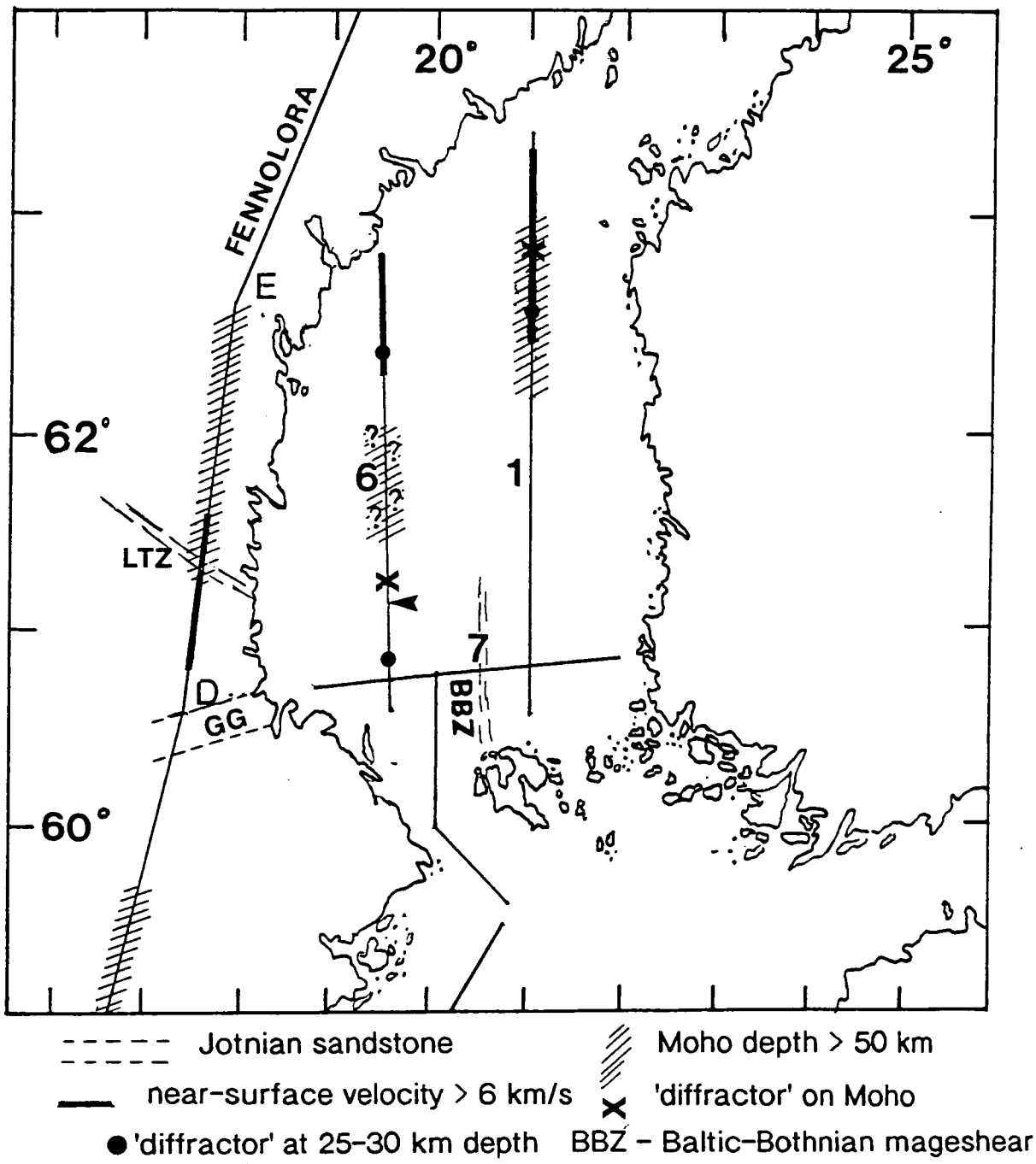

Figure 9.12. Location of features on BABEL lines 6, 1 and 7 and FENNOLORA. GG - Gävle graben. LTZ - Ljusnan thrust zone. Thick lines = near-surface velocities greater than 6 km/s (for line 6 and FENNOLORA), location of Jotnian dolerite sills (line 1). The arrow indicates the sudden change in depth of the reflector between layers 4 and 6 at the southern end of the line 6 model.

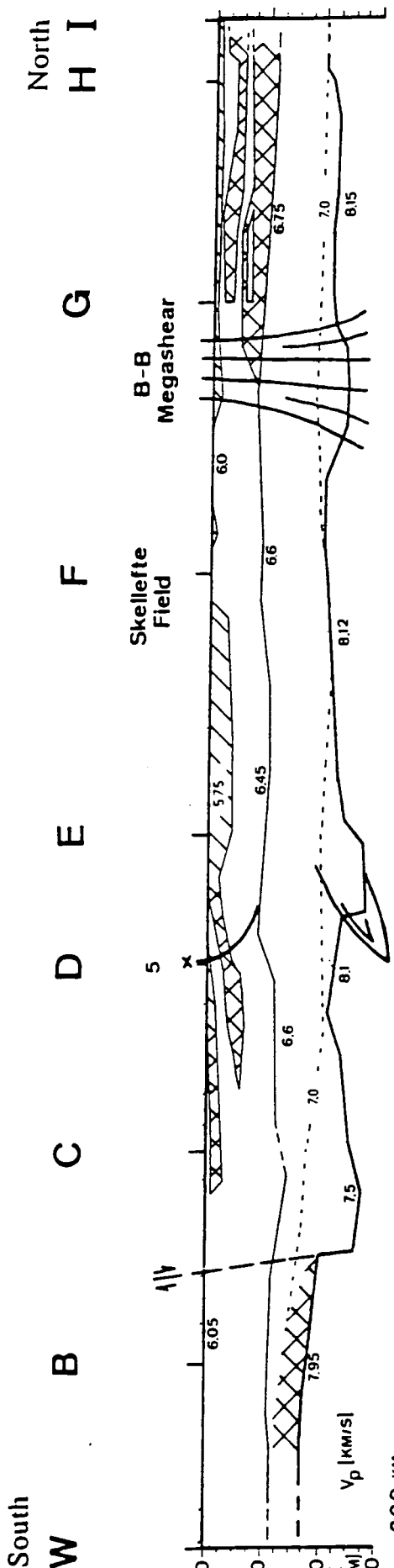

Figure 9.13. Tectonic interpretation of the FENNOLORA model (Guggisberg *et al.*, 1991).

in the mid-crust and the abrupt change in depth of the boundary between layers 4 and 6 (Figure 9.9b) are shown in plan view in Figure 9.12. It may be that the southern mid-crustal diffractor, the Moho diffractor and the abrupt change in depth and the truncation of layer 6 are all part of the Ljusnan thrust zone running out into the Sea of Bothnia. The possible location of the Ljusnan fault is shown in the cartoon for line 6 (Figure 9.8). There is no indication of the 'crocodile tectonics' proposed by Guggisberg *et al.* (1991) in either the line 6 model or the normal-incidence data.

Major crustal faults have been proposed from the results of the MOBIL project which suggested that the Dowsing fault zone was a crustal scale feature, extending down to, and cutting, the Moho (Matthews, 1989, West, 1990). Strong diffraction-type arrivals were seen in the wide-angle data beneath the surface trace of this fault, originating at Moho depth. These arrivals were modelled using structures similar to those used to model the diffraction-type arrivals seen on line 6. Kusznir and Matthews (1988) predicted that the decay of a Moho offset could result in this kind of structure (this will be discussed in more detail in the next chapter).

The variation in water depth along line 6 is shown in Figure 9.9a plotted on the same distance scale as the line 6 model beneath it. Several major changes in depth are seen along the line. The Aranda rift does not appear to be related to a fault cutting the Moho but may be related to the mid-crustal diffractor at the northern end of the line and to the northern truncation of the high velocity layer (layer 5). The Aranda rift is not seen in the normal-incidence data.

A mid-crustal diffractor is seen towards the northern end of line 1 (Figure 9.12). The Aranda rift does not extend this far east and this diffractor may be related to the Strömmingsbädan scarp system (Figure 2.7). An alternative explanation is that the diffractors at the northern ends of line 6 and 1 are related to the intrusion of the Jotnian dolerite sills.

The small region of Jotnian sediments seen at the southern end of line 6 may have been deposited in an offshore extension of the Gävle graben (Figure 9.12). Onshore this graben is filled with Jotnian and younger sediments and, if continued offshore, would cross line 6 in the vicinity of the Jotnian sediments shown in Figure 9.5a. The mid-crustal diffractor at the southern end of line 6 lies directly beneath this feature and it may be that this is related to a fault controlling this graben.

9.4.8 Evolutionary models

Two main evolutionary models have been suggested to describe the growth of the Baltic Shield: a plate tectonic description (e.g. Gaál and Gorbatschev, 1987) or in terms of block tectonics (e.g. Witschard, 1984, Welin, 1987). In the plate tectonic

description, the Svecofennides are explained as having formed by magmatic and sedimentary accretion and no major tectonic structures are expected along line 6. The patchy nature of the normal-incidence data, and the wide-angle arrivals from the edges of some of these patches, support the idea of wide spread intrusions into the crust. No Archaean basement was identified for line 6 which supports the plate tectonic explanation rather than the block tectonic evolution proposed by Welin (1987).

The mantle reflector seen in the normal-incidence data and the mantle arrivals on the wide-angle data may be the relics of a subduction zone which once existed to the north of line 6 (possibly at an intermediate stage during the southwards movement of the subduction zone to beyond the borders of the Svecofennian domain, section 2.3.2). Support for Proterozoic and earlier plate tectonics in the Baltic Shield comes from the more northerly BABEL profiles where a Proterozoic subduction zone has been imaged (BABEL working group 1991b, Snyder, 1992).

CHAPTER X

IS TRADITIONAL RAYTRACING ADEQUATE ?

The line 6 model described in the last chapter is a traditional raytraced model produced by assuming wide-angle arrivals are a series of reflections and diving rays from a series of extensive, roughly horizontal crustal layers (the diffraction-type arrivals modelled for line 6 are a deviation from this traditional assumption). Raytracing packages, such as BEAM87, are designed to model this kind of layered crust. The concept of crustal layers is partly based on physical intuition, which suggests that, since pressure and temperature increase with depth, then chemical changes will lead to a different layers at different depths, and partly from the results of low resolution refraction and wide-angle reflection seismology.

Refraction and wide-angle reflection seismology often appear to show continuous arrivals which can be followed over large distances. Wide-angle reflections are usually modelled as arising from sharp velocity discontinuities in the crust which are laterally continuous. Beneath the sedimentary layers, deep seismic normal-incidence data frequently fails to show the strong laterally continuous reflectors that would be expected from sharp velocity discontinuities. Instead the data shows regions of high and low reflectivity. The regions of high reflectivity appear to consist of numerous short length reflectors (often of about the same length as the Fresnel zone at lower crustal depths) while the intervening regions are almost transparent. The Moho and the Conrad discontinuities have been identified in normal-incidence data as corresponding to transitions from low reflectivity to high reflectivity rather than to a particular reflector.

In some cases the discrepancies between wide-angle models and normal-incidence data can be explained if the wide-angle arrivals are not reflections but are diving rays in layers with steep velocity gradients. Reflections are seen from sharp velocity discontinuities at both normal-incidence and wide-angle but diving rays in velocity gradients are only seen on wide-angle data.

The increased resolution of wide-angle data from projects such as MOBIL and BABEL has shown that wide-angle arrivals are much more complex than was assumed from lower resolution datasets. Arrivals that would have been picked as a single continuous arrival from lower resolution data now appear to consist of a series of overlapping arrivals. Rapid changes in phase and amplitude with offset can be seen in

the higher resolution data. This suggests that the crustal structure is more complex than a series of laterally continuous, horizontal layers. Despite this, the data is often still modelled using computer packages designed for structures consisting of a series of horizontal layers (as for the traditional model for the line 6 data described in the previous two chapters). The problems with this approach are discussed below.

10.1 Problems with the traditional raytracing approach

10.1.1 General Problems

i) The accuracy of the crustal model depends on the accuracy of the selection of the original arrivals from the experimental data. If arrivals cannot be traced over large distances (due to problems with interference or rapid fall off of amplitude) then it is not always possible to determine whether an arrival is a reflection or a diving ray. It is important to re-interpret the data sections as the modelling progresses and as ideas about the possible crustal structure develop. Some crustal arrivals predicted by wide-angle models may not agree with those picked from the experimental data. Re-interpreting the data sections can determine whether the experimental arrivals have been wrongly picked or if this particular arrival was overlooked during the original interpretation or if it is not seen in the experimental data (in which case the model may need to be altered).

ii) Raytracing is designed to model two types of arrivals: diving rays from velocity gradients and wide-angle reflections from velocity contrasts. Other kinds of arrivals, such as point diffractions and head waves, are not modelled. 'Pseudo-head waves' may be modelled as diving rays in a positive velocity gradient beneath a boundary. At offsets greater than 150 km, the amplitudes of immersed rays (diving rays beneath a boundary) are an order of magnitude greater than those of head waves, even for velocity gradients as small as 10 ms^{-1}/km. As a result, pure head waves are rarely seen in experimental data (Červený, 1966). 'Diffraction-type' arrivals, which have a travel-time curve similar to that of point diffractions, may be modelled as diverging reflections from a tightly curved part of the boundary. It has been suggested that the diffractions seen in shallow seismic data may arise from the steep curvature of reflecting boundaries in the vicinity of faults, rather than from true point diffractors.

iii) Wide-angle synthetic sections rarely mimic the complexity of amplitude and phase seen in the experimental data. This is partly because only the major arrivals are modelled and the interference with the arrivals from the previous shot is not included,

but there also appear to be other influences controlling small scale amplitude variations. This suggests that there are lateral changes in crustal composition over short distances (~1 km). These small scale variations in amplitude and phase cannot be modelled by simple reflections and diving rays from a sequence of horizontal layers.

iv) Even using traditional methods for modelling continuous wide-angle arrivals, the wide-angle reflections only constrain short lengths of the model boundaries (see chapter IX, Figures 9.6, 9.9 and 9.11). The continuation of these layers laterally across the model comes from the assumption that wide-angle reflections arise from sharp velocity discontinuities in a layered crust. The reflection could also be interpreted as defining the edges of crustal 'blocks'.

10.1.2 Problems with the line 6 model

i) No extensive horizontal reflectors are seen in the BABEL line 6 normal-incidence data. There is also no sign of the division of the crust into the non-reflective upper crust and reflective lower crust that is often described for deep seismic normal-incidence data ('the typical BIRP', Matthews and Cheadle, 1986) and there is no boundary in the line 6 normal-incidence data that could correspond to a mid-crustal (Conrad) discontinuity. Even the assumed reflection Moho (usually marked by a clear transition from high to low reflectivity) shows a large variation in reflection character along the line.

ii) The geological history of the Svecofennides does not support the idea of a crust consisting of roughly horizontal layers. Nelson (1991) suggests that episodic intrusion of magma into the crust is part of the process of cratonisation and that this should distort original reflectivity patterns. Surface geology shows numerous intrusions of various sizes and of various ages and it seems reasonable that the crustal cross section should show similar features.

iii) All of the models for the previous deep seismic refraction profiles in the Baltic Shield (described in chapter III) and all of the BABEL models described in the previous chapter (with the exception of the line 1 model of Graham (1993)) show similar features: basically horizontal layers, velocity discontinuities across reflecting boundaries, etc. Almost all of these models have been generated by raytracing using BEAM87 or its predecessor SEIS83. The similarity of the models may be a result of a bias of the modelling package towards horizontally layered structures, rather than a true representation of the crustal structure in the Svecofennides.

iv) Ansorge *et al.* (1982) suggested that the selection of arrivals by different interpreters had a greater effect on the form of the final model than the modelling package used. Although this is generally true, the initial approach to modelling the data is affected by the design of the package. For example, in BEAM87, models are defined in terms of horizontal interfaces. The way in which these interfaces are defined makes it easier to add structure at the edges of the model (beneath the common 'shot') than in the centre of the line. This is particularly noticeable when modelling reversed data, since if structure is added in the centre of the model it affects the fit to the experimental data at both ends of the line.

10.2 Alternative crustal models

The problems with the traditional raytracing approach stem from the assumption that the crust consists of a series of layers. Neither the normal-incidence data nor the higher resolution wide-angle data (such as BABEL and MOBIL) support this view. Several simplistic models of alternative crustal structure have been constructed using the BEAM87 raytracing package to show:

a) how simple structures can give rise to a complex series of wide-angle arrivals with rapid variations in amplitude similar to those seen in the experimental data and
b) how wide-angle arrivals which may be mistaken for continuous arrivals can arise from structures similar to those seen at normal-incidence (i.e. from assemblages of short length reflectors).

The complexity of the models is limited by the fact that BEAM87 is designed to model horizontal layers. The alternative models described below are 'semi-horizontal' because of the manner in which interfaces are defined. Fictitious interfaces have been used for sections of the layer boundaries to limit the length of reflectors in the model. The different models are described below.

In all of the examples, apart from the 'WART' (section 10.2.4), the upper crust of the models consists of a 1 km thick layer of water and sediment with a velocity of 1.6 km/s that overlies a layer with a constant velocity of 6.5 km/s down to 25 km depth. The velocity in the lower crust increases gradationally from 6.6 to 7.5 km/s, unless otherwise stated. The source signature for the synthetic seismograms is the MINTROP signal that was used for the line 6 models. The synthetic seismograms have been normalised so that the variation in amplitude is due to the crustal structure rather than an effect of offset (a normalised wide-angle data section is shown in Figure 10.1 for comparison).

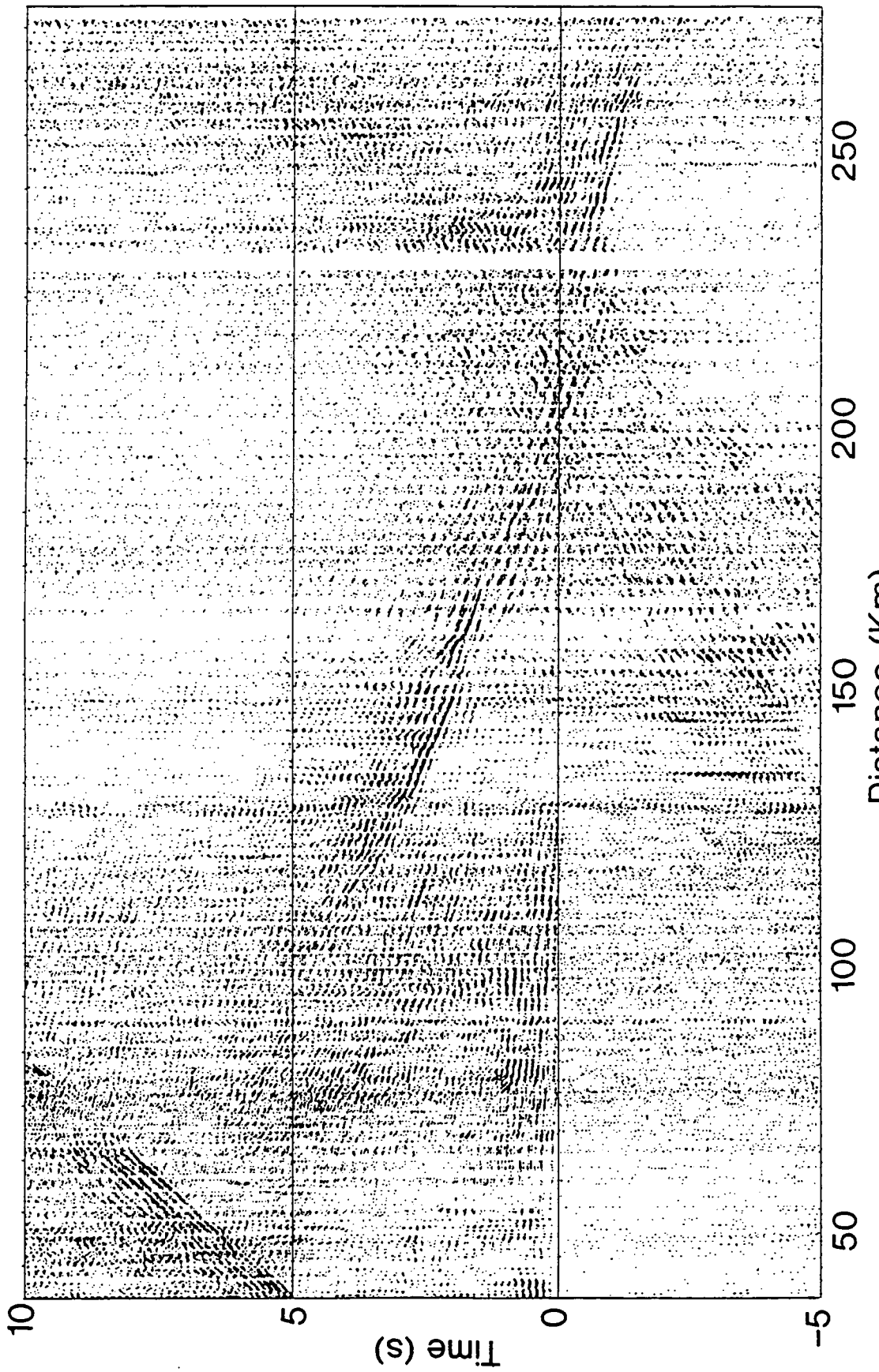

Figure 10.1. Normalised wide-angle data section for BABEL line 6 recorded at station BS5P.

10.2.1 A simple sinusoidal reflector

Wide-angle arrivals impinge upon reflecting boundaries obliquely. As a result, gentle relief on the boundaries can cause focusing of rays in some regions and shadow zones in others (regions of boundaries which are not imaged at wide-angles). An example of this is shown in Figure 10.2 for a simple sinusoidal interface with a peak to trough amplitude of 2 km and a wavelength of 20 km. A complex series of overlapping arrivals is generated, with large numbers of rays from some parts of the boundary and none from others. Rays are focused where the curvature of the boundary is greatest. The amplitudes in the synthetic section for the sinusoidal interface in Figure 10.2 are very variable. At normal-incidence, rays are seen from all parts of the boundary (Figure 10.3). A similar effect has been modelled at normal-incidence from a 3D sinusoidal layer by Blundell and Raynaud (1986).

The wide-angle arrivals generated from the sinusoidal boundary are similar to those seen in experimental data where a series of overstepping arrivals are seen. These have been explained as the result of crustal layering, with arrivals from deeper interfaces with higher velocities overtaking those from shallower layers (e.g. 'Pg shingles', Mereu *et al.*, 1990) or as the effect of near-surface multiples that produce a complex downgoing wavefield which is overprinted on to the wide-angle arrivals (Matthews, 1989, Rowbotham, 1990). The sinusoid is an example of how this pattern of arrivals can be generated from a single interface.

If the synthetic data shown in Figure 10.2 was modelled with no knowledge of the original structure, then the selection of arrivals would make a major difference to the model. Assuming that the series of overlapping arrivals were part of a single reflection from a single interface would give a better model of the true structure than attempting to interpret each of the individual arrivals as reflection branches from a layered structure (the normal-incidence data could be used to suggest which of these structures was more appropriate).

10.2.2 Lower crustal lenses

Figure 10.4 shows the wide-angle arrivals seen from a set of equally spaced lenses at about Moho depths. It has been suggested that the reflectivity of the lower crust at normal-incidence may be the result of lens like structures (e.g. Reston, 1987),

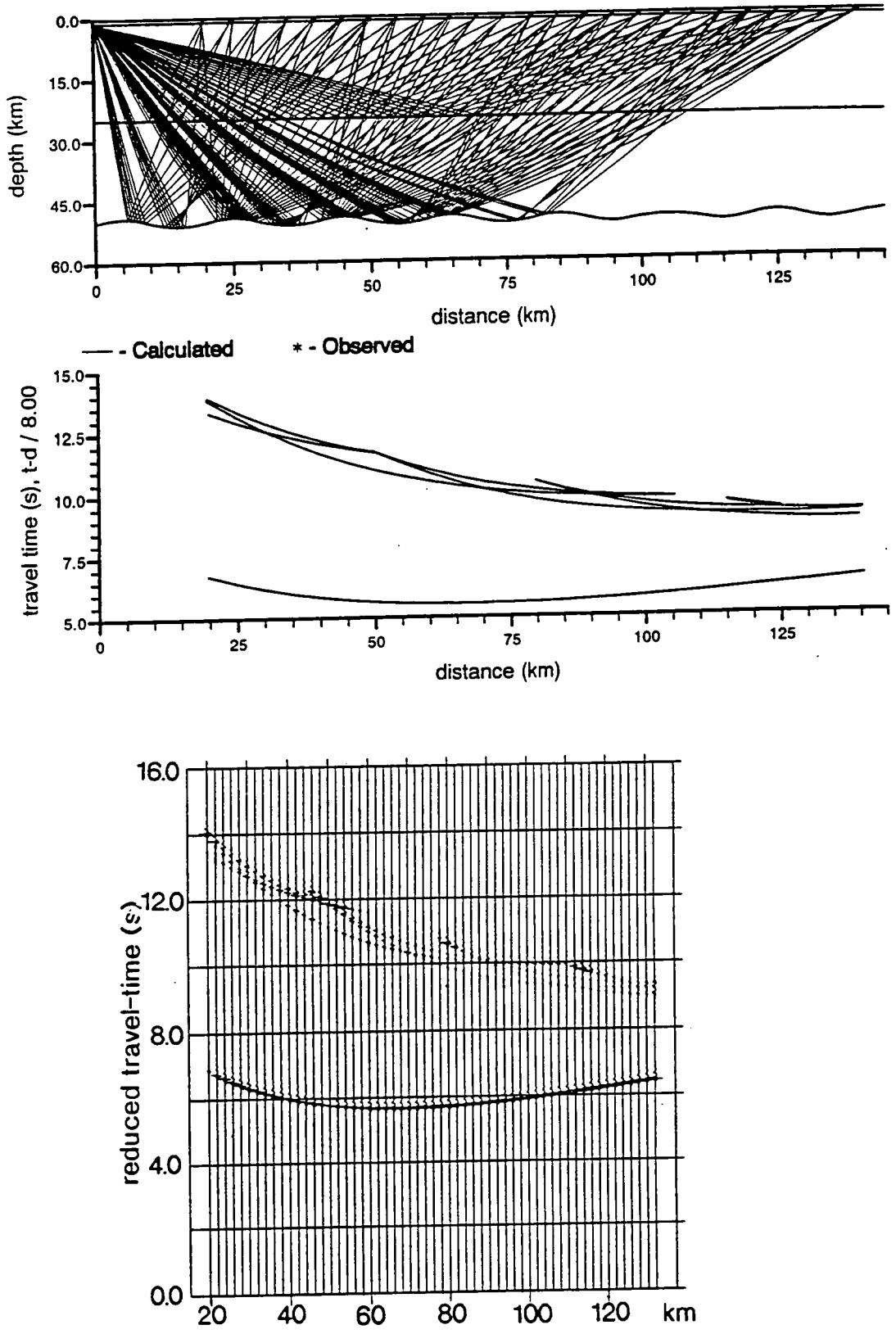

Figure 10.2. Ray diagram, travel times and synthetic section for a simple sinusoidal boundary. Peak to peak amplitude of sinusoid = 2 km, wavelength = 20 km.

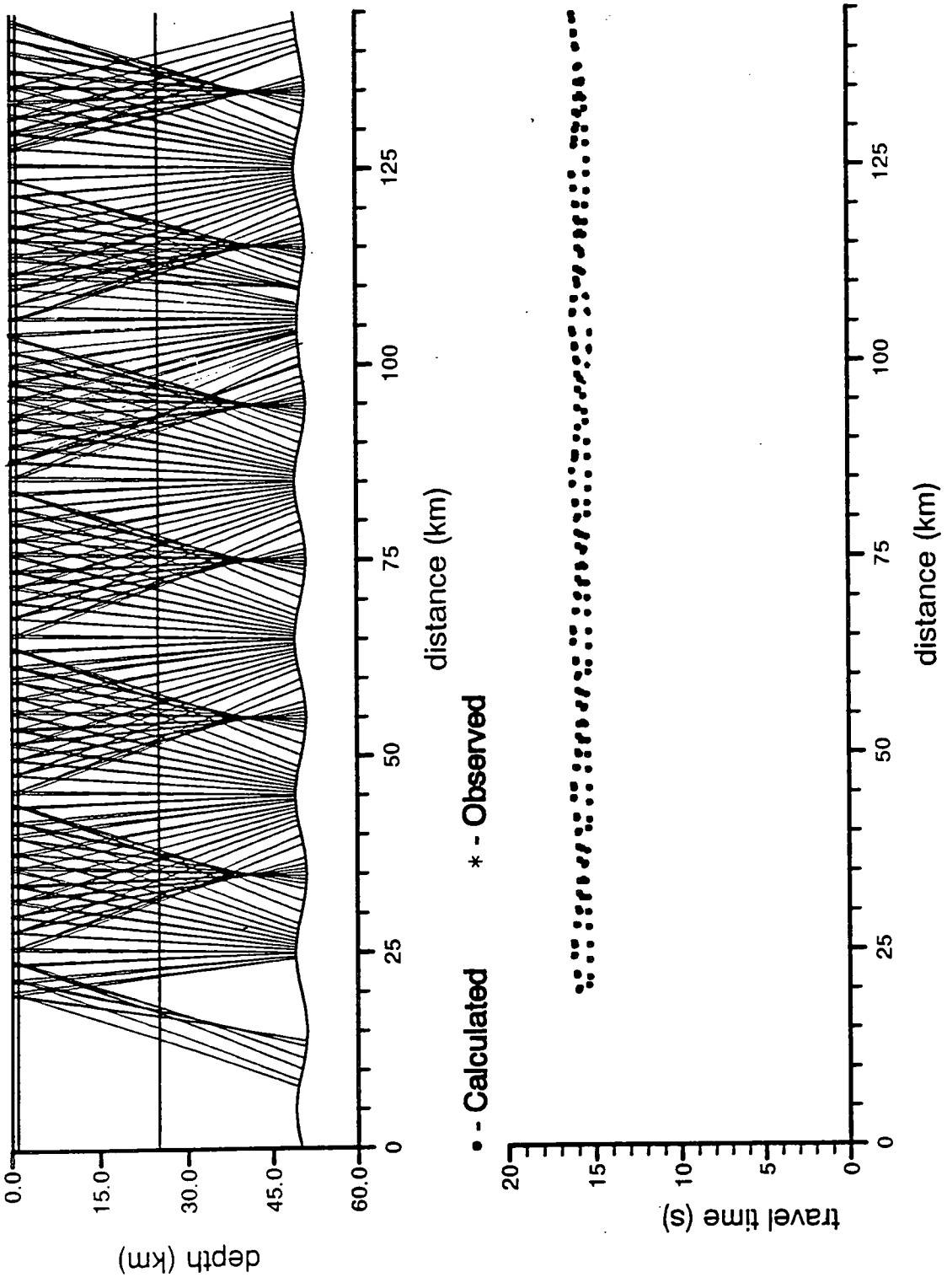

Figure 10.3. Normal-incidence arrivals from the sinusoidal interface shown in Figure 10.2.

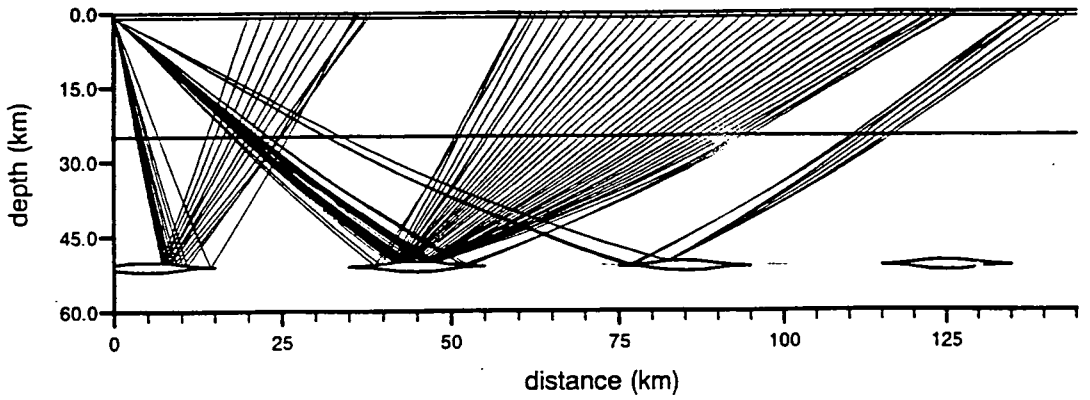

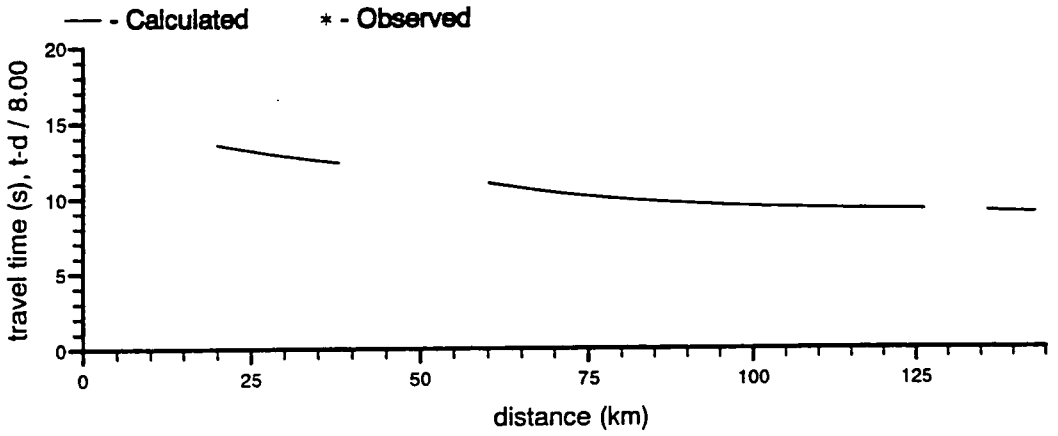

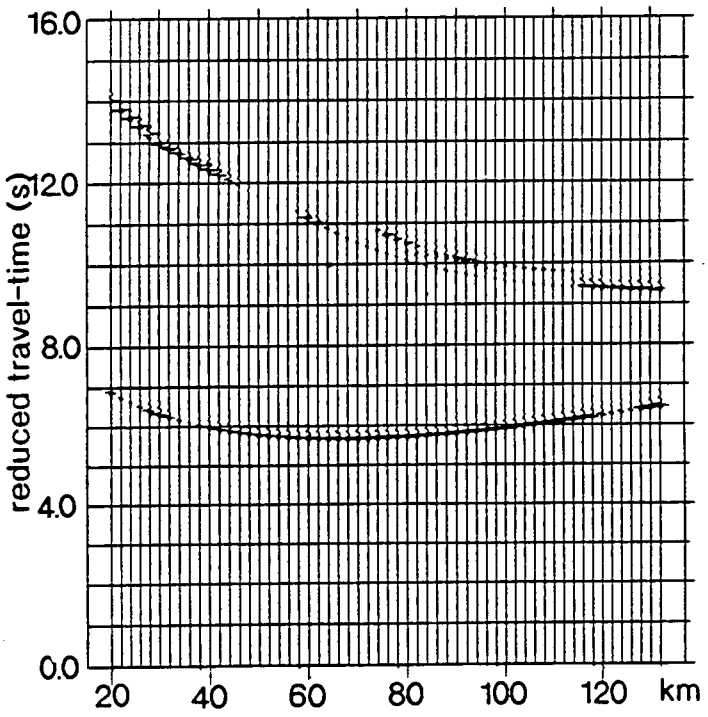

Figure 10.4. Crustal lenses. Lenses are 0.42 km thick and the P-wave velocity in the lenses is 7.6 km/s.

although the cause of these lenses is disputed, (section 6.2.2, Warner and McGreary, 1987). The lenses in the model in Figure 10.4 are fairly thick and extensive (about 0.5 km thick and 20 km in length). The lenses have not been made smaller as it is awkward trying to construct such intricate features with BEAM87. It is also difficult to see the effect that the lenses have on the rays if they are much smaller than those in Figure 10.4. The wide-angle synthetic from this model shows what appears to be a continuous, although variable amplitude, arrival at offsets of 55 to 140 km. The normal-incidence data from this line shows patches of reflectivity which are clearly not from a continuous interface (Figure 10.5).

10.2.3 Short length reflectors in the lower crust

The extensive lower crustal reflectivity seen on deep crustal profiles is often explained in terms of short length reflectors, although the origins of these reflectors are disputed (section 6.2.2). Figure 10.6 shows the wide-angle arrivals produced by a lower crust containing a series of short length reflectors. The lower crust is modelled as fifteen layers of equal thickness and the short length reflectors are part of the interfaces which separate these layers. Each of the layers has a constant velocity. Velocity increases with depth and there is a velocity step of 0.05 km/s across each interface.

The synthetic seismogram for this model does not show the individual reflectors of the model because of the 'smearing' effect of the Gaussian beams (which approximates the amplitudes of the raytraced arrivals to that of waves) and because of interference between the wave train of one reflection with the subsequent arrivals (this is particularly noticeable at long offsets, where the difference between raypaths for the different layers is small). The wide-angle arrivals in the synthetic can be traced continuously across the section and the amplitude changes very rapidly with offset.

If random orientations of the reflectors are also introduced (Figure 10.7) then the pattern of arrivals becomes similar to that seen in the experimental data, with overlapping and interfering arrivals and rapid variations in amplitude along what appear to be continuous arrivals. The reflectors imaged in the lower crust at normal-incidence are of shorter length and more closely spaced than those modelled here. This would tend to make the wide-angle arrivals appear more continuous and will be discussed further in section 10.3.

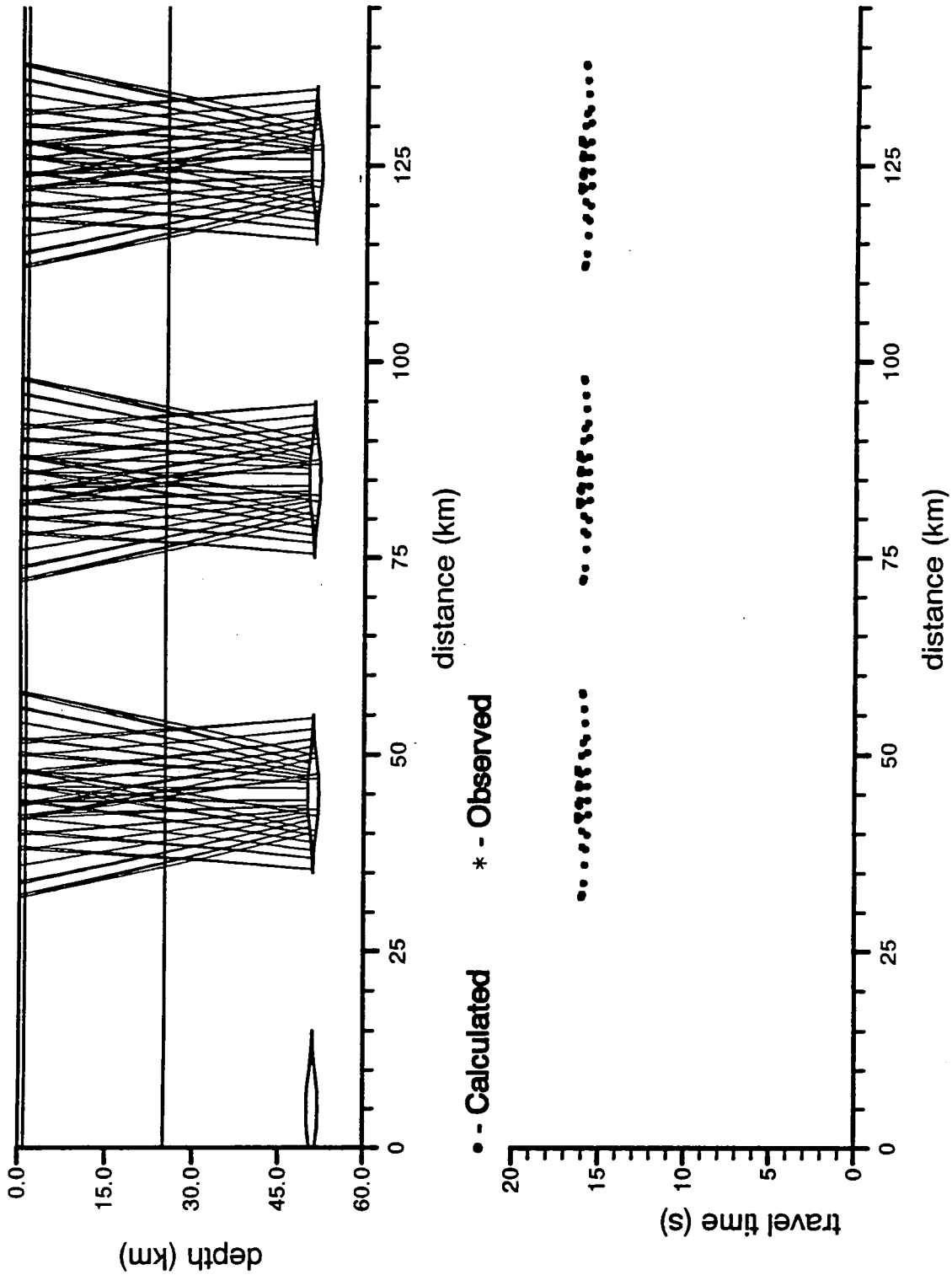

Figure 10.5. Normal-incidence arrivals from the crustal lenses in Figure 10.4.

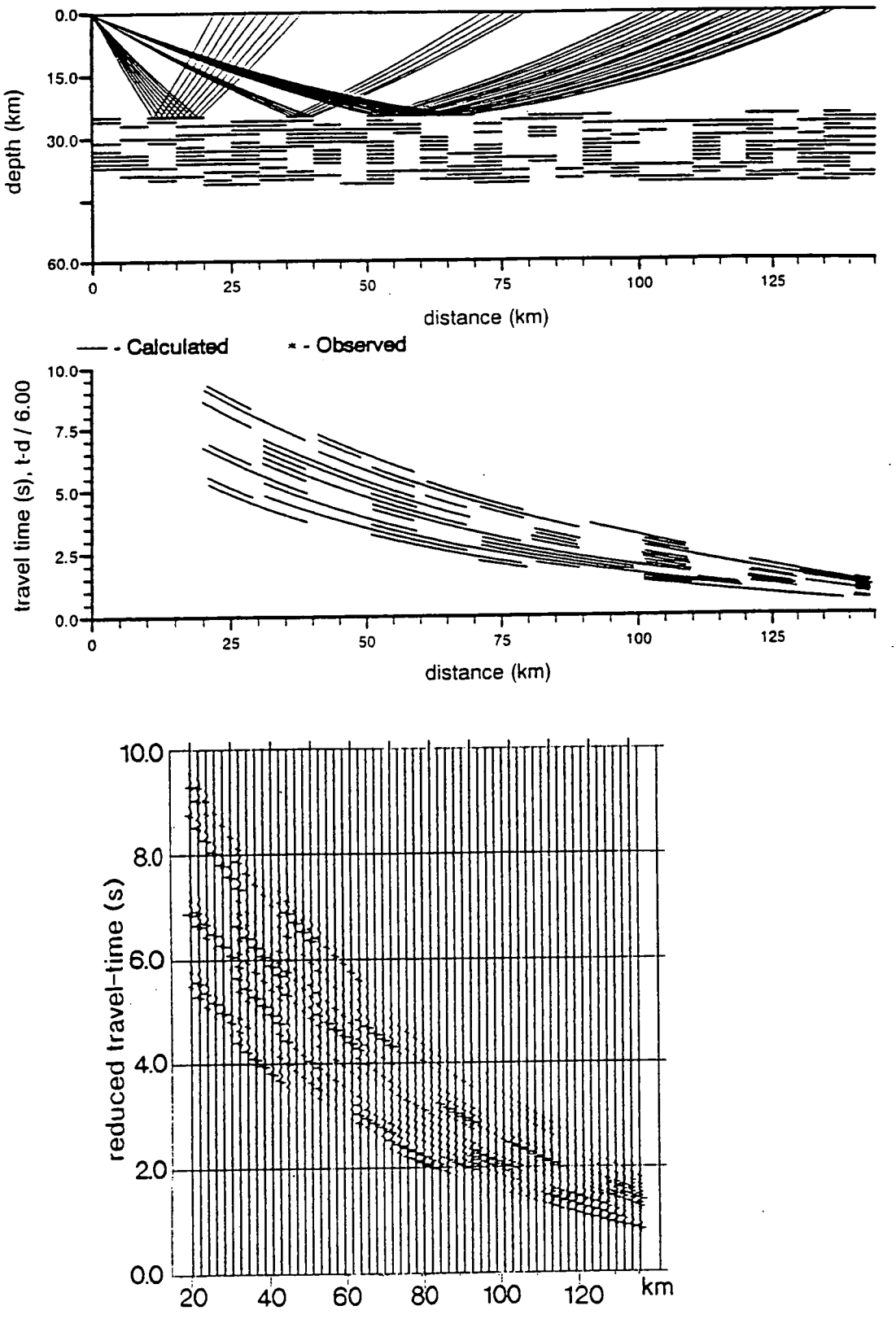

Figure 10.6. Lower crust consisting of short length reflectors. The reflectors are part of interfaces separating fifteen constant velocity layers (1 km thick). The velocity in the uppermost layer is 6.65 km/s and increases by 0.05 km/s for each layer below.

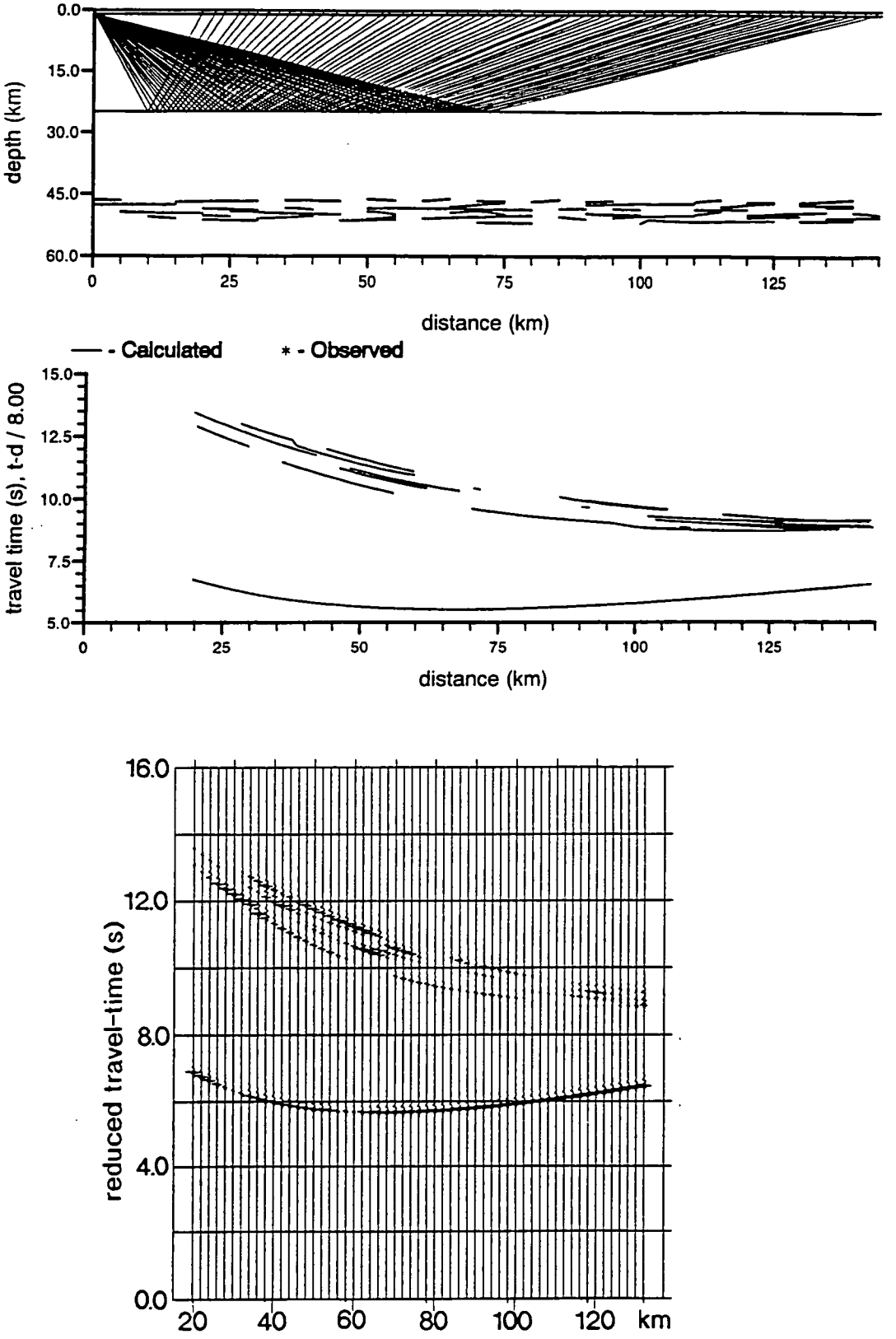

Figure 10.7. Effect of variable angle as well as length on a layered lower crust. The model is similar to that in Figure 10.6 but for fewer layers.

10.2.4 The WART

Kusznir and Matthews (1988) suggested that the decay of Moho topography by ductile flow would be a wavelength dependant feature. Offsets of the Moho would decay over geological time in such a way that intermediate wavelength features (~ 10 km) would be destroyed more rapidly than the long wavelength and short wavelength amplitude components. Ductile flow effectively applies a notch filter to the Moho topography. A simple step on the Moho would decay to give the remanent structure shown in Figure 10.8.

The wide-angle arrivals from this type of structure are shown in Figure 10.9. In Figure 10.9a, the Kusznir-Matthews structure gives rise to a reflection and a diffraction-type arrival. One of the major differences of the BABEL and MOBIL data to that of previous wide-angle surveys has been the identification of 'diffraction-type' arrivals. The highest amplitudes on the wide-angle sections are seen where these arrivals branch off those modelled as reflections. Although only three major diffraction-type arrivals have been modelled for line 6, other examples of this type of arrival may be tentatively identified throughout the section, associated with arrivals from various depths. This pattern of wide-angle reflection and 'diffraction' branches appears to be very common in wide-angle data and have been termed 'WART's (Wide-Angle Reflection Types, Long *et al.*, 1993). A cartoon of a WART is shown in Figure 10.10.

The Kusznir-Matthews structure has been used to model WARTs seen the MOBIL data (West, 1990). These have been used to suggest that crustal faults cut through the Moho, even where there is no obvious offset of the Moho on the normal-incidence data. At normal-incidence, the Kusznir-Matthews structure is not clearly imaged. The normal-incidence synthetic (Figure 10.11) does not show a sharp step between the upper and lower parts of the boundary but rather a gentle slope characterised by several diffraction-type arrivals.

On the MOBIL lines, these WARTs appear to be related to a fault system off the northeast coast of Britain: the Dowsing fault zone. For the BABEL data, the 'step' on the Moho of the line 6 model has a similar structure to that suggested by Kusznir and Matthews (1988); there is only a small offset of the boundary and a WART arrival is seen from the feature in the wide-angle data from BS5P but not from Z2A. This suggests that the Moho step on line 6 may also be related to a crustal scale fault.

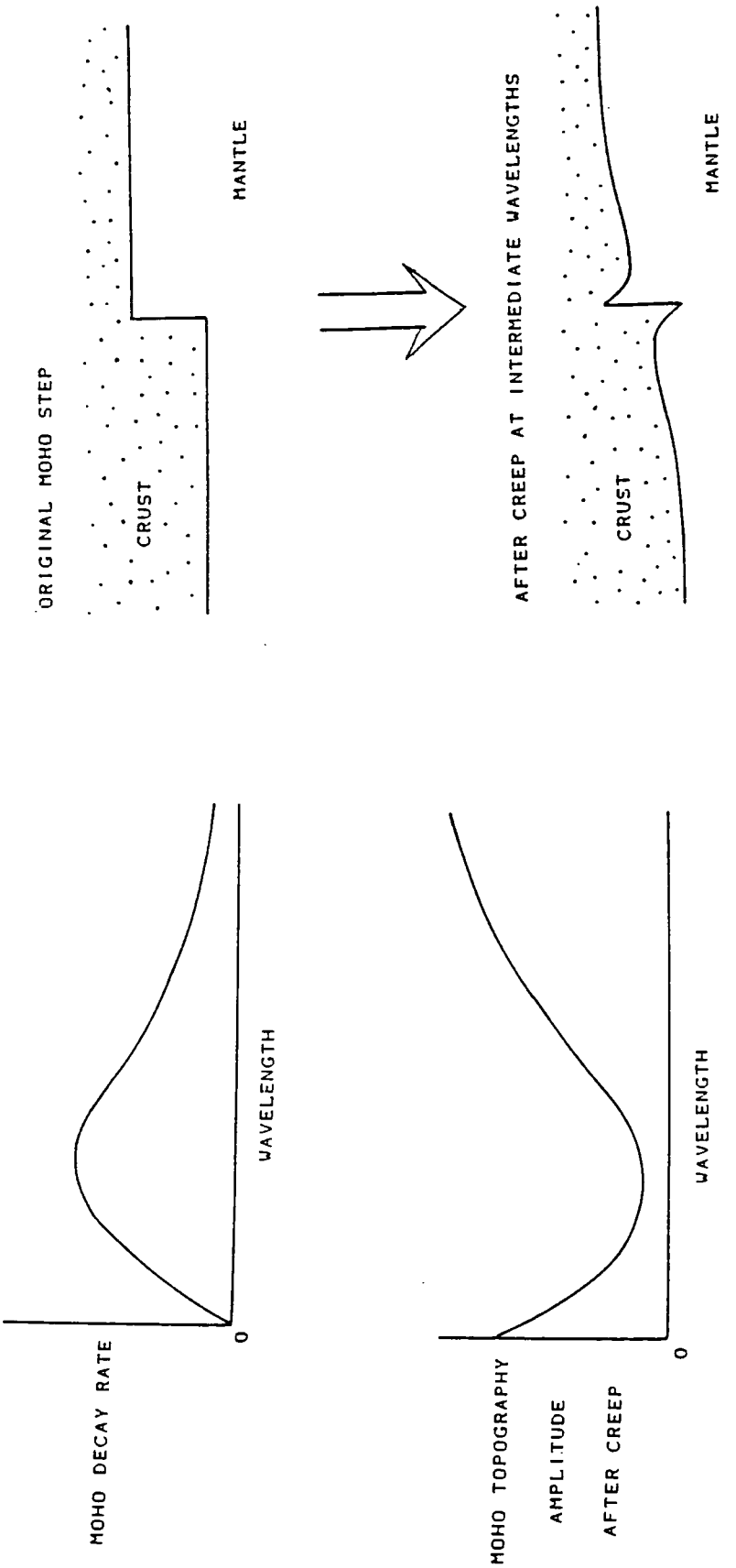

Figure 10.8. Diagram of the decay of a crustal step over geological time (after Kusznir and Matthews, 1988).

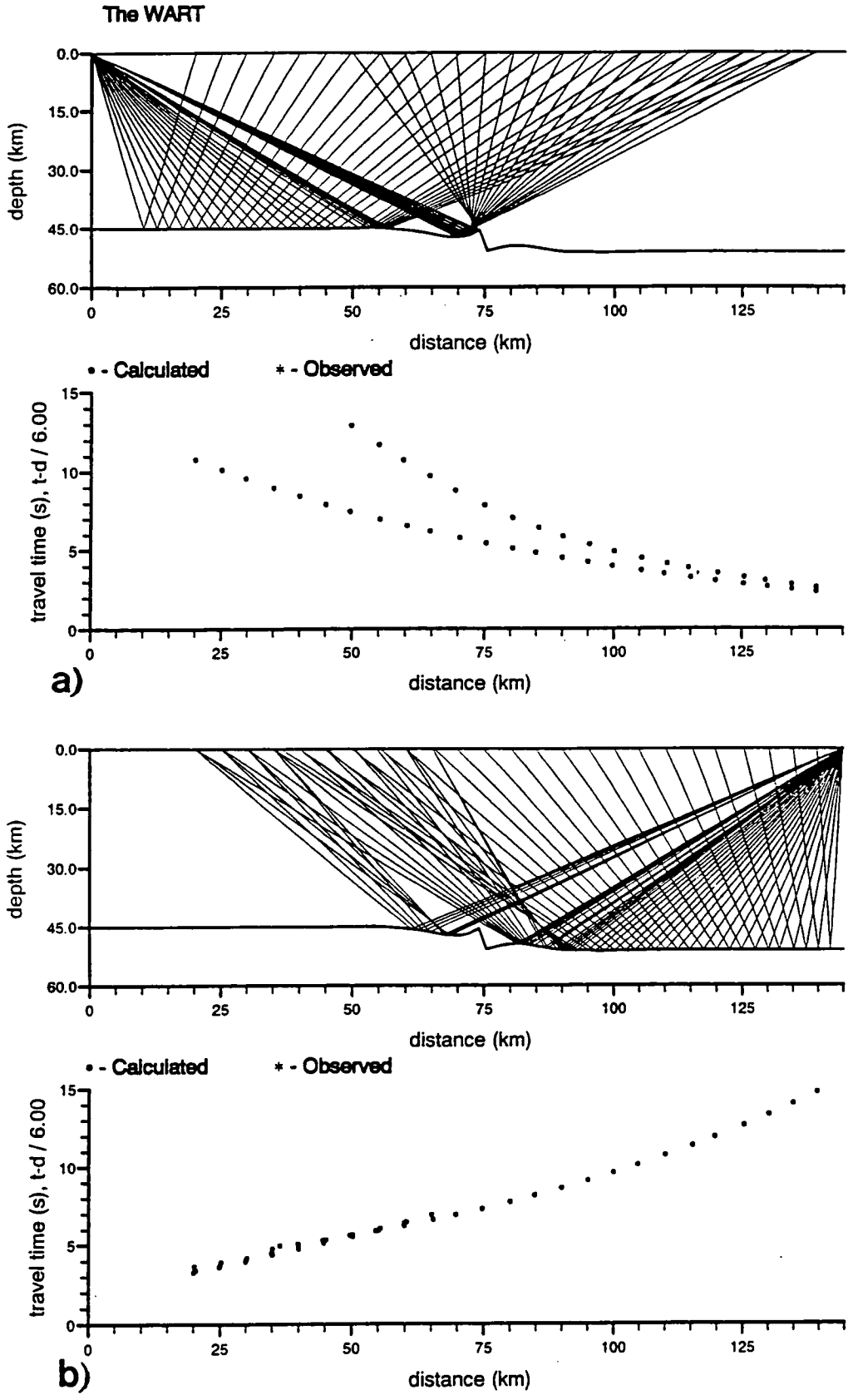

Figure 10.9. Ray diagram and travel-time plots for the remnant decay structure of a Moho step suggested by Kusznir and Matthews (1988) illuminated **a)** from the raised side of the original step (a 'WART' arrival) and **b)** from the lower side of the original step.

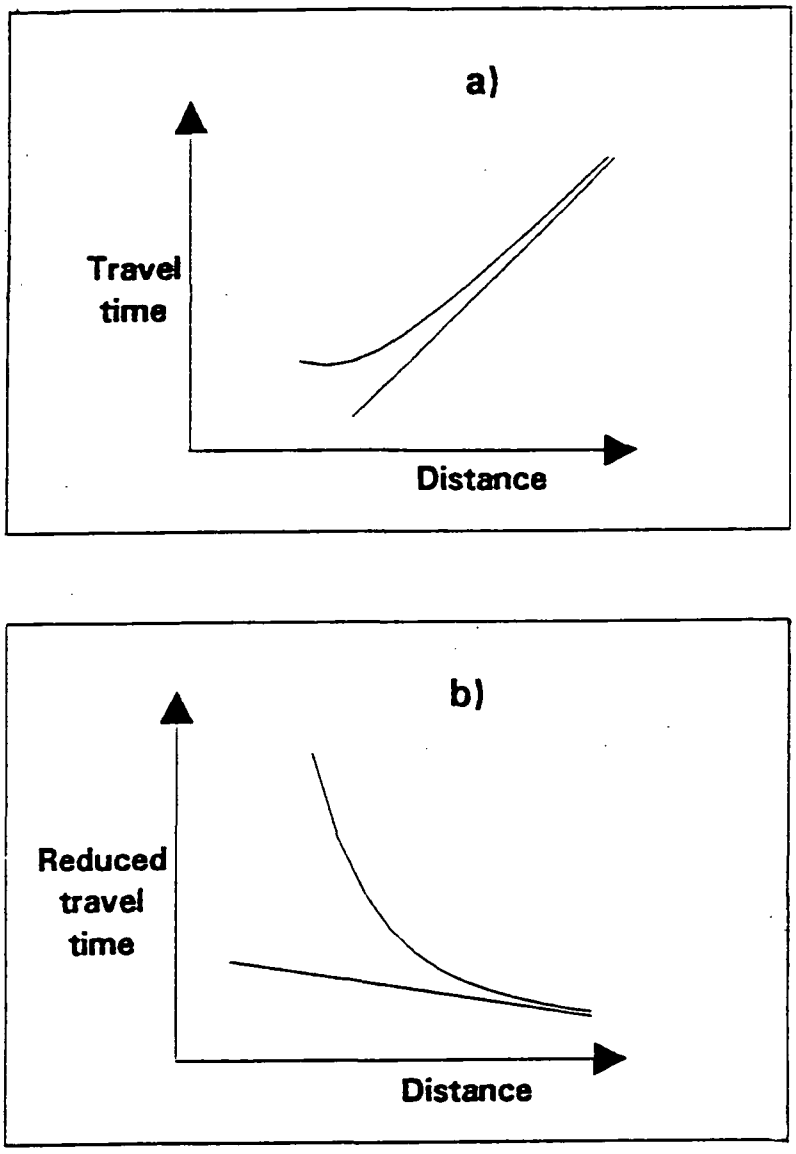

Figure 10.10. Cartoon of a WART (wide-angle reflection type) from Long *et al.* (1993) **a)** on an unreduced travel-time plot, **b)** on a reduced plot.

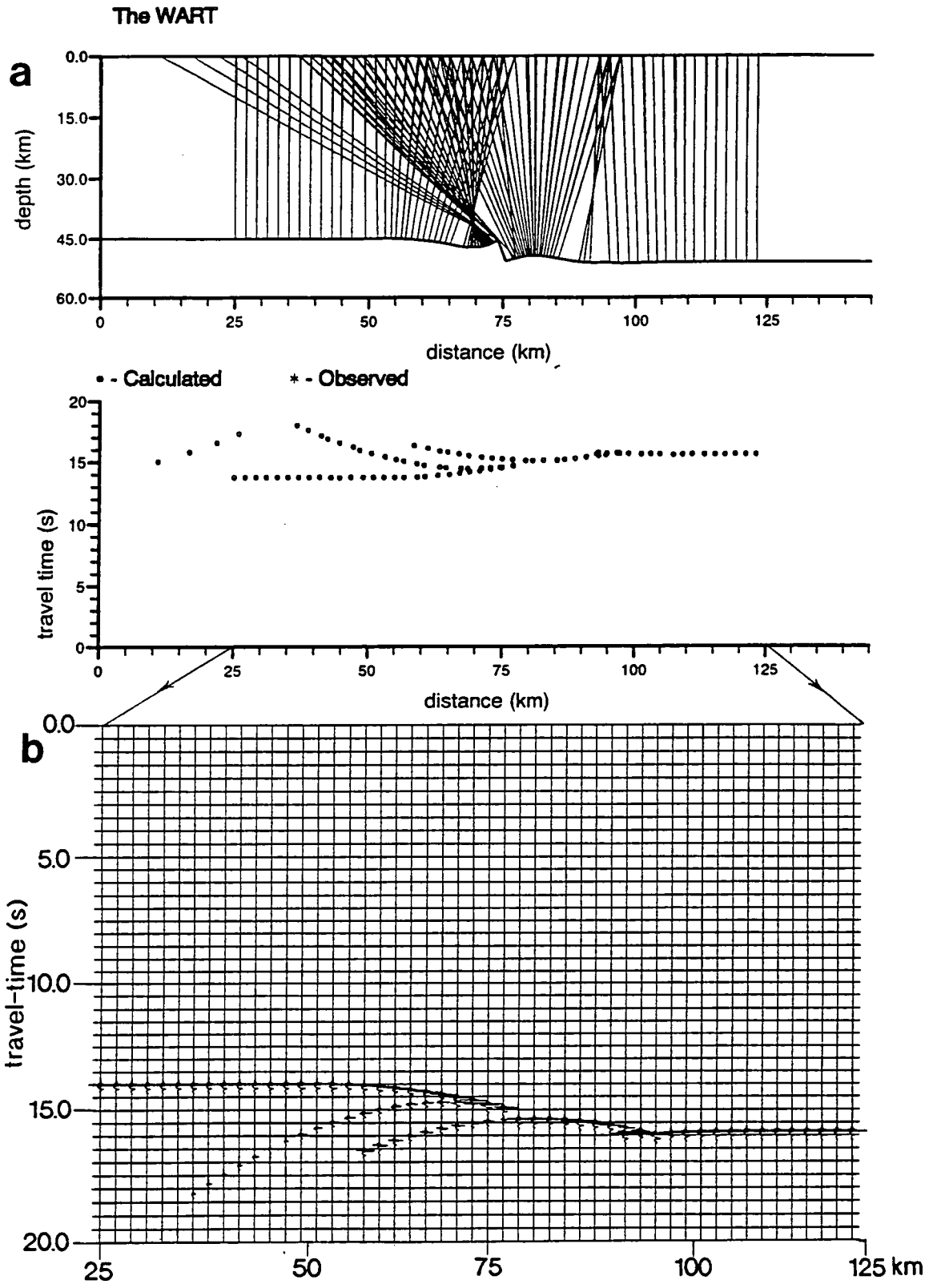

Figure 10.11a) Normal-incidence arrivals from a WART and **b)** BEAM87 normal-incidence synthetic section for the model in a).

10.3 The nature of the lower crust and the seismic Moho

Prior to the advent of the recent high resolution wide-angle datasets (recorded from the same shots as the normal incidence data), wide-angle and normal-incidence data appeared to image different features of the crust. Deep seismic normal-incidence profiles showed a highly heterogeneous crust separated into different zones of reflectivity. These have been used to divide the crust into upper and lower sections and to determine the reflection Moho (Matthews and Cheadle, 1986). Wide-angle data, which had a much lower resolution, showed apparently continuous arrivals from velocity discontinuities. These have been interpreted to give the large scale velocity structure of a series of crustal layers. The refraction Moho has generally been found to correspond to the reflection Moho (Ansorge *et al.*, 1982).

The improved quality of wide-angle data from piggy back experiments such as BABEL (where the wide-angle data is recorded from the same shots as the normal-incidence data) has revealed more wide-angle arrivals and several features not seen in previous wide-angle surveys. For example, the rapid changes in amplitude along apparently continuous arrivals and the diffraction-type arrivals seen in the BABEL data.

Traditional modelling approaches to this high resolution data have generally ignored the rapid amplitude fluctuations and interpreted the crust as a series of layers; an assumption that originally arose from poorer quality data. Where the amplitude changes have been considered, they have generally been explained as the result of multi-layered media such as the 'Pg shingles' seen in the GLIMPCE data (Mereu *et al.*, 1990). The model described in section 10.2.3 shows how changes in amplitude can arise from a series of short length reflectors at a single depth rather than from reflectors progressively deeper in the crust.

These results suggest that what have been assumed to be continuous wide-angle arrivals may come from the assemblages of reflectors in the lower crust which have been seen in normal-incidence data. If the reflectors are closely spaced then arrivals will interfere with each other. The wide-angle arrivals which have been selected as continuous arrivals from the data sections may be the result of edge effects from the patches of highly reflective crust seen in the normal-incidence data.

The large numbers of 'diffraction-type' arrivals, which may be from point diffractors or from very steeply sloping reflectors, suggest that the crustal structure is not laterally continuous. If the crust consists of a series of short length reflectors then diffractions may arise from the ends of these reflectors and the wide-angle data sections may consist of a series of WARTs (Long *et al.*, 1993).

These results suggest that wide-angle and normal-incidence arrivals come from the same features in the crust rather than imaging different aspects of crustal structure. A similar conclusion has been reached by Levander and Holliger (1992) who have used finite difference modelling to show how zones of small amplitude, random velocity fluctuations can produce strong wide-angle reflections.

CHAPTER XI

SUMMARY AND FUTURE WORK

11.1 Summary

11.1.1 The BABEL data

The BABEL data for line 6 is of very high quality due to the quiet recording sites and the good ground coupling (the sedimentary cover in Sweden is thin). Both types of field instrument recorded good P- and S-wave data. The analogue Geostore recorders required little attention during the experiment but the digital PDAS recordings were easier to replay and recorded clear arrivals with little background noise (although this was partly due to a fortuitous choice of recording parameters). The major problem with the data recording was the shot interval. The interval was such that the S-wave arrivals from the previous shot interfered with the P-wave arrivals and vice versa. In future experiments, it would be useful to choose a shot interval which avoided this problem. It should be possible to remove this interference from the BABEL data by velocity filtering (Graham (1993) has attempted to filter the data in F-K space but with little success).

The BABEL wide-angle data show a large number of complex arrivals which have very variable amplitude and phase. Rapid changes in amplitude are seen along apparently continuous arrivals over distances of a few kilometres. Other wide-angle arrivals appear to be of short length and discontinuous. 'Diffraction-type' arrivals are seen throughout the wide-angle data. The normal-incidence data for line 6 consists of patches of high and low crustal reflectivity; there are no strong laterally continuous reflectors and there is no indication of a division into non-reflective upper crust and reflective lower crust.

The frequency spectra of the line 6 wide-angle data appears to be controlled by the resonance of the water column. This resonance produces two major peaks in the frequency spectra of the wide-angle data. It may be possible to use this to investigate the frequency dependence of the observed crustal features since the crust is illuminated by energy at two different frequencies. These peaks have been used to select the best filter parameters for the data or, as in the case of station Z2A, to determine whether

the sections are dominated by station related noise. Adding the water bottom multiple to the synthetic sections improves the match to the experimental data.

The line 6 data was modelled using the BEAM87 Gaussian beam raytracing package. This package is designed for modelling single shots recorded at multiple receivers. Using this to model the reversed case (multiple shots, single receiver) results in errors in amplitudes. These are small unless converted phases are being considered but are an added problem when trying to match amplitudes of arrivals from models to those from experimental data.

A model was produced for line 6 using the traditional approach to raytracing (assuming that the crust consists of a series of quasi-horizontal layers). The major diffraction-type arrivals were also modelled and the normal-incidence data was used to constrain the position of the wide-angle boundaries. The main results from this model are as follows:

11.1.2 Geological and tectonic results

One of the major aims of the northern part of the BABEL project was to answer some of the geological questions about the Baltic Shield that had been raised by previous geological and geophysical studies. Some of these questions (for example, the question of the existence of the Baltic-Bothnian megashear) require further work in integrating the results from the different profiles in the Gulf of Bothnia. Some evidence of the Baltic-Bothnian megashear has been seen on BABEL line 7 (Bruguier, 1992) but it has not been possible to identify common features on lines 1 and 6 that may have been displaced by this feature. The major geological results from the line 6 model are as follows:

1. There is no clear evidence for or against plate tectonic processes controlling the evolution of the Svecofennides. It is suggested that the Svecofennian domain of the Baltic Shield evolved by magmatic and sedimentary accretion within a marginal basin (Berthelsen and Marker, 1986, Gaál and Gorbatschev, 1987) in which case no major plate tectonic features would be expected. Original features may also have been destroyed by subsequent intrusions.

2. The pattern of patchy reflectivity in the normal-incidence data appears to be the result of major intrusions into the crust. Some of these may be related to the original evolution of the Svecofennian crust and some to later intrusive events. The Jotnian dolerite sills seen on line 1 are not clearly seen on line 6 but may be the cause of the high velocity layer at the northern end of the line 6 model. The crust

beneath line 6 shows a gradational increase of velocity with depth. Velocity discontinuities associated with reflecting boundaries are small. Several high velocity layers are seen which may be related to intrusions.

3. There is no indication of the Archaean basement to the Svecofennides that was proposed by Welin (1987). Line 6 did not extend into the northern volcanic province of the Svecofennides that Lundström (1987) suggested was underlain by Archaean crust. The BABEL lines in the Bay of Bothnia have shown crust that was identified as Archaean, which extends no further south than the Karelides (BABEL working group, 1991b).

4. Crustal velocities and thicknesses are similar to those seen on previous studies of the Baltic Shield. However, there is no evidence on line 6 for a Moho trough similar to those modelled on the SVEKA, BALTIC and FENNOLORA profiles. Luosto (1990) suggested that these depressions of the Moho were part of the same feature, crossing the Sea of Bothnia (section 3.3). The absence of a trough beneath line 6 suggests that this is not the case and that the apparent relation of these features in the interpolated map of Moho depths (Luosto, 1990) is an artefact caused by the lack of data from the Sea of Bothnia. The results from line 6 suggest that the depression seen on the BALTIC and SVEKA profiles is related to the Ladoga-Bothnian Bay zone (as was initially suggested) and that the thickening on the FENNOLORA profile is related to a different feature, possibly the Ljusnan thrust zone.

5. The diffraction-type arrivals which have been modelled for line 6 are generated by diffractors in the model that lie in the vicinity of near-surface faults. Those at the southern end of the line may be related to the Ljusnan thrust zone which was seen on the neighbouring FENNOLORA line, although there is no sign of the crustal thickening which was identified as part of this thrust zone in the FENNOLORA model. These diffractions may also indicate an offshore continuation of the Gävle graben.

11.1.3 Wide-angle data and crustal structure

The high resolution of the BABEL wide-angle data revealed a much more complex series of arrivals than were identified for the neighbouring FENNOLORA line. The seismic boundaries in the line 6 model, which consist mainly of horizontal

layers, match the travel-times of the main wide-angle arrivals but do not explain the rapid changes in amplitude that are seen along the apparently continuous arrivals.

The line 6 normal-incidence data shows no laterally extensive zones of reflectivity that would be expected for a crust consisting of laterally homogeneous layers. Instead a pattern of highly reflective and non-reflective patches is seen. The reflective patches are more reflective than is expected for undisturbed cratonic crust which typically shows more diffractions than reflections. The pattern of reflectivity also differs from that generally seen in Phanerozoic crust, which is often divided into unreflective upper crust and reflective lower crust. There are two proposed explanations for the pattern of reflectivity seen along line 6. Either intrusions have disrupted originally reflective lower crust (Nelson, 1991) or the reflective crust may be the result of Phanerozoic tectonics (Dahl-Jensen *et al.*, 1987).

The modelled wide-angle reflections only constrain small parts of reflecting boundaries in the line 6 model, even though it was assumed that they were from continuous boundaries and the rapid changes in amplitude were ignored. Since these lengths of boundary coincide in many cases with the edges of the zones of highly reflective and non-reflective crust, it seems reasonable to assume that the wide-angle reflections are related to these bodies rather than to layers that are not imaged on the normal-incidence data. The geological history of the Svecofennides would also suggest that if a layered crust had existed then it would have been severely disrupted by subsequent intrusions.

Complex wide-angle arrivals may arise from simple structures such as a sinusoidal boundary or from a series of short length reflectors. The latter of these produces rapid variations in amplitude along apparently continuous arrivals similar to those seen in the experimental data. This suggests that the arrivals in wide-angle data, that are usually modelled as arising from velocity discontinuities, may come from the assemblages of short length reflectors seen on the normal-incidence data. The traditional interpretations of wide-angle reflections resulting from a series of roughly horizontal layers are no longer adequate to explain the complexity of the wide-angle and normal-incidence arrivals.

11.2 Future work

11.2.1 Further work on the BABEL data

This study has only involved a small part of the large dataset recorded by Durham University during the BABEL project. Other authors have modelled the online data for line 1 and 7 but the off-line data has not yet been modelled. These different

models need to be interpreted, along with the cross line recordings, to give a three dimensional structure of the Sea of Bothnia. This may yield further data about the existence of the Baltic-Bothnian shear zone and about the relation of features on line 1 to those on line 6 (the wide-angle data recorded from the lines in the Bay of Bothnia have not yet been converted).

The data used in this work has not been processed except for basic frequency filtering. Processing attempts on wide-angle data have only been moderately successful and further work is needed to develop wide-angle processing packages similar to those which are used so successfully with normal-incidence data. In particular, separating the P-wave and S-wave data by velocity filtering would reduce the problems of interference with the previous shot.

The line 6 model could be further constrained by modelling the data from the greater offset stations (Z5A, Z1A etc.). The arrivals predicted from the current line 6 model were compared to the experimental data from these stations in section 8.7. The gravity and magnetic data for line 6 should be modelled to give further information on the geological origins of the patches of high and low reflectivity seen in the normal-incidence data, similar to those suggested by Luosto *et al.* (1992) for line 1 and line 7 anomalies. This may also help constrain the location and extent of the high velocity layers in the line 6 model if these are related to intrusions

Modelling the S-wave data simply by altering the P-wave to S-wave velocity ratio in the layers found from modelling the P-wave data is only useful as a first approximation. An independent model from the S-wave data from BS5P and from a station at the far end of the line (BS1 or BS2) should be developed and compared to the P-wave model. The three component data sets need to be studied to investigate the effects of anisotropy of the crust for both S-waves and for P-waves.

11.2.2 Future geophysical surveys in the Gulf of Bothnia

The BABEL project has again shown that coincident recording and joint interpretation of wide-angle and normal-incident data is very important in determining crustal structure. One of the problems in this interpretation is the absence of intermediate offset data which means that it is not possible to trace features out from normal-incidence to wide-angle. The use of ocean bottom seismometers (OBS) along the recording profiles would provide information on the structure of the crust at offsets between normal-incidence and wide-angle (i.e. between about 3 and 30 km) and may make it possible to relate the features seen on the datasets.

BABEL line 7 is the only high resolution east-west profile in the Svecofennides. It would be useful to have other cross lines to tie the features seen on

line 6 with those seen on line 1. Cross lines would also be expected to image the Baltic-Bothnian megashear. It would be useful to have an east-west profile in the vicinity of the dolerite sills seen on line 1 in order to determine if these are as extensive as has been suggested and if they are related to the high velocity layer seen in the line 6 model. BABEL line 5 was planned to tie lines 1 and 6 at the northern end of the Sea of Bothnia but was unfortunately cancelled.

New gravity and magnetic data may help to determine the nature of the high and low reflectivity patches seen in the normal-incidence data. This may also reveal whether the low reflectivity of the lower crust in the middle of line 6 is caused by the surface geology or is a crustal feature. The low level survey of Sweden and the western half of the Sea of Bothnia should provide this data in the near future.

11.2.3 Development of wide-angle techniques

The majority of models for the profiles in the Baltic Shield have been created using BEAM87 or its predecessor SEIS83. This may have produced a bias in the models because of the way in which they are defined in these packages. The data should be modelled using different raytracing packages and also methods which are not based on asymptotic ray theory (finite difference or finite element modelling).

Travel-time modelling alone does not give a distinct model of crustal structure. Banda *et al.* (1982) studied the amplitudes of the Pg phase and found that different models for the upper crust could not be distinguished from travel-time interpretation but had distinct amplitude-distance characteristics. Synthetic seismogram and amplitude modelling are therefore required to produce a unique model of the crust. There are several problems with amplitude modelling. These include the complexity of the experimental data and the errors in amplitude due to using the raytracing package to model the reverse of the experimental layout. The complexity and accuracy of the synthetic seismograms must be improved before they can be successfully compared to the experimental data.

The increased resolution of wide-angle data has shown large numbers of wide-angle arrivals and 'diffraction-type' arrivals which have not been identified in lower resolution data sets. The nature of the 'diffraction-type' arrivals and of the WARTs need to be further investigated. One possible method for this is to compare the amplitude characteristics of the arrivals seen in the experimental data with those of point diffractions and of 'divergent-reflections' from steep slopes (as were modelled for the line 6 data). A modelling package which uses the full wave solution will be needed for this since true diffractions cannot be modelled with raytracing methods.

Interpreting the line 6 data has raised further questions as to the origins of wide-angle arrivals. The rapid changes in amplitude suggest that the assumption that wide-angle reflections come from laterally continuous velocity discontinuities is incorrect. Attribute analysis may be able to further reveal the nature of wide-angle arrivals (for example, phase analysis can show if the phase is varying with offset as well as the amplitude). Simplistic models of complicated crustal structures (such as short length reflectors) indicate that wide-angle arrivals may arise from the same features as normal-incidence data. More complex modelling packages are needed to pursue this idea.

REFERENCES

Ahjos, T., 1990, A look at Fennoscandian earthquake data. In: *Freeman, R. and Mueller, St. (Eds.), Proceedings of the sixth workshop on the EGT project.* (European Science Foundation), 349-355.

Aki, K. and Richards, P. G., 1980, Quantitative Seismology theory and methods: volume 1. (W. H. Freeman and co.).

Andersson, U. B., 1991, Granitoid episodes and mafic-felsic magma interaction in the Svecofennian of the Fennoscanadian Shield, with main emphasis on the ~1.8 Ga plutonics. *Precambrian Research,* **51,** 127-149.

Ansorge, J., Prohdel, C. and Bamford, D., 1982, Comparative interpretation of explosion seismic data. *J. Geophysics,* **51,** 69-84.

BABEL working group, 1990, Evidence for early Proterozoic plate tectonics from seismic reflection profiles in the Baltic Shield. *Nature,* **138,** 34-38.

BABEL working group, 1991a, Recording marine airgun shots at offsets between 300 and 700 km. *Geophys. Res. Lett.,* **18,** 645-648.

BABEL working group, 1991b, Reflectivity of a Proterozoic shield: examples from BABEL seismic profiles across Fennoscandia. In: *Continental lithosphere: Deep Seismic Reflections,* (American Geophysical Union), Geodynamics series, **22,** 77-86.

BABEL working group, 1993a, Integrated seismic studies of the Baltic Shield using data in the Gulf of Bothnia region. *Geophys. J. Int.,* **112,** 305-324.

BABEL working group, 1993b, Deep seismic reflection/refraction interpretation of crustal structure along BABEL profiles A and B in the southern Baltic Sea. *Geophys. J. Int.,* **112,** 325-343.

Balling, N., 1990, Heat flow and lithospheric temperature along the northern segment of the European Geotraverse. In: *Freeman, R. and Mueller, St. (Eds.), Proceedings of the sixth workshop on the EGT project.* (European Science Foundation), 405-416.

Banda, E., Deichmann, N., Braile, L. W. and Ansorge, J., 1982, Amplitude studies of the Pg phase. *J. Geophys.,* **51,** 153-164.

Barry, K. M., Cavers, D. A. and Kneale C. W., 1975, SEG Special report: Recommended standards for digital tape formats. *Geophysics,* **40,** No 2, 344-352.

Behrendt, J. C., Green, A. C., Cannon, W. F., Hutchinson, D. R., Lee, M. W., Milkereit, B., Agena, W. F. and Spences, C., 1988, Crustal structure of the midcontinental rift system: results from GLIMPCE deep seismic profiles. Geology, **16,** 81-85.

Berkhout, A. J., 1987, Applied seismic wave theory. Advances in exploration geophysics:1, (Elsevier), 197-228.

Berthelsen, A. and Marker, M., 1986, 1.9 - 1.8 Ga strike-slip megashears in the Baltic Shield and their plate tectonic implications. *Tectonophysics,* **128,** 163-181.

Beunk, F. F., Meissner, R., Sadowiak, P. and Thomas, S. A., 1992, BABEL deep seismic reflection data and on-shore geology in southern and central Sweden: tentative interpretations and correlations. In: *Meissner, R., Snyder, D., Balling, N. and Staroste, E. (Eds.), The BABEL project. First progress report.* (Commission of the European communities, EUR 14429EN), 117-122.

Blundell, D. J., and Raynaud, B., 1986, Modelling lower crustal reflections observed on BIRPS profiles. In: *Barazangi, M. and Brown, L., (Eds.), Reflection seismology: a global perspective.* (American Geophysical Union, Geodynamics series), **13,** 287-295.

Blundell, D. J., Hobbs, R. W., Klemperer, S. L., Scott-Robinson, R., Long, R. E., West, T. E., and Duin, E., 1991, Crustal structure beneath the southern North Sea from BIRPS deep seismic reflection profiling. *J. Geol. Soc. London.* **148,** 445-457.

Brown, L., Serpa, L., Setzer, T., Oliver, J., Kaufman, S., Lillie, R. and Steiner, D., 1983, Intracrustal complexity in the United States mid-continent: Preliminary results from COCORP surveys in northeastern Kansas. *Geology,* **11,** 25-30.

Bruguier, N. J., 1992, Crustal structure of the southern Bothnian Sea from wide-angle reflection data: BABEL line 7. *Unpublished M.Sc. thesis,* University of Durham.

Bungum, H., Pirhonen, S. E. and Husebye, E. S., 1980, Crustal thickness in Fennoscandia. *Geophys. J. R. Astr. Soc.,* **63,** 759-774.

Burkhardt, H. and Vees, R., 1975, Explosions in shallow water for Deep Seismic Sounding experiments. *J. Geophys.,* **41,** 463-474.

Buyanov, A. F., 1986, Generalised inversion technique in two-dimensional inverse kinematic seismology problem (in Russian), In: *Mathematical modelling of systems and phenomenon.* (Academy of the Sciences of the USSR, Kola Branch, Geological Institute, Apatity), 93-100.

Cassell, B. R. and Fuchs, K. 1979, Seismic investigations of the subcrustal lithosphere beneath Fennoscandia. *J. Geophys.,* **46,** 369-384.

Červený, V., 1966, On dynamic properties of reflected and head waves in the *n*- layered Earth's crust. *Geophys. J. R. astr. Soc.,* **11,** 139-147.

Červený, V., Molotkov, I. A. and Psencik, I., 1977, Ray methods in seismology. Univerzita Karlova, Praha.

Červený, V., 1983, Synthetic bodywave seismograms for laterally varying layered structures by the Gaussian beam method. *Geophys. J. R. astr. Soc.,* **73,** 389-246.

Červený, V., 1985a, Gaussian Beam synthetic seismograms, *J. Geophys.,* **58,** 44-72.

Červený, V., 1985b, Ray synthetic seismograms for complex two-dimensional and three dimensional structures. *J. Geophys.,* **58,** 2-26.

Chapman, C. H., 1985, Ray theory and its extensions: WKBJ and Maslov seismograms. *J. Geophys.* **58,** 27-43.

Dahl-Jensen, T., Dyrelius, D., Juhlin, C., Palm, H. and Pedersen, L. B., 1987, Deep reflection seismics in the Precambrian of Sweden. *Geophys. J. R. astr. Soc.*, **89,** 371-378.

Flack, C. A., Klemperer, S. L., McGeary, S. E., Snyder, D. B. and Warner, M. R., 1990, Reflections from mantle fault zones around the British Isles. *Geology*, **16,** 528-532.

Fleuh, E. R. and Dickmann, T., 1992, Technical aspects of wide-angle data collection and processing. In: *Meissner, R., Snyder, D., Balling, N. and Staroste, E. (Eds.), The BABEL project. First progress report.* (Commission of the European communities, EUR 14429EN), 123-130.

Fuchs, K. and Müller, G., 1971, Computation of synthetic seismograms with the reflectivity method and comparison with observations. *Geophys. J. R. astr. Soc.*, **23,** 417-433.

Gaál, G., 1986, 2200 million years of crustal evolution: The Baltic Shield. *Bull. Geol. Soc. Fin.*, **58(1),** 149-168.

Gaál, G. and Gorbatschev. R., 1987, An outline of the Precambrian evolution of the Baltic Shield. *Precamb. Res.*, **35,** 15-52.

Gaál, G., Berthelsen, A., Gorbatschev. R., Kesola, R., Lehtonen, M. I., Marker, M. and Raase, P., 1989, Structure and composition of the Precambrian crust along the POLAR profile in the northern Baltic Shield. *Tectonophysics*, **162,** 1-25.

Geise, P., 1976, General remarks on travel-time data and the principles of correlation. In: *Geise, P., Prohdel, C. and Stein, A. (Eds.), Explosion seismology in Central Europe,* (Springer-Verlag), Berlin Heidelberg New York, 137-145.

GLIMPCE seismic refraction working group, 1989, GLIMPCE seismic experiments: Long offset recording. *EOS*, **70,** 841-853.

Gorbonov, G. I., Zardorodny, V. G. and Robonen, W. I., 1985, Main features of the geological history of the Baltic Shield and the epochs of ore formation. *Bull. Geol. Survey. Fin.*, **333,** 17-41.

Grad, M. and Luosto, U. 1987, Seismic models of the crust of the Baltic shield along the SVEKA profile in Finland. *Annales Geophysicae*, **5B(6)**, 639-650.

Graham, D. P., Matthews, P. A. and Long, R. E., 1992, Interpretation of wide-angle and normal-incidence reflection data from BABEL line 1. In: *Meissner, R., Snyder, D., Balling, N. and Staroste, E. (Eds.), The BABEL project. First progress report.* (Commission of the European communities, EUR 14429EN), 93 -96.

Graham, D. P., 1993 (In prep.), A seismic study of the Mid- and Lower-crust beneath the Sea of Bothnia: BABEL line 1. *Unpublished Ph.D. thesis*, University of Durham.

Green, A. S. P., 1984, The crustal suture beneath northern England and adjacent sea areas. *Unpublished Ph. D. thesis*, University of Durham.

Guggisberg, B., Kaminski, W. and Prodehl, C., 1991, Crustal structure of the Fennoscandian Shield: a travel time interpretation of the long-range FENNOLORA seismic refraction profile. *Tectonophysics*, **195,** 105-137.

Hauser, F. and Stangl, R., 1990, The structure of the crust and the lithosphere in Fennoscandia derived from a joint interpretation of P- and S- wave data of the FENNOLORA refraction seismic project. In: *Freeman, R. and Mueller, St. (Eds.), Proceedings of the sixth workshop on the EGT project.* (European Science Foundation), 71-92.

Heikkinen, P. and Luosto, U., 1992, Velocity structure and reflectivity of the Proterozoic crust in the Bothnian Sea. In: *Meissner, R., Snyder, D., Balling, N. and Staroste, E. (Eds.), The BABEL project. First progress report.* (Commission of the European communities, EUR 14429EN), 65-69.

Henkel, R. and Eriksson, L., 1987, Regional aeromagnetic and gravity studies in Scandinavia. *Precamb. Res.*, **35,** 169-180.

Hirschleber, H. B., Lund, C. -E., Meissner, R., Vogel, A. and Weinrebe, W. 1975, Seismic investigations along the 'Blue Road' traverse. *J. Geophys.*, **41,** 135-148.

Hjelt, S. E., 1987, Aspects of the geoelectric models of the Baltic Shield. *Precamb. Res.*, **35,** 181-194.

Hjelt, S. E., 1990, Electromagnetic studies on the EGT northern segment: Summary of results. In: *Freeman, R. and Mueller, St. (Eds.), Proceedings of the sixth workshop on the EGT project.* (European Science Foundation), 287-297.

Hjelt, S. E., 1992, Geophysics in the BABEL/Bothnian Bay area: a preliminary compilation of non-seismic data. In: *Meissner, R., Snyder, D., Balling, N. and Staroste, E. (Eds.), The BABEL project. First progress report.* (Commission of the European communities, EUR 14429EN), 31-34.

Hobbs, R. W. and Levander, A. F., 1992, The fidelity of deep seismic data. In: *5th international symposium on seismic reflection probing of the continents and their margins,* Geological survey of Canada.

Holliger, K. and Levander, A. R., 1992, A stochastic model of the lower crust: evidence from the Ivrea zone and implications for crustal seismic exploration, (abstract), In: *5th international symposium on seismic reflection probing of the continents and their margins,* Geological survey of Canada.

Hyndman, R. D. and Shearer, P. M., 1989, Water in the lower continental crust: modelling magnetotelluric and seismic reflection results. *Geophys. J. Int.*, **98,** 343-365.

Jokat. W. and Fleuh. E., 1987, On the use of airgun arrays for seismic refraction investigations of the crust. *First Break,* **5,** 440-447.

Juhlin, C., 1990, Interpretation of the reflections in the Siljan ring area based on the results from the Gravberg-1 borehole. *Tectonophysics,* **173,** 345-360.

Juhlin, C., 1992, Reflectivity characteristics of sills. In: *Meissner, R., Snyder, D., Balling, N. and Staroste, E. (Eds.), The BABEL project. First progress report.* (Commission of the European communities, EUR 14429EN), 77-80.

Kennett, B. L. N. and Harding, A. J., 1985, Is ray theory adequate for reflection seismic modelling (A summary of reflection methods). *First Break,* **3(1),** 9-14.

Kernighan, B. W. and Ritchie, D. M., 1988, The C Programming language. Second edition. (Prentice Hall).

King, D. W. and Calcagnile, G., 1976, P-wave velocities in the upper mantle beneath Fennoscandia and western Russia. *Geophys. J. R. astr. Soc.*, **46,** 407-432.

Klemperer, S. L. and the BIRPS group, 1987, Reflectivity of the crystalline crust: hypothesis and tests. *Geophys. J. R. astr. Soc.*, **89,** 217-222.

Klemperer, S. L., Hobbs, R. W. and Freeman, B., 1990, Dating the source of lower crustal reflectivity using BIRPS deep seismic profiles across the Iapatus suture. *Tectonophysics*, **173,** 445-454.

Korhonen, H., Kosminskaya, I. P., Azbel, I., Sharov, N., Zagorodny, V. and Luosto, U., 1990, Comparison of crustal structure along DSS profiles in SE. Fennoscandia. *Geophys. J. Int.*, **103,** 157-162.

Kullinger, B. and Lund, C. -E., 1986, A preliminary interpretation of S-wave travel-times from FENNOLORA data. *Tectonophysics*, **126,** 375-388.

Kusznir, N. J. and Matthews, D. H., 1988, Deep seismic reflections and the deformational mechanics of the continental lithosphere. *Journal of Petrology, Special lithosphere issue*, 63-87.

Latham, T. S., Best, J., Chaimov, T., Oliver, J., Brown, L. and Kaufmann, S., 1988, COCORP profiles from the Montana plains: the Archaean cratonic crust and a lower crustal anomaly beneath the Williston basin. *Geology*, **16,** 1073-1076.

Levander, A. R. and Holliger, K., 1992, Small-scale heterogenity and large-scale velocity structure of the continental crust. *J. G. R.*, **97,** 8797-8804.

Lewis, A. H. J., 1986, The deep seismic structure of Northern England and adjecent marine areas from the Caledonia Suture seismic project. *Unpublished Ph. D. thesis*, University of Durham.

Lie, J. E., Pedersen, T. and Husebye, E., 1990, Observations of seismic reflectors in the lower lithosphere beneath the Skagerrak. *Nature*, **346,** 165-168.

Long, R. E., Matthews, P. A., Graham, D. P. and West, T. E., 1993, The nature of crustal boundaries: combined interpretation of wide-angle and normal-incidence seismic data. Submitted to Tectonophysics.

Lund, C. -E., 1979, The fine structure of the lower lithosphere underneath the Blue Road profile in northern Scandinavia. *Tectonophysics*, **56,** 111-122.

Lund, C. -E., 1990, Summary of the results from the FENNOLORA profile. In: *Freeman, R. and Mueller, St. (Eds.), Proceedings of the sixth workshop on the EGT project.* (European Science Foundation), 65-70.

Lund, C. E., Roberts, R. G., Juhlin, C., Bödvarson, B. and Palm, H., 1987, The use of land recorded long-range marine airgun data in crustal reflection-refraction investigations. *Geophys. J. R. astr. Soc.*, **89,** 365-370.

Lundqvist, Th., 1987, Early Svecofennian stratigraphy of southern and central Norrland, Sweden, and the possible existence of an Archaean basement west of the Svecokarelides. *Precamb. Res.*, **35,** 343-352.

Lundström, I., 1987, Lateral variations in supracrustal geology within the Swedish part of the southern Svecokarelian volcanic belt. *Precamb. Res.*, **35,** 353-365.

Luosto, U., 1986, Reinterpretation of SYLEN-PORVOO refraction data. *Institute of Seismology, University of Helsinki,* Report S-13.

Luosto, U., 1990, Seismic data from the northern segment of the EGT and from nearby profiles. In: *Freeman, R. and Mueller, St. (Eds.), Proceedings of the sixth workshop on the EGT project.* (European Science Foundation), 53-63.

Luosto, U., Lanne, E., Korhonen, H., Guterch, A., Grad, M., Materzok, R. and Perchuc, E., 1984, Deep structure of the Earth's crust on the SVEKA profile in central Finland. *Annales Geophysicae,* **2(5),** 559-570.

Luosto, U., Korhonen, H., Kosminskaya, I. P., Zverev, S. M., Lund, C. -E., Sharov, N. V., Lanne, E., Tuppurainen, A., Ilmola, V. -M. and Foursov, A. N., 1985, First results from the DSS study on the BALTIC profile in SE Finland. *Institute of Seismology, University of Helsinki,* Report S-11.

Luosto, U. and Korhonen, H., 1986, Crustal structure of the Baltic Shield based on off-FENNOLORA refraction data. *Tectonophysics,* **128,** 183-208.

Luosto, U., Tiira, T., Korhonen, H., Azbel, I., Burmin, V., Buyanov, A., Kosminskaya, I., Ionkis, V. and Sharov, N., 1990, Crust and upper mantle structure along the DSS BALTIC profile in SE Finland. *Geophys. J. Int.*, **101,** 89-110.

Matthews, D. H. and Cheadle, M. J., 1986, Deep reflections from the Caledonides and the Variscides west of Britain and comparisons with the Himalayas. In: *Barazangi, M. and Brown, L., (Eds.), Reflection seismology: a global perspective.* (American Geophysical Union, Geodynamics series), **13,** 5-19.

Matthews, P. A., 1989, Crustal structure off the North Yorkshire coast from high-resolution wide-angle reflection data. *Unpublished M.Sc. thesis,* University of Durham.

McBride, J. H., Snyder, D. B. and Hobbs, R. W., 1992, In: *Meissner, R., Snyder, D., Balling, N. and Staroste, E. (Eds.), The BABEL project. First progress report.* (Commission of the European communities, EUR 14429EN), 71-76.

Meissner, R. and Wever, Th., 1990, First periodic report to the European Economic Community, Project JOUR-0016-C (MB) (BABEL).

Meissner, R., Wever, Th. and Sadowiak, R., 1991, Continental collisions and seismic signature. *Geophys. J. Int.*, **105,** 15-23.

Mereu, R. F., Epili, D. and Green, A. G., 1990, Pg shingles: preliminary results from the onshore GLIMPCE refraction experiment. *Tectonophysics,* **173,** 617-626.

Mooney, W. D. and Brocher, T. W., 1987, Coincident seismic reflection/refraction studies of the continental lithosphere: A global review, *Geophys. J. R. astr. Soc.*, **86,** 1-6.

Nelson, K. D., 1991, A unified view of craton evolution motivated by recent deep seismic reflection and refraction results. *Geophys. J. Int.*, **105,** 25-35.

Pavlenkova, N. I., 1979, Generalised geophysical model and dynamic processes of the continental crust. *Tectonophysics*, **59,** 381-390.

Pedersen, L. B., Tryggvason, A., Schmidt, J. and Gohl, K., 1992, Synthesis of geophysical data in the Bothnian Sea. In: *Meissner, R., Snyder, D., Balling, N. and Staroste, E. (Eds.), The BABEL project. First progress report.* (Commission of the European communities, EUR 14429EN), 59-64.

Pesonen, l. J., Torsvik, T. H., Elming S.-Å. and Bylund, G., 1989, Crustal evolution of Fennoscandia - palaeomagnetic constraints. *Tectonophysics*, **162,** 27-49.

Reston, T. J., 1987, Spatial interference, reflection character and the structure of the lower crust under extension: results from 2D modelling. *Annales Geophysicae*. **5,** 339-347.

Rowbotham, P. S., 1990, Near-surface structure from wide-angle seismic reflection data. *Unpublished M. Sc. thesis*. University of Durham.

Sellevoll, M. A., 1973, Mohorovicic discontinuity beneath Fennoscandia and adjacent parts of the Norwegian Sea and North Sea. *Tectonophysics*, **20,** 359-366.

Snyder, D. B, 1992, Tectonic implications of BABEL normal-incidence data in Bothnian Bay. In: *Meissner, R., Snyder, D., Balling, N. and Staroste, E. (Eds.), The BABEL project. First progress report.* (Commission of the European communities, EUR 14429EN), 35-39.

Telford, W. M, Geldart, L. P. and Sheriff, R. E., 1990, Applied Geophysics: second edition, (Cambridge University Press).

Trappe, H., 1989, Deep seismic profiling in the North German Basin. *First Break*, **7 (5),** 173-184.

Warner, M. and McGeary, S., 1987, Seismic reflection coefficients from mantle fault zones. *Geophys. J. R. astr. Soc.*, **89,** 223-230.

Weber, M., 1988, Computation of seismograms in absorbing 2-D media using the Gaussian beam methods: comparison with exact methods. *Geophys. J.*, **92,** 9-24.

Welin, E., 1987, The depositional evolution of the Svecofennian supracrustal sequence in Finland and Sweden. *Precamb. Res.*, **35,** 95-113.

West, T. E., 1990, A high resolution wide-angle seismic study of the crust beneath the Northumberland trough. *Unpublished Ph.D. thesis*, University of Durham.

Winterhalter, B., 1972, On the geology of the Bothnian Sea, an epeiric sea that has undergone Pleistocene glaciation. *Bulletin of the Geological Survey of Finland*, **258.**

Witschard, F., 1984, The geological and tectonic evolution of the Precambrian of northern Sweden - a case for basin reactivation ? *Precamb. Res.*, **23,** 273-315.

Wonik, T. and Hahn, A. 1990, Compilation of the central and northern European Aeromagnetic Surveys: Methods, difficulties and results. In: *Freeman, R. and Mueller, St. (Eds.), Proceedings of the sixth workshop on the EGT project.* (European Science Foundation), 213 - 224.

APPENDIX A

SEGY-WAR specification

This form of SEGY is modified to allow for wide-angle seismic reflection and earthquake data as well as normal-incidence data.

Reel identification header.

1. 40 EBCDIC CARD IMAGE (BYTES 1-3200)

C1 Project name.

2. BINARY CODE (BYTES 3201-3600)

3205-3208 Line number.

3209-3212 Reel number for this line.

3213-3214 Number of traces per record.

3215-3216 Number of non-seismic traces per record (e.g. UTC code and clock).

3217-3218 Sample period (microsecs).

3221-3222 Number of samples per data trace (if zero or blank then determine from trace header).

3225-3226 Data format:

1 = floating point (4 bytes, IBM R*4 format);
2 = fixed point (4 bytes, PDAS format);
3 = fixed point (2 bytes, PDAS format);
4 = fixed point with gain code (2 bytes, PDAS format);
5 = floating point (4 bytes, IEEE format, ASCII).

3255-3256 Measurement system: 1=metres, 2=feet.

Trace header

13-16 Trace / channel / station number.

17-20 Shot / event number.

29-30 Trace identification code:

1 = seismic data;
2 = dead channel;
3 = dummy channel;
7 = utc time code;
9 = local clock code (Geostore).

37-40 * Horizontal distance from shot to receiver (metres).

41-44 Receiver elevation: positive above sea level, negative below.

45-48 Surface elevation at source (signed as 41- 44).

49-52 Source depth below surface.

53-56 Datum elevation at receiver.

57-60 Datum elevation at source.

61-64	Water depth at source.	
65-68	Water depth at receiver.	
69-70	Scalar for 41- 68 to give real values: positive multiplier, negative divider.	
71-72	Scalar for bytes 73 - 88 to give real values: positive multiplier, negative divider.	
73-76	Source coordinate - X (longitude, positive to east).	
77-80	Source coordinate - Y (latitude, positive to north).	
81-84	Receiver coordinate - X (longitude. positive to east).	
85-88	Receiver coordinate - Y (latitude, positive to north).	
89-90	Coordinate units: 1= length, 2 = secs of arc.	
109-110 *	Delay between shot instant and trace start (ms part).	
115-116	Number of sample in this trace.	
117-118	Sample interval in microsecs for this trace.	
121-122	Instrument gain constant.	
141-142	Alias filter frequency.	
143-144	Alias filter slope.	
149-150	Low-cut frequency.	
153-154	Low-cut slope.	
157-158	Year	
159-160	Day	
161-162	Hour	Time at start of trace.
163-164	Minute	
165-166	Second	
187-188	Millisec	
167-168	Time basis 1=local, 2= UT (used for all time logs).	
191-192	Year	
193-194	Day	
195-196	Hour	Time of event (shot time).
197-198	Minute	
199-200	Second	
201-202	Millisec	
207-208 *	Delay between shot instant and start of trace (secs).	
211-212 *	Reduction velocity (km/s x 10) used to define trace window.	
215-216 *	Reduced time at start of trace (secs).	
221-224	Four-character station code (ASCII).,	
225-228	Four-character channel code (ASCII), NS, EW, Z, MSF, etc.	

NOTE: All elevations should normally be taken from datum, in which case bytes 53-60 would be zero. For earthquake data bytes 49 - 52 would be focal depth.

* Where a reduction velocity (v) is specified (i.e. not zero or undefined) then the offset (T) of the trace window from the shot instant is calculated from the relation:

$$T = \frac{x}{V} - r$$

where x is the station-shot offset and r is the user defined 'run-in' time. The value of T is placed in bytes 207-208 (whole secs) and 109-110 (fractional secs). Where no reduction velocity is specified T is arbitrarily defined by the user.

APPENDIX B
Conversion program - CONVERT

The C program 'CONVERT' was written to convert the BABEL field data into SEGYi format, as described in Chapter V. A flow chart for the program is shown in Figure Bi and the program is described in detail below (a full listing of the main program and the three libraries of subroutines, READ.C, UTIL.C and WRITE.C, is given at the end of this appendix). The names of subroutines called during conversion are shown in square brackets in Figure Bi.

CONVERT reads field data from the PDAS file and information from three other files: a file of station details (STATION), a file of shot details (EVENT) and an options file (OPTIONS). These three files and the first PDAS data file should be specified on the command line in the following order:

CONVERT [*PDAS filename*] OPTIONS STATION EVENT.

The options file contains various user defined parameters. These include values used during conversion (reduction velocity, data format, etc.) and switches which define how the converted traces are to be written. There are two possible output file formats; the trace headers and trace data may be written to separate binary files or each trace may be written to an individual file. In both cases, the binary and ASCII SEGY file headers are written into separate files. The BABEL SEGYi data were written in the latter of these two formats which was compatible with existing software. All of the integers and floating point numbers were written with the high order byte in the lowest address (i.e. backwards from the standard P.C. format). This is the correct format for the SUN machines to which the data was transferred.

A sample options file is given in table Bi (the options in the file take the format LABEL:SPECIFICATION). The trace length in samples is usually calculated from the length in seconds (given in the options file) and the sample rate (read from the PDAS header).

Flow chart for CONVERT.C

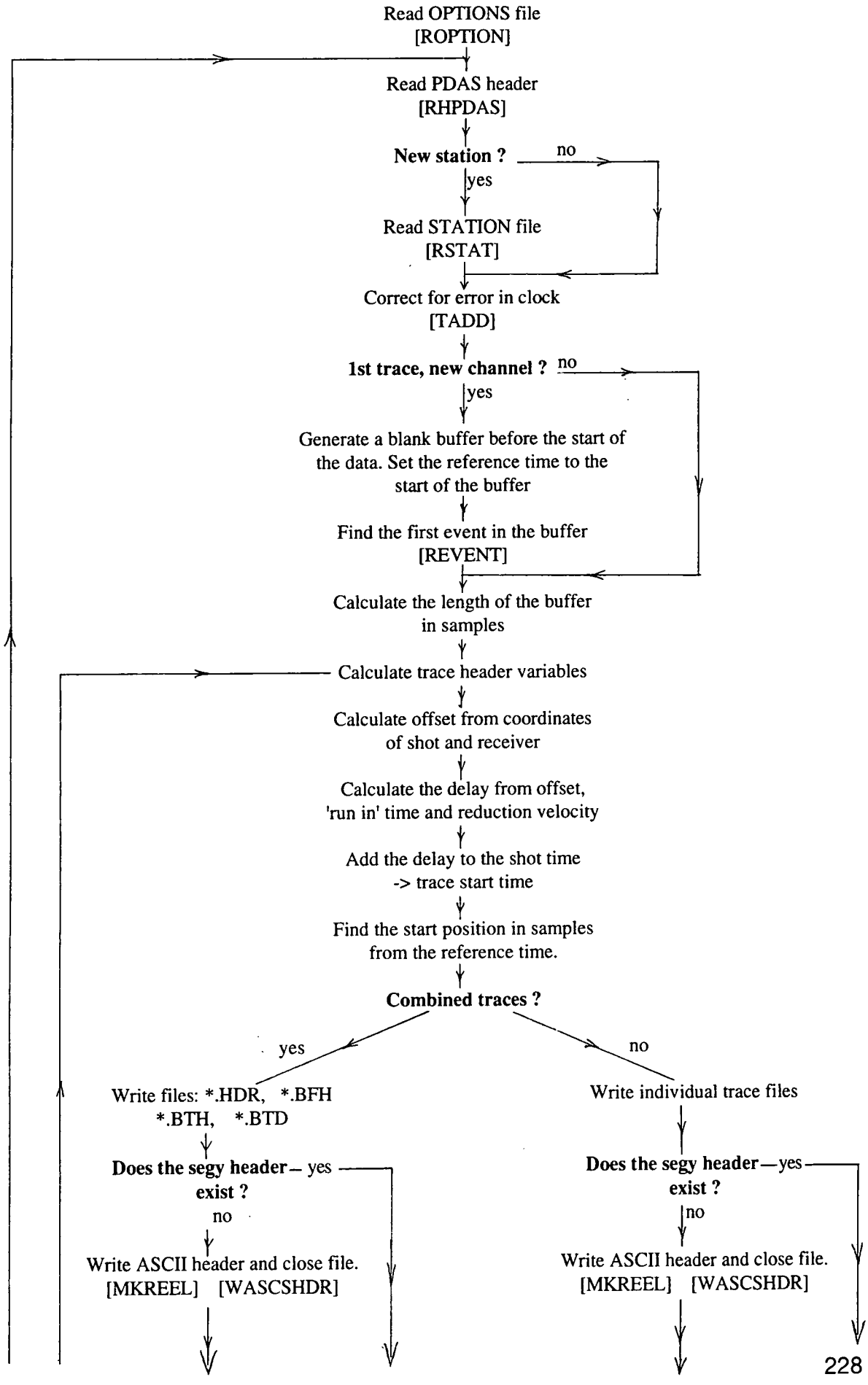

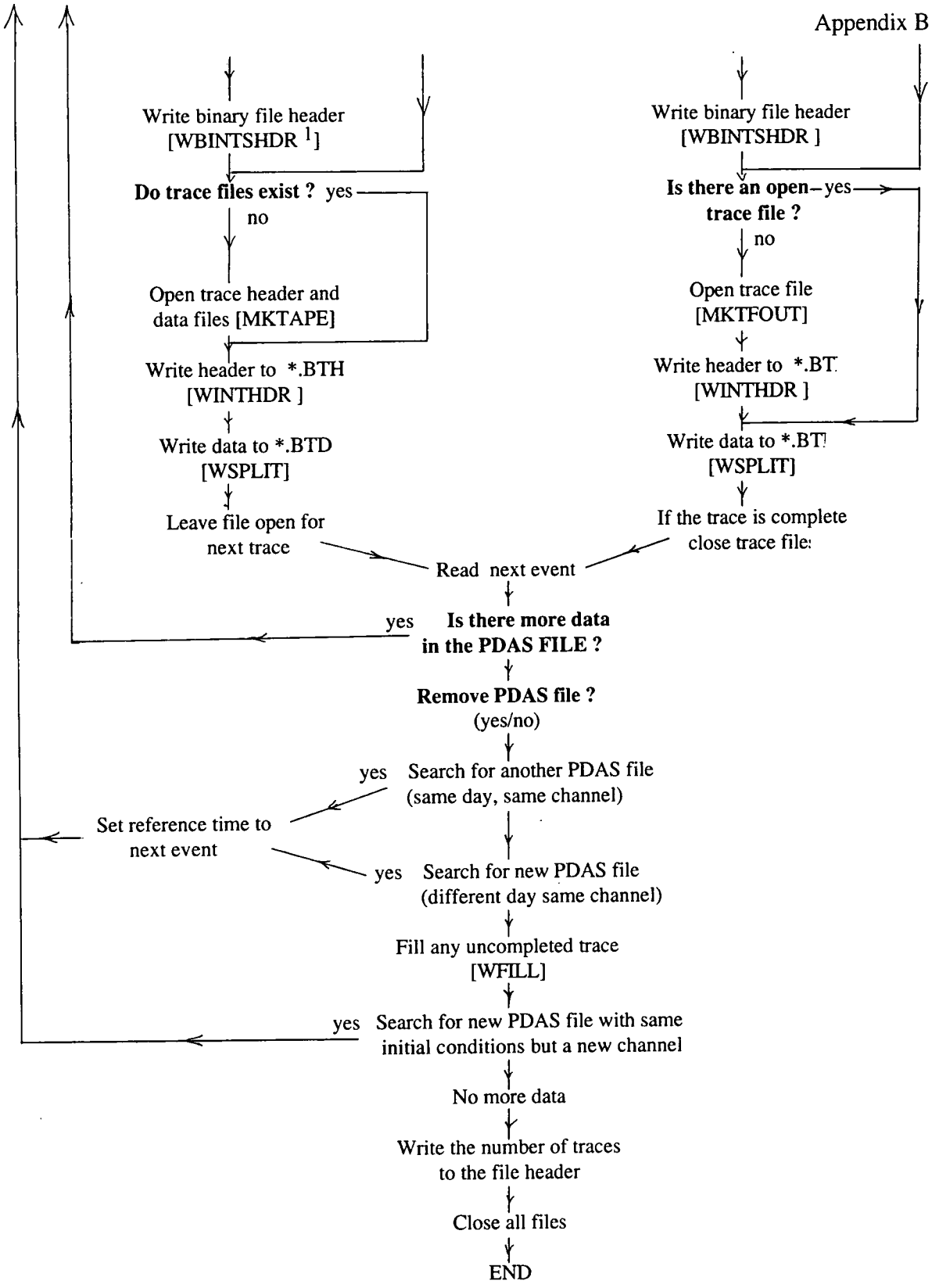

Figure Bi: Flow chart for program CONVERT.

---

[1] WBINTSHDR and WINTHDR both write out all values as 4 byte integer and floating point numbers. Alternate routines WBSYHDR and WTRACEHDR write out header values as 2 and 4 byte integers.

OPTIONS FILE	DESCRIPTION
PROJECT_NAME:BABEL-WAR	Project name (ASCII).
STATION_NAME:BS5P	Station name (4-char ASCII).
REEL:1	Reel number.
SEISMIC:6	Number of seismic traces in reel.
NONSEISMIC:2	Number of non-seismic channels.
OUT_FORMAT:1	Output format.
MEASUREMENT:1	Units for distances.
COORD_UNITS:2	Units for coordinates.
COMBINE:Y	Combine trace data and headers ?
DEL_PFILE:N	Delete used PDAS files ?
TIMEBASIS:2	Time (local or universal).
VR:6000	Reduction velocity (m/s).
PRE_RUN:6000	Reduced time at start of trace (msec).
LENGTH:30	Trace length (secs).
SAMPLES:6000	Trace length in samples
COMMENTS:	This should be the last line of the options file.

Table Bi. Example OPTIONS file for the program CONVERT

For direct access files, all of the records must be of the same length. If the sample rate varies between PDAS files (such as in the case of the pseudo-PDAS files generated from the Geostore data) then the trace length in samples must be specified in the options file. When the sample rate does not vary, the SAMPLES option is ignored and may either be set to 9999 or excluded from the options file.

Header	Description
DATASET P1107022271	Name of the PDAS File.
FILE_TYPE INTEGER	Data type (Integer = 2 byte, Long = 4 byte)
VERSION next	Sets the filename to the next sequence number.
SIGNAL MSF	Channel name (as given during set-up).
DATE 9-22-89	Date on which data was recorded.
TIME 17:59:50.50(500)	Time at which data was recorded.
INTERVAL 0.010	Sample interval in seconds.
VERT_UNITS Counts	Always counts.
HORZ_UNITS Sec	Always seconds.
COMMENT GAINRANGED	Data type.
DATA	Beginning of Binary file data.

Table Bii. Example of an ASCII header for a gainranged PDAS data file.

An example PDAS header is shown in table Bii. The time and date recorded in the PDAS header are from the internal clock and must be corrected to universal time (UT). The correction time, and other details for the particular recording sites, are found from the station file using the station name (from the options file) and the channel number (from the PDAS header). The station details are only re-read if the channel number in the PDAS file header changes.

The format of the station file is shown in table Biii. Time corrections in the station file are the average difference between the internal clock of the PDAS or Geostore system and universal time. Drift errors in the internal clocks are considered in sections 5.3.

DESCRIPTION	COLUMNS	FORMAT
Station name (4-char ASCII)	1-4	A4
Channel number	5-6	I2
Channel name (4-char ASCII)	7-9	A4
Elevation	10-12	I3
Blank	13	1X
Datum elevation	14-17	14
Blank	18	1X
Water depth	19-24	F6.1
Blank	25	1X
latitude (deg, min, sec, N/S)	26-34	I3,I2,F5.2,A1
Blank	35	1X
Longitude (deg, min, sec, E/W)	36-44	I2
Gain	45-50	I6
Blank	51	1X
Type (P, GB, GO)	52-53	A2
Blank	54	1X
Time correction (msec)	55-60	I6

Table Biii. Format of the station file (P - PDAS, GB - Geostore base station, GO - Geostore outstation). All depths and elevations are in metres.

The PDAS data may be considered as a stream of data blocks and separated by blank gaps (Figure Bii). CONVERT creates a blank buffer of twice the trace length infront of the first PDAS file. This is so that any traces that lie only partially in the first data file are extracted (for subsequent files, a blank buffer is created between the end of the previous file and the start of the new file for the same reason).

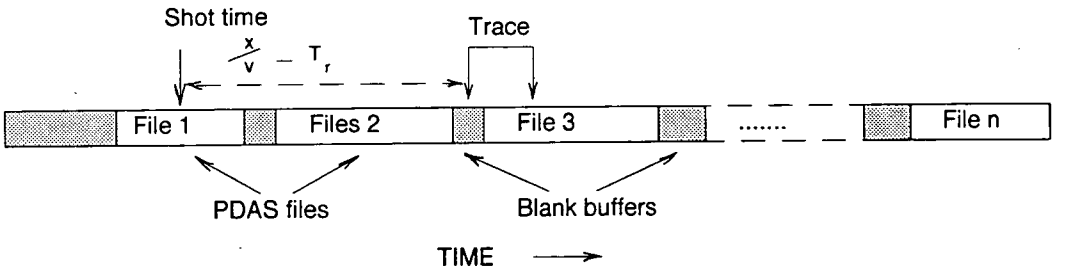

Figure Bii. PDAS data files as a continuous stream of data separated by blank gaps.

The shot times from the event file (table Biv) are read to find the time of the first shot after the start of the blank buffer. The details for this shot are used to calculate the shot-receiver offset and the start time of the trace. The trace corresponding to this event is extracted, beginning at the calculated start time, and written to the hard disk of the PC.

DESCRIPTION	COLUMNS	FORMAT
Line number (A=1,B=2, etc.)	1-2	I2
Time (hour, min,sec, msec)	3-11	I2,I2,I2,I3
Shot number	12-15	I4
Latitude (deg, min, sec)	16-24	I2,I2,F5.2
Longitude (deg, min, sec)	25-33	I2,I2,F5.2
Shot depth	34-38	F6.1
Elevation	39-42	I4
Datum	43-46	I4
Water depth	47-52	F6.1
Julian day	53-56	I4

Table Biv. Format of the event file. All depths and elevations are in metres.

The converted data is written to a drive specified by the user. CONVERT creates a directory on this drive named after the line and the station (i.e. L10BS3 for line 1, base station 3). The ASCII and binary tape headers are written into this directory. Sub-directories are created for individual channels; the trace headers and trace data files are written into these. If the line changes, the user is asked whether to proceed. If the answer is yes, then a new line directory is created.

The process is then repeated for the next shotpoint in the event file and so on, until there is no more data or the end of the event file is reached. When there are no more shots or data for a particular channel, the program checks to see if there are any data files with the same initial values but with a different channel number. If so, then the user is asked whether these should also be converted. When there are no more data files the program terminates. During conversion, the PDAS file from which data is being read and the trace that is being extracted are printed to the screen.

A complete listing of CONVERT is given in the remainder of this appendix.

1. CONVERT. H

```
                                        /* Convert.h */
/* HEADER FILE for the program CONVERT */
/* PAM 1990 */
#define TRUE 1
#define FALSE 0
#define VOID 0
typedef struct thdr THDR;
typedef struct shdr SHDR;

unsigned char pfile[64];
unsigned char ofile[64];
unsigned char sfile[64];
unsigned char efile[64];
unsigned char tfout[64];
unsigned char thfout[64];
unsigned char sfout[64];
unsigned char sbfout[64];

FILE *fppdas, *fpopt, *fpstat, *fpeve;
FILE *fptout, *fpsout, *fpthout, *fpsbout;
fpos_t data_strt;

struct shdr{                    /* SEGY TAPE HEADER      */
   char project[20];            /* project name 20 chars */
   long line;                   /* line number           */
   long reel;                   /* reel number           */
   short notr;                  /* no. traces per record */
   short nonseis;               /* no. non seismic traces*/
   short period;                /* sample period         */
   short number;                /* samples per data trace*/
   short format;                /* data format           */
   short measure;               /* measurement system    */
   };
struct coord{
   long lgdit;                  /* longditude            */
   long lat;                    /* latitude              */
   };
struct elev{
   long elv;                    /* elevation above s. l. */
   long datum;                  /* datum elevation       */
   long water;                  /* water depth           */
   };
struct time{
   short year;                  /* year                  */
   short day;                   /* julian day            */
   short hour;                  /* 0 - 24                */
   short min;                   /* 0 - 59                */
   short sec;                   /* 0 - 59                */
   short msec;                  /* millisec              */
   };
struct filt{
   short freq;
   short slope;
   };
struct thdr{                    /* SEGY TRACE HEADER     */
   char statn[5];               /* 4-char station code   */
   char channel[5];             /* 4-char channel code   */
   long field;                  /* field record number   */
   long trace;                  /* trace number          */
   long source;                 /* shot/event number     */
   long utrace;                 /* number in cdp gather  */
   short trid;                  /* trace id code         */
   long dist;                   /* horizontal dist       */
   struct elev relv;            /* reciever elevtn       */
   struct elev selv;            /* source elvt n                 * /
   long sdepth;                 /* source depth          */
   short escale;                /* scalar for elevations */
   short cscale;                /* scalar for coords     */
   struct coord rco;            /* reciever coords       */
   struct coord sco;            /* source coords         */
   short cunits;                /* coord units           */
   struct time delay;           /* delay shot to trace start */
   short sample;                /* no. samples in this trace*/
   long intvl;                  /* sample int -should be short int for SEGY      */
   short gain;                  /* inst gain const       */
   struct filt alias;           /* alias filter          */
   struct filt low              /* low cut filter        */
   struct time start;           /* start of trace        */
   struct time event;           /* event time            */
```

```
  short tbasis;              /* time basis                */
  short rvel;                /* reduction velocity        */
  short rtime;               /* reduced time at start s   */
  short shotsiz;             /* shot size in kg           */
  };
THDR *pt;
SHDR *ps;
struct time began, *pb, strtbuff, *psbt,correct, *ptc;
struct time pretime, *pret;

double ltosec(char[]);          /* FUNCTION DEFINITIONS   */
double olltosec(char[]);
long ltodist(THDR *pt);
long difference(struct time p1,struct time p2);
unsigned char *mkbuffer(int gaplength);
int wsplit(unsigned long gaplength, char datatype, unsigned long *c);
int rnxtevent(SHDR *ps, THDR *pt, struct time *pst);
int rnxtoevent(SHDR *ps, THDR *pt, struct time *pst);
float dgr(short grdata);
short hextoi(unsigned char hexchar);
unsigned char itohex( int number);
```

2. CONVERT.C

```
                                        /* CONVERT.C */
/* PAM 1990 */
/* PDAS type files are read in from the directory u:. Traces are split out, depending on the options
chosen, and blank traces written out to fill in the events between PDAS data files. Output traces
are written to the correct directory on v:. Functions are in the files UTIL.C READ.C WRITE.C.
Values are written out in reverse PC format with the least significant byte last. The trace and
SEGY header formats are given in appendix A. Length of traces must be constant for a direct
access file. The length of the traces can calculated from the file length in secs and the sample
rate (if constant). If not, then it is read from the options */

/* header data is in the file convert.h */
#include <stdio.h>
#include <stdlib.h>
#include "convert.h"

/******************** MAIN PROGRAM **********************/
/*  - Files should be entered in the order pdasfile,.options, station, event. */
?main(int argc, char *argv[])
{
int i,dec,sign,ch,b;
int tstatus=0;                  /* flag values showing current trace status */
int lstatus=0;
int skip=0;
int next_trace=0;
int next_pfile=0;
long stom=1000000;              /* convert nanosec to msec */
long tlength,pretimes,pretimem;
long slength=9999;   /* 9999 = use default (if samp rate constant)          */
long gap, gaplength, fillin, c, start;
double tmp,gtmp,stmp;
float srtime;
char *tmp2;
char datatype;
char combine,rmpfile;
short inserial, incount, inpdasday, inchan;
short  serial, count, pdasday, chan;
unsigned char fltype,channel[2];
unsigned char *ptrace,hexchan;
```

```
for(i=0;i<120;i++){pfile[i]=sfout[i]=tfout[i]=0;}          /* Zero arrays          */
for(i=0;i<120;i++){ofile[i]=sfile[i]=efile[i]=0;}          /* Zero arrays          */

ps=(SHDR *)malloc(sizeof(SHDR));                    /* allocated memory for the headers */
pt=(THDR *)malloc(sizeof(THDR));
                                /* assign pointers                                  */
pb=&began;                      /* pb =pointer to time pfile starts                 */
psbt=&strtbuff;       /* psbt=pointer to start of the buffer        */
ptc=&correct;         /* ptc=pointer to correction time                   */
pret=&pretime;                  /* pret= pointer to run in time for the first trace        */
pt->escale=10;                  /*multiplier to make relv and selv positive real */
pt->cscale=100;                 /*multiplier to make  coordinates positibe real  */
pt->utrace=1;         /* number within cdp gather */

/*-------------------------------------------------------------------------------------*/
?if(argc !=5){                              /* CHECK - four file entered */
   fail('1',NULL,argv[0]);
   }
for(i=2;i<argc;i++){                /* CHECK - files exist and can be read */
   if(fexist(argv[i])==FALSE){    /* FEXIST.....util.c   */
      fail('2',NULL,argv[0]);
      }
   }

/*-------------------------------------------------------------------------------------*/
?strcpy(ofile,&argv[2][0]);         /* READ the options file...read.c */
roption(ofile, ps, pt, &tlength, &combine, &rmpfile,&slength);

/*-------------------------------------------------------------------------------------*/
/* ASSIGN the pdas file name bits to the initial values. Future calls to find the next pdas file can
just use mkfile and the previous value or initial values */

sscanf(&argv[1][0],"%1c%1c%3d%3d%*1c%3d",&fltype,&hexchan,&serial,&incount,
&inpdasday);                        /* initial values                   */

inchan=hextoi(hexchan);
chan=inchan;                        /*   counter values     */
count=incount;
pdasday=inpdasday;
                                    /* GENERATE the pdasdata file name....util.c  */
mkpfile( pfile, fltype, chan, serial, count, pdasday);

/*=====================================================*/
/* NEW TAPE LOOP. */

while(next_pfile==0){

 printf("\n Pdas datafile....%s",pfile);
 rhpdas(pfile, ps,pt, pb,&datatype );       /* READ the pdas datafile....read.c */
                                             /* pb is the start time of the new pdas file */

/*+++++++++++++++++++++++++++++++++++++++++++++++++++++++++++++++++++++++++++++++++++++*/
if(strncmp(&pfile[5],&argv[1][2])==0){
   strcpy(sfile,&argv[3][0]);                /* READ the station file...read.c   */
   sprintf(channel,"%1d",chan);
   rstat(channel, sfile, ps, pt,ptc);
   }                                                    /* ptc is the correction time that must be
added on */

/*+++++++++++++++++++++++++++++++++++++++++++++++++++++++++++++++++++++++++++++++++++++*/
  /* tcorrect   -  CORRECT for drift of the clock   */
tadd(pb,ptc);                       /* add ptc to pb */

/*+++++++++++++++++++++++++++++++++++++++++++++++++++++++++++++++++++++++++++++++++++++*/
/* DO FOR FIRST TRACE NEW CHANNEL */
/* If datafile is the first for a particular channel then start the buffer 2x tlength  before the start of
the pdasdata file. Makes sure that none of] the data is lost */

 if(strncmp(&pfile[5],&argv[1][2])==0){             /* Do for new channel */
   pt->trace=1;                                     /* first trace for new channel */
   pt->alias.freq=0;
   pt->alias.slope=0;
   pt->low.freq=0;
   pt->low.slope=0;

   memcpy(psbt,pb,sizeof(struct time));              /* copy structure */
                                                        /* CALCULATE the start of the
data buffer */
   pret->sec=(2*tlength)%60;                        /* get pre start seconds */
   pret->min=(2*tlength)/60;                         /* get pre start minutes */
```

```
  while(pret->min>=60){
     pret->min-=60;
     pret->hour++;
     }
  tsub(psbt,pret);

/*-------------------------------------------------------------------------------*/
   strcpy(efile,&argv[4][0]);                  /* READ the event file ....read.c   */
   roevent(efile, ps, pt, psbt);

   }  /* END of loop for 1st trace new channel */

/*+++++++++++++++++++++++++++++++++++++++++++++++++++++++++++++++++*/
/* Calculate the number of blank samples before the next data file */
  gap=difference(*pb, *psbt);                  /* calculate time difference in millisecs */
  if(gap<0){                                   /* if the next event is in the next pfile -
problem ! */
     memcpy(psbt,pb,sizeof(struct time));
     gap=0;
     skip=1;
  }else{
     skip=0;
     }
  gtmp=((double)gap*stom)/pt->intvl;          /* multiply by sample rate in nsecs */
  dtol(gtmp,1,&gaplength);                    /* convert from a double to a long */

/*-------------------------------------------------------------------------------*/
/* Now calculate the other values to go in all of the headers */
   if(slength==9999){                                  /* if length in samples not given...
*/
      pt->sample=tlength*(1000000000.0/pt->intvl);     /*... calculate it */
   }else{
      pt->sample=slength;
      }
   ps->number=pt->sample;

 /*=============================================================*/
 /* Calculate and include extra bits for this trace header */

   while(next_trace==0&&next_pfile==0){
```

```
   pt->dist=ltodist(pt);                              /* DISTANCE */
   pt->trid=0;                                        /* TRACE identifier */
   if(strncmp("DEAD",pt->channel,4)==0)
      pt->trid=2;                                     /* dead channel  */
   else if((strncmp("DUMY",pt->channel,4)==0)||(strncmp("RF",pt->channel,2)==0))
      pt->trid=3;                                     /* dummy channel */
   else if(strncmp("MSF",pt->channel,3)==0)
      pt->trid=7;                                     /* utc          */
   else if(strncmp("IC",pt->channel,2)==0)
      pt->trid=9;                                     /* local clock */
   else
      pt->trid=1;                                     /* seismic data */

/* Calculate the delay time to reduce the traces. */

   srtime=pt->rtime/1000.0;                           /* convert to secs */
  if(pt->rvel==0){
   tmp=0.0000;
  }else{
   tmp=((float)pt->dist)/pt->rvel+srtime;             /* DELAY */
   }
   tmp2=fcvt(tmp,3,&dec,&sign);                       /* Convert to string then read */
   if(dec>=0){                                        /* more than an 1sec. */
      if((b=sscanf(&tmp2[dec],"%d",&pt->delay.msec))==EOF){
         pt->delay.msec=0;
         }
      tmp2[dec]='\0';
      if((b=sscanf(tmp2,"%d",&pt->delay.sec))==EOF){
         pt->delay.sec=0;
         }
   }else{                                             /* less than a second */
      pt->delay.sec=0;
      if((b=sscanf(tmp2,"%d",&pt->delay.msec))==EOF){
         pt->delay.msec=0;
         }
   }
   if(sign !=0){
    pt->delay.msec=-pt->delay.msec;
    pt->delay.sec=-pt->delay.sec;
    }
```

```
    pt->delay.min=0;
    pt->delay.hour=0;          /* time structure for delay time */
    pt->delay.day=0;
    pt->delay.year=0;

     /* calculate start time */
    memcpy(&pt->start,&pt->event,sizeof(struct time));          /* time copy */
    tadd(&pt->start,&pt->delay);

/*-------------------------------------------------------------------------------*/
  if(tstatus==0||skip==1){
                          /* Find the start position in samples from the start of the buffer */
     start=difference(pt->start,*psbt);          /*  in msecs */
     stmp=((double)start*stom)/pt->intvl;
     dtol(stmp,1,&c);
     }
pt->field=pt->trace;          /* field number is the same as the trace no. */

/*-------------------------------------------------------------------------------*/
if(c+pt->sample<gaplength){          /* mark the blank traces */
   pt->trid=3;
   }
switch(combine){                     /* combine hdr and data files ? */

/*^^^^^^^^^^^^^^^^^^^^^^^^^^^^^^^^^^^^^^^^^^^^^^^^^^^^^^^^^^^^^^^^^^^^^^^^^^^^*/
case 'N':                            /* write individual trace files */

  if(mksfout(sfout,ps, pt)==0){      /* If segy header doesnt exist: */
    wascshdr(ps,fpsout);
    wbintshdr(ps,fpsout);            /* WRITE SEGY HEADER */
                                     /* to write ascii/IEEE segy wbsyhdr(ps,fpsout)  */
    }
  if(tstatus==0){
     mktfout(tfout,ps, pt);          /* create trace file */
     printf("\n writing trace....%s",tfout);
     }

 /*-------------------------------------------------------------------------------*/
```

```
/* Write out the trace data to the trace file. If the pdasdata file ends in the middle of a trace then
don't close the trace file, get the next pdasdata file and see if it carries on directly. Don't make a
new trace header. If this is the case tstatus=1 */

 if(tstatus==0){
     wintthdr(pt,fptout);                    /* Write trace header out */
                                  /* to write ascii/IEEE segy  use wtracehdr(pt,fptout) */
     }
 next_trace=wsplit(gaplength, datatype, &c );
 if(next_trace==0){
     fclose(fptout);
     }
 tstatus=next_trace;

 break;
/*^^^^^^^^^^^^^^^^^^^^^^^^^^^^^^^^^^^^^^^^^^^^^^^^^^^^^^^^^^^^^^^^^^^^^^^^^^^^/
 case 'Y':

  if(mkreel(sfout,sbfout, ps, pt)==0){          /* If segy header doesnt exist: */
     wascshdr(ps, fpsout);
     wbintshdr(ps, fpsbout);                    /* WRITE SEGY HEADER */
                                  /* to write ascii/IEEE segy wbsyhdr(ps,fpsbout)  */
     fclose(fpsout);
     }

 if(tstatus==0){
     mktape(tfout,thfout,ps,pt);                          /* don't exist then make them. */
     printf("\n writing trace %d", pt->trace);
      wintthdr(pt,fpthout);                     /* write out the trace header */
                                                /* to wrtie ascii/IEEE segy

wtracehdr(pt,fpthout) */
     }
 next_trace=wsplit(gaplength,datatype,&c);          /* write trace data */
 tstatus=next_trace;

 break;

/*^^^^^^^^^^^^^^^^^^^^^^^^^^^^^^^^^^^^^^^^^^^^^^^^^^^^^^^^^^^^^^^^^^^^^^^^^^^^*/
 default:
  fail('7',fptout,tfout);
```

```
  break;
 }

/*^^^
```

```
    fclose(fptout);
    }
 }
if(next_pfile==1){
    count=incount;              /* channel with same initial values. */
    pdasday=inpdasday;
    while(chan<15&&next_pfile==1){
     chan++;
     mkpfile(pfile,fltype,chan, serial,count,pdasday);
     if(fexist(pfile)==TRUE){
        printf ("\n %s \n New channel: continue Y/N ? \n",pfile);
        ch=getchar();
        while(ch !='Y' && ch !='N'){
           ch=getchar();
           }
        if(ch=='N'){
           fcloseall();
           exit(2);
           }
        next_pfile=0;                   /* new file */
        c=0;
        if(lstatus==2){
         lstatus=0;
         }
        }
     }
    }
 if(next_pfile==0){
    next_trace=0;
    memcpy(psbt,&pt->start,sizeof(struct time));      /* start at next event */
    }

 }     /* If another file is found, play it again !! */

/* End of " While new data file exists " loop.....*/

/*=========================================================*/
printf("\n No more pdasdata files found. Program ends. \n");
fcloseall();
return(0);
}     /* END OF MAIN */
```

3. READ.C

```
                                        /* READ.C */
/* FUNCTIONS to read data from various files */
#include <stdio.h>
#include <stdlib.h>
#include <ctype.h>
#include "convert.h"

/*************************** RHPDAS ************************/
/* PAM 1990 */
/* RHPDAS reads in the data from the PDAS header, performs the necessary calculations and
writes values into the correct place in the header structures. The start time of the pdas file is
copied to pb */

rhpdas(char *pfile, SHDR *ps, THDR *pt, struct time *pb, char *pdatatype)
{
unsigned char *cptr, cbuf[80];
int i, data_flag, l_dash, colon1, colon2;
int j;
double atof(), in;
unsigned char dataset[20],date[20],stime[20],interval[20];
unsigned char signal[20];

for(i=0;i<4;i++){(pt->channel)[i]=0;}                    /* zero arrays */
for(i=0;i<20;i++){dataset[i]=date[i]=stime[i]=
            interval[i]=signal[i]=0;}

/* Open the pdasfile */
if((fppdas=fopen(pfile, "rb"))==NULL){                    /* check file is read binary */
   fail('3',fppdas,pfile);
   }
/* Input file is in DaDisp format, data is read from the header, giving SIGNAL, DATE, TIME,
INTERVAL. These are written into pt->channel,pt->sample and struct time began (*pb). ASCii
values are only capitals and numerals to make the conversion into EBDIC easier */

data_flag=1;
/* Read just the header */

while(data_flag==1){                                    /* while there is data to read */
cptr=&cbuf[0];
while((*cptr++=getc(fppdas)) !='\r');                   /* read line in header */
*cptr=getc(fppdas);
cptr--;
*cptr='\0';

if(strncmp("DATASET",cbuf,7)==0){          /* ie p1107048270 */
   strcpy(dataset,&cbuf[8]);
   }
if(strncmp("FILE_TYPE",cbuf,9)==0){
   if(strncmp("INTEGER",&cbuf[10],7)==0){
      *pdatatype='I';
   }else if(strncmp("OFFSET",&cbuf[10],6)==0){
      *pdatatype='O';
   }else if(strncmp("LONG",&cbuf[10],4)==0){
      *pdatatype='L';
      }
   }
if(strncmp("SIGNAL",cbuf,6)==0){                    /* ie N-S */
   strcpy(signal,&cbuf[7]);
   for(j=i=0;(i<4)&&(j<4);i++){                     /* create 4 char channel name */
      if(isalnum(signal[i])){                                /* ignoring non alphas */
         pt->channel[j]=signal[i];
         j++;
         }
      }
    if(strncmp("AUX",pt->channel,3)==0){          /* can't name a directory  'aux ' */
      pt->channel[1]=' ';
      pt->channel[2]=' ';                                    /* call it A instead */
   }
   while((j=strlen(pt->channel))<4){
      pt->channel[j]=' ';
      j++;
      }
   pt->channel[4]='\0';
   }
if(strncmp("DATE",cbuf,4)==0){                     /* ie 9-27-89  */
   strcpy(date,&cbuf[5]);
   }
if(strncmp("TIME",cbuf,4)==0){                     /* ie 23:42:57.50 (500) */
```

```
    strcpy(stime,&cbuf[5]);
    }
  if(strncmp("INTERVAL",cbuf,8)==0){              /* ie 0.010 */
    strcpy(interval,&cbuf[9]);
    in=atof(interval);
    }
  if(strncmp("COMMENT",cbuf,7)==0){
    if(strncmp("GAINRANGED",&cbuf[8],10)==0){
      *pdatatype='G';
      }
    }
  if((strncmp("DATASET",cbuf,7)!=0)&&(strncmp("DATA",cbuf,4)==0)){
    data_flag=0;                                   /* if heading=data then end of
pdas header */
    if(fgetpos(fppdas,&data_strt) !=0){
      perror("fgetpos error");
      }
    }
  }
/* write the required values from the pdas header into the headers */
ps->period=1000000*in;                             /* sample period in microsecs */
pt->intvl=1000000000*in;                           /* sample rate in nano secs  */
for(i=0;i<strlen(date);i++){                       /* start time of pdas tape */
  if(date[i]=='-'){l_dash=i;}
  }
(pb->year)=1900+atoi(&date[l_dash+1]);             /* pdas year */
(pb->day)=atoi(&dataset[8]);                       /* pdas day  */
(pb->hour)=atoi(&stime[0]);                        /* pdas hour */
colon1=colon2=0;
for(i=0;i<strlen(stime);i++){                      /* divide time up */
  if(stime[i]==':'){
    if(colon1==0){
      colon1=i;
    }else{
      colon2=i;
    }
    }
  }
(pb->min)=atoi(&stime[colon1+1]);                  /* pdas min */
(pb->sec)=atoi(&stime[colon2+1]);                  /* pdas sec */
for(i=0;i<strlen(stime);i++){                      /* read msecs from the brackets */
  if(stime[i]=='('){
    pb->msec=atoi(&stime[i+1]);                    /* pdas msecs */
    }
  }
} /* END */

/****************** ROPTION ************** */
/* PAM 1990 */
/* reads the initial data values from the options file */

roption(char *ofile, SHDR *ps, THDR *pt, long *ptlength, char
*combine,char *remove,long *sampertr)
{
unsigned char *cptr, cbuf[80];
int i,j, data_flag;

for(i=0;i<20;i++){ps->project[i]=0;}
for(i=0;i<80;i++){cbuf[i]=0;}

/* OPEN options file */

if((fpopt=fopen(ofile,"r"))==NULL){
  fail('3',fpopt,ofile);
  }

/* values are written directly into the two headers THDR and SHDR */
data_flag=1;                                       /* READ values line by line  */
while(data_flag==1){
  cptr=&cbuf[0];
for(i=0;(*cptr=getc(fpopt)) !='\n';++i){
  cptr++;                                          /* read each line */
  }
  *cptr='\0';

  if(strncmp("PROJECT_NAME:",cbuf,13)==0){         /* Ascii project name */
    strcpy(ps->project,&cbuf[13]);
    }
  if(strncmp("STATION_NAME:",cbuf,13)==0){         /* ascii */
    strcpy(pt->statn,&cbuf[13]);
```

```
  while((j=strlen(pt->statn))<4){
    pt->statn[j]=' ';
    j++;
    }
  pt->statn[4]='\0';
  }
if(strncmp("REEL:",cbuf,5)==0){                    /* tape number */
  ps->reel=atoi(&cbuf[5]);
  }
if(strncmp("SEISMIC:",cbuf,8)==0){                 /* seismic traces */
  ps->notr=atoi(&cbuf[8]);
  }
if(strncmp("NONSEIS:",cbuf,8)==0){                 /*non seismic traces */
  ps->nonseis=atoi(&cbuf[8]);
  }
if(strncmp("OUT_FORMAT:",cbuf,11)==0){    /* 1 to 4 */
  ps->format=atoi(&cbuf[11]);
  }
if(strncmp("MEASUREMENT:",cbuf,12)==0){     /* metres or feet */
  ps->measure=atoi(&cbuf[12]);
  }
if(strncmp("COORD_UNITS:",cbuf,12)==0){             /* length or sec arc */
  pt->cunits=atoi(&cbuf[12]);
  }
if(strncmp("COMBINE:",cbuf,8)==0){                  /* seperate traces or */
  *combine=cbuf[8];                                 /* combined into hdr and data */
  }                                                         /* files */
if(strncmp("DEL_PFILE:",cbuf,10)==0){               /* remove pfile after reading ?*/
  *remove=cbuf[10];
  }
if(strncmp("TIMEBASIS:",cbuf,10)==0){                /* local or ut */
  pt->tbasis=atoi(&cbuf[10]);
  }
if(strncmp("VR:",cbuf,3)==0){                       /* reduction velocity */
  pt->rvel=atol(&cbuf[3]);
  }
if(strncmp("PRE_RUN:",cbuf,8)==0){                  /* reduced time start of trace */
  pt->rtime=(-atoi(&cbuf[8]));
  }
if(strncmp("LENGTH:",cbuf,7)==0){                   /* length of trace in secs */
  *ptlength=atoi(&cbuf[7]);
  }
if(strncmp("SAMPLES:",cbuf,8)==0){                  /* length of trace in samples */
  *sampertr=atoi(&cbuf[8]);                         /* if = 9999 then calculate */
  }                                                 /* length from ptlength.*/
if(strncmp("COMMENTS:",cbuf,9)==0){                 /* This must be the last line of */
  data_flag=0;                                      /* options file.          */
  }
 }
fclose(fpopt);

} /* END */

/******************** RSTAT ********************/
/* PAM 1990 */
/* Modified by C.Pierce to cope with all lats and longs */
    /* reads in the data for the channel in question */

rstat( char chan[], char *sfile, SHDR *ps, THDR *pt, struct time *ptc)
{
/* DEFINE the form of the station input lines ready to read them in. */

#define FORM  "%6c %4s %d %d %lf %10s %1s %10s %1s %d \
          %2s%ld%*1c"

#define VAR schan,cname,&elev,&datelv,&depth,lat, \
        &latn,longdit,&longn,&gain,type,&tcorr

int elev, datelv;
int c,gain, match;
double depth,lg ,lt;
long tcorr;
unsigned char statn[5],cname[5],type[3],lat[10],longdit[10];
unsigned char latn,longn,channo[3];
unsigned char schan[7];

/* OPEN the station file */

if((fpstat=fopen(sfile, "r"))==NULL){
  fail('3',fpstat,sfile);
```

```
  }
match=0;                                /* FIND correct station and channel */
while(match==0){
  if((strcmp(statn,pt->statn)==0)&&(strcmp(chan,channo)==0)){
      match=1;                          /* Does it match ? */
  }else{                                 /* if not, get next line */
      if((c=fscanf(fpstat,FORM,VAR))==EOF){
        fail('4',fpstat,sfile);         /* end of file */
      }else if(c==0){
        fail('5',fpstat,sfile);         /* file is empty */
        }
      schan[6]='\0';
      sscanf(schan,"%4c%s",statn,channo);
      }
  }
/* calculate the correction time */
ptc->sec=tcorr/1000L;           /* tcorr is specified in stat file */
ptc->msec=tcorr%1000L;
while(ptc->sec>=60){
  ptc->min++;
  ptc->sec-=60;
  }
while(ptc->min>=60){
  ptc->min-=60;
  ptc->hour++;
  }
while(ptc->hour>=24){
  ptc->day++;
  ptc->hour-=24;
  }
                                /* COPY values into header */
pt->relv.elv=elev*pt->escale;       /* reciever elevation */
pt->relv.datum=datelv*pt->escale;       /* datum elevation   */
dtol(depth,pt->escale,&pt->relv.water);     /* water depth at reciever */

lg=ltosec(longdit);                     /* convert lat/long to secs (double) */
lt=ltosec(lat);
            /* convet double to long without rounding errors */
dtol(lg,pt->cscale,&pt->rco.lgdit);         /* reciever longditude */
dtol(lt,pt->cscale,&pt->rco.lat);           /* reciever latitude */
pt->gain=gain;                          /*instrument gain */

}  /* END */

/******************** ROEVENT ******************************/
/* PAM 1990 */
    /* reads in the information for the first event ccontained in the pdasdata file by matching the
finding the event time just before the start of the pdas tape. */
/***** OLD VERSION - NEW VERSION IS REVENT WHICH DEALS WITH ALL LATS AND
LONGS AND ALSO INCLUDES THE SIZE OF THE SHOT IN THE HEADER. THIS VERSION
READS THE OLD STYLE EVENT FILE ****/

roevent( char *efile, SHDR *ps, THDR *pt, struct time *pst)
{
/* DEFINE the form of the event input lines ready to read them in. */

#define KIND "%2ld%2d%2d%2d%3d%4ld%9s%9s%6lf%4ld%4ld%6lf%4d"
#define STRING &lineno, &ehour, &emin, &esec, &emsec, &shotno, \
ltit, lgdit,&sdepth, &elev, &datum, &depth, &day

int i,c,d, ehour,emin, esec,emsec, day, match;
long lineno, elev, datum, shotno;
double depth,sdepth;
double lg, lt;
unsigned char event[60],ltit[10],lgdit[10];

/* OPEN the event file */

if((fpeve=fopen(efile, "r"))==NULL){
  fail('3',fpeve,efile);
  }

/*FIND the first event that occurs after the start of the buffer, psbt in the main program, pst in this
function. The pdasdata starts a trace length after this time. */

match=0;                                    /* look for a match */
while(match==0){
  if((d=fscanf(fpeve,"%58c", event))==EOF){     /* READ the event file */
    fail('4',fpeve,efile);                  /* event not in efile  */
```

```
  }else if(d==0){
     fail('5',fpeve,efile);                    /* no data in event file */
  }
  event[57]='\0';
  for(i=0;i<=56;i++){                          /* replace spaces with zeros */
     if(event[i]==' '){
        event[i]='0';
        }
     }

sscanf(event,KIND,STRING);

/* SEE if the event read comes just after the start of the buffer, if it does, write values into the
header, otherwise get the next event */
   if(day>pst->day){
    match=1;
   }else if(day==pst->day){
    if(ehour>pst->hour){
     match=1;
    }else if(ehour==pst->hour){
     if(emin>pst->min){
      match=1;
     }else if(emin==pst->min){
      if(esec>pst->sec){
       match=1;
      }else if(esec==pst->sec){
       if(emsec>=pst->msec){
        match=1;
       }
      }
     }
    }
   }
}


 /* WRITE values to headers */

 lg=olltosec(lgdit);                           /* convert lat/long to secs */
 lt=olltosec(ltit);
                                                        /* convert double to long */
dtol(lg,pt->cscale,&pt->sco.lgdit);          /* source longditude */
dtol(lt,pt->cscale,&pt->sco.lat);            /* source latitude   */
ps->line=lineno;                             /* line number */
pt->selv.elv=elev*pt->escale;
pt->selv.datum=datum*pt->escale;
                                  /* values are zero because datum is sea level */
dtol(depth,pt->escale,&pt->selv.water);
dtol(sdepth,pt->escale,&pt->sdepth);
pt->source=shotno;                                      /* shot number */
pt->event.year=pst->year;                    /* year as read from the pdas header */
pt->event.day=day;                           /* time of first event for this tape */
pt->event.hour=ehour;
pt->event.min=emin;
pt->event.sec=esec;
pt->event.msec=emsec;

}  /* END */

/******************** RNXTOEVENT *****************************/
/* PAM 1990 */
     /* reads the next event from the event file pointed to by fpeve */
/* OLD VERSION- NEW VERSION = RNXTEVENT, MODIFIED TO READ THE MODIFIED
EVENT FILE */

rnxtoevent( SHDR *ps, THDR *pt, struct time *pst)
{
/* DEFINE the form of the event input lines ready to read them in. */

#define KIND "%2ld%2d%2d%2d%3d%4ld%9s%9s%6lf%4ld%4ld%6lf%4d"
#define STRING &lineno, &ehour, &emin, &esec, &emsec, &shotno, \
ltit, lgdit,&sdepth, &elev, &datum, &depth, &day

int i,c,d, ehour,emin, esec,emsec, day, match;
long lineno, elev, datum, shotno;
double depth,sdepth;
double lg, lt;
unsigned char event[60],ltit[10],lgdit[10];
int lineflag=0;
```

```
if((d=fscanf(fpeve,"%58c", event))==EOF){        /* READ the event file */
fail('4',fpeve,efile);                           /* event not in efile  */
   printf("End of Event file reached");
   lineflag=2;
}else if(d==0){
   fail('5',fpeve,efile);                                  /* no data in event file */
}
event[57]='\0';
for(i=0;i<=56;i++){                              /* replace spaces with zeros */
   if(event[i]==' '){
      event[i]='0';
      }
   }
if(lineflag !=2){
  sscanf(event,KIND,STRING);

  /* WRITE values to headers */

  lg=olltosec(lgdit);                                     /* convert lat/long to secs */
  lt=olltosec(ltit);
                                                 /* convert double to long */
  dtol(lg,pt->cscale,&pt->sco.lgdit);             /* source longditude */
  dtol(lt,pt->cscale,&pt->sco.lat);               /* source latitude   */
  if(lineno !=ps->line){
     lineflag=1;
     ps->line=lineno;                    /* line number */
     }
  pt->selv.elv=elev*pt->escale;
  pt->selv.datum=datum*pt->escale;
                              /* values are zero because datum is sea level */
  dtol(depth,pt->escale,&pt->selv.water);
  dtol(sdepth,pt->escale,&pt->sdepth);
  pt->source=shotno;                                      /* shot number */
  pt->event.year=pst->year;               /* year as read from the pdas header */
  pt->event.day=day;                      /* time of first event for this tape */
  pt->event.hour=ehour;
  pt->event.min=emin;
  pt->event.sec=esec;
  pt->event.msec=emsec;
  }
```

```
return lineflag;

} /* END */
```

4. UTIL.C

```
#include <stdio.h>
#include <stdlib.h>
#include <math.h>
#include <ctype.h>
#include <dos.h>
#include "convert.h"
                                        /* UTIL.C */
        /* FUNCTIONS - general utiliy functions */

unsigned char dat_dir[]={"u:\\"};          /* virtual drive assigned in the batch */
unsigned char out_dir[]={"v:\\"};                  /* file PTOS.BAT u-> data v->segy */

/* ************* FEXIST ********************************** */
/* - checks for the existance of a file and if read access is allowed. Returns TRUE or FALSE as
defined in CONVERT.H. This is the only routine that uses a MS-DOS specific command. If
neccessary it may be replaced by trying to open the file but that takes time. */

fexist(char filename[])
{
struct find_t file;

if((_dos_findfirst(filename,_A_NORMAL,&file))==0){  /* see if file exists */
   return(TRUE);
}else{
   return(FALSE);
   }
} /* END */


/* ******************** MKPFILE ************************** */
/* PAM 1990 */
/* creates the name of the pdasdata file from the channel number,serial number, count and the
day. pfile, pt and ps are defined in convert.h and are external variables to the program */

mkpfile(char *pfile, char fltype, short chan, short serial ,short count,
     short pdasday){
int i, j;
unsigned char name[20];
unsigned char hchan;
for(i=0;i<20;i++){name[i]=0;}

strcpy(pfile, &dat_dir[0]);                /* copy root directory */
name[0]=fltype;                            /* make the pdas filename */
j=1;
hchan=itohex(chan);
j+=sprintf(&name[1],"%1c%3d%3d",hchan,serial,count);
name[8]='.';
j+=sprintf(&name[9],"%3d",pdasday);
name[j+1]='\0';
for(i=0;i<=j;i++){                         /* replace spaces with zeros */
  if(name[i]==' '){
    name[i]='0';
    }
  }
strcat(pfile,&name[0]);                            /* copy filename on the root directory */
return(0);
}  /* END */

/**************** FAIL *************************/
/* PAM 1990 */
     /*  error messages, c is the error message number called from the program */

fail(char c, FILE *fp, unsigned char filenm[])
{
switch (c){
  case '1':
    printf("\n Command line incorrect \n");
    break;
  case '2':
    printf(" File(s) do not exist\\no read access \n");
    break;
  case'3':
    printf("\n ******** Error opening %s ****** \n",filenm);
    break;
  case '4':
    printf("\n ******* value not found in %s ******** \n",filenm);
    break;
  case '5':
```

```
      printf("\n ******* no data in %s ******** \n",filenm);
      break;
    case '6':
      printf("\n ******* attempt to duplicate tracefile %s *****\n",filenm);
      break;
    case '7':
      printf("\n ***** Data type wrong in %s ****** \n",filenm);
      break;
    case '8':
      printf("\n ** Cannot delete %s ** \n",filenm);
      break;
    default:
      printf( "\n Wrong call to FAIL. \n");
      break;
    }
if(fp !=NULL){ fclose(fp);}                    /* close file pointer */
fcloseall();
exit(1);
}     /* END */

/***************** DTOL ****************************/
/* PAM 1990 */
  /* converts a long double to a long integer without the rounding off pronblems sometimes seen */

dtol(double value,short scalar, long *panswer)
{
double tmp;
long result;
int decimal,sign;
char *string;
int precision=0;

tmp=value*scalar;                              /* multiply by scalar to make real */
string=fcvt(tmp,precision,&decimal,&sign);     /* read into string up to point */
*panswer=atol(string);                         /* convert sting to long */
}     /* END */

/****************** LTOSEC ***********************************/
/* PAM 1990 */
/* altered by C.Pierec 1991 to read 3digits for degrees */
/* Convert lat and long into secs of arc and returns result */

double ltosec(char s[])
{
double answer,secs;
double degrees,minutes;
sscanf(&s[0], "%3lf",&degrees);
sscanf(&s[3],"%2lf", &minutes);
sscanf(&s[5],"%5lf",&secs);
answer=secs+(degrees*3600.0)+(minutes*60.0);
return answer;
}     /* END */


/***************OLLTOSEC ****************************/
/* PAM 1990 */
/* Convert lat and long into secs of arc and returns result */

double olltosec(char s[])
{
double answer,secs;
double degrees,minutes;
sscanf(&s[0], "%2lf",&degrees);
sscanf(&s[2],"%2lf", &minutes);
sscanf(&s[4],"%5lf",&secs);
answer=secs+(degrees*3600.0)+(minutes*60.0);
return answer;
}     /* END */

/***************** LTODIST ***************************/
     /* Adapted from DISTAZ, A.Bowen (1985).Calculates the distance in m and the azimuth,
only dist is returned.*/
/* Modified by C.Peirce to cope with either side of Greenwich */

long ltodist(THDR  *pt)
{
double lt1,lg1,lt2,lg2;
double esq1rt,e,rrlt1,rrln1,rrlt2,rrln2,dln,snlt1,snlt2,cslt1,cslt2,tnlt1;
double rn1,rn,rt,a,rg,rh,sna,csa,rs,rhsq,d;
long dist;
```

```
/* set constants */
double std=3600.00;                     /* secs to degrees */
double dtr=0.01745329251994329;         /* degrees to radians */
double er=6378.2064;                    /* equatorial radius */
double esq=0.00676866;                  /* square of eccentricity */
double  pi2=1.570796327;                /* pi over two */
double one=1.00;                        /* one !! */

lt1=(double)pt->rco.lat/pt->cscale;
lg1=(double)pt->rco.lgdit/pt->cscale;
lt2=(double)pt->sco.lat/pt->cscale;
lg2=(double)pt->sco.lgdit/pt->cscale;

/* calculate eccentricities */
esq1rt=sqrt(one-esq);
e=sqrt(esq);

/* convert the input coordinates to radians */
rrlt1=(lt1/std)*dtr;
rrlt2=(lt2/std)*dtr;

if(lg1<=324000.0&&lg2>=972000.0){       /* 324000 =90 deg */
   rrln2=((1296000.0-lg2)/std)*dtr;     /* 972000= 270 deg */
   rrln1=(lg1/std)*dtr;                 /* 1296000 = 360 deg */
   dln=rrln1-rrln2;
} else if(lg2<=324000.0&&lg1>=972000.0){
   rrln1=((1296000.0-lg1)/std)*dtr;
   rrln2=(lg2/std)*dtr;
   dln=-1.0*(rrln1+rrln2);
} else {
   rrln1=(lg1/std)*dtr;
   rrln2=(lg2/std)*dtr;
   dln=rrln1-rrln2;
   }

/* calculate the constants */
snlt1=sin(rrlt1);
snlt2=sin(rrlt2);
cslt1=cos(rrlt1);
cslt2=cos(rrlt2);
tnlt1=tan(rrlt1);

/* get intermediate values */
rn1=er/sqrt(one-esq*(pow(snlt2,2)));
rn=er/sqrt(one-esq*(pow(snlt2,2)));
rt=atan((one-esq)*tnlt1+(esq*rn1*snlt2)/(rn*cslt1));
a=atan2(sin(dln),(cslt2*tan(rt)-snlt2*cos(dln)));
rg=e*snlt2/esq1rt;
rh=e*cslt2*cos(a)/esq1rt;
sna=sin(a);
csa=cos(a);
if(sna==0.0){
   rs=asin(cslt2*sin(rt)-snlt2*cos(rt));
   }
if(csa>=0.0&&rs<0.0){rs=-rs;}
if(csa<0.0&&rs>0.0){rs=-rs;}
if(sna !=0.0){
   rs=asin(sin(dln)*cos(rt)/sna);
   }
rhsq=pow(rh,2);

d=rn1*rs*(one-(pow(rs,2)*rhsq*(one-rhsq)/6.0)+
(pow(rs,3)*rg*rh*(one-2.0*rhsq)/8.0)+
((pow(rs,4)/120.0)*(rhsq*(4.0-7.0*rhsq)-3.0*pow(rg,2)*(one-7.0*rhsq)))-
((pow(rs,5)/48.0)*rg*rh));
a=a/dtr;
d=fabs(d*1000.0);
dtol(d,1,&dist);

return dist;
}   /* END */

/******************** MKSFOUT ************************/
/* PAM 1989 */
    /* make the name and dirctories to contain the segyheader, then see if it already exists. If it
does then the program returns 1 and the wsegyhdr is not run. If it doesn't exist then the new
header is written to file SEGY.HDR in directory ie L6BS5P. File pointer to this file is fpsout as
defined in convert.h */
```

```
mksfout(char *sfout, SHDR *ps, THDR *pt)
{
int a, p;
unsigned char  statnm[4];
unsigned char newdir[40];
unsigned char fileout[40];

strcpy(newdir, &out_dir[0]);                    /* make name of base directory */
strcat(newdir, "\");
a=strlen(newdir);
sprintf(&newdir[a],"%d%s",(short)ps->line,pt->statn);
mkdir(newdir);                                  /* make linestation directory */
strcpy(sfout,newdir);
strcat(sfout,"\\segy.hdr");

/* OPEN the segyheader file if it doesn't already exist */
p=0;
if(fexist(sfout)==TRUE){
   p=1;
   }
if(p==0){
   if((fpsout=fopen(sfout,"wb"))==NULL){
      fail('3',fpsout,sfout);
      }
   }
return p;
}     /* END */

/****************** MKTFOUT ***************************/
/* make the trace output file */

mktfout(char *tfout, SHDR *ps, THDR *pt)
{
int a;
unsigned char newdir[40];
unsigned char name[20];
unsigned char point='.';

strcpy(newdir, &out_dir[0]);                    /* make name of base directory */
strcat(newdir, "\");
a=strlen(newdir);
sprintf(&newdir[a],"%d%s",(short)ps->line,pt->statn);
strcat(newdir,"\\");
a=strlen(newdir);
sprintf(&newdir[a],"%s",pt->channel);
mkdir(newdir);                                  /* make channel directory */
strcat(newdir,"\\");
a=strlen(newdir);
sprintf(&newdir[a],"%d",pt->start.day);
mkdir(newdir);                                  /* make day directory */
strcpy(tfout,newdir);
strcat(tfout,"\\");                             /* make file name  */
sprintf(&name[0],"%d%d%d%c%d",pt->start.hour,pt->start.min,pt->start.sec,\
point,pt->trace);
strcat(tfout,name);
if(fexist(tfout)==TRUE){                        /* check to see if the file slready exists */
   fail('6',NULL,tfout);
   }
if((fptout=fopen(tfout,"wb"))==NULL){           /* opentrace file, write binary */
   fail('3',fptout,tfout);
   }
}     /* END */

/****************** DGR ***************************/
/* PAM 1990 */
/*  Designed by R. Long 1990. Degainranges the pdasdata files and returns a 4-byte floating
point number */
float dgr(short grdata)
{
float fman,v;
short exp;
int i;
long mult=268435456;
fman=grdata&0xfffc;
exp=5-(grdata&0x0003);
if(exp<0){
   for(i=exp;i<0;i++){
      fman=fman/8.0;
      }
}else{
```

```
  for(i=0;i<exp;i++){
    fman=fman*8.0;
    }
  }
if(strcmp(pt->channel,"MSF ")==0){
  v=20*(fman/mult)/pt->gain;
}else{
  v=(fman/mult)/pt->gain;
  }
return(v);
} /* END */

/****************** TADD ******************************/
/* PAM 1990 /
/* Adds time two to time one while maintaining structure type */

tadd(struct time *pt1, struct time *pt2)
{
pt1->msec+=pt2->msec;                    /* msec */
while(pt1->msec<0||pt1->msec>=1000){
  if(pt1->msec<0){
    pt1->sec--;
    pt1->msec+=1000;
  }else if(pt1->msec>=1000){
    pt1->sec++;
    pt1->msec-=1000;
    }
  }
pt1->sec+=pt2->sec;                              /* seconds */
while(pt1->sec<0||pt1->sec>=60){
  if(pt1->sec<0){
    pt1->min--;
    pt1->sec+=60;
  }else if(pt1->sec>=60){
    pt1->min++;
    pt1->sec-=60;
    }
  }
pt1->min+=pt2->min;                      /* minutes */
while(pt1->min<0||pt1->min>=60){
  if(pt1->min<0){
    pt1->hour--;
    pt1->min+=60;
  }else if(pt1->min>=60){
    pt1->hour++;
    pt1->min-=60;
    }
  }
pt1->hour+=pt2->hour;                    /* hours */
while(pt1->hour<0||pt1->hour>=24){
  if(pt1->hour<0){
    pt1->day--;
    pt1->hour+=24;
  }else if(pt1->hour>=24){
    pt1->day++;
    pt1->hour-=24;
    }
  }
pt1->day+=pt2->day;                              /* days (leap year or not ) */
  if(pt1->day<0){
    if((pt1->year%4==0&&pt1->year%100 !=0)||pt1->year%400==0){
      pt1->day+=366;
    }else{
      pt1->day+=365;
      }
    pt1->year--;
  }else if(pt1->day>=365){
    pt1->year++;
    if((pt1->year%4==0&&pt1->year%100!=0)||pt1->year%400==0){
      if(pt1->day>=366){
        pt1->day-=366;
      }else{
        pt1->year--;
        }
    }else{
      pt1->day-=365;
      }
    }
  pt1->year+=pt2->year;                  /* years */
    if(pt1->year<0){
```

```
        printf("\n opps past the beginning of time");
        exit(1);
        }
} /* END */

/****************** TSUB ************************/
/* PAM 1990 */
/* subtract time two from time one keeping time structure */

tsub(struct time *pt1, struct time *pt2)
{
pt1->msec-=pt2->msec;                    /* milliseconds */
while(pt1->msec<0||pt1->msec>=1000){
   if(pt1->msec<0){
      pt1->sec--;
      pt1->msec+=1000;
   }else if(pt1->msec>=1000){
      pt1->sec++;
      pt1->msec-=1000;
      }
   }
 pt1->sec-=pt2->sec;                              /* seconds */
 while(pt1->sec<0||pt1->sec>=60){
   if(pt1->sec<0){
      pt1->min--;
      pt1->sec+=60;
   }else if(pt1->sec>=60){
      pt1->min++;
      pt1->sec-=60;
      }
  }
 pt1->min-=pt2->min;                              /* minutes */
 while(pt1->min<0||pt1->min>=60){
    if(pt1->min<0){
      pt1->hour--;
      pt1->min+=60;
    }else if(pt1->min>=60){
      pt1->hour++;
      pt1->min-=60;
      }
  }
pt1->hour-=pt2->hour;                            /* hours */
while(pt1->hour<0||pt1->hour>=24){
  if(pt1->hour<0){
     pt1->day--;
     pt1->hour+=24;
  }else if(pt1->hour>=24){
     pt1->day++;
     pt1->hour-=24;
     }
  }
pt1->day-=pt2->day;                              /* days */
  if(pt1->day<0){
     if((pt1->year%4==0&&pt1->year%100 !=0)||pt1->year%400==0){
        pt1->day+=366;
     }else{
        pt1->day+=365;
        }
     pt1->year--;
   }else if(pt1->day>=365){
     pt1->year++;
     if((pt1->year%4==0&&pt1->year%100!=0)||pt1->year%400==0){
        if(pt1->day>=366){
           pt1->day-=366;
        }else{
           pt1->year--;
           }
     }else{
        pt1->day-=365;
        }
     }
  pt1->year-=pt2->year;                          /* years */
     if(pt1->year<0){
        printf("\n opps past the beginning of time");
        exit(1);
        }
} /* END */

/************* DIFFERENCE ************************/
/* PAM 1990 */
```

```
/* calculates the difference between time1 and time2 in milliseconds */

long difference(struct time time1, struct time time2)
{
long diff=0;
int year;
long stomsec=1000;
long mtomsec=60000;
long htomsec=3600000;
long dtomsec=86400000;
struct time *p1, *p2;

p1=&time1;
p2=&time2;
diff=p1->msec-p2->msec;                 /* millsecs*/
diff+=(p1->sec-p2->sec)*stomsec;        /* + secs converted to msec */
diff+=(p1->min-p2->min)*mtomsec;        /* + mins in secs */
diff+=(p1->hour-p2->hour)*htomsec;      /* + hours in secs */
diff+=(p1->day-p2->day)*dtomsec;        /* + days in seconds */
if((year=p1->year-p2->year)<=1&&year>=-1){
   if((p1->year%4==0&&p1->year%100 !=0)||p1->year%400==0){
      diff+=year*366*dtomsec;
   }else{
      diff+=year*365*dtomsec;
      }
}else{
   printf("\n Time difference is too great ");
   exit(1);
   }
return diff;
} /* END */

/************ MKTAPE ************************/
/* PAM 1990 */
/* make the directory and the file to contain the combined segy tape, then see if it already exists, if
it does then write the traces out to it. \if it doesn't then a new segy header is written to the  newly
created file. File pointer is fpsout, fptout is assigned to the same point so that traces are written to
the file. */

mktape(char *tfout, char *thfout, SHDR *ps, THDR *pt)
{
int a,p,i;
unsigned char newdir[40];
unsigned char fileout[40];
unsigned char statnm[5], channm[5];

strcpy(newdir, &out_dir[0]);
strcat(newdir,"l");
a=strlen(newdir);
i=0;
while(isalnum(pt->statn[i])){
   statnm[i]=pt->statn[i];
   i++;
   }
statnm[i]='\0';
sprintf(&newdir[a],"%d%s",(short)ps->line,statnm);
strcat(newdir,"\\");
a=strlen(newdir);
i=0;
while(isalnum(pt->channel[i])){
   channm[i]=pt->channel[i];
   i++;
   }
channm[i]='\0';
sprintf(&newdir[a],"%s",channm);
mkdir(newdir);
strcat(newdir,"\\");
a=strlen(newdir);
sprintf(&newdir[a],"%ld",ps->reel);
strcat(newdir, "_l");
a=strlen(newdir);
sprintf(&newdir[a],"%d%s", (short)ps->line,statnm);
strcpy(thfout,newdir);
strcat(thfout,".bth");
strcpy(tfout,newdir);
strcat(tfout,".btd");

/* open tape files if they don't already exist */
p=0;
if(fexist(tfout)==TRUE||fexist(thfout)==TRUE){
```

```
   p=1;
   }
if(p==0){
   if((fptout=fopen(tfout,"wb"))==NULL){
      fail('3',fptout,tfout);
      }
   if((fpthout=fopen(thfout,"wb"))==NULL){
      fail('3',fpthout,thfout);
      }
   }
return p;
}   /* END */

/***************** MKREEL ***************************/
/* PAM 1989 */
    /* make the name and dirctories to contain the segyheaders, then see if it already exists. If it
does then the program returns 1. Two files are created one for the ascii bit and one for the binary
section, pointers are fpsout ( to sfout) and fpsbout to the binary section sbfout. */

mkreel(char *sfout, char *sbfout, SHDR *ps, THDR *pt)
{
int a, p, i;
unsigned char newdir[40];
unsigned char fileout[40];
unsigned char statnm[5], channm[5];

strcpy(newdir, &out_dir[0]);
strcat(newdir, "l");
a=strlen(newdir);
i=0;
while(isalnum(pt->statn[i])){
   statnm[i]=pt->statn[i];
   i++;
   }
statnm[i]='\0';
sprintf(&newdir[a],"%d%s",(short)ps->line,statnm);
mkdir(newdir);                              /* make linestation directory */
strcat(newdir,"\\");
a=strlen(newdir);
sprintf(&newdir[a],"%ld",ps->reel);
strcat(newdir,"_l");
a=strlen(newdir);
sprintf(&newdir[a],"%d%s",(short)ps->line,statnm);
strcpy(sfout,newdir);
strcpy(sbfout,newdir);
strcat(sfout,".hdr");
strcat(sbfout,".bfh");

/* OPEN the segyheader file if it doesn't already exist */
p=0;
if(fexist(sfout)==TRUE){
   p=1;
   }
if(p==0){
   if((fpsout=fopen(sfout,"w"))==NULL){
      fail('3',fpsout,sfout);
      }
   if((fpsbout=fopen(sbfout,"wb"))==NULL){
      fail('3',fpsbout,sbfout);
      }
   }
return p;
}    /* END */

/***************** ITOHEX ********************************/
/* PAM 1990 */
/* converts digit to a hexidecimal number */

unsigned char itohex(int number){
char hexno;
char buffer[2];

if(number<10){
   itoa(number,buffer,10);
   hexno=buffer[0];
}else{
   if(number==10) hexno='A';
   if(number==11) hexno='B';
   if(number==12) hexno='C';
   if(number==13) hexno='D';
```

```
  if(number==14) hexno='E';
  if(number==15) hexno='F';
  if(number>15){
     printf("\nNo single char hex equivalent.");
     exit(1);
     }
  }
return(hexno);
}

/***************** HEXTOI ****************************/
/* PAM 1990*/
/* Changes a hexidecimal number to an integer */

short hextoi(unsigned char hexchar){
short intno;
unsigned char buffer[2];
int a;

if((a=isdigit(hexchar))!=0){
   buffer[0]=hexchar;
   buffer[1]='\0';
   intno=atoi(buffer);
}else{
   switch(hexchar){
            case 'A':   intno=10; break;
            case 'B': intno=11; break;
            case 'C': intno=12; break;
            case 'D': intno=13; break;
            case 'E':   intno=14; break;
            case 'F': intno=15; break;
      default :
         printf("\n Non hexidecimal number ");
         exit(1);
         break;
      }
   }
 return(intno);
 }
```

5. WRITE.C

```
                                        /*WRITE.C */
#include <stdio.h>
#include <io.h>
#include <malloc.h>
#include "convert.h"

/**************** WRITE.C ********************************/
/* Files to write the headers and the data to the correct directories. Traces are in individual files or
data files and header files in the channel directories for each line/station. All of the integers are
stored with the high order byte in the lowest address (i.e. backwards from the standard P.C.
frormat). Each line/station directory has a segy header (3600bytes) and the data values for each
trace are preceeded by a 240 byte header. The byte order must be reversed for long and short
integers and for the floating point data, as the values are to be used on a Sun Unix system but
are written on the DOS based PC. */

/**************** WASCSHDR ********************************/
/* PAM 1990 */
/* Write the ascii part of the segy header to its file. If the combine option is chosen then the segy
header is written in two parts, 1 ascii and 1 binary. */

wascshdr(SHDR *ps ,FILE *fpa)
{
unsigned char space=' ';                /* Blank value to fill unused bytes */
int i;

fprintf(fpa,"%s",ps->project);                          /* write the ASCII section */
for(i=strlen(ps->project);i<3200;i++){  /* fill in the rest with blanks */
   fputc(space,fpa);
   }
}/* END */

/************** WSPLIT ****************************/
/* PAM 1990 */
/*  Split the trace out from the PDAS data file, depending on the sample rate and the length
specified in the options file. Trace starts at pt->start and has length determined by the options
file. If there is no PDAS data for a certain trace then write a blank value out to it. If there is any
data left over from
the previous pfile then the routine checks to see whether it is included in the new trace. */

int  wsplit(unsigned long  gaplength, char datatype, unsigned long *c)
{
unsigned char *ptr;
char p[5];
static long bufflength;         /* Previous pfile */
static long intold;             /* sample int for buffer */
static long sampold;                    /* length of old trace in samples */
static int tsize;               /* size of trace written */
int i,j,k;
int problem=0;
float blank=0.0;                /* fillin value */
static float buffer[12000];
fpos_t pos;                     /* file pointer to trace start */
float value;
long *ldata,offset,length,position;
short *sdata;

/* Move the pdas file pointer fppdas back to the beginning of the data in teh
pfile. */

if(fsetpos(fppdas,&data_strt) !=0){     /* set pointer to start of pdasdata */
   perror("fsetpos error");
   }

if(*c>gaplength){                               /* if the trace starts in the pfile... */
   offset=*c-gaplength;                 /* offset in samples */
                                        /* Is the data gainranged ? */
   if(datatype=='L'){
      offset*=4;                        /* offset in bytes (long) */
      fseek(fppdas,offset,SEEK_CUR);    /* find start of the trace  */
      fgetpos(fppdas,&pos);                     /* remember the start point */
   }else{
      offset*=2;                        /* offset in bytes (short) */
      fseek( fppdas,offset,SEEK_CUR);   /*find start of the trace  */
      fgetpos(fppdas,&pos);                     /* remember the start point */
      }
}
length=filelength(fileno(fppdas));      /* find the length of the pfile */

/* If the trace starts after the buffer then set the buffer to zero ready for
```

```
the next time. */
if(*c>=bufflength&&bufflength !=0&&tsize==0||pt->trace==1){
   bufflength=0;                          /* cancel reading the buffer */
   }

if(pt->trace==1){
   intold=pt->intvl;
   sampold=pt->sample;
   tsize=0;
   }                                                  /* start from the begining */

/* If the trace is incomplete and a new pdas file has been found to finish it then check that the old
and new sample rates are the same. If not then pad the trace with blanks and use the old sample
rate */

if(pt->intvl !=intold){                   /* if the sample rate changes.... */
   for(i=tsize;i<sampold;i++){            /* complete the trace with blanks */
      ptr=(unsigned char *)&blank;
      ptr+=3;
      for(j=0;j<4;j++){
         fputc(*ptr,fptout);
         ptr--;
         }
      }
      problem=0;                          /* trace completes */
      sampold=pt->sample;
      intold=pt->intvl;
      bufflength=0;              /* empty buffer */
}else{
/* extract the trace from the buffer or/and the pfile */

for(i=tsize;i<pt->sample;i++){   /* write the trace length requested */
   if(*c<bufflength){            /* if there is some data left over from */
      k=*c/4;                          /* the last pfile, read that 1st. */
      ptr=(unsigned char *)&buffer[k];
   }else if(*c<gaplength){      /* if the new file hasn't started write blanks */
      ptr=(unsigned char *)&blank;
   }else{
     if((position=ftell(fppdas))<length){              /* if in the pfile...*/
      switch(datatype){

case 'L':                                  /* degainranged data */
   p[0]=fgetc(fppdas);
   p[1]=fgetc(fppdas);                                  /* pdas data file. */
   p[2]=fgetc(fppdas);
   p[3]=fgetc(fppdas);
   p[4]='\0';
   ldata=(long *)&p[0];
   value=(float)*ldata;
   break;

case 'G':                                  /* Gainranged data */
   p[0]=fgetc(fppdas);
   p[1]=fgetc(fppdas);
   p[2]='\0';
   sdata=(short *)&p[0];
   value=dgr(*sdata);                      /* degainrange data */
   break;

case 'O':                        /* integer data (geostore) */
   p[0]=fgetc(fppdas);
   p[1]=fgetc(fppdas);
   p[2]='\0';
   sdata=(short *)&p[0];
   *sdata-=2048;                 /* offset binary data */
   value=(float)*sdata;
   break;

case 'I':
   p[0]=fgetc(fppdas);
   p[1]=fgetc(fppdas);
   p[2]='\0';
   sdata=(short *)&p[0];
   value=(float)*sdata;
   break;

default:                                   /* error in option specification */
   fail('7',fptout,tfout);
   break;
}
   ptr=(unsigned char*)&value;
```

```
}else{                                  /* if you run out of data.....*/
  printf("\n next file required to complete trace. \n");
  problem=1;                    /* trace status 1....need next file */
  intold=pt->intvl;                     /* remember the sample intvl for buffer */
  sampold=pt->sample;   /* remember trace length in samples */
  *c=0;                         /* zero the count for the beginning of the next go */

  fsetpos(fppdas,&pos);   /* reset pointer to the start of trace */
  for(k=0;k<i;k++){             /* write partial trace to buffer */
   switch(datatype){
   case 'L':                            /* degainranged data */
      p[0]=fgetc(fppdas);
      p[1]=fgetc(fppdas);               /* pdas data file. */
      p[2]=fgetc(fppdas);
      p[3]=fgetc(fppdas);
      p[4]='\0';
      ldata=(unsigned long *)&p[0];
      buffer[k]=(float)*ldata;
      break;

   case 'G':                    /* Gainranged data */
      p[0]=fgetc(fppdas);
      p[1]=fgetc(fppdas);
      p[2]='\0';
      sdata=(short *)&p[0];
      buffer[k]=dgr(*sdata);
      break;

   case 'I':
      p[0]=fgetc(fppdas);
      p[1]=fgetc(fppdas);
      p[2]='\0';
      sdata=(short *)&p[0];
      buffer[k]=(float)*sdata;
      break;

   case 'O':
      p[0]=fgetc(fppdas);
      p[1]=fgetc(fppdas);
      p[2]='\0';
      sdata=(short *)&p[0];
      *sdata-=2048;
      buffer[k]=(float)*sdata;
      break;

     default:                   /* error in option specification */
       fail('7',fptout,tfout);
       break;
       }
     (*c)+=4;
     }
    bufflength=*c;              /* length of the buffer */
    break;
    }
  }

    ptr+=3;                             /* reverse the byte order... */
    for(j=0;j<4;j++){                   /* write 4-byte floating point no. char by char */
      fputc(*ptr,fptout);
      ptr--;
      }
    (*c)++;
  }
} /* end of the 'sample int change' if statement */

tsize=i;                        /* tsize=0 if trace is complete */
if(problem==0){                         /* if trace isn't finished don't close it */
  tsize=0;
  }
return problem;
} /* END */

/************ WFILL ********************************/
/* PAM 1990 */
/* fillin the remainder of the trace with blanks */

int  wfill(unsigned long  length )
{
unsigned char *ptr;
int j;
```

```
int problem=0;
float blank=0.0;
long position;

while((position=ftell(fptout)%length) !=0){  /* until trace is the right length */
   ptr=(unsigned char *)&blank;                    /* fill out with zeros */
   ptr+=3;
   for(j=0;j<4;j++){                               /* write 4bytefloating point no char by char */
      fputc(*ptr,fptout);
      ptr--;
      }
   }
return problem;
} /* END */

/************ WBINTSHDR ****************************/
/* PAM 1990 */
/* Write the segy header to its file , segy.hdr. The file is created and opened in  MKSFOUT in
UTIL.C and file pointer fpsout assigned to it. The file is written in an internal format with all 2byte
integers outputted as 4-byte integers. This makes the data more portable although it's not really
segy. */

wbintshdr(SHDR *ps , FILE *fpb)
{
unsigned char *cptr;
int i;
long lghdr[17];                          /* array for long integers  */
long blank[48];

for(i=0;i<17;i++){lghdr[i]=0;}     /* zero the array */
for(i=0;i<48;i++){blank[i]=0;}

lghdr[16]=ps->notr;
lghdr[15]=ps->nonseis;                   /* copy long values into long array */
lghdr[14]=1;
lghdr[13]=ps->period;
lghdr[11]=ps->number;                    /* in reverse order, to make it */
lghdr[7]=1;                        /* easier to reverse the byte order. */
lghdr[3]=ps->format;
lghdr[2]=ps->reel;
lghdr[1]=ps->line;
lghdr[0]=ps->measure;

cptr=(unsigned char *)&lghdr[16];        /* convert the array to 1byte chars */
cptr+=3;                                 /* Move to the end  */
for(i=1;i<=56;i++){                              /* and write them out one by one  */
   fputc(*cptr,fpb);                     /* backwards */
   cptr--;
   }
cptr=(unsigned char *)&lghdr[2];
cptr+=3;
for(i=57;i<=112;i++){
   fputc(*cptr,fpb);
   cptr--;
   }

cptr=(unsigned char *)&blank[47];          /* Pad file out to 400 bytes */
cptr+=3;
for(i=112;i<400;i++){
   fputc(*cptr,fpb);
   cptr--;
   }
}     /* END */

/***************** WINTTHDR ********************/
/* PAM 1990 */
/* write the trace header to the start of the trace file created in MKTFOUT in UTIL.C. File pointer
is fptout and file is left open so that the trace data can be written to the same file,
WRTRACEDAT. If the OPTION COMBINE is chosen then there is a different file pointer for the
trace headers and for the corrosponding data and they are written to different files. Again the
format is not really segy, 2byte values are written as 4byte. */

wintthdr(THDR *pt, FILE *fp)
{
unsigned char *cptr;
long  lghdr[46];
long xtra[32];
long blank[54];
float flhdr[17];
```

```
float ntomi=1000;
unsigned char ascii[9];
int i;

for(i=0;i<46;i++){lghdr[i]=0;}     /* zero the main output array */
for(i=0;i<17;i++){flhdr[i]=0;}
for(i=0;i<32;i++){xtra[i]=0;}
for(i=0;i<54;i++){blank[i]=0;}

strcpy(ascii,pt->statn);           /* create a string for the ascII code */
strcat(ascii,pt->channel);

lghdr[43]=pt->trace;               /* copy long variables to a long array */
lghdr[42]=pt->trace;
lghdr[41]=pt->source;
lghdr[40]=1;                              /* copy short variables into the correct place */
lghdr[39]=pt->utrace;
lghdr[38]=pt->trid;
lghdr[34]=pt->cunits;
lghdr[26]=pt->delay.msec;
lghdr[23]=pt->sample;
lghdr[13]=pt->alias.freq;
lghdr[12]=pt->alias.slope;
lghdr[9]=pt->low.freq;
lghdr[7]=pt->low.slope;
lghdr[5]=pt->start.year;
lghdr[4]=pt->start.day;
lghdr[3]=pt->start.hour;
lghdr[2]=pt->start.min;
lghdr[1]=pt->start.sec;
lghdr[0]=pt->tbasis;

flhdr[16]=pt->dist;
flhdr[15]=pt->relv.elv/(float)pt->escale;          /* un scale and convert to float */
flhdr[14]=pt->selv.elv/(float)pt->escale;
flhdr[13]=pt->sdepth/(float)pt->cscale;
flhdr[12]=pt->relv.datum/(float)pt->escale;
flhdr[11]=pt->selv.datum/(float)pt->escale;
flhdr[10]=pt->selv.water/(float)pt->escale;
flhdr[9]=pt->relv.water/(float)pt->escale;
flhdr[8]=pt->sco.lgdit/(float)pt->cscale;
flhdr[7]=pt->sco.lat/(float)pt->cscale;
flhdr[6]=pt->rco.lgdit/(float)pt->cscale;
flhdr[5]=pt->rco.lat/(float)pt->cscale;
flhdr[2]=pt->intvl/ntomi;                  /* convert from nanosecs to microsecs */
flhdr[1]=pt->gain;

xtra[12]=pt->delay.sec;
xtra[11]=pt->start.msec;
xtra[8]=pt->event.year;
xtra[7]=pt->event.day;
xtra[6]=pt->event.hour;
xtra[5]=pt->event.min;
xtra[4]=pt->event.sec;
xtra[3]=pt->event.msec;
xtra[2]=pt->rvel;
xtra[1]=pt->rtime;
xtra[0]=pt->shotsiz;

          /* Start writing out the values.*/
cptr=(unsigned char *)&lghdr[45];     /* read as a 1byte char array  */
cptr+=3;
for(i=1;i<185;i++){                          /* i=byte number of the header  */
  fputc(*cptr,fp);                    /* output 1char at a time.     */
  cptr--;
  }
cptr=(unsigned char *)&flhdr[16];     /* float values */
cptr+=3;
for(i=185;i<253;i++){
  fputc(*cptr,fp);
  cptr--;
  }
cptr=(unsigned char *)&xtra[12];
cptr+=3;
for(i=253;i<261;i++){
  fputc(*cptr,fp);
  cptr--;
  }
cptr=&ascii[0];                       /* oops...ascii bit */
for(i=261;i<269;i++){
```

```
   fputc(*cptr,fp);
   cptr++;
   }
cptr=(unsigned char *)&xtra[8];
cptr+=3;
for(i=269;i<305;i++){
   fputc(*cptr,fp);
   cptr--;
   }
cptr=(unsigned char *)&blank[52];
cptr+=3;
for(i=305;i<=512;i++){
   fputc(*cptr,fp);
   cptr--;
   }

/* file left open. CONVERT>C controls whether traces are combined or left
seperate. */
}  /* END */
```

Isaiah 53: 1